AD-A243 436

ENHANCED BACKSCATTERING FROM ROUGH

SURFACES

DTIC

S ELECTE **D**

DEC 6 1991

C

Principal Investigator: J C Dainty
Contractor: Imperial College
Contract Number: DAJA45-87-C-0039

Final Report

APPENDIX

UNIVERSITY OF LONDON

Imperial College of Science, Technology, and Medicine

Blackett Laboratory

Applied Optics

Enhanced Backscattering of Light
from Randomly Rough Diffusers

by

Andrew Jonathan Sant

September 1991

Thesis submitted in par
requirements for the
Doctor of Philosophy
and for the
Diploma of Imperial College

DRAFT COPY

91 12 6 001

To my parents Helen and Tony,
my brother Philip,
and my wife Helen.

Acknowledgements

My sincere and unreserved thanks go to my supervisor Prof. Chris Dainty, whose encouragement and intuition have made this work a very rewarding pursuit. His genuine interest in scientific research has given me the opportunity to meet others with a similar, contagious enthusiasm on both formal and social occasions (although I will think twice about letting Manuel order, next time!).

I would particularly like to thank Professors Bob Collin and Gary Brown for the time, patience, and hospitality that they kindly afforded me — keep that Beetle rollin' Gary!

Life as a postgraduate in the Applied Optics group just would not have been the same without the wit and assistance of colleagues past and *still* present; namely the 612 lot, the 6M lot, or those down the corridor: Roddy (Bill the Cat) Cañas, Dave (the skip) Gale, Andrew Creeke, Nick (SunOS) Wooder, Andrew West, Bernie (Lucan) Dolan, Stella Cacoullis, Bron (!!) Ley, Colin Cox, Niel Bruce, Roger Troth, Kevin McKoen, Theo Mavroidis ... to name but a few! Thanks folks.

Others of whom I have required advice and assistance include the late Walter Welford, Nick Jackson, the 3rd Year Undergraduate Laboratory staff for the loan of their cylindrical lens (you can have it back now!), and Dionaea Muscipula (affectionately known as Fred) who has been a source of much philosophical inspiration to me.

I extend my gratitude to the managers of The Technology Partnership Ltd. without whose support the last few months of putting pen to paper would have been quite dire.

My parents continue to be an unfaltering source of encouragement and support for me in whatever I pursue, and it is to them that I dedicate this work. Thanks for *everything* Mum and Dad.

Finally, I can not thank my wife Helen enough for the love, patience, and answers that she gives to me on the many occasions when I can not provide my own.

Abstract

An investigation into the scattering of light by randomly rough diffusers is presented. Emphasis is placed on the phenomenon of enhanced backscattering, i.e. when the brightness of the incoherently scattered light peaks sharply in the direction of the illuminating source. Both experimental and theoretical aspects of the problem are addressed, comparing real measurements with numerical calculations.

The experimental equipment employed for this study is able to take light measurements close to the backscatter direction enabling the backscatter peak, if present, to be observed. Measurements taken from a Lambertian reflectance standard ($BaSO_4$) exhibit strong backscatter enhancement.

A method of fabricating Gaussian, randomly rough diffusers is described. Their surface proifles are characterized using a Talystep profilometer and an analysis is presented of finite-tip-size effects on the measured statistical parameters. A replication method is described which faithfully reproduces the random profile of a fabricated diffuser.

A rigorous, one-dimensional analysis based on the Helmholtz-Kirchhoff integral equation is presented. Numerical calculations are critically compared with scattered light measurements from identical, metallic and dielectric diffusers, examining the influence of the medium on the diffusers' scattering properties. The effect of changing the radiation wavelength is also investigated.

A one-dimensional, analytic solution is presented and is shown to have some validity for dielectric diffusers where single scattering is the dominant mechanism. A simple geometrical ray-tracing model produces surprisingly accurate results, even when surface structures are of the order of a wavelength.

The Mueller matrices relating the incident and scattered Stokes vectors are measured for one-dimensional diffusers. Analysis of these measurements leads to an interpretation of the scattering events at the diffuser's surface. Observations are presented confirming recently predicted scattering structures for oblique incidence on one-dimensional diffusers. These structures are clearly related to enhanced backscattering but occur away from the backscatter direction, under more general conditions.

Contents

1

List of Figures

4.20 Comparisons between experimentally measured [o] and theoretically predicted [——] scattering cross-sections. Measurements: dielectric diffuser #46; calculations: perfect dielectric. $\tau/\lambda = 0.937$ and $\sigma_h/\lambda = 0.361$; $N = 2 \times 200$ realizations; surface length $L = 40\lambda$; sampling interval $\Delta \approx \lambda/10$; refractive index $n = 1.412$; wavelength $\lambda = 3.39 \ \mu m$. $\Xi_{pp}^{rc}(\theta_i, \theta_s)$: A) $\theta_i = 0°$, B) $\theta_i = -20°$, C) $\theta_i = -40°$. 120

4.21 Comparisons between experimentally measured [o] and theoretically predicted [——] scattering cross-sections. Measurements: dielectric diffuser #46; calculations: perfect dielectric. $\tau/\lambda = 2.76$ and $\sigma_h/\lambda = 1.06$; $N = 2 \times 200$ realizations; surface length $L = 40\lambda$; sampling interval $\Delta \approx \lambda/10$; refractive index $n = 1.412$; wavelength $\lambda = 3.39 \ \mu m$. $\Xi_{ss}^{rc}(\theta_i, \theta_s)$: A) $\theta_i = 0°$, B) $\theta_i = -20°$, C) $\theta_i = -40°$. 121

4.22 Comparisons between experimentally measured [o] and theoretically predicted [——] scattering cross-sections in transmission. Measurements: dielectric diffuser #39; calculations: perfect dielectric. $\tau/\lambda = 4.69$ and $\sigma_h/\lambda = 1.86$; $N = 2 \times 200$ realizations; surface length $L = 40\lambda$; sampling interval $\Delta \approx \lambda/10$; refractive index $n = 1.411$; wavelength $\lambda = 0.633 \ \mu m$. $\Xi_{pp}^{tr}(\theta_i, \theta_s)$: A) $\theta_i = 0°$, B) $\theta_i = -20°$, C) $\theta_i = -40°$, D) $\theta_i = -60°$. 123

4.23 Comparisons between experimentally measured [o] and theoretically predicted [——] scattering cross-sections in transmission. Measurements: dielectric diffuser #39; calculations: perfect dielectric. $\tau/\lambda = 4.69$ and $\sigma_h/\lambda = 1.86$; $N = 2 \times 200$ realizations; surface length $L = 40\lambda$; sampling interval $\Delta \approx \lambda/10$; refractive index $n = 1.411$; wavelength $\lambda = 0.633 \ \mu m$. $\Xi_{ss}^{tr}(\theta_i, \theta_s)$: A) $\theta_i = 0°$, B) $\theta_i = -20°$, C) $\theta_i = -40°$, D) $\theta_i = -60°$. 124

4.24 Numerically calculated scattering cross-sections for p [——] and s [- - -] incident polarizations in transmission. $\tau/\lambda = 5.02$ and $\sigma_h/\lambda = 1.93$; $N = 2 \times 200$ realizations; surface length $L = 40\lambda$; sampling interval $\Delta \approx \lambda/10$; the refractive index has been artificially increased from $n = 1.411$ to $n = \sqrt{10.0}$; wavelength $\lambda = 0.633 \ \mu m$. $\Xi^{tr}(\theta_i, \theta_s)$: A) $\theta_i = 0°$, B) $\theta_i = -40°$. 125

4.25 Experimental scattering cross-sections measured from gold-coated diffuser #46 for the indicated wavelengths. $\tau = 3.18 \ \mu m$ and $\sigma_h = 1.22 \ \mu m$. $\Xi_{pp}(\theta_i, \theta_s)$ [o]; $\Xi_{ss}(\theta_i, \theta_s)$ [△]: A) $\theta_i = 0°$, B) $\theta_i = -30°$, C) $\theta_i = -60°$. 127

List of Tables

Chapter 1

Light Scattering by Rough Surfaces

1.1 Introduction

All surfaces are rough to one degree or another. If a collimated light beam were to strike even the most highly polished mirror, the illuminated spot would be observable in almost any direction in front of the mirror, not only in the direction of the specular, or mirror-like, reflection. The power contained in the coherent (specular) component would be almost 100 per cent of the incident beam power. A small fraction of the energy would be dissipated through inevitable absorption and Joule losses in the material of the mirror. The remainder of the power forms the incoherent (non-specular) or diffuse component and is described as being *scattered* by the surface. It should be emphasized that light can be incoherently scattered into the specular direction.

As the illuminated surface deviates more and more from a flat interface in a continuous but random manner, the power contained in the incoherent component increases at the expense of the coherent component. When the surface undulations reach a certain degree of roughness the coherent component can not be distinguished and the light is entirely incoherently scattered. Precisely if and when this occurs will depend on the wavelength of the illuminating radiation and the surface roughness. The diffusers investigated in this dissertation have roughnesses just beyond this point where a phenomenon known as *enhanced backscattering* can occur.

Describing the light as being *scattered* gives the impression that the incident radiation undergoes some form of random interaction before propagating away from the diffusing surface. One model of the interaction processes simplistically represents the scattering mechanisms by pencil rays reflected or refracted at local tangent planes along the surface. A more realistic treatment involves calculating the surface current

induced by the incident radiation via Maxwell's equations. This surface current in turn generates fields which radiate away from the interface in a manner determined by the surface profile and the boundary conditions across it. Both of these models are used to investigate light scattering by randomly rough diffusers in this dissertation. For certain cases the results from these two models were found to agree with each other almost exactly and to compare favourably with controlled experimental data. Such investigations can aid our understanding not only in how electromagnetic radiation interacts with materials, but also in how these interactions can be modelled.

1.1.1 Thesis Synopsis

The remainder of this chapter contains a brief literature review introducing key and interesting papers in the field of light scattering by randomly rough diffusers.

The physical quantities which are represented by the measurements and calculations appearing throughout this dissertation are defined in chapter two. This chapter also contains a detailed description of the experimental equipment and definitions of the polarization notations which were adopted. Calibration of the scattering equipment using a reflection standard introduces the first measurement of the enhanced backscatter effect.

Chapter three deals with the fabrication of randomly rough surfaces having micrometer features, in particular one-dimensionally rough diffusers. Details are given of how these random surfaces can be faithfully reproduced into silicone elastomer to produce identical dielectric diffusers. This procedure has made it possible to compare the scattering properties of identical metal-coated (gold) and transparent dielectric diffusers. An important aspect of the work reported in this dissertation is the characterization of the rough surfaces using a Talystep profilometer. The measurement of the statistical roughness parameters and a simple analysis of the errors which can be introduced by the finite tip-size are discussed in this chapter.

Starting from the Helmholtz-Kirchhoff theorem, rigorous integral equations are derived in chapter four and their numerical solutions are compared with experimental data. Scattered light measurements are presented for identical metallic and dielectric diffusers illuminated by monochromatic radiation over the wavelength range 0.63–10.60 μm. The differences between the two diffuser types emphasize the effects that

the medium has on the diffuser's scattering properties. Interesting observations are drawn from the database of experimental results supporting possible mechanisms for the enhanced backscatter phenomenon.

In chapter five an analytical solution is presented which adopts a transmission line approach to the scattering problem. In order to reduce the complexity of the analysis certain assumptions are made on the degree of surface roughness and on the order of scattering which is considered. Comparisons are made between the derivation of this theory and another much reported analytical solution which does not include the limiting assumptions.

Possibly the most interesting and informative of all the experimental and numerical results are those presented in chapter six. The third and most simple of all the numerical simulations considered is the tracing of geometrical rays. Taking into account only the fundamental laws of reflection and refraction, surprisingly good results are achieved which enable a number of explanations to be proposed about the scattering mechanisms. It is shown in chapter two how the Muller matrix relating the incident and scattered Stokes vectors is simplified for a one-dimensional diffuser. The Stokes parameter measurements presented in chapter six collectively reveal an insight into the way light interacts with random metallic and dielectric media. Consequently, conclusions are drawn concerning the origin of the enhanced backscatter effect.

An alternative form of scattering system to those investigated in other chapters of this dissertation is that of a thin dielectric diffuser mounted on a reflecting substrate. The light scattering properties of this particular system are quite different to those of the other diffuser types and observed backscatter peaks are strongly enhanced. The effects of varying the mean separation of the random profile and the reflecting substrate are also investigated.

An interesting effect is demonstrated in chapter six which exists away from the backscatter direction, that of *antibackscatter* enhancement. This effect occurs when a one-dimensional diffuser is tilted backwards slightly so that the light is obliquely incident on the surface. The scattered structures previously observed as backscatter enhancement are reproduced in a related direction in the cone of scattered light but *not* in the backscatter direction. Under certain conditions these antibackscatter structures are not reproduced unless the light is actually backward scattered. This effect has only recently been recognized and has received little attention, but it is

clearly related to the phenomenon of enhanced backscatter.

A summary of the main conclusions which have been drawn from the analysis presented in this dissertation is given in chapter seven.

1.1.2 Literature review

The problem which has been addressed in this dissertation, and has confronted both experimental and theoretical workers alike over the past years, is a very simple one to pose: "If I shine light of a certain wavelength onto a known surface in this direction, what will I see at any point where I choose to view it from?". The answer to this question is much more difficult to provide; indeed no single solution has yet been found, only fragments of the unified theory have been proffered.

Apart from the fundamental interest of why light interacts with matter in the way that it does, a practical application for rigorous light scattering is in the determination of surface roughness using a non-contact, and hence non-destructive, light probe [82]. Hapke and van Horn [40] investigated the scattering properties of a number of complex surfaces in an attempt to reproduce the optical properties exhibited by the moon's surface; the moon's brightness peaks sharply at full moon. Their prime objective was to find a scattering structure which exhibited a high reflectance in the backscatter direction, and they found that finely pulverized dielectric particles showed this effect. Hapke [39] subsequently proposed some interesting models for multiple scattering from a distribution of particles. Light rays can retrace their paths back towards the source without being 'blocked', whereas multiply scattered rays in neighbouring angles would be blocked which would lead to more light in the backscatter direction, producing a peak. In similar studies by Oetking [64] using a high resolution scatterometer ($\approx 1°$), all of the structures he investigated exhibited backscatter enhancement. It is interesting to note that Egan and Hilgeman [33] suggested the opposition effect they observed may have been due to multiple scattering, in analogy to the glory effect.

More recently, controlled volume scattering experiments [45, 83] have better defined the situations which give rise to backscatter enhancement (particle size and concentration) and the structure of the backscatter peak itself has been studied. Some of the mechanisms suggested in earlier work have been developed in recent the-

oretical studies using sophisticated analytical methods to incorporate many-particle interactions [30, 78]. Van Albada and Lagendijk [46, 79] observed similarities between the volume backscattering effect and Anderson localization of electrons in a random potential, describing it as weak localization of light. Coming down one scale in dimensionality, Celli [22] and McGurn [53, 54] predicted localization of resonantly induced surface polaritons (evanescent waves) in light scattering from randomly rough surfaces. These localization effects were shown to be directly related to the presence of a sharply defined peak in the backscatter direction.

There has been renewed interest in light scattering from randomly rough diffusers in recent years with the advent of new theories and numerical methods to account for multiple scattering mechanisms [15, 29, 50, 60]. There was particular stimulus for investigations into surface light scattering following the experiments of Mendez and O'Donnell [55, 63]. They observed interesting polarization structures about the backscatter peak produced by a two-dimensional, randomly rough, metallic diffuser. They concluded that enhanced backscattering was primarily based on a multiple scattering mechanism owing to the cooperative effect between forward and time-reversed light paths in the backscatter direction. Their interpretations of the observed phenomena invoked much discussion and debate concerning the origins of the enhanced backscatter peak [10].

With a moderate computing budget and the presently available computing power there have been a number of reports presenting numerical solutions to rigorous integral equations [49, 68, 73]. Although these solutions have been able to investigate the conditions under which enhanced backscattering occurs, they have been limited to *one-dimensionally rough diffusers, or random gratings.* Enhanced backscattering from one-dimensional diffusers has recently been confirmed experimentally [44] including investigations by the author and other workers into the relative scattering properties of identical metallic and dielectric (transparent) diffusers [48, 70]. An important result is the absence of a peak in the backscattered light from a dielectric diffuser, whereas that from an equivalent metallic diffuser is strong. Although new theories have attracted keen attention, renewed interest in some early, well-established models have yielded very encouraging results. In particular the inclusion of a 'double-bounce' or multiple scatter term to the Kirchhoff approximation [18, 19, 77] exhibits a very clear backscatter peak in the 'double-bounce' contribution, and the calculations

overall agree well with more rigorous formulations.

Not surprisingly, enhanced backscattering has been found to occur in scattering systems other than metallic diffusers, such as thin-film, dielectric diffusers in front of reflecting planes [42, 47]. A number of possible mechanisms have been proposed for this particularly pronounced form of backscattering based on multiple scattering arguments. Enhanced scattering of a different sort has been reported by Depine [27, 28] whereby light is obliquely incident on a one-dimensional diffuser. The enhanced scattering structures are of the same form as in previous reports, but can be produced away from the backscatter direction. The results from this work suggest that enhanced backscattering from random gratings is a special case of this more generalized situation of oblique incidence. Observations of this effect are reported in chapter six.

Some of the most recent experimental reports have measured all of the independent elements of the simplified Mueller matrix for one-dimensional, metallic and dielectric diffusers [20]. The complete description of the diffuser's scattering properties is afforded by the use of Stokes' parameters and their analysis can reveal information about even the most subtle of scattering mechanisms. New theroetical models are being produced which go some way towards removing limiting assumptions present in other theories. Brown [16, 17] presents a refined application of the method of smoothing, which incorporates a normalization procedure to remove the limitations of small surface heights and slopes previously encountered with this method. Maystre *et al* [52] have recently introduced a new theory to account for the two-dimensional scattering problem, and preliminary calculations and comments certainly appear to be quite promising.

The latest experimental and theoretical reports indicate the potential for very exciting developments in the field of rough surface scattering in the next few years.

Chapter 2

Preparation for Experimental Investigation

2.1 Introduction

In this chapter I will describe the optical equipment that was used to obtain the experimental data presented in this dissertation, including some comments on the difficulties involved in setting it up. Two alternative geometries of the experimental arrangement were employed depending on the scattering properties of the diffuser being studied. Each arrangement *is given* the general name 'scatterometer', or may be referred to informally as the 'scattering rig', and will be discussed in detail.

I will start by introducing the topic of light scattering from a radiometric point of view, i.e. discuss it in terms such as radiant power and directional reflectance. This will lead to a physical interpretation of what the data from the scattering rig represents. In order to check the response of the scatterometer it was characterized using a special scattering medium, and from these measurements the phenomenon of enhanced backscatter will be introduced.

To describe the state of the light and the direction in which it travels, definitions will be given for the polarization notation, and the angles of incidence and scatter which will be used throughout this dissertation. Equivalent notations used to describe polarization in other electromagnetic studies will be given to aid the reader in deciding precisely which case of data are being presented.

2.2   Radiometry of scattering

Much of the work considered in this section is described only as far as its application here requires. For a more detailed discussion the reader is referred to papers by Nicodemus [57, 58].

When light is incident on the surface S of a medium, whether the medium be opaque or transparent, each surface element ΔA will reflect a certain proportion of the light throughout the hemisphere above it. Similarly, for the case of a transparent or partially absorbing medium, each element will transmit a certain proportion of the light throughout its lower hemisphere. Introducing a quantity $L(\theta, \phi)$ known as the *radiance* [57], one can specify directional variations in reflectance, or transmittance, of a surface element ΔA. This quantity remains constant along a given direction (θ, ϕ) within a lossless, isotropic, and homogeneous medium. Formally, the radiance describes the radiant flux (or power) P, per unit solid angle Ω, passing through unit projected area $A\cos(\theta)$, i.e.

$$L(\theta, \phi) = \frac{\partial^2 P}{\partial A \cos(\theta) \, \partial \Omega} \qquad [Wm^{-2}sr^{-1}]$$

where $d\Omega = \sin(\theta) \, d\theta \, d\phi$ is the angular content of an elemental area of surface in spherical co-ordinates; see Figure 2.1. For a narrow beam collimated within $\delta\Omega_i$ the radiant power incident on ΔA from the direction (θ_i, ϕ_i) is

$$P_i = L_i(\theta_i, \phi_i)\Delta A \cos(\theta_i)\,\delta\Omega_i \qquad [W]$$

Similarly, the power reflected into the scatter solid angle $\delta\Omega_s$ in the direction (θ_s, ϕ_s) from ΔA is

$$P_r = L_s(\theta_s, \phi_s)\Delta A \cos(\theta_s)\,\delta\Omega_s \qquad [W]$$

The radiant reflectance ρ is defined to be the ratio of reflected radiant power to incident radiant power [57]

$$\rho = \frac{P_r}{P_i} \Rightarrow \frac{L_s \cos(\theta_s)\,\delta\Omega_s}{L_i \cos(\theta_i)\,\delta\Omega_i}$$

The scattering property of the surface element is then described by a quantity called the *Bidirectional Reflectance Distribution Function* (BRDF) f_r. The BRDF for element ΔA is defined by [57, equation (5)]

$$f_r(\theta_i, \phi_i; \theta_s, \phi_s) = \frac{L_s}{L_i \cos(\theta_i)\,\delta\Omega_i} \qquad [sr^{-1}]$$
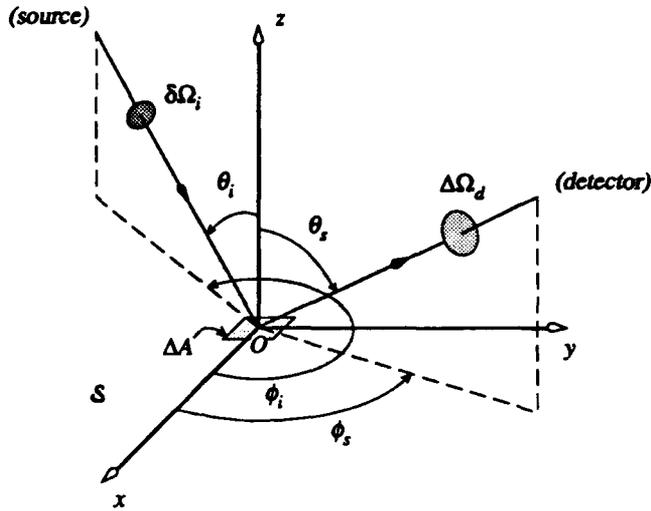
Figure 2.1: Local scattering geometry of surface element ΔA illuminated by a narrow, collimated beam. Normal to ΔA coincides with z axis. Source and detector subtend solid angles $\delta\Omega_i$ and $\Delta\Omega_d$ at ΔA, respectively. For transmission, $\theta_s \rightarrow \pi - \theta_s$.

The laser provides an excellent light source for investigating the scattering properties of surface interfaces; it produces an intense, collimated, coherent beam of light with a known wavelength λ. The intensity at each point in the hemisphere above (or below) the interface is determined by the addition of individual phase vectors scattered from each illuminated surface element. This produces a so-called *speckle pattern* (a random field of constructive and destructive interference) overlying the average intensity distribution. Experimentally, a field lens was placed in front of the detector aperture, imaging the rough surface onto the detector element, to spatially integrate over the speckles entering the lens. This has the effect of averaging out the spatial intensity fluctuations, reducing the speckle noise. Integrating over many speckles enables the detector to measure the mean radiant power transmitted by the lens. Consider the illuminated surface S in Figure 2.1 to be an ensemble of independent, statistically identical, surface elements ΔA. All such elements reflect a certain radiant power in the direction of the detector which is then integrated by the field lens over the solid angle of detection. The response of a linear detector R_d can then

be written as

$$R_d = \mathcal{A} \int_{\Delta\Omega_d} \langle f_r \rangle \cos(\theta_s) P_i \, \mathcal{W}(\theta_s, \phi_s) \, d\Omega_s \qquad (2.1)$$

simply describing the power falling on the detector element where $\mathcal{A}$ is a constant of proportionality, $\mathcal{W}$ is a weight function accounting for vignetting of $\Delta\Omega_d$, and $\langle f_r \rangle$ represents a BRDF averaged over the ensemble of surface elements in the direction (θ_s, ϕ_s)

2.2.1 The differential scattering cross-section

If I_0 is the irradiance $[Wm^{-2}]$ of light incident on S and $Jd\Omega_s$ represents the radiant power $[W]$ scattered into a solid angle $d\Omega_s$, we can then define the *differential scattering cross-section* (DSCS) as

$$\frac{d\sigma}{d\Omega_s} = \frac{J(\theta_s, \phi_s)}{I_0} \qquad [m^2 sr^{-1}]$$

Substituting for $I_0 = P_i/\Delta A$ and averaging over an ensemble of surface elements ΔA

$$\left\langle \frac{1}{\Delta A} \frac{d\sigma}{d\Omega_s} \right\rangle = \frac{\langle J(\theta_i, \phi_i; \theta_s, \phi_s) \rangle}{P_i} \Rightarrow \Xi(\theta_i, \phi_i; \theta_s, \phi_s) \qquad (2.2)$$

which will be represented by the symbol Ξ (pronounced "csi"). The detector response may be expressed in terms of the *mean radiant intensity* $\langle J \rangle$, as

$$R_d = \mathcal{A} \int_{\Delta\Omega_d} \langle J \rangle \mathcal{W}(\theta_s, \phi_s) \, d\Omega_s$$

Thus, by comparison with equation (2.1) one obtains the relation

$$\Xi(\theta_i, \phi_i; \theta_s, \phi_s) \equiv \langle f_r(\theta_i, \phi_i; \theta_s, \phi_s) \rangle \cos(\theta_s) \qquad (2.3)$$

and this quantity will be used to describe the scattering properties of the diffusers studied in this dissertation. This treatment of radiometric terms is not confined to the case of reflection, similar expressions may be derived for transmission with appropriate changes in notation; see caption of Figure 2.1.

Generally, a certain fraction of the incident power is lost through absorption in the diffusing medium and does not propagate to the far-field. This is due to either finite conductivity of metal coatings, or small losses in dielectric media. In order to investigate what physical mechanisms play a rôle in the phenomenon of enhanced backscatter, emphasis was placed on the *relative* distributions of the DSCS curves

and not on their absolute values. Primarily, then, the diffusers investigated were considered to be either perfect conductors or lossless dielectrics. For the case of a perfect conductor, the DSCS curves were normalized to unity according to the relation

$$\int_h \Xi \, d\Omega_s = 1 \tag{2.4}$$

or, equivalently,

$$\int_h \langle J \rangle d\Omega_s = P_i$$

where

$$\int_h d\Omega_s = \begin{cases} \int_0^\pi d\phi_s \int_{-\frac{\pi}{2}}^{\frac{\pi}{2}} \sin(\theta_s) \, d\theta_s & \text{for two-dimensional diffusers} \tag{2.4a} \\[2ex] \int_{-\frac{\pi}{2}}^{\frac{\pi}{2}} d\theta_s & \text{for one-dimensional diffusers} \tag{2.4b} \end{cases}$$

This assumes that the total radiant power is equal to the total incident power. Normalization for the two-dimensional diffusers also assumes rotational symmetry of the DSCS curve about the z axis.

For the case of a lossless dielectric, however, it was not experimentally possible to measure both the reflected DSCS Ξ^r *and* the transmitted DSCS Ξ^t. It was also not practicable to measure the undeviated incident beam; comparison with Ξ^r would require a great deal of attenuation, possibly introducing errors in proportion to the quantity being calculated. Instead, the dielectric experimental data are presented in terms of an un-normalized *relative* scattering cross-section, although all graphs for a particular sample are shown with the same incident power.

2.3 The optical equipment

The equipment comprises of a continuously working (CW) laser source, lenses, polarization-sensitive optics, beam-steering mirrors, and a selection of linear detectors.

Two laser sources were employed to provide linearly polarized radiation ranging from visible through to far infra-red wavelengths. These were a 20 mW He-Ne laser (Jodon HN20G) with interchangeable mirror sets and a 4 W CO_2 laser (Edinburgh Instruments WL-4). The He-Ne laser provides wavelengths at $\lambda = 0.633$, 1.152, and 3.392 μm and the CO_2 laser provides a single wavelength at 10.6 μm. Three types

of detector were used according to the wavelength and power of the illuminating radiation:

•0.633 μm; 20 mW	Hamamatsu photomultiplier tube (PMT) R647.
•1.15 μm; 5 mW ⎫ •3.39 μm; 3 mW ⎭	⎧ Cincinatti Electronics Indium ⎪ Antimonide (InSb). The detector ⎨ element was cooled (liquid N_2) ⎩ to reduce thermal noise.
•10.6 μm; 4 W	Plessey PLT222 pyroelectric detector.

The lenses used for the visible wavelength could also be used at 1.152 μm (optical glass transmits out to $\sim$ 2.5 μm, typically). For 3.39 μm transparent CaF_2 lenses were used and for 10.6 μm the lenses used were made from CdS. One of the main problems of working with an infra-red radiation source is knowing precisely in what direction the radiation is travelling. A small alignment He-Ne (visible 0.633 μm) is very useful in overcoming this problem and for that reason it is important that the lens materials also transmit visible wavelengths. To align the visible and infra-red beams one can use two small apertures separated by a distance of approximately 1 m. Fluorescent cards may be used to locate the raw infra-red beam which shows up as a dark spot. Once the infra-red beam is passing through both apertures the alignment beam can also be directed through them by introducing two tilting mirrors. Apart from slight differences in focal lengths and beam divergence, the alignment beam should give a fair indication of where the infra-red radiation will go.

A problem arises when intending to carry out experiments at the 3.39 μm wavelength; for only a few mW of power there are presently no fluorescent cards that fluoresce around 3 μm. The only way to even check that the laser is actually 'lasing' at this wavelength is to switch on the detector and point it at a diffusing target. In this way it is possible to align the beam with an external visible He-Ne laser using the two-aperture method. If a sufficiently small aperture can be placed somewhere along the beam path then the visible discharge given off by the laser cavity can also be used as an alignment aid. These two methods are only rough guides indicating the path of the infra-red beam; precise positioning of focal points and alignment through lens apertures can only be achieved while the detector is looking at a diffusing target, 'down-stream' of all the optics.

Suitable half-wave plates, or retarders, were used to orientate the linear polariza-

tions of the respective wavelengths. Dichroic acetate sheets were employed as linear polarization analysers for the wavelengths 0.633 and 1.15 μm while wire-grid polarizers were used for 3.39 and 10.6 μm. An integrating lens was placed between the detector and the analyser to reduce the speckle noise. A 5 mm diameter 3× objective was used for the wavelengths 0.633 and 1.15 μm, providing an angular resolution of detection of approximately 0.5°. For the wavelengths 3.39 and 10.6 μm a 10 mm diameter CdS lens was used, providing a resolution of approximately 1°.

If one considers a coherent beam of light with wavelength λ scattered from a diffusing surface, each speckle is approximately the same size as the Airy disc that would be formed in the absence of the diffuser. In the detection plane this corresponds to a diameter s which may be written as

$$ s \approx \frac{1.2\,\lambda\,z}{w} $$

where z is the distance from the diffuser to the detection plane, and w is the diameter of the illuminated area at the diffuser. For an illuminated area of 10–15 mm diameter this meant that at 0.633 μm wavelength approximately 10^5 speckles were being averaged, while at 3.39 μm approximately 10^4 speckles were averaged over. The fractional statistical noise introduced by the intensity fluctuations of the speckles is proportional to $N^{-\frac{1}{2}}$, where N is the number of speckles entering the lens. As the wavelength is increased one would expect the speckle noise to become more apparent; this effect was observed in the experiments carried out over the range of wavelengths available, the noisiest case being for the wavelength 10.6 μm.

2.4   The scatterometer

The scatterometer consists of a combination of basic optical components and computer controlled stepper motors, arranged in a fashion convenient for changing the wavelength of the illuminating radiation. The wavelength presents something of a 'yard-stick' to the problem of electromagnetic scattering from rough surfaces; it is the unit of length by which the surface structures are measured. The scattering properties of a given diffuser are very much affected by the wavelength. For short wavelengths the surface asperities might appear quite coarse and large in texture, encouraging multiple interactions and high orders of scattering. For longer wavelengths

the surface will appear proportionately finer and smoother, whereupon one would expect more mirror-like reflection.

Two alternative arrangements for the scatterometer were employed, depending on what the scattering properties of the sample dictated. These are discussed below.

2.4.1 Diverging beam geometry

This arrangment was used when the sample did not exhibit a coherently (or specularly) reflected component; this was generally the case for the wavelengths $0.633, 1.15$, and $3.39 \mu m$ with the diffusers investigated in this dissertation. The geometry allowed measurements to be made very close to the backscatter direction. The diverging beam geometry is illustrated in Figure 2.2.

For all of the wavelengths employed the laser beam was 'chopped' at a known reference frequency (typically 83 Hz, or 830 Hz for weaker signals) and the signal from the detector was fed into a phase lock-in amplifier (Stanford Research SR530). This heterodyning method of signal processing was essential in separating the infra-red signal from the background radiation within the laboratory. It was also used for the visible wavelength, but more for convenience than of necessity. When taking intensity measurements from a highly reflecting surface (e.g. one that has been gold-coated) a thin, variable, neutral density (ND) filter was used to attenuate the beam power. For surfaces whose reflectance is dependent on the angle of incidence (e.g. dielectric surfaces) fixed ND filters were used to stop the beam down by known amounts, when necessary.

After being approximately collimated, the linear polarization of the radiation was orientated with a half-wave retarder. The beam was then focused, via a periscope arrangement of mirrors, onto a pointed or sliver mirror and directed towards the diffuser under investigation. Consequently, the beam was diverging slightly as it propagated towards the sample, typically illuminating a spot of 10–20 mm diameter with a divergence of $\sim 1°$. The reason for using a sliver mirror stems from the desire to observe the scattered intensity in the backward direction, along the line of incidence. This method of observing the backscattered light caused minimal obstruction of the detector, losing only $\sim 1.5°$. An alternative method would have been to use a good quality beam-splitter to direct the light onto the surface. However, it would be
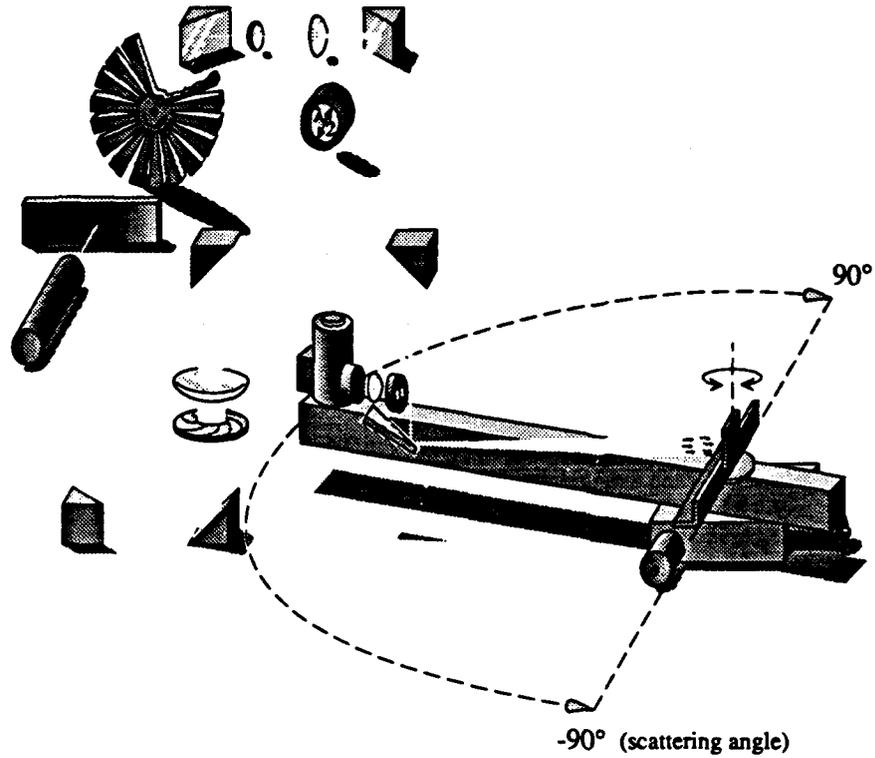
Key to Optical Components				
cw laser	variable ND filter	45° mirror	plano-convex lens	halfwave retarder
iris	sliver mirror	randomly rough diffuser	linear polarizer	detector

Figure 2.2: Illustration of the diverging beam geometry. This arrangement was used for diffusers exhibiting backscatter enhancement.

difficult to know precisely how much attenuation was introduced by the beam-splitter and would require calibrating for each wavelength and polarization.

The detector was mounted on an arm approximately 65 *cm* away from the sample holder. The detector arm and sample mount could be rotated by computer-controlled stepper motors about an axis passing through the centre of the sample, each motor having a minimum angular step of two minutes of arc. For a typical measurement, then, the sample would be rotated to a certain position to set the angle of incidence. This position would remain fixed during the measurement and the detector arm would be rotated over a range of scatter angles, pausing at prescribed intervals. At each interval a number of readings were taken from the detector which were then averaged to reduce random errors. This produces a set of average intensity readings as a function of scatter angle, measured in the plane of incidence only. It was also possible to measure the average intensity in transmission for transparent samples.

If the sample exhibited a specularly reflected component, the peak would not be confined to a single scatter angle when measured with the diverging beam geometry. This indicates that the detector is not actually in the far-field. However, this geometry is used for samples which strongly scatter the incident light over a wide range of angles. One would therefore expect the slight divergence of the incident beam to have little influence on the directional scattering properties of the sample. This was, in fact, found to be the case when measurements taken with this geometry were compared with those taken using the converging beam geometry.

2.4.2   Converging beam geometry

This arrangement was used when the asperities of the diffusing surface were small compared to the incident wavelength, resulting in a strong coherent reflection; this was generally the case when carrying out experiments with the wavelength 10.6 μm. The converging beam geometry is illustrated in Figure 2.3

The main difference between this arrangement and the diverging beam geometry is the position at which the illuminating radiation is brought to a focus. To ensure that the detector was in the far-field, the undeviated beam was focused at the plane of the integrating lens. This meant that the coherent component from a diffusing surface would be detectable at only one scatter angle; that of the specular direction.

90°

-90° (scattering angle)

Key to Optical Components				
cw laser	variable ND filter	45° mirror	plano-convex lens	halfwave retarder
iris	spherical mirror	randomly rough diffuser	linear polarizer	detector

Figure 2.3: Illustration of the converging beam geometry. This arrangement was used for diffusers exhibiting a strong coherent (specular) reflection.

The disadvantage with this geometry is the angular obstruction of the detector due to the width of the final mirror, which was approximately 8° in the backscatter direction.

The computer-controlled data acquisition, simplicity of the optics, and stability of the laser source meant a high reproducibility of measurements. Apart from linearity of the de tor the only real sources of error were systematic; namely analogue-to-digital (A/D) conversion of the detector signal, background interference and noise (affecting the signal), and amplification of the signal. Comparing two scatter envelopes taken from the same diffuser, over the same scatter angles, they are virtually identical. Hence none of the graphs shown in this dissertation will have any error bars on them; the choice of plotting symbol will reflect the accuracy of the intensity measurements, but as 'a rule of thumb' the total errors were *within* three per cent of the measured value.

2.5 Polarization notation

An arbitrary monochromatic wave can be described by the superposition of two orthogonal electric vectors. Defining a plane of reference we can choose two such basis vectors. The reference plane is chosen to contain the propagation direction of the incident field $\vec{k}_i$ and the mean surface normal $\vec{n}$, and constitutes the *plane of incidence*. The basis vector $\vec{e}_s0$ is defined to be perpendicular to this plane and $\vec{e}_p0$ is defined to lie in it, perpendicular to $\vec{k}_i$. The sense chosen is such that $\vec{e}_S \times \vec{e}_p$ is parallel to the propagation direction; see Figure 2.4.

Describing the light field as a plane wave with propagation constant k and circular frequency ω, the transverse electric vector can be written as

$$\vec{E}_T = \Re e \left[\vec{E}_0 \; e^{i(kz - \omega t)} \right]$$

where

$$\vec{E}_0 = E_p \vec{e}_p + E_s \vec{e}_s. \tag{2.5}$$

This expression generally describes an elliptically polarized field; the particular polarization state depends on the relative values of the complex amplitudes E_p and E_s. These amplitudes are themselves expressed in terms of positive amplitudes a_p, a_s and phases δ_p, δ_s:

$$E_p \;\; = \;\; a_p \; e^{-i\delta_p}$$
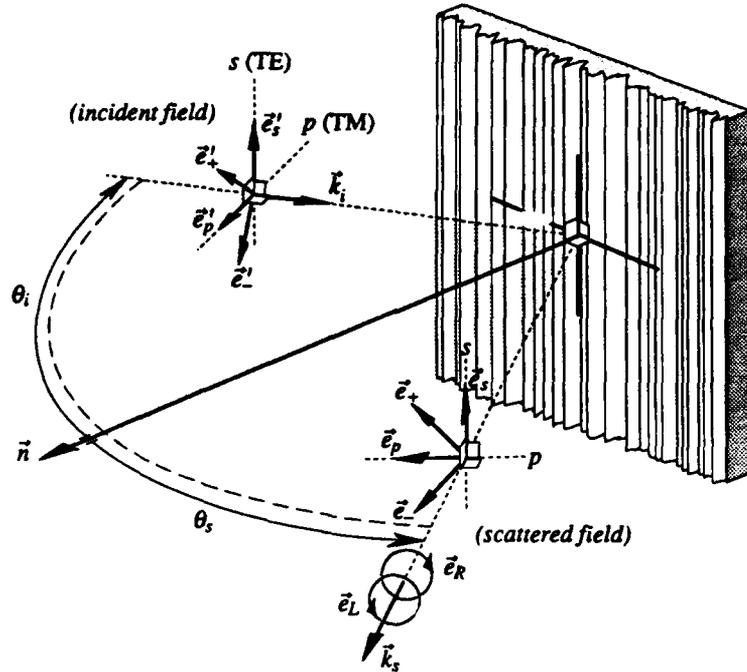
Figure 2.4: Light scattering from a one-dimensional diffuser — notation used to describe polarization states of the incident and scattered light f lds.Vectors $\vec{e}_p$ and $\vec{e}_s$ contain the linear polarizations p and s, respectively; $\vec{e}_+$ and $\vec{e}_-$ represent $\vec{e}_s$ and $\vec{e}_p$ rotated through 45°; $\vec{e}_R$ and $\vec{e}_L$ represent right and left-hand circular polarizations, respectively, looking *towards* the source. Note that the angle of scatter θ_s is measured in the opposite sense to the angle of incidence θ_i; backscatter therefore occurs at $\theta_s = -\theta_i$.

$$E_s \;=\; a_s\, e^{-i\delta_s}$$

If $a_s = 0$ the incident field is described as being p polarized; similarly, if $a_p = 0$ the incident field is described as being s polarized. Other notations used in similar studies have the following equivalent descriptions:

$$\left.\begin{array}{l}\text{transverse magnetic (TM),}\\ V \text{ polarization,}\\ \text{or, S polarization}\end{array}\right\} p \text{ polarization}$$

and

$$\left.\begin{array}{l}\text{transverse electric (TE),}\\ H \text{ polarization,}\\ \text{or, P polarization}\end{array}\right\} s \text{ polarization.}$$

2.5.1 Stokes' parameters

The general polarization state of a monochromatic, electromagnetic wave can be fully described in terms of its four *Stokes parameters*. Each parameter describes an irradiance based on the combination of a particular pair of polarization states: either p and s linearly polarized; $+45°$ and $-45°$ linearly polarized; or right-hand and left-hand circularly polarized. The directions of these polarization cases are illustrated in Figure 2.4 by the vectors $\vec{e}_p$ and $\vec{e}_s$, $\vec{e}_+$ and $\vec{e}_-$, and $\vec{e}_R$ and $\vec{e}_L$, respectively. After passing through suitable polarizers, the respective irradiances measured by the detector are represented by the symbols I_p and I_s, I_+ and I_-, and I_R and I_L. Van de Hulst [81, chapter 5] uses the symbols I, Q, U, V to denote Stokes' parameters. The algebraic derivation of these parameters is omitted, but is quite straightforward — the reader is referred to the very readable text of Bohren and Huffman [14, pages 46–50]. Ignoring a factor $\frac{k}{2\omega\mu_0}$, the parameters can be defined as follows:

$$
\begin{aligned}
I &= I_s + I_p &\Rightarrow& \quad \langle E_s E_s^* + E_p E_p^* \rangle \\
Q &= I_s - I_p &\Rightarrow& \quad \langle E_s E_s^* - E_p E_p^* \rangle \\
U &= I_+ - I_- &\Rightarrow& \quad \langle E_s E_p^* + E_p E_s^* \rangle \\
V &= I_R - I_L &\Rightarrow& \quad i\langle E_s E_p^* - E_p E_s^* \rangle
\end{aligned}
$$

where the conjugate complex value is represented by an asterisk and the angular brackets represent the average over an ensemble of rough surfaces. The values are all real numbers satisfying the relation

$$ I^2 \geq Q^2 + U^2 + V^2 \tag{2.6} $$

If the equality is true the light is said to be *fully* polarized. The inequality holds for natural or *unpolarized* light (where $Q = U = V = 0$) and, more generally, for *partially* polarized light as obtained from a quasi-monochromatic source.

The above descriptions are by no means definitive; various linear combinations of the Stokes parameters can also be used as suitable Stokes parameters. One alternative set (I_p, I_s, U, V) replaces the parameters I and Q with I_p and I_s, where

$$
\begin{aligned}
I_p &= E_p E_p^* \\
I_s &= E_s E_s^*
\end{aligned}
$$

The relationship between the parameters in this new set can be obtained easily from

equation (2.6) and the same arguments qualify the inequality.[†]

$$4I_p I_s \geq U^2 + V^2$$

The Mueller matrix

The merit of Stokes' parameters becomes apparent when one considers them as a four element column vector, or *Stokes vector*. The polarization state of the scattered light field (I_p, I_s, U, V) can then be written in terms of the incident field $(I_{p0}, I_{s0}, U_0, V_0)$ and a scattering matrix $\tilde{\mathbf{M}}$:

$$(I_p, I_s, U, V) = \tilde{\mathbf{M}} \ (I_{p0}, I_{s0}, U_0, V_0) \tag{2.7}$$

Here $\tilde{\mathbf{M}}$ is a 4×4 array matrix describing the scattering properties of the diffuser, called a *Mueller matrix*. Each element in the array is a real function of the directions of incidence and scattering. A complementary relationship exists between the complex amplitudes of the incident and scattered light fields:

$$(E_p, E_s) = \tilde{\mathbf{A}} \ (E_{p0}, E_{s0}) \tag{2.8}$$

Here $\tilde{\mathbf{A}}$ is a 2×2 array of complex numbers. What is more, the elements of the scattering matrix $\tilde{\mathbf{M}}$ are quadratic expressions of the elements in the amplitude matrix $\tilde{\mathbf{A}}$.

Experimentally, the characterization of a general scattering matrix involves a lengthy procedure of measurements and is by no means a simple task. Careful selection of the incident Stokes vector and the detector's analysing polarizer can yield a specific element from the Mueller matrix. However, slight imperfections in the polarization optics, ellipticity of the incident field, or misalignment of a component's principal axis can mean that the element is not being measured at the exclusion of others in the matrix. A detailed discussion of this procedure is given by Bickel and Bailey [13], describing useful combinations of optical components necessary for analysing particular polarizations.

In most applications, considerations of symmetry can reduce the number of independent terms in the scattering Mueller matrix [81, pages 46-58]. Cases of particular interest occur when the scattering object has a structure which is very elongated

---

[†]More specifically, in this set natural light occurs when $I_p = I_s$ and $U = V = 0$.

in one dimension: e.g. a volume which contains parallel, cylindrical scatterers or a surface which has a grating-like or corrugated structure. Such a surface would be described as being approximately *one-dimensional* since its height profile is dependent on only one spatial variable, $h \approx h(x)$. If the incident beam is such that the plane of incidence is orthogonal to the surface corrugations, then the scattered light will also be confined to this plane. Moreover, if the incident field is either entirely p or s polarized, the scattered field will retain this state of polarization; i.e. no *depolarization* will occur. The general expression for the light field amplitude in equation (2.5) is then the sum of two independent oscillating modes and, consequently, the amplitude scattering matrix $\bar{\mathbf{A}}$ is diagonal: from equation (2.8) this can be written as

$$\begin{pmatrix} E_p \\ E_s \end{pmatrix} = \begin{bmatrix} a_{11} & 0 \\ 0 & a_{22} \end{bmatrix} \begin{pmatrix} E_{p0} \\ E_{s0} \end{pmatrix}$$

This greatly simplifies the associated Mueller matrix for a one-dimensional surface, reducing it to only four independent terms. From equation (2.7) the scattered Stokes vector $\mathbf{S}$ can be written as

$$\mathbf{S} = \bar{\mathbf{M}} \, \mathbf{S}_0 \tag{2.9}$$

where $\mathbf{S}_0$ is the incident Stokes vector and $\bar{\mathbf{M}}$ is the Mueller matrix of the diffuser. For the parameter set (I_p, I_s, U, V) this can be written as

$$\begin{pmatrix} I_p \\ I_s \\ U \\ V \end{pmatrix} = \begin{bmatrix} m_{11} & 0 & 0 & 0 \\ 0 & m_{22} & 0 & 0 \\ 0 & 0 & m_{33} & m_{34} \\ 0 & 0 & -m_{34} & m_{33} \end{bmatrix} \begin{pmatrix} I_{p0} \\ I_{s0} \\ U_0 \\ V_0 \end{pmatrix}$$

Theoretically, one can calculate the terms in this Mueller matrix from the second order moments of the amplitude matrix elements a_{11} and a_{22} [81, page 44]. However, it is experimentally possible to extract each element by combining specific incident and detected polarizations.

Measurement of the matrix elements

Four incident Stokes vectors $\mathbf{S}_0$ are considered below which introduce the Mueller matrix elements into the scattered vectors $\mathbf{S}$ from equation 2.9.

$$\triangleright \qquad \mathbf{S}_0 = \mathbf{S}_p = \begin{pmatrix} 1 \\ 0 \\ 0 \\ 0 \end{pmatrix} \longrightarrow \mathbf{S} = \begin{pmatrix} m_{11} \\ 0 \\ 0 \\ 0 \end{pmatrix}$$

i.e. the scattered light retains the p polarized state of the incident field. With reference to Figure 2.4, measurement of this scattered field with a linear polarizer parallel to $\vec{e}_p$ will yield the element m_{11} from the Mueller matrix.

$$\triangleright \qquad \mathbf{S}_0 = \mathbf{S}_s = \begin{pmatrix} 0 \\ 1 \\ 0 \\ 0 \end{pmatrix} \longrightarrow \mathbf{S} = \begin{pmatrix} 0 \\ m_{22} \\ 0 \\ 0 \end{pmatrix}$$

the scattered field this time retains the s polarized state. Aligning a linear polarizer parallel to $\vec{e}_s$ will yield the element m_{22}.

$$\triangleright \qquad \mathbf{S}_0 = \mathbf{S}_+ = \frac{1}{2} \begin{pmatrix} 1 \\ 1 \\ 2 \\ 0 \end{pmatrix} \longrightarrow \mathbf{S} = \frac{1}{2} \begin{pmatrix} m_{11} \\ m_{22} \\ 2m_{33} \\ -2m_{34} \end{pmatrix}$$

all four matrix elements are present for this case with m_{33} and m_{34} appearing in the U and V components of the Stokes vector.

$$\triangleright \qquad \mathbf{S}_0 = \mathbf{S}_R = \frac{1}{2} \begin{pmatrix} 1 \\ 1 \\ 0 \\ 2 \end{pmatrix} \longrightarrow \mathbf{S} = \frac{1}{2} \begin{pmatrix} m_{11} \\ m_{22} \\ 2m_{34} \\ 2m_{33} \end{pmatrix}$$

which is a similar result to the $\mathbf{S}_0 = \mathbf{S}_+$ case; the only differences are the positions of the m_{33} and m_{34} elements, with a sign change in the V component.

The direct measurement of the first two elements m_{11} and m_{22} can be achieved in a relatively straightforward manner, aligning the incident and detected polarizations along $\vec{e}_p$ and $\vec{e}_s$, respectively. The two remaining elements m_{33} and m_{34} can be measured with either $\mathbf{S}_0 = \mathbf{S}_+$ or $\mathbf{S}_0 = \mathbf{S}_R$. The circularly polarized state $\mathbf{S}_R$ can be difficult to achieve experimentally, without any ellipticity, i.e. $I_p = I_s$, and so the $\mathbf{S}_+$ state was used. The V component in the scattered Stokes vector can be measured by

using a quarter-wave retarder in combination with a linear polarizer, which is placed in front of the detector. Orientating the retarder's principal axis along $\vec{e}_+$ and the linear polarizer along $\vec{e}_p$, the right-hand circular irradiance I_R can be measured. The left-hand case I_L is measured by rotating the retarder through 90°. In the majority of cases, experimental data presented in this dissertation will concentrate on the two scattering cross-sections p and s only. The measurement of the *complete parameter* set $(I_p,\ I_s,\ U,\ V)$ will be limited to certain cases.

With reference to Figure 2.4 it is useful to define the incident and scattering angles θ_i and θ_s, respectively. Both angles are measured in the plane of incidence with respect to the mean surface normal $\vec{n}$, i.e. the normal one would describe from a flat surface with no roughness. The angles are, by convention, measured in opposite senses. This means that for an angle of incidence $\theta_i = 10°$ the specular, or mirror-like, reflection would occur at $\theta_s = 10°$. Conversely, for $\theta_i = -10°$ the *backscatter* or anti-specular reflection would occur at $\theta_s = 10°$. In fact, this will be the case for all graphs presented in this dissertation; the backscatter direction will be to the *right-hand-side* of the graphs, corresponding to $\theta_s \geq 0$.

In the graphs representing the measured DSCS curves, the incident and detected polarizations a and b respectively, will be denoted by Ξ_{ab}. Thus for s incident and p detected polarizations the corresponding symbol will be Ξ_{sp}. In general, to describe cases where the detected polarization is either parallel or orthogonal to the incident polarization, the respective terms *co-* and *cross-polarized* will be used. Such measurements will be represented by the symbols Ξ_{co} (e.g. Ξ_{pp} or Ξ_{ss}) and Ξ_{cross} (e.g. Ξ_{ps} or Ξ_{sp}). Where the data analysis calls for an incoherent sum of co- and cross-polarized measurements, the resulting DSCS curve will be denoted by Ξ_{tot}, where

$$\Xi_{tot} = \Xi_{co} + \Xi_{cross}$$

2.6 Scatterometer response

In order to characterize the response of a particular system, one requires a set of stimuli from which standard measurements will result. Ordinarily the task of setting the standards, which encompass all possible demands that may be made of the system, is the subject of much debate. For the scatterometer, setting the standard measurements is a somewhat simple matter to resolve.

If one considers a perfect mirror, from which no light is randomly scattered, then the measurement from this stimulus would resemble a Dirac delta-function $\delta(\theta_s, \phi_s)$ in the far-field; i.e. all of the light incident on the mirror is reflected in the specular direction and is observable at only one position in the far-field. In this case the ideal scatterometer response would be of the form

$$\Xi(\theta_i, \phi_i; \theta_s, \phi_s) = \frac{\delta(\theta_i - \theta_s)\delta(\phi_i - \phi_s \pm \pi)}{\sin(\theta_s)}$$

Here, the BRDF f_r is non-zero for one direction of reflection only — the specular direction. However, if f_r is constant for all directions, assuming negligible absorption, from equation (2.3) the measurement would be of the form

$$\Xi(\theta_i, \phi_i; \theta_s, \phi_s) = \frac{1}{\pi}\cos(\theta_s) \tag{2.10}$$

and would be *independent* of the angle of incidence. The latter stimulus is known as a *Lambertian* diffuser, i.e. one whose reflected radiance is constant irrespective of direction. Since it is associated with *all* angles of incidence and detection, the Lambertian diffuser provides a more comprehensive test stimulus than does the perfect mirror. The problem arises when one tries to find a suitably diffusing sample with the required constant BRDF.

There are several possible methods for preparing a Lambertian-like diffuser. They mainly entail coating a flat substrate with a layer of extremely small particles which induce multiple light scattering within the volume of the layer. One method is to deposit magnesium oxide (MgO) on a silver substrate, given off by a burning ribbon of magnesium [84, pages 20–21]. A surface layer 0.5 mm thick will reflect about 97 per cent of the incident light when fresh, although this value will drop significantly after a few days. Another method is to use fine barium sulphate ($BaSO_4$) powder, supplied by Eastman Kodak as a white reflectance standard [38]. A 'solid' block is formed by compressing the powder into a special plastic holder which has a cylindrical recess, 51 mm diameter and 9 mm deep. With care a smooth, flat surface can be achieved from which light scattering measurements may be taken. The experimenter should ensure that the surface does not have a glazed or polished appearance, otherwise unwanted specular reflections will occur. This may be checked by looking at how ordinary daylight is reflected at glancing angles. The reflectance values of compressed $BaSO_4$ over the visible wavelengths are shown in Table 2.1. The $BaSO_4$ powder is

Wavelength / nm	Reflectance
250	0.957
300	0.969
350	0.981
400	0.994
500	0.993
700	0.994

Table 2.1: Reflectance values of compressed $BaSO_4$ for visible wavelengths.

prescribed for use over the wavelength range 0.2 - 2.5 μm, so measurements from this form of Lambertian diffuser were taken at the wavelengths 0.633 and 1.15 μm. Graphs representing the DSCS curves measured for normal incidence for the wavelengths $\lambda = 0.633$ and 1.15 μm are shown in Figure 2.5. For each incident polarization, the co- and cross-polarized measurements have been summed incoherently and the total normalized according to equation (2.4a). The three curves are compared to the ideal, normalized response of a Lambertian diffuser, i.e. equation (2.10).

The measured response of the scatterometer shows close agreement with the ideal cosine for both polarizations, at each wavelength. However, the light scattering properties of the compressed $BaSO_4$ exhibit the prescence of a sharply defined peak directed back towards the illuminating source. Graphs representing the DSCS curves measured for the incidence angles $\theta_i = -30°$ and $-60°$ are shown in Figure 2.6 for the wavelength 0.633 μm. One can see from these measurements that this peak is indeed directed back along the line of incidence. (The data points where the detector passed behind the sliver mirror have been removed.) Such a peak in the mean radiant intensity, restricted to a narrow cone of angles around the backscatter direction, will from now on be referred to as an *enhanced backscatter peak*. As the incidence angle is increased, the measurements from the compressed $BaSO_4$ show closer agreement to the ideal cosine. This illustrates how the scattering properties of a true Lambertian diffuser are independent of the angle of incidence; a point emphasised by equation (2.10). For completeness, the corresponding DSCS measurements for the wavelength 1.15 μm are shown in Figure 2.7. Generally, all measurements show a *cosine response with particularly good agreement for large scattering angles*. This phenomenon has been observed from $BaSO_4$ paint, amongst other materials, by Egan
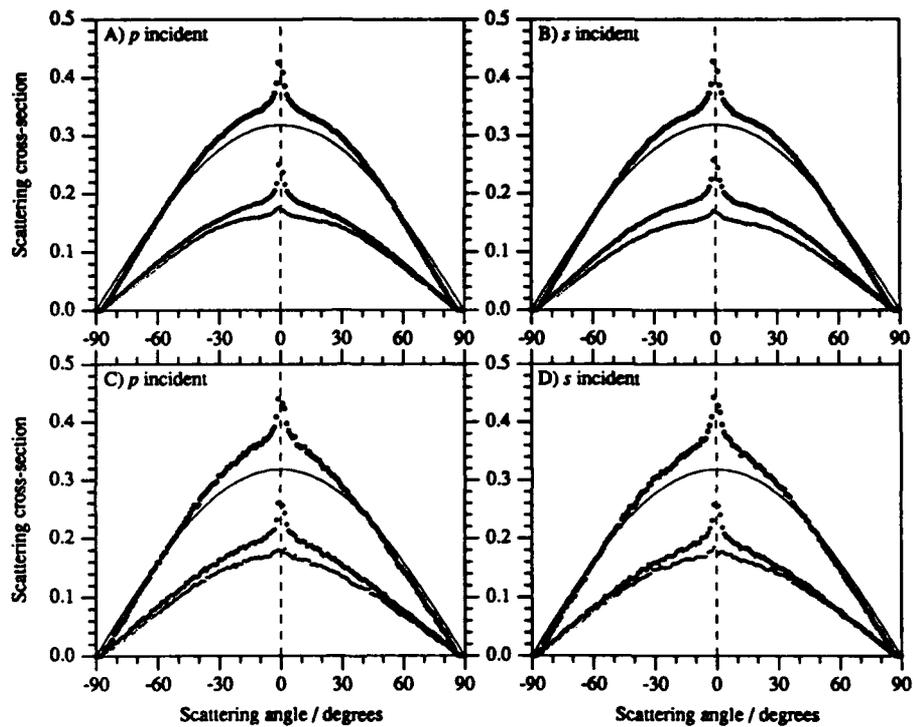
Figure 2.5: Scatter envelopes from a flat $BaSO_4$ surface for $0°$ incidence; A) and B) $\lambda = 0.633$ μm, p and s incident polarizations respectively; C) and D) $\lambda = 1.15$ μm, p and s incident polarizations respectively. Ξ_{co} denoted by 'o'; Ξ_{cross} denoted by '+', and Ξ_{tot} denoted by 'o'. Lambertian cosine represented by solid curve; backscatter is denoted by a vertical dashed line.

and Hilgeman [32, 33], measuring the *opposition effect* (enhanced backscattering).

An approximate Lambertian diffuser was not available to measure the response of the scatterometer at the two remaining wavelengths $\lambda = 3.39$ and $10.6\ \mu m$. However, the diverging beam geometry employed for the wavelength $\lambda = 3.39\ \mu m$ is also used for $\lambda = 0.633$ and $1.15\ \mu m$ which has been shown to give a good cosine response. The scatterometer response of the $10.6\ \mu m$ geometry (converging beam) was measured using the wavelength $\lambda = 0.633\ \mu m$ using the CdS infra-red lenses and, although not presented, was found to give similar results.

The consequence of measuring a Lambertian standard is more easily understood by considering its effect on equation (2.1). $\langle f_r \rangle$ is held constant by definition and so any deviation in detector response from $\cos(\theta_s)$ is due to the weight function $\mathcal{W}(\theta_s, \phi_s)$, assuming P_i is constant. This means that the solid angle of detection $\Delta\Omega_d$ is itself dependent on the direction in which the light is scattered. Since the compressed $BaSO_4$ is only an approximate Lambertian diffuser (e.g. the presence of a backscatter peak) and the measurements' agreement to the ideal cosine is good, we shall assume that $\Delta\Omega_d$ is independent of scatter direction for each of the wavelengths. Ignoring any normalization, then, scatter envelopes presented in this dissertation will be as seen by the detector, no 'shaping' of the curves will be done.

One final point which should be made concerning the DSCS $\Xi(\theta_i, \phi_i; \theta_s, \phi_s)$ is that its measurement is limited to the plane in which the detector arm rotates — the plane of incidence. This means that the arguments of $\Xi(\theta_i, \phi_i; \theta_s, \phi_s)$ reduce to $\Xi(\theta_i; \theta_s)$. As discussed in § 2.5.1, only one measurement of the scattered light is required for each of the incident linear polarizations p and s. For the case of a two-dimensional diffuser the light may be scattered throughout an entire hemisphere (upper and lower) and this complicates its complete experimental measurement. Since present studies are concentrating on the simplified, but little understood, case of one-dimensional scattering, two-dimensional diffusers will not be considered in this dissertation.
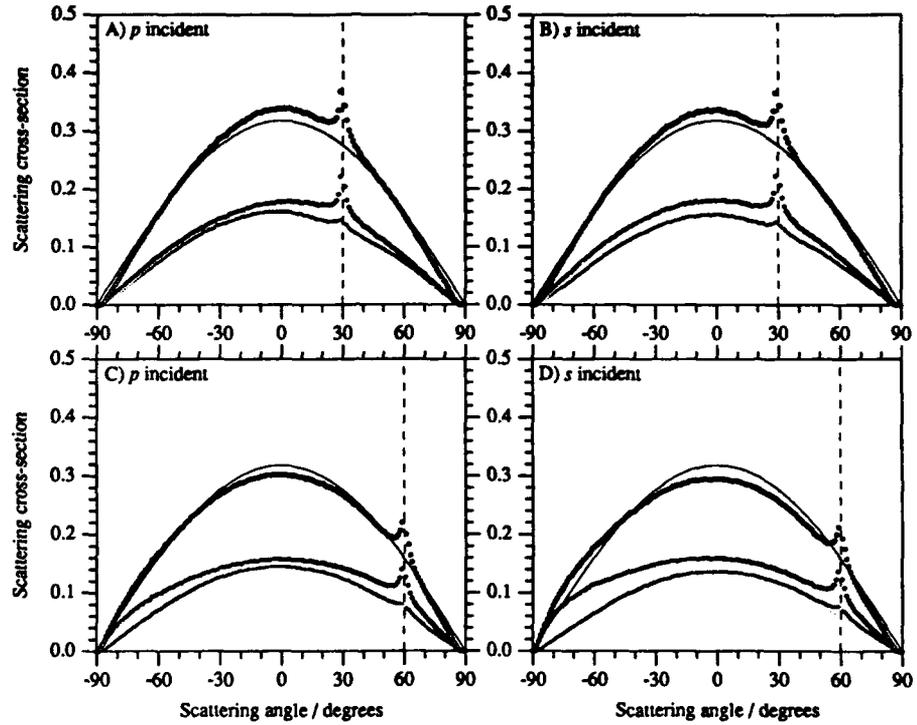
Figure 2.6: Scatter envelopes from a flat BaSO$_4$ surface for $\lambda = 0.633$ μm; A) and B) $-30°$ incidence, p and s incident polarizations respectively; C) and D) $-60°$ incidence, p and s incident polarizations respectively. Ξ_{co} denoted by 'o'; Ξ_{cross} denoted by '+', and Ξ_{tot} denoted by 'o'. Lambertian cosine is represented by a solid curve; backscatter is represented by a vertical dashed line.
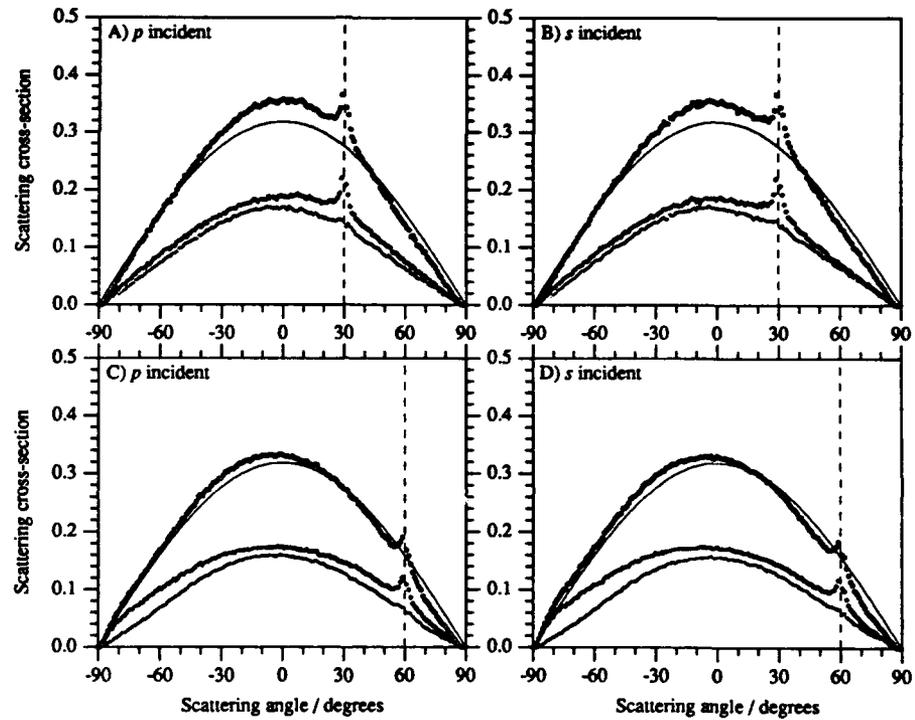
Figure 2.7: Scatter envelopes from a flat BaSO$_4$ surface for $\lambda = 1.15$ μm; A) and B) $-30°$ incidence, p and s incident polarizations respectively; C) and D) $-60°$ incidence, p and s incident polarizations respectively. Ξ_{co} denoted by 'o'; Ξ_{cross} denoted by '+', and Ξ_{tot} denoted by 'o'. Lambertian cosine is represented by a solid curve; backscatter is represented by a vertical dashed line.

Chapter 3

Fabrication of High Sloped Diffusers

3.1   Introduction

The problem of experimental light scattering from rough diffusers is only partially specified if one knows the illuminating wavelength and scatterometer response. For complete specification of the problem one also requires a detailed knowledge of certain properties of the diffuser. These include the bulk material's complex permittivity ε and the rough, surface height profile $h = h(x,y)$.

Theoretical studies of light scattering from rough surfaces generally assume the surface profile to be governed by a particular random process, solving either numerically for a generated a set of statistically identical profiles [62], or analytically for a particular distribution [10]. For both cases certain statistical parameters of the rough profile are required, depending on the particular process involved. Until recently, experimental light scattering studies have been limited to *assuming* the statistical nature of the surfaces examined, usually Gaussian; e.g. see Reference [12].

For critical comparisons between experiment and theory it is necessary to know, as precisely as possible, the parameters governing the surface height fluctuations. It was for this reason that a method was developed for fabricating randomly rough diffusers of known statistics which could be reliably characterized [37]. Following the investigations of Méndez and O'Donnell [55, 63], attention was placed on the fabrication of diffusers whose surface asperities were of the order of optical wavelengths, with slopes approaching unity. In this regime the phenomenon of enhanced backscatter is known to occur for highly reflecting diffusers.

47

3.2   Random variables

In describing the surface profile as being *randomly rough* we mean that the surface height at an arbitrary point cannot be predicted in advance. All that is known about the height is that it has a *probability* of being a certain value h. It is convenient to introduce two quantities — the *random variable* $H(h)$, and the *probability distribution function* $F_H(h)$. The random variable H consists of all possible outcomes h, including a measure of their respective probabilities. The distribution function $F_H(h)$ describes H in terms of the probability of it being less than or equal to h; formally, F_H is defined by the relationship

$$F_H(h) = \text{Prob}\,\{H \leq h\}$$

where Prob $\{\ldots\}$ means the probability of the event $\{\ldots\}$ occurring. F_H is a monotonically increasing function of h, where $-\infty \leq h \leq \infty$, with the limits

$$F_H(-\infty) = 0 \qquad F_H(+\infty) = 1 \tag{3.1}$$

The probability that the surface height lies in the range $h \leq H \leq h + \delta h$ is

$$\text{Prob}\,\{H \leq h + \delta h\} - \text{Prob}\,\{H \leq h\} = F_H(h + \delta h) - F_H(h)$$

We can define a quantity called the *probability density function* (pdf) $p_H(h)$ such that

$$p_H(h) = \lim_{\delta h \to 0} \frac{F_H(h + \delta h) - F_H(h)}{\delta h} \Rightarrow \frac{d\,F_H(h)}{dh} \tag{3.2}$$

Thus, one can recognize the importance of the density function:

$$\text{Prob}\,\{h \leq H \leq h + dh\} = p_H(h)\,dh$$

From equations (3.2) and (3.1) it follows that

$$\int_{-\infty}^{\infty} p_H(h)\,dh = F_H(\infty) - F_H(-\infty) \Rightarrow 1$$

Due to the nature of F_H, the density function also has the property that

$$p_H(h) \geq 0$$

3.2.1   Gaussian random processes

The concept of a random variable can be extended to the _random process_, whereby the unpredictable event is a function (e.g. of space and/or time) rather than a set of numbers. In most situations where random pheṇomena are encountered, the overall process is governed by many additive, independent events. Such a process can be described by employing _Gaussian_ statistics, by virtue of the central limit theorem [35, page 31]. The case of Gaussian statistics is often favoured by theorists because of its general application and mathematical elegance. In support of this theme I shall concentrate on the fabrication of randomly rough diffusers whose statistics are governed by Gaussian random processes.

The pdf of the Gaussian random variable $H(h)$ is

$$p_H(h) = \frac{1}{\sigma_h \sqrt{2\pi}} \exp\left\{ -\frac{(h - \langle h \rangle)^2}{2\sigma_h^2} \right\}$$

The parameters $\langle h \rangle$ and σ_h are defined as follows:

the _first moment_ (mean value, expectation value)

$$\langle h \rangle = \int_{-\infty}^{\infty} h \, p_H(h) \, dh$$

the _second central moment_ (variance)

$$\sigma_h^2 = \int_{-\infty}^{\infty} (h - \langle h \rangle)^2 \, p_H(h) \, dh$$

Also of importance is the _second moment_ (mean-square value)

$$\left\langle h^2 \right\rangle = \int_{-\infty}^{\infty} h^2 \, p_H(h) \, dh$$

and is related to the mean and variance by the general expression

$$\sigma_h^2 = \left\langle h^2 \right\rangle - \langle h \rangle^2 \tag{3.3}$$

Therefore, for a zero-mean, random process the root-mean-square value (rms) is simply the _standard deviation_ σ_h. Combining n random variables, one can construct an n-th order pdf describing the probability that $(U_1, U_2, U_3, \ldots, U_n)$ take on the values $(u_1, u_2, u_3, \ldots, u_n)$. In practice only up to second order is required for complete description of a zero-mean, Gaussian random process.

The autocorrelation function

The rms height σ_h gives a measure of the dispersion of point heights on the random surface about the mean plane, i.e. the vertical roughness of the surface profile. A measure of the horizontal scaling can be achieved by considering the *autocorrelation function* of $H(h)$

$$\Gamma_H(h_1, h_2) = \iint_{-\infty}^{\infty} h_1 h_2 \, p_H(h_1, h_2) \, dh_1 dh_2 \qquad (3.4)$$

where $p_H(h_1, h_2)$ is the second order pdf of $H(h)$ and

$$h_1 = h(x_1, y_1) \qquad h_2 = h(x_2, y_2)$$

The autocorrelation function, then, is the first moment of the second order pdf $\langle h_1 h_2 \rangle$ and, assuming $\langle h \rangle = 0$, this function is equal to the *autocovariance* of $H(h)$

$$
\begin{aligned}
C_H(h_1, h_2) &= \langle (h_1 - \langle h_1 \rangle)(h_2 - \langle h_2 \rangle) \rangle = \langle h_1 h_2 \rangle - \langle h_1 \rangle \langle h_2 \rangle \qquad (3.5) \\
&= \Gamma_H(h_1, h_2)
\end{aligned}
$$

The second order pdf of the random variable $H(h)$ is

$$p_H(h_1, h_2) = \frac{1}{2\pi\sigma^2\sqrt{1-\varrho^2}} \exp\left(-\frac{h_1^2 + h_2^2 - 2\varrho h_1 h_2}{2\sigma_h^2(1 - \varrho^2)} \right) \qquad (3.6)$$

The quantity ϱ is called the *correlation coefficient* and is defined as

$$
\begin{aligned}
\varrho &= \frac{C_H(h_1, h_2)}{\sigma_h^2} \\
&= \frac{\langle h_1 h_2 \rangle}{\sigma_h^2} \qquad (3.7)
\end{aligned}
$$

The correlation coefficient, in this case, is a measure of the similarity between the height fluctuations at a point (x_1, y_1) and those at a second point (x_2, y_2). If the rough surface is isotropic and the random process governing the height fluctuations is stationary[†], then the coefficient is dependent on only the relative displacement l of the two points, where

$$l^2 = (x_2 - x_1)^2 + (y_2 - y_1)^2$$

It follows from equations (3.7) and (3.3) that

$$\varrho(l = 0) = 1$$

[†]In other words, the n-th order pdf of the random variable is independent of any fixed origin either temporal, spatial, or otherwise.

Another important property of the correlation coefficient is that it tends to zero as $|l| \to \infty$. The reason for this is that the heights at two widely separated points on a randomly rough surface are uncorrelated. The explicit form of the correlation coefficient is not uniquely determined by the above conditions — the choice of this function merely reflects how rapidly ϱ decays with increasing l. Choosing a Gaussian correlation function

$$C_H(l) = \sigma_h^2 \exp\left(-\frac{l^2}{\tau^2}\right) \tag{3.8}$$

and

$$\varrho(l) = \exp\left(-\frac{l^2}{\tau^2}\right)$$

The horizontal scaling of the surface profile is then described in terms of the transverse correlation length τ; it is the distance over which the correlation function is reduced by a factor $1/e$ from its value at the origin.

3.3   Fabrication of diffusers

Several methods exist for producing either a random-phase screen or a randomly undulating surface profile. Both cases can introduce random phase fluctuations in the transmitted radiation, which spatially modulates the irradiance of the light in the far-field. Photographic techniques are generally limited by the granularity of the emulsions, which can affect the diffusing properties of the phase screen. Ground glass has been a popular choice of diffuser for experimenters investigating light scattering phenomena [12, 36]. Although the mean size of the surface asperities can be influenced during the grinding process, the surface structure is very jagged and not smoothly undulating. Such a structure is very difficult to describe and would present unnecessary complications to theoretical treatments of the problem.

A method of producing a smoothly varying surface profile of known statistics has been described by Gray [37]. He exposed photoresist-coated substrates to the spatially random light distribution of a laser speckle pattern. Méndez and O'Donnell [55, 63] used a similar method to produce gold-coated, Gaussian random surfaces from which the backscattered light was strongly enhanced. This method was adapted in this present work for producing deep, random surface profiles with Gaussian height pdf and autocorrelation functions. Details of the coating and etching procedures are

discussed in the next sections.

3.3.1 Spin-coating procedure

The aim of this procedure is to coat a glass substrate with a photoresist film of $\sim 11 \ \mu m$ thickness that is flat, uniform, and free from dust particles. One of the best methods to achieve at least a flat, uniform film is to spin-coat the substrate. In order for the film to have a sufficient thickness, the type of resist and spin speed have to be carefully selected. If the resist is not viscous enough, or the spin speed too high, then the film thickness may be less than $1 \ \mu m$.

The substrates used were relatively flat (~ 5 fringes at $546 \ nm$) $50 \times 50 \times 3 \ mm$ glass plates. The extra thickness improves handling of the substrates and greatly reduces the possibility of breakage. The initial stage is to clean the substrates as thoroughly as possible, in a relatively dust-free environment. Although several procedures exist for preparing clean substrates, the following routine was found to be reliable.

STEP 1. Wash in hot water and detergent.

STEP 2. Thoroughly wipe with acetone.

STEP 3. "Zero-G" wipe with acetone.

STEP 4. Wipe with isopropanol, to remove smears left by the acetone.

STEP 5. "Zero-G" wipe with isopropanol.

With the exception of step one, all wipes are done with lens cleaning tissues. The "zero-G" wipes involve dragging a single tissue across the substrate surface while the solvent soaks into the tissue and evaporates; see Figure 3.1. If sufficient is applied, the whole surface is wetted with solvent which should all evaporate before reaching the end of the tissue. This reduces the possibility of the solvent leaving smeary deposits on the substrate. Between steps, the occasional blast of compressed air can help to remove loose dust particles.

The photoresist used was Shipley S1400-37 which is a high resolution, thick film resist and has a good linear response curve of surface height against exposure time. With the substrate suitably attached to the centre of the turntable, the following

Figure 3.1: The "zero-G" wipe: a lens cleaning tissue is dragged across the substrate in the direction indicated; the solvent spreads across its surface and evaporates before reaching the end of the tissue.

procedure gave a uniform, flat resist film of 10–12 μm thickness. This procedure should be carried out in a filtered, dust-free environment.

STEP 1. Syringe ~ 3 ml of photoresist onto centre of stationary substrate.

STEP 2. Spin substrate at 300 r.p.m. for four minutes.

STEP 3. Syringe another 3 ml of photoresist onto stationary substrate.

STEP 4. Spin substrate for a further four minutes.

The resist was applied from a 5 ml glass syringe fitted with a 2 μm filter. Care was taken not to let air bubbles interrupt the flow of resist; they are difficult to remove from the film completely. It was necessary to empty the syringe when not in use because the viscous resist has a tendency to 'stick' if left for any length of time. The plunger and cylinder were separated and placed in a shallow bath of acetone. When needed again a full charge of resist, slightly diluted with acetone, was loaded and discharged from the syringe to remove any residual acetone.

Once coated, the plates were allowed to dry at room temperature for 24 hours. This period allows minor striations in the layer to even out and enough solvent to evaporate for the resist to become 'touch-dry'. The plates were then baked at a

temperature of 90 °C for 30 minutes. The resulting layer, although fully dried, is extremely susceptible to being scratched, even by lens tissues; any subsequent dust contamination should be gently blown off with compressed air.

3.3.2 First-order speckle statistics

In order to understand the reasons for employing laser speckle patterns to generate the diffusers, other than the fact that they are random, it is useful to briefly discuss first-order speckle statistics, i.e., the statistical properties at a single point in the observation plane; see Figure 3.2. It is assumed that the speckle pattern is perfectly polarized and monochromatic.
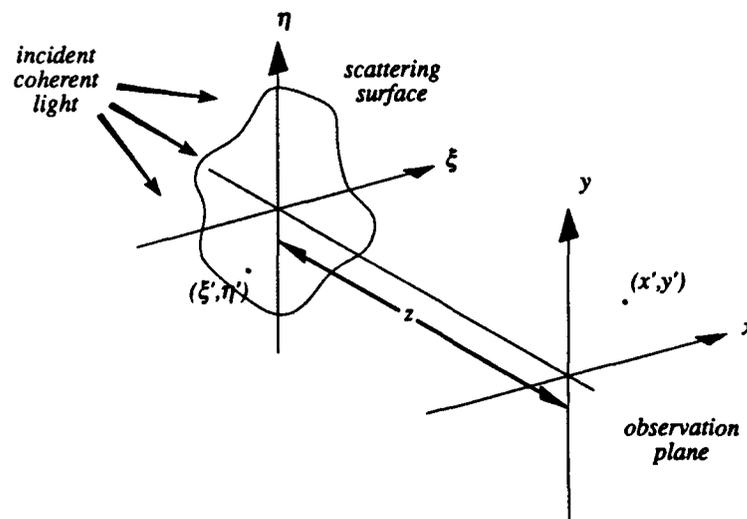
Figure 3.2: Generation of a speckle pattern using a diffusing screen.

The complex amplitude at a point (x', y') in the observation plane can be considered to consist of a large number of elementary phasors from each point (ξ', η') on the scattering surface. If the individual phases are uniformly distributed over the range $(-\pi \rightarrow \pi)$, i.e. the diffusing surface is rough compared to a wavelength, then the real and imaginary components of the amplitudes obey Gaussian statistics (the central limit theorem). Their joint probability density is then of the form given in

equation (3.6) with $\varrho = 0$, since the real and imaginary components are uncorrelated. The intensity, then, of a speckle pattern obeys *negative exponential* statistics and its pdf is

$$p_I(I) = \frac{1}{\langle I \rangle} \exp\left(-\frac{I}{\langle I \rangle}\right)$$

where $\langle I \rangle$ is the mean intensity. The standard deviation σ_I of a polarized speckle pattern is

$$\sigma_I = \langle I \rangle$$

If the incident beam at the scattering surface in Figure 3.2 has a Gaussian cross-section, the correlation coefficient [equation (3.7)] of the speckle pattern is

$$\varrho_I(\Delta x, \Delta y) = \exp\left(-\left[\frac{\sqrt{2}\,\pi\omega_\xi\Delta x}{\lambda z}\right]^2\right) \exp\left(-\left[\frac{\sqrt{2}\,\pi\omega_\eta\Delta y}{\lambda z}\right]^2\right) \qquad (3.9)$$

where $\omega_{\xi(\eta)}$ is the $1/e$ radius of the intensity profile at the scattering surface in the direction $\xi(\eta)$; z is the distance between the scattering surface and the observation plane; and λ is the wavelength. If the beam is circularly symmetric, then $\omega_\xi = \omega_\eta = \omega$ and the correlation length of the speckle pattern is

$$\tau = \frac{\lambda z}{\sqrt{2}\,\pi\omega}$$

in any direction in the observation plane. However, if the beam is shaped such that its cross-section is much greater along the ξ-axis than the η-axis, then $\omega_\xi \gg \omega_\eta$ and the correlation lengths in the observation plane become

$$\tau_x = \frac{\lambda z}{\sqrt{2}\,\pi\omega_\xi} \qquad \tau_y = \frac{\lambda z}{\sqrt{2}\,\pi\omega_\eta}$$

therefore $\tau_x \ll \tau_y$. In other words, the speckle pattern is elongated along the y-axis. If the incident beam at the scattering surface is a straight line, such as would be produced at the focal plane of a cylindrical lens, then the resulting speckle pattern will be approximately *one-dimensional*. (Unless stated otherwise, it is assumed that the speckle correlation lengths $\tau_x = \tau$ and $\tau_y \to \infty$.)

If N uncorrelated speckle patterns with equal mean intensities are superimposed, the resulting intensity pdf is [26, page 23]

$$p_I(I) = \frac{I^{N-1}N^N}{(N-1)!\,\langle I \rangle^N} \exp\left(-\frac{NI}{\langle I \rangle}\right)$$

The variance of the intensity in this case is

$$\sigma_I^2 = \frac{\langle I \rangle^2}{N} \tag{3.10}$$

Figure 3.3 shows the intensity pdf functions for the cases $N = 1, 3, 8$, and 20; the dashed line represents the Gaussian pdf whose variance is calculated from equation (3.10) for $N = 8$. As the number of uncorrelated speckle patterns increases, the
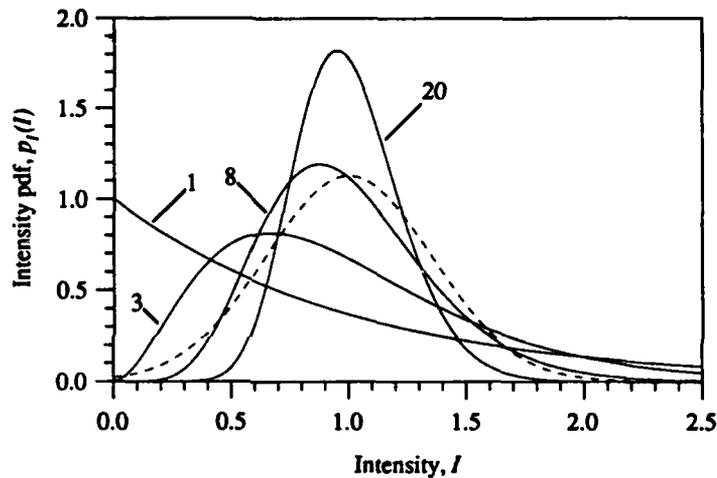
Figure 3.3: Intensity pdf functions resulting from the incoherent addition of $N = 1, 2, 3, 8$, and 20 speckle patterns with equal mean intensities. The dashed line represents the Gaussian pdf for σ_I corresponding to $N = 8$ in equation (3.10).

pdf assumes a more Gaussian-like distribution becoming progressively narrower; this demonstrates how the variance is inversely proportional to N. There will be, therefore, a 'trade-off' between the contrast of the total distribution and its Gaussianity. If the contrast is too low, although it may be accurately Gaussian, the structures of the resulting diffuser will be shallow compared to a wavelength.

3.3.3 Etching procedure

Accepting inevitable non-linearity of the photoresist, *eight* was chosen as the number of independent speckle patterns to be superimposed onto a single coated substrate.

This would be expected to produce an approximately Gaussian diffuser with nominally deep structures.

In order to comply to the limitations of present theoretical light scattering studies [49, 62], it was necessary to produce a diffuser which was rough in only one dimension, i.e. having a random corrugation. As discussed in § 3.3.2 this can be achieved by incorporating a cylindrical lens in the illumination geometry which generates the speckle pattern. The exposure geometry used to produce a one-dimensional diffuser is illustrated in Figure 3.4. The coherent light source was an Argon-ion laser operating at the blue wavelength 457.9 nm. The sensitivity of the resist increases towards ultra-violet wavelengths, but green and longer wavelengths have almost no effect.

spatial filter:	200 mm	200 mm	ground-glass	photoresist-coated
20x0.4 objective	spherical lens	cylindrical lens	diffuser	substrate
15 µm pinhole				
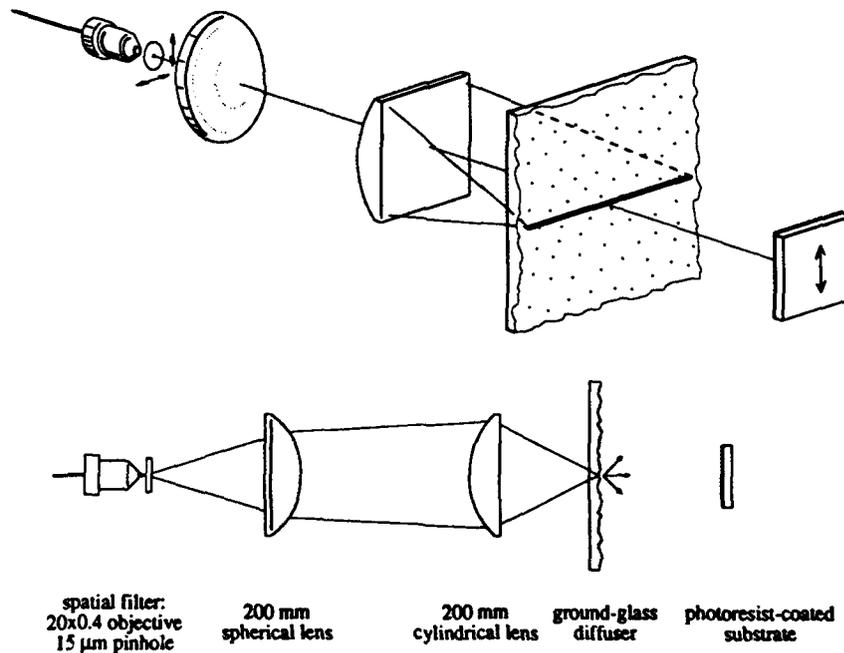
Figure 3.4: Exposure geometry for producing a one-dimensional diffuser. The speckle pattern is elongated vertically, as illustrated on the substrate. The light source is an Argon-ion laser (457.9 nm).

The laser light was passed through a spatial filter to produce a relatively 'clean' Gaussian beam profile. A spherical lens approximately collimated the beam towards

a large aperture (80 × 95 *mm*) cylindrical lens. The ground-face of a glass diffuser was placed at the focal plane of the cylindrical lens, facing the coated substrate. This ensured that the plane face of the diffuser did not interfere with the generated speckle pattern.

For a given distance from the diffuser to the substrate, the speckle correlation length τ is determined by the length of the Gaussian line focus. Moving the substrate towards the diffuser linearly reduces τ, but also reduces the area over which the speckle pattern can be considered to have a uniform mean intensity. The intensity of the speckle pattern must at least appear to the eye to be uniform over the photoresist film. This is much easier to accomplish when producing a two-dimensional pattern without the cylindrical lens since the majority of the diffuser is illuminated, not just a narrow line.

The rear (uncoated) face of the substrate was sprayed with matt black paint to reduce the effects of internal reflections. With the substrate in the desired position, the photoresist was exposed to eight independent speckle patterns for equal exposure times. For one-dimensional patterns this simply meant moving the diffuser vertically by ~ 1 *cm* to illuminate a new part of it. Care was taken to ensure that the diffuser remained in the focal plane of the cylindrical lens. For two-dimensional patterns the whole diffuser was replaced for another.

When the exposures were completed, the photoresist was developed in a linear developer (Shipley AZ-303), at a 1 : 5 dilution by volume with water, at room temperature for 30 *s*. The developed plate was then washed in running water for approximately three minutes and finally dried using compressed air. The fabricated diffuser was then examined for signs of over-exposure or development, where the resist has been removed down to the substrate. If not, it is then a question of characterizing the surface profile, calculating its statistical parameters.

3.4   Surface characterization

Many techniques are available for the measurement of surface roughness [76, chapters 2,3] and each one has factors limiting its scope of application. The techniques include using light as a non-contact probe; monitoring electrical properties such as capacitance or field emission current; and mechanical contact employing some kind of

stylus. Methods involving scattered light, of one form or another, cannot be expected to work where multiple scattering can occur, i.e., from surfaces rough compared to the wavelength. For the diffusers studied in this work, the latter method of mechanical profiling was used, employing the Rank Taylor-Hobson Talystep instrument fitted with a sharp, diamond stylus.

3.4.1 Stylus profiling

The principal behind stylus instruments is quite straightforward. A certain load is applied to the stylus, e.g. from a hairspring, to prevent it 'bouncing' and losing contact with the surface. As it is dragged across the surface its vertical displacements are converted into electrical oscillations via a transducer. This electrical signal can then be amplified, filtered, and analysed to obtain any desired roughness parameter. The horizontal resolution of the instrument depends on the stylus dimensions; the vertical resolution is limited by the thermal noise of the amplifying electronics and mechanical stability of the environment.

The Talystep was fitted with a pyramidal-shaped, diamond stylus having the dimensions $1.8 \times 0.5~\mu m$ across the flat end, and a 70° included angle between _its_ sides. This shape of stylus is particularly well suited to profiling one-dimensional structures; the direction of stylus travel being along the smaller dimension ($0.5~\mu m$). The load applied to the stylus at the middle of its displacement range was 6 mg; this meant that, during a typical measurement, the load would vary from $\sim 2~mg$ for deep structures (valleys) up to $\sim 10~mg$ for high structures (peaks).

Using a facility available on the Talystep to relocate the stylus at the beginning of a previous measurement, it was possible to examine the effects of repeated measurements along a portion of the surface. In Figure 3.5 are shown three successive surface profiles of the same location on a one-dimensional surface. The traces were measured with the vertical and horizontal magnification factors $\times 5000$ and $\times 2000$, respectively. The stylus was kept in contact with the surface during relocation so, although trace A is the first measurement, traces B and C actually correspond to the third and fifth passes of the stylus, respectively. There are no features in trace A which are not reproduced in traces B or C. The only differences occur at some of the highest peaks, where the stylus load is greatest, which become slightly rounded;
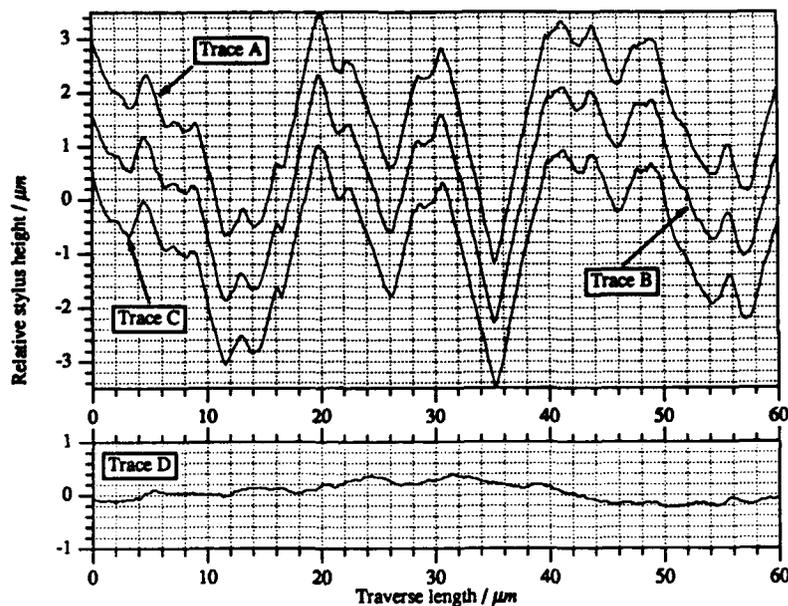
Figure 3.5: Talystep profiles of a one-dimensionally rough, photoresist surface. Traces A, B, and C correspond to the first, third, and fifth measurements *across* the random corrugations, respectively. The stylus does not have any appreciable effect, even on the smallest surface structures. Trace D represents a measurement *along* the corrugations which, ideally, are flat.

these effects are so small that they can be considered to be negligable. The lower graph, trace D, is a profile taken *along* the surface corrugations instead of *across* them. This shows how well the surface approximates a one-dimensional structure; ideally the profile would be a straight line. One can imagine how a light ray incident on trace A, at some arbitrary angle, will be reflected in a random direction. However, the same ray incident on trace D is likely to be reflected within a small angle about its specular (mirror-like) direction. Hence the light scattered from such a structure (reflection and transmission) will be approximately confined to a plane[†].

The experimental work presented in the chapters to follow is based mainly around two *one-dimensional* diffusers: diffusers #39 and #46. The details of alternative (e.g. two-dimensional) diffusers which have been investigated will be discussed where they are introduced. Surface profiles were characterized by measuring six traces at different

---

[†]For grating-like structures, if the plane of incidence is not normal to the plane containing the grating, the scattered light will actually describe a conical surface — conic diffraction.

locations across the surface. Each trace consisted of 9000 point height measurements with a horizontal interval of 0.2 μm. The stylus was always traversed at the slowest available speed of 2.5 $\mu m\,s^{-1}$. After removing the d.c. offset (fitting a zero-mean line), each profile was analysed to obtain its rms height σ_h, from equation (3.3), and its $1/e$ correlation length τ, from equation (3.5). Examples of the probability density and autocorrelation functions measured for diffusers #39 and #46 are shown in Figure 3.6. It can be seen that these measured functions are very closely Gaussian. The statistical parameters for each diffuser, expressed as mean values of six individual measurements, are shown in Table 3.1. The skewness and kurtosis are the third and

Diffuser	rms height $\sigma_h/\mu m$	$1/e$ correlation length $\tau/\mu m$	skewness Sk	kurtosis K
#39	1.18 ± 0.02	2.97 ± 0.05	-0.12 ± 0.01	2.84 ± 0.06
#46	1.22 ± 0.01	3.18 ± 0.07	-0.11 ± 0.02	2.84 ± 0.07

Table 3.1: Statistical parameters of two one-dimensional diffusers.

fourth central moments of the height pdf, respectively. They assume the values zero and three for true Gaussian distributions.

3.4.2 Effects of a finite-sized tip

A trace recorded by the Talystep instrument will not be identical to the surface profile of the sample. From the very nature of the profiling method, there will always be some effects due to the finite dimensions of the stylus. The type of effects which one can expect when tracing a smoothly varying surface are illustrated in Figure 3.7. The figure shows the *effective profile* recorded by a sharp stylus tip, and is the locus of the tip's centre which is spherical in section. If the surface curvatures are less than that of the tip, the stylus will closely record the surface profile. However if they become comparable, the finite size of the tip will tend to broaden peaks and sharpen valleys.

To assess the effects of a finite tip-size on the recorded trace, it is useful to consider the average power distribution over spatial frequency, or *power spectrum* $S(\nu)$, of the true profile. A special relationship, known as the Weiner-Khinchin theorem [35, page 74], holds between the power spectrum and the autocorrelation function — they form
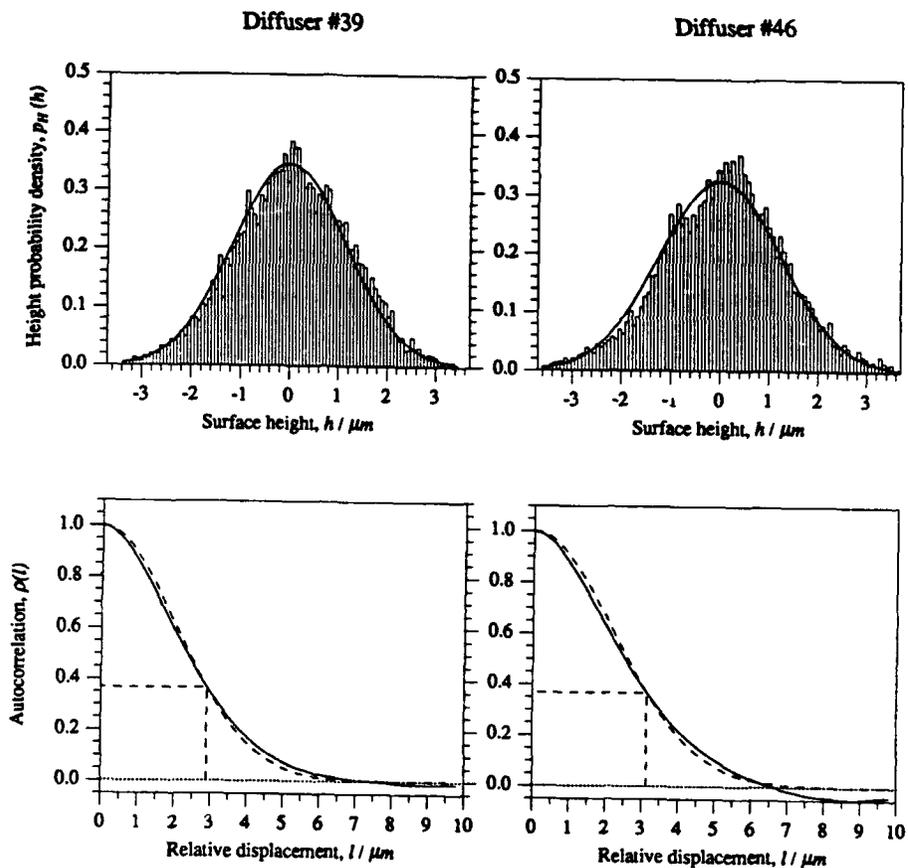
Figure 3.6: Examples of measured probability density and autocorrelation functions for diffusers #39 and #46. The Gaussian distributions for the same measured values of σ_h and τ are represented by solid lines (height pdf) and dashed lines (autocorrelation), respectively.

stylus tip   *recorded profile*

low curvatures   **high curvatures**
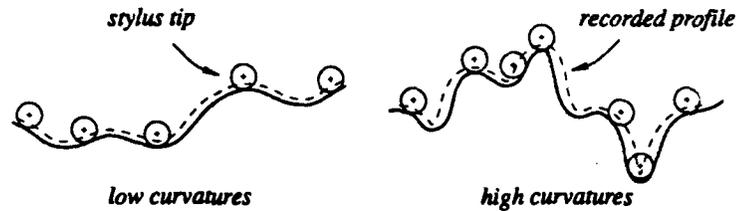
Figure 3.7: Effects of a finite-sized tip on the recorded profile. The peaks can become exaggerated while the valleys may be reduced to sharp points, depending on the surface curvatures.

a Fourier transform pair:

$$S(\nu) = \int_{-\infty}^{\infty} \Gamma(l) e^{-i2\pi\nu l} dl \qquad (3.11)$$

$$\Gamma(l) = \int_{-\infty}^{\infty} S(\nu) e^{i2\pi\nu l} d\nu \qquad (3.12)$$

From equation (3.11), the power spectrum for a random variable with Gaussian autocovariance [equation (3.8)] is

$$S_H(\nu) = \sqrt{\pi}\,\sigma^2\tau \exp\left(-[\pi\tau\nu]^2\right) \qquad (3.13)$$

The rms curvature γ of a one-dimensional profile $h = h(x)$ is defined to be

$$\gamma^2 = \left\langle \left(\frac{d^2h}{dx^2}\right)^2 \right\rangle$$

but can equally be written as the fourth moment of the power spectrum

$$\gamma^2 = \int_{-\infty}^{\infty} S_H(\nu)\,(2\pi\nu)^4\,d\nu$$

Introducing a quantity called the *rms radius of curvature* $\kappa = 1/\gamma$, the stylus tip can be considered sharp relative to the surface structures if its radius R satisfies the relation

$$R \ll \kappa \qquad (3.14)$$

For a Gaussian surface,

$$\kappa = \frac{\tau^2}{\sqrt{12}\,\sigma}$$

The values of κ, measured for diffusers #39 and #46, are shown in Table 3.2. These

Diffuser	rms radius of curvature $\kappa/\mu m$
#39	2.17 ± 0.06
#46	2.38 ± 0.08

Table 3.2: Measured rms radii of curvature.

values are significantly larger than the nominal tip radius of $R \sim 0.25\ \mu m$ used for recording the surface profiles and hence satisfy condition (3.14).

The true analytical description of the tip is probably somewhere between a flat chisel shape and a cylindrical rod. A mathematical compromise may be to use a description such as $(x/A)^m + (y/B)^m = 1$ with suitable choices of the parameters A, B, and m. However, considering the non-linearity of the stylus-surface interaction such a calculation would be extremely complicated and possibly unnecessary in this case. To investigate the likely magnitudes of the finite-tip-size effects we will employ the reasonably well behaved model of a circular tip of radius $R \ll \kappa$.

Although in the sharp tip limit the stylus smoothly follows the surface, it experiences an offset which is dependent on the surface slope; see Figure 3.8. The measured surface height $h_{meas}(x)$ is related to the actual surface height $h(x)$ by the relation [23]

$$h_{meas}(x) = h(x) + \frac{R}{2}\dot{h}^2\left(1 - \frac{1}{4}\dot{h}^2 + \cdots\right) + \frac{R^2}{2}\dot{h}^2\ddot{h}\left(1 - \dot{h}^2 + \cdots\right) \qquad (3.15)$$

where $\dot{h} = dh/dx$. Equation (3.15) expresses the measured profile in terms of the true profile and the tip radius R. From equations (3.5) and (3.8) the autocorrelation function of the measured Gaussian profile may then be expressed as [23]

$$\begin{aligned}
C_{meas}(l) &= \sigma^2 e^{-X^2}\left[1 - \frac{\gamma^2 R^2}{3}\left(1 - 3\mu^2\right)\left(1 - 2X^2\right)\right] + \\
&\quad + \sigma^2 e^{-2X^2}\frac{\gamma^2 R^2}{6}\left(1 - \frac{3}{2}\mu^2\right)^2\left(1 - 2X^2\right)^2 + \qquad (3.16) \\
&\quad + \sigma^2 e^{-4X^2}\frac{\gamma^2 R^2}{8}\mu^4\left(1 - 2X^2\right)^4 + \cdots
\end{aligned}$$

where $X = l/\tau$ and $\mu = \sqrt{2}\sigma/\tau$ is the rms slope. Expanding equation (3.16) in terms of X^2 and comparing it to the expanded form of equation (3.8) we have the relations

$$\sigma_{meas}^2 = \sigma^2\left[1 - \frac{\gamma^2 R^2}{6}\left(1 - 3\mu^2 - 3\mu^4\right) + \cdots\right]$$

$$\tau_{meas}^2 = \tau^2\left[1 - 15\gamma^2 R^2\left(\frac{\sigma}{\tau}\right)^4 + \cdots\right]$$
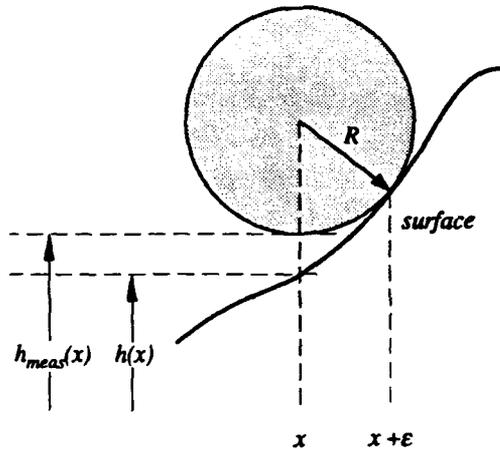
Figure 3.8: The stylus tip experiences an offset due to its finite size. The actual point of contact is at $x' = x + \varepsilon$

For diffusers #39 and #46 the magnitudes of these correction terms are listed in Table 3.3. Comparing them with the statistical errors in Table 3.1 it is evident that the effects of the finite tip-size are practically negligable. Since $(\gamma R)^2 \ll 1$ we do not need to consider a more realistic model.

Diffuser	% increase in σ	% decrease in τ
#39	0.03	0.24
#46	0.01	0.18

Table 3.3: Estimates of tip-size effects on measured surface parameters.

3.5   Replication of diffusers

In any investigation, varying certain parameters independently can aid the analysis of a system's mechanisms. For the case of light scattering from random surfaces, the parameters involved are the wavelength of the radiation λ; the angle of incidence θ_i; the statistical parameters of the surface profile σ_h and τ; and the permittivity of the medium ε. Experimentally, the wavelength can be easily varied through the use of

suitable lasers, but not generally at the exclusion of the permittivity. The surface profile parameters can be altered during fabrication of the diffuser: σ_h is governed by the total exposure time, and τ by the speckle pattern's correlation statistics at the substrate. It is unlikely, however, that changing the surface statistics will provide much more information than will changing the wavelength. Varying the permittivity is potentially more gainful, as it is related to the material's reflectivity. In order to ensure that ε could be varied without affecting σ_h and τ, a method of replicating a random surface profile was developed.

The replication method described in this section employs a silicone elastomer (Dow Corning Sylgard 182) and an epoxy resin (Araldite MY778 and hardener HY956). Diffuser #39 was initially over-coated with gold (by vacuum deposition) and characterized using the Talystep profiling instrument. A set of scattered light measurements was taken from the diffuser, over a range of incident angles, using the equipment described in Chapter 2 at the wavelength 633 nm. A positive replica of diffuser #39 was then produced using the procedure described below.

STEP 1. Thoroughly mix $\sim$ 30 ml of elastomer and curing agent in the ratio 10:1 by weight, and de-gas under partial vacuum.

STEP 2. Place diffuser rough-side-up in a shallow receptacle and gently pour in the elastomer, ensuring that no air bubbles get trapped.

STEP 3. Cure the elastomer at a temperature of 80 $^{\circ}C$ for eight hours.

STEP 4. Release the elastomer from the receptacle and gently peel out the diffuser, to reveal a flexible mould.

STEP 5. Thoroughly mix $\sim$ 20 ml of resin and hardener in the ratio 6:1 by weight, and de-gas.

STEP 6. Pour the resin into the mould, again ensuring that no air gets trapped.

STEP 7. Allow the resin to cure at room temperature for 24 hours.

STEP 8. Gently peel the replica diffuser from the mould.

Although the procedure is straightforward, there are some practical points that are worth mentioning.

i) When weighing out the elastomer or resin, only put in $\sim 5\ g$ at a time followed by the curing agent or hardener, building up a 'sandwich' to the required volume. This enables the components to be mixed more thoroughly.

ii) During de-gassing the liquid should be placed in a glass container with a large base area and moderately tall sides to allow for expansion. The elastomer is less viscous than the resin and will yield all trapped air. The resin may retain a few small bubbles which will not be visible by the eye at atmospheric pressure unless the experimenter has been over-ambitious, in which case the resin has already cured! Do not wait much longer than 30 minutes; the vacuum will continue to pull off any volatiles in the mixture. Although it will cure more rapidly if baked, the resin tends to discolour and shrink, and any trapped air may expand when heated.

iii) For the receptacle mentioned in step two, I attached a 10 mm deep aluminium ring (inside diameter 75 mm) to a flat sheet of perspex with three self-tapping screws. The screw heads were counter-sunk to allow the perspex base to lie flat without tilting. This construction has the advantage that the aluminium ring can be removed from the perspex base allowing easy access to the cured elastomer.

3.5.1 Verification of procedure

To check whether the resin replica is a faithful reproduction of the original, the replica was over-coated with gold and a set of measurements, corresponding to that for diffuser #39, was taken for comparison; the results are shown in Figure 3.9. The measured DSCS curves of the original and replica overly almost exactly. The slight discrepancies can be attributed to misalignment of the plane of scatter with respect to the plane of incidence, i.e. the corrugations of the surface(s) were not exactly vertical during the measurement. For normal incidence (Figure 3.9: graphs A and B) a strong enhanced backscatter peak is observed with subsidiary maxima.
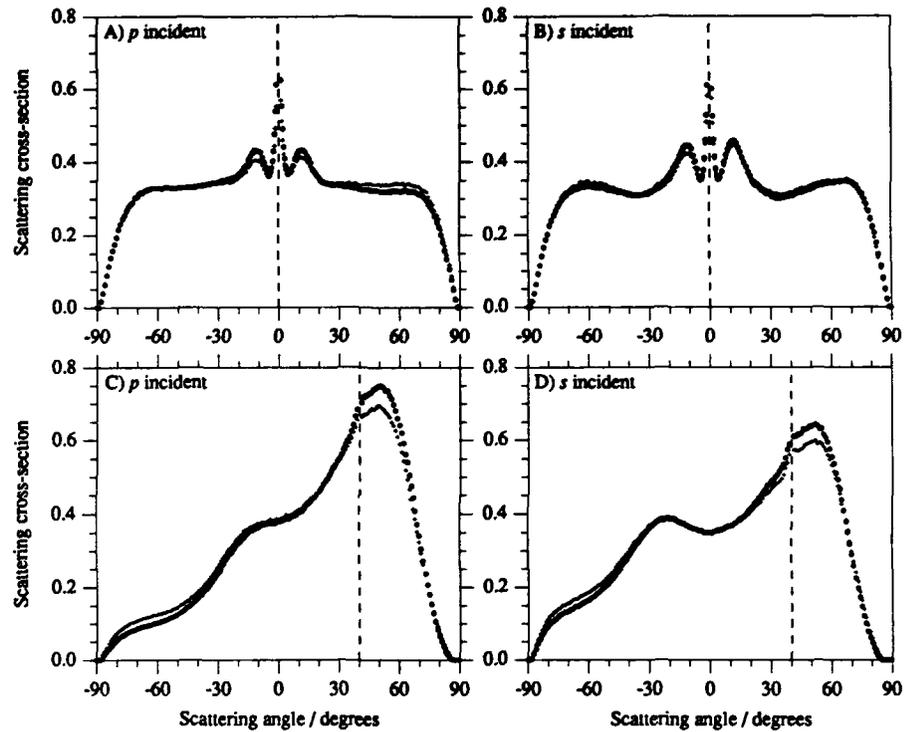
Figure 3.9: Scatter envelopes from gold-coated original #39 (o) and replica (+) diffusers, for wavelength $\lambda = 633\ nm$; A) and B) 0° incidence, p and s incident polarizations, respectively; C) and D) $-40°$ incidence, p and s incident polarizations, respectively. Dashed line denotes backscatter direction.

The corresponding measurements for $-40°$ incidence (graphs C and D) do not show enhancement, although the majority of the light is scattered in a backward direction. Whatever the fine-scale limitations of the elastomer and resin, the resolution of these materials seems sufficient to reproduce the scattering processes present on the original diffuser; from the wavelength involved, one could estimate a resolution of $\ll 1$ μm.

It is possible, using the technique described above, to cast a number of replicas from the same mould and then coat them with, e.g., different metals. Although there may be measureable differences in absorptions and scattered light distributions, it is likely that the changes would only be subtle over the wavelengths available for study. What would be more interesting would be to compare the scattering properties of a metal-coated diffuser (e.g. gold) with a transparent, dielectric replica, i.e. one that has very little absorption. The silicone elastomer material, used to form the mould in the replication procedure, has these required properties. The resin, although reasonably transparent, does not handle as well as the elastomer; its viscosity makes it difficult to ensure a homogeneous mix and to de-gas fully. The elastomer also has the advantage of being directly in contact with the original diffuser

3.5.2   Dielectric diffuser assembly

The procedure for producing an elastomer replica is similar to steps one to four already described in this section, but with two modifications. The first is that, instead of being a complete mould, the elastomer only needs to have the same dimensions as the original. The second, more important, modification comes in step three during the curing process. To investigate the light scattering properties of a transparent, rough surface, the spurious reflection caused by the rear face of the sample has to be suppressed. For the case of a one-dimensional diffuser, this reflection can be directed away from the plane in which the detector moves by including an angle between the front and back faces of the diffuser. An angle of $\sim 5°$ can be included during the curing process by propping up one end of the original diffuser with a blank, glass substrate. This produces a wedge-shaped, dielectric replica which can be assembled as shown in Figure 3.10 when taking light scattering measurements. The neutral density filter acts as a beam dump and is optically coupled to the diffuser with an oil of refractive index 1.47 (compared with the dielectric's estimated index of 1.43). The
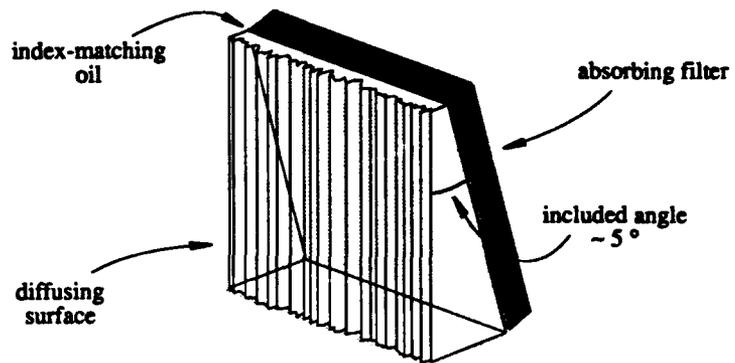
Figure 3.10: Assembly of a wedge-shaped dielectric diffuser and ND 4.0 absorbing filter.

same technique was applied to two-dimensional, dielectric diffusers but the spurious reflection could not be totally removed from the detector's field of view.

Chapter 4

Rigorous Scattering Theory and Comparison with Experimental Results

4.1 Introduction

Our theoretical treatment of light scattering by randomly rough diffusers will begin with a discussion of the way electromagnetic waves interact with materials. Of particular importance are the conditions that the waves must satisfy at the boundary between two media, where there is a discontinuous change in electrical properties, i.e. the permittivity ϵ and permeability μ.

Owing to the limitations of computational speed and data storage, the problem will be simplified by considering a scattering surface with height fluctuations in only one dimension (hence a *one-dimensional* surface) and can be considered to be a random grating. This simplification can be imposed without detracting from the scattering mechanisms occuring at the surface. The solutions for the scattered wave amplitudes will be shown to depend on the amplitudes and normal derivatives of the waves at the diffuser's surface, by a single integral equation. By imposing the extinction theorem boundary condition [65], solutions for these surface fields can be obtained by inverting two matrix equations. This use of the extinction theorem has been implemented in a number of similar investigations [51, 61, 62, 73]. The theorem constitutes what is, in effect, an exact approach to the problem and does not place any conditions on either the rms height σ_h or the correlation length τ.

An experimental data set of scattered-light measurements, representing the mean differential scattering cross-section (DSCS) Ξ, will be presented for identical gold-coated and dielectric diffusers (#46). For each of the wavelengths available (0.63,

71

1.15, 3.39, and 10.6 μm), measurements will concentrate on the two principal linear polarization states p and s for selected angles of incidence. By comparing experimental measurements with numerically calculated results, the validity of the scattering model can be assessed. If agreement is favourable, the model may then be employed to investigate how certain parameters, not easily varied experimentally (e.g. the permittivity ϵ), affect the spatial modulation of the scattered light field. Conclusions drawn from such results may lead to an understanding of the scattering mechanisms involved, particularly those behind the phenomenon of enhanced backscattering.

4.2 Electromagnetic fields in materials

The phenomenon of light propagation through vacuum or dielectric medium is a direct consequence of the relationship that exists between time-varying electric and magnetic fields — an oscillating magnetic field induces an electric field (Faraday's Law), and *vice versa*. The equations describing this mutual interaction are collectively known as *Maxwell's equations*, and govern the behaviour of a time-varying electromagnetic field:

$$\nabla \times \mathbf{E} = -\frac{\partial \mathbf{B}}{\partial t}$$

$$\nabla \times \mathbf{H} = \mathbf{J} + \frac{\partial \mathbf{D}}{\partial t}$$

$$\nabla \cdot \mathbf{D} = \rho$$

$$\nabla \cdot \mathbf{B} = 0$$

$$\nabla \cdot \mathbf{J} = -\frac{\partial \rho}{\partial t}$$

The symbols are all generally functions of position $\mathbf{r} = (x, y, z)$ and time t (e.g., $\mathbf{E}(\mathbf{r}, t)$) and represent the following quantities:

$\mathbf{E}$ — electric field strength $[V/m]$
$\mathbf{H}$ — magnetic field strength $[A/m]$
$\mathbf{D}$ — electric displacement $[C/m^2]$
$\mathbf{B}$ — magnetic flux density $[Tesla]$
$\mathbf{J}$ — volume current density $[A/m^2]$
ρ — volume charge density $[C/m^3]$

In a linear material the electric vectors $\mathbf{E}$ and $\mathbf{D}$ are related by the equation

$$\mathbf{D} = \epsilon \mathbf{E} \tag{4.1}$$

where ϵ is the permittivity. A similar relationship couples the magnetic vectors **H** and **B**

$$\mathbf{B} = \mu\mathbf{H} \tag{4.2}$$

where μ is the permeability. Both ϵ and μ are, in general, complex quantities which are constant if the medium is isotropic and homogeneous. If the material is also conducting, a conduction current **J** is induced by the applied electric field

$$\mathbf{J} = \sigma\mathbf{E}$$

where σ is the conductivity.

Assuming steady-state, monochromatic waves, the physical electric field $\mathbf{E}'(\mathbf{r}, t)$ is represented by the notation

$$\mathbf{E}'(\mathbf{r}, t) = \Re e\left[\mathbf{E}(\mathbf{r})\,e^{-i\omega t}\right]$$

where ω is the angular radian frequency. Assuming a time dependence $e^{-i\omega t}$ throughout, the electric field is then described by the complex phasor $\mathbf{E} = \mathbf{E}(\mathbf{r})$. The time derivatives $\partial/\partial t$ can simply be replaced by $-i\omega$ and, implementing equations (4.1) and (4.2), we can write Maxwell's equations in the form

$$\nabla \times \mathbf{E} = i\omega\mu\,\mathbf{H} \tag{4.3b}$$

$$\nabla \times \mathbf{H} = -i\omega\epsilon\,\mathbf{E} + \mathbf{J} \tag{4.3c}$$

$$\nabla \cdot \mathbf{E} = 0 \tag{4.3d}$$

$$\nabla \cdot \mathbf{H} = 0 \tag{4.3e}$$

for a source-free region ($\rho = 0$) of the medium. Eliminating **H** between equations (4.3b) and (4.3c), using the vector identity $\nabla \times \nabla \times \mathbf{E} = \nabla\nabla \cdot \mathbf{E} - \nabla^2\mathbf{E}$ and equation (4.3d), we obtain the equation

$$\nabla^2\mathbf{E} + i\omega\mu(\sigma - i\omega\epsilon)\mathbf{E} = 0 \tag{4.4}$$

or

$$\nabla^2\mathbf{E} + k^2\mathbf{E} = 0$$

which is commonly referred to as the *Helmholtz equation*, where $k^2 = \omega^2\epsilon\mu + i\omega\mu\sigma$. In vacuum, the quantity k is equal to the free-space wavenumber $k_0 = \omega\sqrt{\epsilon_0\mu_0}$.

In a dielectric medium ($\sigma = 0$) with negligible losses ($\Im m\,[\varepsilon] \approx 0$) the wavenumber $k = \omega\sqrt{\varepsilon\mu_0}$ [†] and the velocity of propagation $v = c/n$, where c is the speed of light in vacuum and $n = \sqrt{\varepsilon/\varepsilon_0}$ is the refractive index of the medium. In a medium with finite conductivity σ, the term $-i\omega\varepsilon\,\mathbf{E}$ in equation (4.4) is the displacement current density while $\sigma\mathbf{E}$ is the conduction current density. For all metals the ratio $\omega\varepsilon/\sigma \approx 10^{-18}\omega$ and consequently for all frequencies up to, and including, the visible spectrum the displacement current is negligible in comparison to the conduction current. Equation (4.4) can then be written as

$$\nabla^2\mathbf{E} + i\omega\mu\sigma\mathbf{E} = 0$$

which describes the electric field in a metal in terms of a *diffusion equation*. Eliminating the electric field $\mathbf{E}$ from equation (4.3c), in a manner similar to that described above, the magnetic field $\mathbf{H}$ can also be shown to satisfy equation (4.4). The electromagnetic fields can therefore be thought of as *diffusing* into the metal's surface, undergoing attenuation and phase retardation. The fields can be shown to decay exponentially with depth below the metal's surface, enabling the *skin-depth δ* to be defined as the depth at which the fields are attenuated by a factor $1/e$:

$$\delta = \left(\frac{2}{\omega\mu\sigma}\right)^{\frac{1}{2}} \tag{4.5}$$

4.2.1   Boundary conditions

The solutions to Maxwell's equations for the fields inside unbounded, homogeneous media are relatively simple to obtain. Of more practical importance are the solutions for the fields in the presence of conducting or dielectric material bodies. The boundary of a body determines the point at which there is a discontinuous change in the electrical parameters ε and μ. At the surface S of a body the time-varying, electromagnetic fields are subject to the following conditions:

$$\mathbf{n} \times \left(\mathbf{E}^+(\mathbf{r}_s) - \mathbf{E}^-(\mathbf{r}_s)\right) = 0 \tag{4.6a}$$

$$\mathbf{n} \times \left(\mathbf{H}^+(\mathbf{r}_s) - \mathbf{H}^-(\mathbf{r}_s)\right) = 0 \tag{4.6b}$$

[†] In anything other than a ferromagnetic material, μ is negligibly different from the permeability of free-space μ_0; e.g., for bismuth, which is the strongest diamagnetic material known, $\mu = 0.99983\,\mu_0$.

where $\mathbf{r_s}$ is a point on S and $\mathbf{n}$ is the outward, unit normal to the surface. The superscripts $+$ and $-$ denote evaluation at the surface when approached from above and below the interface, respectively. The *boundary conditions* (4.6a) and (4.6b) express the continuity of the tangential components of the $\mathbf{E}$ and $\mathbf{H}$ fields, and are sufficient requirements for energy flow to be conserved across the boundary separating media with different electrical properties. Continuity of the tangential components of $\mathbf{E}$ and $\mathbf{H}$ across a boundary also ensures continuity of the normal components of the fields $\mathbf{B}$ and $\mathbf{D}$ respectively [66, page 320]

$$\mathbf{n} \cdot \left(\mathbf{B}^+(\mathbf{r_s}) - \mathbf{B}^-(\mathbf{r_s})\right) = 0 \qquad (4.7a)$$

$$\mathbf{n} \cdot \left(\mathbf{D}^+(\mathbf{r_s}) - \mathbf{D}^-(\mathbf{r_s})\right) = 0 \qquad (4.7b)$$

The conditions (4.6a) and (4.7a) are valid at the boundary separating any two media. This is a direct consequence of equation (4.3b). However, examination of equation (4.3c) suggests that, in the presence of a current flowing at the boundary, a discontinuity will occur in the corresponding conditions for the $\mathbf{H}$ and $\mathbf{D}$ fields. However, the contribution from a *volume* current density will be zero since we are considering the fields which are infinitesimally close to both sides of the boundary, and so only a true *surface* current $\mathbf{J_s}$ will not vanish. The modified boundary conditions are [66, pages 239,89]

$$\mathbf{n} \times \left(\mathbf{H}^+(\mathbf{r_s}) - \mathbf{H}^-(\mathbf{r_s})\right) = \mathbf{J_s} \qquad (4.8a)$$

$$\mathbf{n} \cdot \left(\mathbf{D}^+(\mathbf{r_s}) - \mathbf{D}^-(\mathbf{r_s})\right) = \rho_s \qquad (4.8b)$$

where $\mathbf{J_s}$ is the surface current density $[A/m]$ and ρ_s is the surface charge density $[C/m^2]$. Thus the tangential component of $\mathbf{H}$ is discontinuous across a conduction current sheet, and also the normal component of $\mathbf{D}$ is discontinuous across a surface charge sheet. Furthermore, there is a continuity relationship between the surface charge and current densities:

$$\nabla \cdot \mathbf{J_s} = -\frac{\partial \rho_s}{\partial t}$$

Increasing the conductivity σ of a metal reduces the depth to which an electromagnetic field can penetrate the conductor's surface, as can be seen from equation (4.5) — this is the *skin effect*. The induced current flows in a narrower and narrower skin

layer until, at the limit of infinite conductivity (i.e. a *perfect conductor*), the current only occupies the conductor's surface, the electromagnetic field inside it being zero. From equation (4.8a), since the internal fields are zero, the surface current density

$$\mathbf{J}_s = \mathbf{n} \times \mathbf{H}^+ \tag{4.9}$$

and from equation (4.7a) the normal component of the magnetic field is zero. Thus, $\mathbf{H}^+$ is tangential to the surface, perpendicular to $\mathbf{J}_s$, and of magnitude J_s. Similarly, from equation (4.6a), the tangential component of the electric field is zero

$$\mathbf{n} \times \mathbf{E}^+ = 0$$

and so $\mathbf{D}^+$ must be normal to the surface and of magnitude ρ_s.

4.3 Electromagnetic scattering: rigorous theory

4.3.1 Transverse electric field (TE)

Consider an electric line source $\mathbf{J}_e = J_e \hat{\mathbf{z}}$ generating an electric field $\mathbf{E} = E\hat{\mathbf{z}}$ above a semi-infinite, dielectric medium as illustrated in Figure 4.1. Eliminating the mag-

$\mathbf{E} = (0, 0, E)$
$\mathbf{H} = (H_x, H_y, 0)$
$\mathbf{n} = (n_x, n_y, 0)$
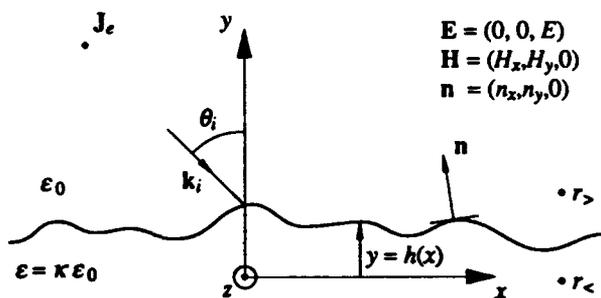
Figure 4.1: Electric line source above a semi-infinite dielectric medium. The corrugated profile $h = h(x)$ separates vacuum from dielectric.

netic field from equations (4.3b) and (4.3c) we obtain the inhomogeneous Helmholtz equation

$$\nabla^2 E + k_0^2 E = -i\omega\mu_0 J_e$$

for the scalar electric field above the surface $(y > h)$. The equivalent homogeneous equation for the field inside the source-free dielectric $(y < h)$ is

$$\nabla^2 E + k_1^2 E = 0$$

where $k_1^2 = \kappa k_0^2$, $\kappa = \varepsilon/\varepsilon_0$ being the *relative permittivity.*

The solutions for the TE fields above and below the dielectric interface must satisfy boundary conditions (4.6a) and (4.6b). From condition (4.6a) we have that

$$\mathbf{n} \times (\mathbf{E}^+ - \mathbf{E}^-) = (n_y\,\hat{\imath} - n_x\,\hat{\jmath})\,(E^+ - E^-) = 0$$

Hence the transverse electric field is continuous across the boundary, i.e.

$$E^+ = E^-$$

From equation (4.3b), condition (4.6b) can be written as

$$\mathbf{n} \times \left(\frac{1}{\mu^+} \nabla \times \mathbf{E}^+ - \frac{1}{\mu^-} \nabla \times \mathbf{E}^- \right) = 0$$

Using the vector identity $\mathbf{a} \times (\nabla \times \mathbf{b}) = \nabla(\mathbf{a} \cdot \mathbf{b}) - (\mathbf{a} \cdot \nabla)\mathbf{b} - (\mathbf{b} \cdot \nabla)\mathbf{a} - \mathbf{b} \times (\nabla \times \mathbf{a})$, and noting that $\mathbf{n} \cdot \mathbf{E} = 0$. $\mathbf{E} \cdot \nabla \equiv 0$ and $\nabla \times (\mathbf{n}/\mu)$ is parallel to $\mathbf{E}$, we can show that the normal derivative $\mathbf{n} \cdot \nabla$ of the transverse electric field satisfies the continuity equation

$$\frac{1}{\mu^+} \frac{\partial E^+}{\partial n} = \frac{1}{\mu^-} \frac{\partial E^-}{\partial n}$$

4.3.2   Transverse magnetic field (TM)

For this case the field is generated by a magnetic line source $\mathbf{J}_m = J_m\hat{\mathbf{z}}$ (analogous to the electric line source $\mathbf{J}_e$ for TE waves) producing a magnetic field $\mathbf{H} = H\hat{\mathbf{z}}$ above a dielectric medium; see Figure 4.2. Considering the symmetry between the electric and magnetic fields described in Maxwell's equations, we can construct the relations

$$\nabla \times \mathbf{H} \;=\; -i\omega\varepsilon\,\mathbf{E} \qquad\qquad (4.10a)$$

$$\nabla \times \mathbf{E} \;=\; i\omega\mu\,\mathbf{H} - \mathbf{J}_m \qquad\qquad (4.10b)$$

by analogy with equations (4.3b) and (4.3c) respectively. Eliminating the electric field we obtain the equations

$$\nabla^2 H + k_0^2 H = -i\omega\varepsilon_0\,J_m$$
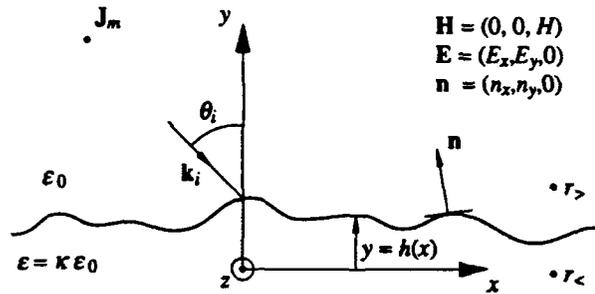
Figure 4.2: Magnetic line source above a semi-infinite, dielectric medium. The corrugated profile $h = h(x)$ separates vacuum from dielectric.

for the field above the surface $(y > h)$, and

$$\nabla^2 H + k_1^2 H = 0$$

below the surface $(y < h)$.

As for the case of TE waves, the solutions for the TM fields must satisfy boundary conditions (4.6a) and (4.6b). Condition (4.6b) expresses the continuity of the transverse magnetic field across the boundary:

$$\mathbf{n} \times (\mathbf{H}^+ - \mathbf{H}^-) = (n_y \mathbf{i} - n_x \mathbf{j})(H^+ - H^-) = 0$$

and hence

$$H^+ = H^-$$

Condition (4.6a) can be written in the form

$$\mathbf{n} \times \left(\frac{1}{\varepsilon^+} \nabla \times \mathbf{H}^+ - \frac{1}{\varepsilon^-} \nabla \times \mathbf{H}^- \right) = 0$$

Following similar arguments as for the TE case, the normal derivative of the transverse magnetic field can be shown to satisfy the continuity equation

$$\frac{1}{\varepsilon^+} \frac{\partial H^+}{\partial n} = \frac{1}{\varepsilon^-} \frac{\partial H^-}{\partial n}$$

4.3.3 The scattering equations

Considering the symmetry of the equations governing the TE and TM fields in sections 4.3.1 and 4.3.2, the fields above and below the dielectric interface for both

polarizations are found by solving the following scalar Helmholtz equations:

$$\nabla^2 \phi(\mathbf{r}_>) + k_0^2 \phi(\mathbf{r}_>) = -j(\mathbf{r}_>) \quad (y > h) \tag{4.11a}$$

$$\nabla^2 \phi(\mathbf{r}_<) + k^2 \phi(\mathbf{r}_<) = 0 \quad (y < h) \tag{4.11b}$$

where $j(\mathbf{r})$ describes the respective line source terms. The field solutions can be obtained by invoking Green's second theorem in and around the dielectric medium. This approach is discussed in Appendix A and results in the solutions being expressed in terms of *Helmholtz-Kirchhoff integral equations.*

The field scattered into vacuum by the rough dielectric surface is given by equation (A.9):

$$\phi_{re}(\mathbf{r}_>) = \oint_{C^+} \left[\phi(\mathbf{r}_s) \nabla G(\mathbf{r}_s, \mathbf{r}_>) - G(\mathbf{r}_s, \mathbf{r}_>) \nabla \phi(\mathbf{r}_s) \right] \cdot d\mathbf{s} \tag{4.12}$$

where $\mathbf{r}_>$ denotes a point in vacuum and $\mathbf{r}_s$ is a point on the surface. Since the problem has been reduced to considering only scattering in one dimension, the surface integral in equation (A.9) becomes a line integral in equation (4.12). Thus the line segment vector $d\mathbf{s} = \mathbf{n}ds$ is taken along the contour C^+ which is infinitesimally close to the vacuum side of the true contour C, defined by the dielectric interface $h = h(x)$ and a semi-circle of infinite radius enclosing the dielectric medium. The function $G(\mathbf{r}, \mathbf{r}')$ is the cylindrical-wave Green's function and has the form

$$G(\mathbf{r}, \mathbf{r}') = \frac{i}{4} H_0^{(1)}(k|\mathbf{r} - \mathbf{r}'|) \tag{4.13}$$

where $H_0^{(1)}(kr)$ is the zero-th order Hankel function of the first kind. Note that the wavenumber $k = k_0$ in vacuum, but $k = \sqrt{\kappa}k_0$ in the dielectric medium. The scattered field will satisfy a radiation condition at infinity and so the contribution from the line integral over the semi-circle of i.. nite radius vanishes, leaving only the integral along the interface. Therefore the surface scattered field becomes

$$\phi_{re}(\mathbf{r}_>) = \int_{-\infty}^{\infty} dx_s \left[\phi^+(\mathbf{r}_s) \frac{\partial G^+(\mathbf{r}_s, \mathbf{r}_>)}{\partial n} - G^+(\mathbf{r}_s, \mathbf{r}_>) \frac{\partial \phi^+(\mathbf{r}_s)}{\partial n} \right] \sqrt{1 + \left(\frac{dh}{dx_s} \right)^2}$$

where $\partial/\partial n = \mathbf{n} \cdot \nabla$ denotes the derivative along the surface normal. The normal derivative of the Green's function

$$\frac{\partial G(\mathbf{r}, \mathbf{r}')}{\partial n} = \frac{i}{4} k H_1^{(1)}(k|\mathbf{r} - \mathbf{r}'|) \, \mathbf{n} \cdot \hat{\mathbf{t}} \tag{4.14}$$

where $H_1^{(1)}(kr)$ is the first order Hankel function of the first kind and $\hat{t}$ is a unit vector in the direction $\mathbf{r'} - \mathbf{r}$. By making the following substitutions

$$\mathcal{A}^{\pm}(\mathbf{r}_s) = \phi^{\pm}(\mathbf{r}_s)\sqrt{1 + \left(\frac{dh}{dx_s}\right)^2}$$

$$\mathcal{B}^{\pm}(\mathbf{r}_s) = \frac{\partial\phi^{\pm}(\mathbf{r}_s)}{\partial n}\sqrt{1 + \left(\frac{dh}{dx_s}\right)^2}$$

where the symbols $+$ and $-$ indicate evaluation on the vacuum and dielectric sides of the interface respectively, the *reflected* field scattered into the vacuum may be written as

$$\phi_{re}(\mathbf{r}_>) = \int_{-\infty}^{\infty} dx_s \left[\mathcal{A}^+(\mathbf{r}_s)\frac{\partial G^+(\mathbf{r}_s,\mathbf{r}_>)}{\partial n} - G^+(\mathbf{r}_s,\mathbf{r}_>)\mathcal{B}^+(\mathbf{r}_s)\right] \qquad (4.15)$$

The corresponding expression for the field scattered by the surface into the dielectric half-space, or the *transmitted* field, is given by equation (A.11):

$$\phi_{tr}(\mathbf{r}_<) = -\int_{-\infty}^{\infty} dx_s \left[\mathcal{A}^-(\mathbf{r}_s)\frac{\partial G^-(\mathbf{r}_s,\mathbf{r}_<)}{\partial n} - G^-(\mathbf{r}_s,\mathbf{r}_<)\mathcal{B}^-(\mathbf{r}_s)\right] \qquad (4.16)$$

In order to evaluate these scattered fields above and below the surface, the values of the field and its normal derivative at the interface must be combined with those of the Green's function. Since the Green's function is known, the problem is reduced to finding the values ϕ and $\partial\phi/\partial n$ at the interface of a known surface profile $h = h(x)$.

The line source is assumed to be in the far-field of the rough, dielectric surface and so the incident field can be expressed as a plane wave incident at an angle θ_i, such that

$$\phi_{in}(\mathbf{r}) = \phi_0 \exp(i\mathbf{k}_i \cdot \mathbf{r}) \qquad (4.17)$$

where $\mathbf{k}_i = k_0(\sin\theta_i\,\hat{\imath} - \cos\theta_i\,\hat{\jmath})$, is the propagation direction of the incident field. From equation (A.10) we have the mathematical form of the *extinction theorem* [65]:

$$0 = \phi_{in}(\mathbf{r}_<) + \int_{-\infty}^{\infty} dx_s \left[\mathcal{A}^+(\mathbf{r}_s)\frac{\partial G^+(\mathbf{r}_s,\mathbf{r}_<)}{\partial n} - G^+(\mathbf{r}_s,\mathbf{r}_<)\mathcal{B}^+(\mathbf{r}_s)\right] \qquad (4.18)$$

This equation expresses the extinction of the incident field inside the dielectric by the fields induced at the surface which, in the vacuum, give rise to the reflected field. This relation can be interpreted as an expression of the boundary condition that must be satisfied by the fields on the vacuum side of the dielectric interface. The analogous condition for the surface fields on the dielectric side is given by equation (A.12):

$$0 = \int_{-\infty}^{\infty} dx_s \left[\mathcal{A}^-(\mathbf{r}_s)\frac{\partial G^-(\mathbf{r}_s,\mathbf{r}_>)}{\partial n} - G^-(\mathbf{r}_s,\mathbf{r}_>)\mathcal{B}^-(\mathbf{r}_s)\right] \qquad (4.19)$$

Using the tangential continuity conditions described in § 4.2.1 it is possible to obtain solutions to ϕ and $\partial\phi/\partial n$ above and below the interface from the coupled integral equations (4.18) and (4.19). A method of numerically calculating these solutions for a known profile $h = h(x)$ is outlined in the next section.

4.4 Numerical implementation

The extinction theorem has been used as a boundary condition in an attempt to construct multiple scattering models based on perturbative series approximations [51, 59, 72, 74]. Due to the nature of these methods, such calculations are restricted to shallow, rough surfaces. However, it is possible to calculate the field and its normal derivative at the surface from the extinction theorem without having to resort to perturbation methods, thereby placing no restrictions on the surface roughness. Such a solution is very important for modelling multiple scattering interactions on randomly rough surfaces and predicting new observations. The only drawback with this method is the lack of information revealed concerning the actual mechanisms involved; the contributions from single and multiple scattering cannot be separated and the shadowing mechanisms may not be determined. Up until this point no assumptions have been made concerning either the behaviour of the field at the surface, or the degree of surface roughness. However, the mathematical rigour of the solution has to be sacrificed for workability of the computer formulation.

To implement a numerical simulation, a randomly undulating function has to be generated to represent the surface profile of the diffuser. The diffusers described in Chapter 3 are fabricated in such a way that the surface height is approximately a Gaussian random process with a Gaussian correlation function. There are a number of methods available for numerically generating random profiles of known statistics; e.g. see reference [34]. The statistical parameters which govern the above Gaussian random surface are the rms height σ_h and the $1/e$ correlation length τ.

4.4.1 Random surface generation

Briefly, the method used for generating the random profiles was as follows. The surface profile $h(x)$ can be expressed as the convolution of a zero-mean, Gaussian, uncorrelated noise function $g(x)$ with a correlation function $c(x)$. If the functions

$H(u)$, $G(u)$, and $C(u)$ represent the Fourier transforms of $h(x)$, $g(x)$, and $c(x)$ respectively, in Fourier space we can then write

$$H(u) = G(u)\,C(u)$$

From Parseval's theorem, the average value $\langle |G(u)|^2 \rangle$ can be shown to be equal to $\langle |g(u)|^2 \rangle = \sigma_h^2$ for an uncorrelated process. Expressing the autocorrelation function [equation (3.4)] of the surface profile in Fourier space we find, by comparison with equation (3.11), that

$$|H(u)|^2 = S_H(u) = \sqrt{\pi}\,\sigma_h^2 \tau \exp\left(-[\pi\tau u]^2\right)$$

where $S_H(u)$ is the power spectrum of the surface profile [equation (3.12)]. Hence we can show that

$$C(u) = \sqrt{\tau\sqrt{\pi}}\exp\left(-\frac{[\pi\tau u]^2}{2}\right)$$

The surface profile is then simply obtained by taking the inverse Fourier transform of the product $G(u)C(u)$. This method is quick and straightforward to use. A complex inverse-transform algorithm can be used to generate two independent profiles at the same time, if two uncorrelated noise functions $G_r(u)$ and $G_i(u)$ are generated initially.

4.4.2 Surface field calculation

Describing the random profile as a set of discrete points introduces the first approximation to this theoretical treatment of the problem. The effect of this approximation can be reduced by increasing the density of points used to describe the surface. Since the surface fields rapidly fall to zero outside the illuminated region, we will only consider a finite surface length L which includes this region. Typically, the sampling interval is $\sim \lambda/10$ and the length L of the surface is long enough to include ~ 10 asperities [73, page 370]. Figure 4.3 illustrates a short length L of the random surface profile $h = h(x)$ described by $N + 1$ points such that $L = N\Delta$, where Δ is the horizontal point separation. Having made this approximation, we can express the Helmholtz-Kirchhoff integrals in a form which is suitable for numerical evaluation. The continuous integral over the surface can be replaced by a summation of discrete integrals over each line segment, i.e.

$$\int_{-\infty}^{\infty} dx_s \, [\cdots] \approx \int_{-\frac{L}{2}}^{\frac{L}{2}} dx_s \, [\cdots] = \sum_{j=0}^{N-1} \int_{j\Delta}^{(j+1)\Delta} dx_s \, [\cdots]$$
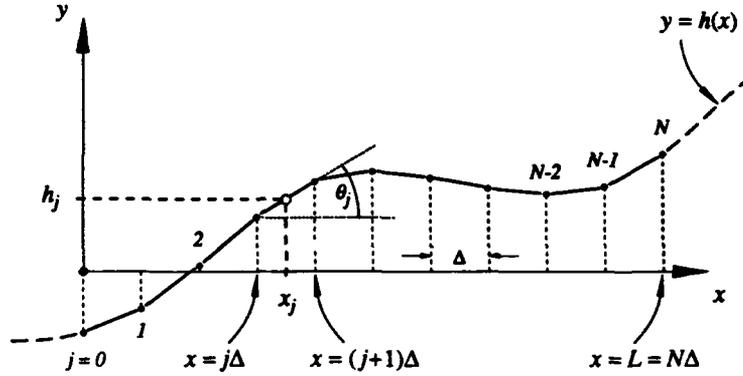
Figure 4.3: The random profile $h = h(x)$ is described by a set of discrete points at $\mathbf{r}_{sj} = (x_j, h_j)$ with a fixed horizontal separation Δ. The coordinates of the j-th line segment are specified at its mid-point. θ_j is the angle that the j-th line segment subtends to the horizontal, $\tan\theta_j = (dh/dx)_j$.

From the expression of the extinction theorem in equation (4.18) we have the condition inside the dielectric medium that

$$\phi_{in}(\mathbf{r}_<) = -\sum_{j=0}^{N-1} \int_{j\Delta}^{(j+1)\Delta} dx_s \left[\mathcal{A}_j^+ \frac{\partial G^+(\mathbf{r}_{sj}, \mathbf{r}_<)}{\partial n} - G^+(\mathbf{r}_{sj}, \mathbf{r}_<)\mathcal{B}_j^+ \right]$$

where $\mathbf{r}_{sj} = (x_j, h_j)$ and

$$\mathcal{A}_j^\pm = \phi^\pm(\mathbf{r}_{sj})\sec\theta_j \qquad \mathcal{B}_j^\pm = \frac{\partial\phi^\pm(\mathbf{r}_{sj})}{\partial n}\sec\theta_j \qquad (4.20)$$

At the limit as the observation point approaches the dielectric side of the interface $\mathbf{r}_< \rightarrow \mathbf{r}_{si}$, the condition at the boundary becomes

$$\phi_{in_i} = -\sum_{j=0}^{N-1} \int_{j\Delta}^{(j+1)\Delta} dx_s \left[\mathcal{A}_j^+ \frac{\partial G_{ij}^+}{\partial n} - G_{ij}^+ \mathcal{B}_j^+ \right]$$

where $\phi_{in_i} = \phi_{in}(\mathbf{r}_{si})$ and $G_{ij}^\pm = G^\pm(\mathbf{r}_{sj}, \mathbf{r}_{si})$. If the interval Δ is sufficiently small that $\mathcal{A}_j^+$ and $\mathcal{B}_j^+$ can be considered constant over each line segment, we can write

$$\phi_{in_i} \simeq -\sum_{j=0}^{N-1} \left[\mathcal{A}_j^+ \int_{j\Delta}^{(j+1)\Delta} dx_s \frac{\partial G_{ij}^+}{\partial n} - \mathcal{B}_j^+ \int_{j\Delta}^{(j+1)\Delta} dx_s G_{ij}^+ \right]$$

Introducing the quantities

$$U_{ij}^\pm = \int_{j\Delta}^{(j+1)\Delta} dx_s \frac{\partial G_{ij}^\pm}{\partial n} \qquad V_{ij}^\pm = \int_{j\Delta}^{(j+1)\Delta} dx_s G_{ij}^\pm \qquad (4.21)$$

we can construct the following matrix equation

$$-\mathbf{\Phi}_{in} = \widetilde{U}^{+}\mathcal{A}^{+} - \widetilde{V}^{+}\mathcal{B}^{+} \tag{4.22}$$

From equation (4.19), we have a second condition that must be satisfied by the fields at the boundary of the medium

$$0 = \sum_{j=0}^{N-1} \int_{j\Delta}^{(j+1)\Delta} dx_s \left[\mathcal{A}_{j}^{-}\frac{\partial G_{ij}^{-}}{\partial n} - G_{ij}^{-}\mathcal{B}_{j}^{-} \right]$$

Assuming, again, that $\mathcal{A}_{j}^{-}$ and $\mathcal{B}_{j}^{-}$ remain constant over the interval Δ, we can write

$$0 = \sum_{j=0}^{N-1} \left[\mathcal{A}_{j}^{-}U_{ij}^{-} - \mathcal{B}_{j}^{-}V_{ij}^{-} \right]$$

and can therefore construct a second matrix equation

$$0 = \widetilde{U}^{-}\mathcal{A}^{-} - \widetilde{V}^{-}\mathcal{B}^{-} \tag{4.23}$$

The matrices $\mathbf{\Phi}_{in}$, $\mathcal{A}^{\pm}$, and $\mathcal{B}^{\pm}$ are N element column vectors, each element being evaluated at a corresponding *point on the surface*. The matrices $\widetilde{U}^{\pm}$ and $\widetilde{V}^{\pm}$are $N \times N$ arrays which account for point-wise interactions across the surface (e.g. multiple scattering and shadowing).

From § 4.3.1, the transverse electric field was found to satisfy the boundary conditions

$$E^{+} = E^{-} \qquad \frac{\partial E^{+}}{\partial n} = \frac{\partial E^{-}}{\partial n}$$

(assuming $\mu^{+} = \mu^{-}$) across the dielectric interface. Hence for the case of TE or s polarized incident radiation

$$\mathcal{A}_{TE}^{+} = \mathcal{A}_{TE}^{-} \Rightarrow \mathcal{A}_{TE} \qquad \mathcal{B}_{TE}^{+} = \mathcal{B}_{TE}^{-} \Rightarrow \mathcal{B}_{TE}$$

Therefore, from the simultaneous matrix equations (4.22) and (4.23) we can obtain the solutions for the surface field and its normal derivative above and below each line segment describing the dielectric interface for TE waves:

$$\begin{aligned}
\mathcal{A}_{TE} &= \left[\widetilde{V}^{+} \cdot \left[\widetilde{V}^{-} \right]^{-1} \cdot \widetilde{U}^{-} - \widetilde{U}^{+} \right]^{-1} \mathbf{\Phi}_{in} \\
\mathcal{B}_{TE} &= \left[\widetilde{V}^{-} \right]^{-1} \cdot \widetilde{U}^{-} \mathcal{A}_{TE}
\end{aligned} \tag{4.24}$$

From § 4.3.2 the transverse magnetic field was shown to satisfy the following conditions at the dielectric boundary:

$$H^+ = H^- \qquad \frac{1}{\varepsilon^+}\frac{\partial H^+}{\partial n} = \frac{1}{\varepsilon^-}\frac{\partial H^-}{\partial n}$$

Therefore, the field quantities $\mathcal{A}$ and $\mathcal{B}$ for TM or p polarized incident radiation must satisfy the conditions

$$\mathcal{A}_{TM}^+ = \mathcal{A}_{TM}^- \Rightarrow \mathcal{A}_{TM} \qquad \mathcal{B}_{TM}^+ = \frac{1}{\kappa}\mathcal{B}_{TM}^-$$

across the dielectric interface. Therefore, from matrix equations (4.22) and (4.23) we can construct the solutions for the surface field and its normal derivative on both sides of the interface for TM waves:

$$
\begin{aligned}
\mathcal{A}_{TE} &= \kappa \left[\widetilde{V}^+ \cdot \left[\widetilde{V}^- \right]^{-1} \cdot \widetilde{U}^- - \kappa \widetilde{U}^+ \right]^{-1} \Phi_{in} \\
\mathcal{B}_{TM}^+ &= \frac{1}{\kappa}\left[\widetilde{V}^- \right]^{-1} \cdot \widetilde{U}^- \mathcal{A}_{TM} \\
\mathcal{B}_{TM}^- &= \kappa \mathcal{B}_{TM}^+
\end{aligned}
\tag{4.25}
$$

4.4.3   Scattered field calculation

Perfect dielectric diffuser

The field scattered in reflection by the rough dielectric surface, described by equation (4.15), can be written as

$$\phi_{re}(\mathbf{r}_>) = \sum_{j=0}^{N-1} \int_{j\Delta}^{(j+1)\Delta} dx_s \left[\mathcal{A}_j^+ \frac{\partial G^+(\mathbf{r}_{sj}, \mathbf{r}_>)}{\partial n} - G^+(\mathbf{r}_{sj}, \mathbf{r}_>)\mathcal{B}_j^+ \right] \tag{4.26}$$

The case we are interested in calculating is that of the field in the far-zone of the diffuser, i.e., $\lim_{r_> \to \infty} \phi_{sc}(\mathbf{r}_>)$. The Green's functions are given by Hankel functions of the first kind [equations (4.13) and (4.14)]. The asymptotic values of the Hankel functions are [1]

$$\lim_{r \to \infty} H_0^{(1)}(kr) \approx \sqrt{\frac{2}{\pi kr}} e^{i(kr - \frac{\pi}{4})}$$

$$\lim_{r \to \infty} H_1^{(1)}(kr) \approx \sqrt{\frac{2}{\pi kr}} e^{i(kr - \frac{3\pi}{4})}$$

The far-zone argument of the Hankel functions in equation (4.26) is $k_0 r_j = k_0 |\mathbf{r}_> - \mathbf{r}_{sj}|$ and can be evaluated from Figure 4.4. At the asymptotic limit
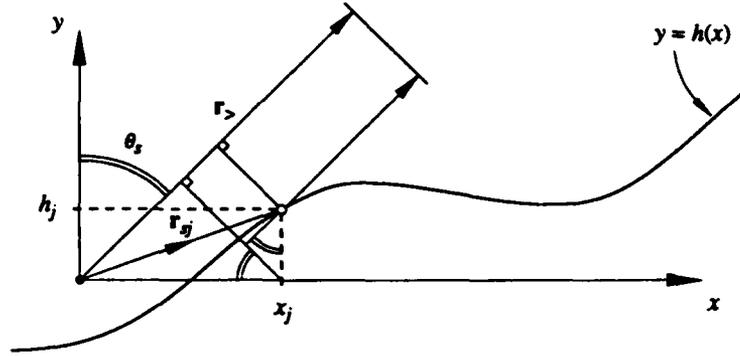
Figure 4.4: The planar field distribution in the far-zone is a function only of the scatter angle θ_s.

$$\lim_{r_> \to \infty} r_j = r_> - h_j \cos \theta_s - x_j \sin \theta_s$$

$$= r_> - \mathbf{r}_{sj} \cdot \hat{\mathbf{r}}_>$$

and the unit vector in the direction of the scattered wave

$$\lim_{r_> \to \infty} \hat{\mathbf{t}} = \hat{\mathbf{r}}_>$$

For a sufficiently small interval Δ, the field quantities $\mathcal{A}$ and $\mathcal{B}$ are assumed to be constant over each line segment, and so

$$\lim_{r \to \infty} \phi_{re}(\mathbf{r}) = \sqrt{\frac{2}{\pi k_0 r}} e^{i(k_0 r - \frac{\pi}{4})} \frac{\Delta}{4i} \sum_{j=0}^{N-1} \left[i \mathcal{A}_j^+ k_0 \mathbf{n} \cdot \hat{\mathbf{r}} + \mathcal{B}_j^+ \right] \exp\left(-ik_0 \mathbf{r}_{sj} \cdot \hat{\mathbf{r}}\right) \quad (4.27)$$

Following a similar set of arguments, from equation (4.16) the transmitted field in the far-zone is found to be

$$\lim_{r \to \infty} \phi_{tr}(\mathbf{r}) = \sqrt{\frac{2}{\pi k_1 r}} e^{i(k_1 r - \frac{\pi}{4})} \frac{\Delta}{4i} \sum_{j=0}^{N-1} \left[i \mathcal{A}_j^- k_1 \mathbf{n} \cdot \hat{\mathbf{r}} + \mathcal{B}_j^- \right] \exp\left(-ik_1 \mathbf{r}_{sj} \cdot \hat{\mathbf{r}}\right) \quad (4.28)$$

The remarkably similar field expressions in equations (4.27) and (4.28) represent the far-zone fields in reflection and transmission, respectively, scattered by the randomly rough surface of a semi-infinite, homogeneous, dielectric medium.

Perfectly conducting diffusers

If the scattering medium is perfectly conducting, these expressions are somewhat simplified. From § 4.2.1, the electromagnetic field inside the medium will be zero

indicating that $\mathcal{A}^- = \mathcal{B}^- = 0$, and hence the transmitted field $\phi_{tr}(\mathbf{r}) = 0$. For the case of TE waves, the tangential electric field is continuous across the boundary, and so $\mathcal{A}^+_{TE} = \mathcal{A}^-_{TE} = 0$. Therefore the TE reflected field expression is reduced to finding only the normal derivative of the surface field, given by

$$\mathcal{B}^+_{TE} = \left[\widetilde{V}^+\right]^{-1} \Phi_{in}$$

requiring the inversion of only one matrix. The corresponding boundary conditions for TM waves can be obtained from equation (4.9). Although the internal magnetic field is zero, the external, tangential field has the non-zero magnitude J_s. In a region on the perfect conductor's surface illuminated with a uniform TM wave, the induced surface current $\mathbf{J}_s$ will also be uniform, and so

$$\nabla \times \mathbf{J}_s = \nabla \times \left(\mathbf{n} \times \mathbf{H}^+\right) = 0$$

Therefore, since $\nabla \cdot \mathbf{H}^+ = 0$, we have the condition

$$\frac{\partial H^+}{\partial n} = 0 \quad \longrightarrow \quad \mathcal{B}^+_{TM} = 0$$

at the surface. Hence the TM reflected field expression requires only the surface field given by the matrix equation

$$\mathcal{A}^+_{TM} = -\left[\widetilde{U}^+\right]^{-1} \Phi_{in}$$

The perfect conductor equations are very much simpler, and subsequently faster, to calculate than the corresponding real metal equations. This being so we will assume that the gold coating on the diffusers is at least a very good conductor if not perfect.

The matrix elements

Describing the surface profile by a set of short linear segments with mean coordinates $\mathbf{r}_{sj} = (x_j, h_j)$, the complex, plane-wave amplitude incident on each segment is given by [equation 4.17]

$$\phi_{in_j} = \phi_0 \exp\left(ik_o \left[x_j \sin\theta_i - h_j \cos\theta_i\right]\right)$$

and hence the incident field matrix

$$\Phi_{in} = \left\{\phi_{in_j}\right\}$$

The elements of the matrices $\widetilde{U}^\pm$ and $\widetilde{V}^\pm$[equation (4.21)] can be evaluated by numerical integration of equations (4.13) and (4.14). However, to first order in Δ, the off-diagonal elements were calculated from the approximate values

$$U_{ij}^\pm \simeq i\frac{\Delta}{4}k^\pm H_1^{(1)}\left(k^\pm \left|\mathbf{r}_{sj} - \mathbf{r}_{si}\right|\right)\mathbf{n}_j \cdot \hat{\mathbf{t}}$$

$$V_{ij}^\pm \simeq i\frac{\Delta}{4}H_0^{(1)}\left(k^\pm \left|\mathbf{r}_{sj} - \mathbf{r}_{si}\right|\right)$$

(4.29)

where $k^+ = k_0$ and $k^- = nk_0$. Calculation of the diagonal elements $U_{jj}^\pm$ and $V_{jj}^\pm$ involves integration of the Hankel functions $H_1^{(1)}(kr)$ and $H_0^{(1)}(kr)$ over each line segment in the limit ar r tends to zero. Both Hankel functions have singularities for zero arguments, but that of $H_0^{(1)}(kr)$ is integrable. Integration of $H_1^{(1)}(kr)$ is achieved by incorporating the geometric factor $\sec\theta_j$ which, for convenience of notation, is present in the surface field matrix $\mathcal{A}$. This procedure was developed by Andreasen [3] involving the principal value of the integral and leads to the expressions

$$U_{jj}^+ = \frac{\cos\theta_j}{2k_0} \qquad U_{jj}^- = -\frac{\cos\theta_j}{2nk_0}$$

with the elements $\mathcal{A}_j^\pm$ as defined in equation (4.20). For the case of the medium having a complex refractive index (an absorbing dielectric or finite conductor) calculation of $\widetilde{U}^-$ and $\widetilde{V}^-$ involves Hankel functions of complex arguments. Although not considered in this present work, numerical studies of the backscattering properties of randomly rough metals have been carried out by other investigators [49, 56, 68].

4.4.4   The differential scattering cross-section

To compare the results of a numerical calculation with those of a corresponding experimental measurement, the scattered amplitudes (4.27) and (4.28) have to be related to some measurable light flux density. From equation (2.2) we have the definition of the mean differential scattering cross-section (DSCS) which, for one-dimensional diffusers, is given by

$$\Xi(\theta_i; \theta_s) = \frac{\langle J(\theta_i; \theta_s)\rangle}{P_{in}} \qquad [sr^{-1}]$$

where $\langle J\rangle$ is the mean radiant intensity $[W\, sr^{-1}]$ averaged over an ensemble of rough surfaces and P_{in} is the power incident on each surface. For a given angle of incidence

we can write

$$\Xi(\hat{\mathbf{r}}) = \frac{\langle J(\hat{\mathbf{r}})\rangle}{P_{in}} \qquad (4.30)$$

where $\hat{\mathbf{r}}$ is a unit vector in the direction of the scattered light field. The time averaged Poynting vector represents the flow of power (in magnitude and direction) per unit area (perpendicular to the direction) and is given by [66, page 313]

$$\langle \mathbf{S}\rangle = \frac{1}{2}\Re e\left[\mathbf{E} \times \mathbf{H}^*\right] \qquad (4.31)$$

where the asterisk [*] denotes the complex-conjugate value. In the present case of an infinite cylindrical geometry we need only consider the Poynting vector to have the dimension $[W\,m^{-1}]$. Hence the time-averaged power flowing into the angular segment $\theta_s \to \theta_s + d\theta_s$ can be expressed in terms of the mean radiant intensity

$$\langle \mathbf{S}\rangle \cdot \hat{\mathbf{r}}\,r d\theta_s = \langle J(\hat{\mathbf{r}})\rangle \, d\theta_s \qquad [W] \qquad (4.32)$$

TE (s) polarization

Making the substitution $\mathbf{H}^* = (i/\omega\mu)\nabla \times \mathbf{E}^*$ in equation (4.31), allows us to write the time-averaged Poynting vector in the form

$$\langle \mathbf{S}\rangle^{TE} = \frac{1}{2\omega\mu}\Im m\left[E^*\nabla E\right] \qquad (4.33)$$

The incident field is assumed to be a plane wave of the form

$$\mathbf{E}_{in}(\mathbf{r}) = E_0\exp\left(i\mathbf{k}_i \cdot \mathbf{r}\right)\hat{k}$$

where $\mathbf{k}_i = k_0\hat{\mathbf{r}}_i$ is the incident wavevector in the direction $\hat{\mathbf{r}}_i = \sin\theta_i\,\hat{\imath} - \cos\theta_i\,\hat{\jmath}$. Substituting $\mathbf{E}_{in}$ into equation (4.33), the power incident on a diffuser of length L is

$$\left|\langle \mathbf{S}\rangle_{in}^{TE} \cdot \mathbf{L}\right| = \frac{k_0}{2\omega\mu_0}\left|E_0\right|^2 L\left|\hat{\mathbf{r}}_i \cdot \hat{\jmath}\right|$$

where $\mathbf{L} = L\hat{\jmath}$ is the mean surface normal, and hence

$$P_{in}^{TE} = \frac{k_0 L\cos\theta_i}{2\omega\mu_0}\left|E_0\right|^2 \qquad (4.34)$$

The scattered far-zone field above the diffuser [equation (4.27)] is of the form

$$\lim_{r\to\infty}\mathbf{E}_{re}(\mathbf{r}) = \mathcal{E}_{re}(\hat{\mathbf{r}})\frac{e^{ik_0 r}}{\sqrt{r}}\hat{k}$$

where $\mathcal{E}_{re}(\hat{\mathbf{r}})$ is a function of direction only. From equation (4.33) we can show that

$$\lim_{r \to \infty} \langle \mathbf{S} \rangle_{re}^{TE} = \frac{k_0}{2\omega\mu_0 r} \left\langle |\mathcal{E}_{re}(\hat{\mathbf{r}})|^2 \right\rangle \hat{\mathbf{r}}$$

and hence, from equations (4.30), (4.32), and (4.34) the scattering cross-section can be expressed as

$$\Xi_{ss}^{re}(\hat{\mathbf{r}}) = \frac{\left\langle |\mathcal{E}_{re}(\hat{\mathbf{r}})|^2 \right\rangle}{|E_0|^2 L \cos\theta_i}$$

where

$$\mathcal{E}_{re}(\hat{\mathbf{r}}) = -\sqrt{\frac{2}{\pi k_0}} e^{i\frac{\pi}{4}} \Delta \sum_{j=0}^{N-1} \left[i\mathcal{A}_{TE_j}^+ k_0 \mathbf{n}_j \cdot \hat{\mathbf{r}} + \mathcal{B}_{TE_j}^+ \right] \exp\left(-ik_0 \mathbf{r}_{sj} \cdot \hat{\mathbf{r}} \right)$$

The scattered far-zone field in transmission [equation (4.28)] is of the form

$$\lim_{r \to \infty} \mathbf{E}_{tr}(\mathbf{r}) = \mathcal{E}_{tr}(\hat{\mathbf{r}}) \frac{e^{ink_0 r}}{\sqrt{r}} \hat{k}$$

where the index of refraction $n = n' + in''$ is generally a complex value with $n' > 1$ and $n'' \geq 0$. For anything other than a pure dielectric medium $n'' > 0$ and the transmitted field will undergo absorption being attenuated by a factor $\exp(-n''k_0 r)$, and so the far-zone field will be zero. Following the same steps as for the reflected field, the far-zone transmitted scattering cross-section can be shown to equal

$$\Xi_{ss}^{tr}(\hat{\mathbf{r}}) = \frac{n \left\langle |\mathcal{E}_{tr}(\hat{\mathbf{r}})|^2 \right\rangle}{|E_0|^2 L \cos(\theta_i)}$$

where $n = n'$, and

$$\mathcal{E}_{tr}(\hat{\mathbf{r}}) = \sqrt{\frac{2}{\pi n k_0}} e^{i\frac{\pi}{4}} \Delta \sum_{j=0}^{N-1} \left[i\mathcal{A}_{TE_j}^- n k_0 \mathbf{n}_j \cdot \hat{\mathbf{r}} + \mathcal{B}_{TE_j}^- \right] \exp\left(-ink_0 \mathbf{r}_{sj} \cdot \hat{\mathbf{r}} \right)$$

TM (p) polarization

Making the substitution $\mathbf{E} = (i/\omega\varepsilon)\nabla \times \mathbf{H}$ in equation (4.31), we can write the time-averaged Poynting vector as

$$\langle \mathbf{S} \rangle^{TM} = \frac{1}{2\omega\varepsilon_0} \Im m \left[\frac{1}{\kappa} H^* \nabla H \right] \tag{4.35}$$

where the relative permittivity $\kappa = n^2$. The incident plane-wave for this case takes the form

$$\mathbf{H}_{in}(\mathbf{r}) = H_0 \exp\left(i\mathbf{k}_i \cdot \mathbf{r} \right) \hat{k}$$

Substituting $\mathbf{H}_{in}$ into equation (4.35), the incident power on a diffuser of length L can be shown to equal

$$P_{in}^{TM} = \frac{k_0 L \cos \theta_i}{2\omega\varepsilon_0} |H_0|^2$$

Following arguments similar to those for TE polarization, we can express the TM polarized, reflected scattering cross-section as

$$\Xi_{pp}^{re}(\hat{\mathbf{r}}) = \frac{\left\langle |\mathcal{H}_{re}(\hat{\mathbf{r}})|^2 \right\rangle}{|H_0|^2 L \cos \theta_i} \tag{4.36}$$

where

$$\mathcal{H}_{re}(\hat{\mathbf{r}}) = \sqrt{\frac{2}{\pi k_0}} e^{i\frac{\pi}{4}} \Delta \sum_{j=0}^{N-1} \left[i \mathcal{A}_{TM_j}^+ k_0 \mathbf{n}_j \cdot \hat{\mathbf{r}} + \mathcal{B}_{TM_j}^+ \right] \exp\left(-ik_0 \mathbf{r}_{sj} \cdot \hat{\mathbf{r}}\right)$$

Assuming again a perfect, semi-infinite, dielectric material the transmitted far-zone scattering cross-section can be shown to equal

$$\Xi_{pp}^{tr}(\hat{\mathbf{r}}) = \frac{\left\langle |\mathcal{H}_{tr}(\hat{\mathbf{r}})|^2 \right\rangle}{n |H_0|^2 L \cos \theta_i}$$

where

$$\mathcal{H}_{tr}(\hat{\mathbf{r}}) = \sqrt{\frac{2}{\pi n k_0}} e^{i\frac{\pi}{4}} \Delta \sum_{j=0}^{N-1} \left[i \mathcal{A}_{TM_j}^- n k_0 \mathbf{n}_j \cdot \hat{\mathbf{r}} + \mathcal{B}_{TM_j}^- \right] \exp\left(-ink_0 \mathbf{r}_{sj} \cdot \hat{\mathbf{r}}\right)$$

4.4.5 Comments

As mentioned in § 4.4.2, the surface length L was chosen to include approximately ten asperities of the generated profile, typically $L \sim 20\lambda$ with a sampling interval $\Delta \sim \lambda/10$. For surface roughness in the resonance region ($1/e$ correlation length, $\tau \simeq \lambda$) this degree of sampling appears to define sufficiently the surface fields for the calculations to be considered reliable [61, 73]. Reducing the sampling interval had negligible effects on the calculated DSCS curves for individual surface realizations. However, maintaining a sufficient sampling interval for surfaces with very fine-scale structures ($\tau \lesssim \lambda/10$) would result in a surface length of only a few wavelengths being considered. The influence of edge effects (diffraction by finite aperture) would then be strong, affecting the angular distribution of the scattered light. The Monte-Carlo method of calculating the scattered fields would not be reliable in this region; being computationally intensive, it is not a realistic option to simply increase the

number of points. For a surface described by $\sim$ 200 points, calculation of the DSCS for each realization on a Sun 4/260 workstation with floating-point accelerator, using fully optimized code, takes $\sim$ 30 minutes: $\sim$ 200 such realizations are required to adequately reduce the 'speckle' noise, i.e. approximately four days computing time.

The major rate-determining step of the DSCS calculation is computing the inverse matrices in equations (4.24) and (4.25). From equation (4.29) it is clear that the inverse matrices are dependent only on the surface profile and not on the angle of incidence. Hence much computing time is saved if a number of incident angles are simultaneously considered for each realization. Another short-cut is to consider the surface profile $h(-x)$ to be a second surface realization with the same Gaussian statistics as $h(x)$ and for which the inverse matrices have already been calculated. Hence from N generated random surfaces, the effect of averaging over $2N$ realizations can be achieved, but in half the time. A subsidiary effect of this 'trick' is to produce a rather aesthetically pleasing, symmetrical scattering cross-section for an incident angle of zero degrees!

A condition which must be satisfied by the calculated scattering cross-section in reflection Ξ^{re} and transmission Ξ^{tr}, for perfect conductors and lossless dielectrics, is that of unitarity:

$$\int_{-\frac{\pi}{2}}^{\frac{\pi}{2}} \Xi^{re}(\theta_s)\, d\theta_s + \int_{-\frac{\pi}{2}}^{\frac{\pi}{2}} \Xi^{tr}(\theta_s')\, d\theta_s' \;=\; 1$$

$$\int_{-\frac{\pi}{2}}^{\frac{\pi}{2}} \left\langle J^{re}(\theta_s) \right\rangle d\theta_s + \int_{-\frac{\pi}{2}}^{\frac{\pi}{2}} \left\langle J^{tr}(\theta_s') \right\rangle d\theta_s' \;=\; P_{in}$$

Although this is a necessary condition it is not sufficient to guarantee accuracy, but does at least give an indication of whether the calculations are reasonable. For real metals or absorbing dielectrics, where there is energy dissipation, the unitarity condition must at least hold for the identical surfaces formed in lossless materials. Each of the calculated cross-sections presented in the following sections is accompanied by its unitarity value U. This value is the mean of the unitarities calculated for each surface realization. The largest standard deviation of these unitarity values was 2.5% out of all the cases considered, but was typically $< 1\%$.

One final point that should be mentioned before comparing numerical simulation with experimental measurement, is that the enhanced backscatter effect is present in the *incoherent* component of the scattered field. The differential scattering cross-

sections given in § 4.4.4 describe the total scattered fields $\phi(\theta_s)$; i.e., coherent plus incoherent. The coherent, or specularly reflected, component is associated with the mean of the scattered field $|\langle\phi(\theta_s)\rangle|^2$ and hence the incoherent component is given by its variance $\langle|\phi(\theta_s)|^2\rangle - |\langle\phi(\theta_s)\rangle|^2$. The two components can therefore be separated numerically; a more detailed discussion of the mean scattered power is given in § 5.4.

4.5 Experimental results

The data presented in this section were collected during experimental measurements of the light scattered by randomly rough diffusers. The procedure of collecting the data is described in Chapter 2 which includes a description of the apparatus used for these investigations. The diffusers were specially fabricated to have a highly one-dimensional (grating-like) structure, to comply as closely as possible to the conditions of the numerical simulations. A method was developed in Chapter 3 of faithfully reproducing a diffuser's profile into transparent, dielectric materials. This process has made it possible to say, with confidence, that any differences between two measured scattering cross-sections are due entirely to the differences between the materials' reflectivities.

The following sections contain a catalogue of comparisons between experimental measurement and theoretical prediction based on two types of diffuser:

1) scattered light measurements from a gold-coated diffuser compared with numerical calculations based on a perfect conductor with the same roughness parameters;

2) scattered light measurements from a transparent, dielectric diffuser compared with numerical calculations based on a perfect dielectric with the same roughness parameters.

To reduce the monotony of these comparisons, points raised by the results will be discussed throughout the following sections. The diffusers employed for these comparisons are the same as those used in previous investigations [69, 70] and have been characterized as being Gaussian diffusers (Gaussian height density and correlation functions) with the following statistical parameters [refer to table 3.1]:

Diffuser	rms height $\sigma_h/\mu m$	$1/e$ correlation length $\tau/\mu m$
#39	1.18 ± 0.02	2.97 ± 0.05
#46	1.22 ± 0.01	3.18 ± 0.07

Table 4.1: Statistical parameters of the one-dimensional diffusers used during the experimental measurements.

The diffusers are highly one-dimensional, as was verified by measuring the cross-polarized scattering cross-sections in the following experiments. Although the amount of depolarized light was visibly non-zero (at least for the visible wavelength), the light flux was always below the sensitivity of the detector that was necessary to measure the co-polarized cross-section. All cross-polarized measurements resulted in zero irradiance readings and, hence, are not presented in the Figures. Being only approximately one-dimensional, the diffusers scatter light over a small range of angles above and below the plane of scatter ($\sim 16°$ in total). As a consequence not all of the scattered light is detected; however, the undetected light does not carry any more information than that local to the scatter plane.

4.5.1 Metallic scattering

Wavelength $\lambda = 0.633 \ \mu m$

We first consider the case of light scattered from a gold-coated diffuser (#46) for a TM, or p, polarized incident beam whose wavelength $\lambda = 0.633 \ \mu m$. For this wavelength the surface parameters scale to the values $\tau/\lambda = 5.02$ and $\sigma_h/\lambda = 1.93$. Shown in Figure 4.5 are the experimental measurements and corresponding numerical calculations, based on the extinction theorem for a perfect conductor, of the scattering cross-sections for the incidence angles $\theta_i = 0°, -20°, -40°$. The calculated cross-sections have been averaged over $N = 2 \times 200$ realizations and the experimental data normalized assuming 100% reflectivity of the gold coating [equation (2.3)]. The vertical dashed line in each graph indicates the backscatter direction. For incidence angles $\theta_i = 0°$ and $-20°$ the experimental data exhibit a sharply defined peak of finite width centred about the backscatter direction, enhanced over the incoherently scattered light at neighbouring angles. The reader may be reassured that this is indeed enhanced backscattering by the absence of data points precisely at backscatter.
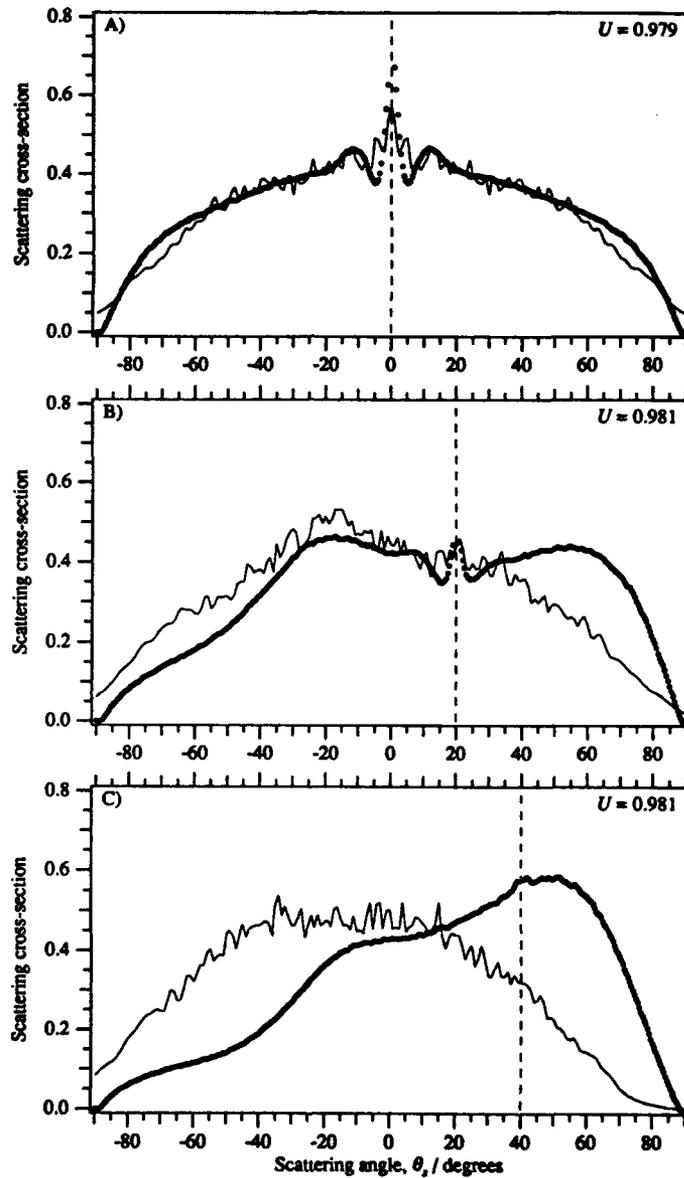
Figure 4.5: Comparisons between experimentally measured [o] and theoretically predicted [—] scattering cross-sections. Measurements: gold-coated diffuser #46; calculations: perfect conductor. $\tau/\lambda = 5.02$ and $\sigma_h/\lambda = 1.93$; $N = 2 \times 200$ realizations; surface length $L = 40\lambda$; sampling interval $\Delta \approx \lambda/10$; wavelength $\lambda = 0.633 \ \mu m$. $\Xi_{pp}(\theta_i, \theta_s)$: A) $\theta_i = 0°$, B) $\theta_i = -20°$, C) $\theta_i = -40°$.

This is due to the blind-spot of the experimental set-up where the detector effectively passes behind the source. The backscatter enhancement appears particularly strong for normal incidence ($\theta_i = 0°$) and gradually reduces in size as the incidence angle is increased. For normal incidence, subsidiary maxima are prominent about the backscatter direction and, although a well-defined peak is still observable for $-20°$ incidence, only the contiguous minima can be distinguished. For $-40°$ incidence the backscatter peak can be barely discerned above the neighbouring incoherently scattered light, but the majority of the light is scattered in the backscatter quadrant ($0° < \theta_s < 90°$).

The agreement of the perfect conductor calculations for normal incidence is quite good, even down to the presence of the subsidiary maxima. The theoretical and experimental data curves agree well for $|\theta_s| \lesssim 60°$, but for larger scatter angles the calculated results do not predict as large a cross-section as is observed experimentally; that is, except at grazing angles $\theta_s = \pm 90°$ where the experimental data fall to zero, as one would expect from oblique shadowing, whereas the calculated cross-section is finite. For $-20°$ incidence the measured and calculated results show some marked differences, particularly for scattering beyond the backscatter direction $\theta_s > 20°$. The calculated cross-section does rise slightly around backscatter, but the presence of an actual peak is obscured by the 'speckle' noise; increasing the number of surface realizations N would probably enable a peak to be resolved. The comparison for $-40°$ incidence is somewhat disappointing with the numerical results bearing little resemblance to the experimental data. The amount of light scattered into the backscatter quadrant ($0° < \theta_s < 90°$) is greatly underestimated, with too much light being foward-scattered.

The comparisons between experiment and theory for a TE, or s, polarized beam over the same incidence angles show similar characteristics as in the TM case; see Figure 4.6. The agreement for normal incidence is very good, particularly the definition of the backscatter peak and the subsidiary maxima. The agreement is not so good for $-20°$ incidence particularly beyond the backscatter direction ($\theta_s > 20°$). For $-40°$ incidence the agreement is poor with much less light being backward scattered than is observed experimentally.

It is interesting to note that, between the two polarizations, the calculated results show very little difference whereas, in the experimental results, the ss measurements
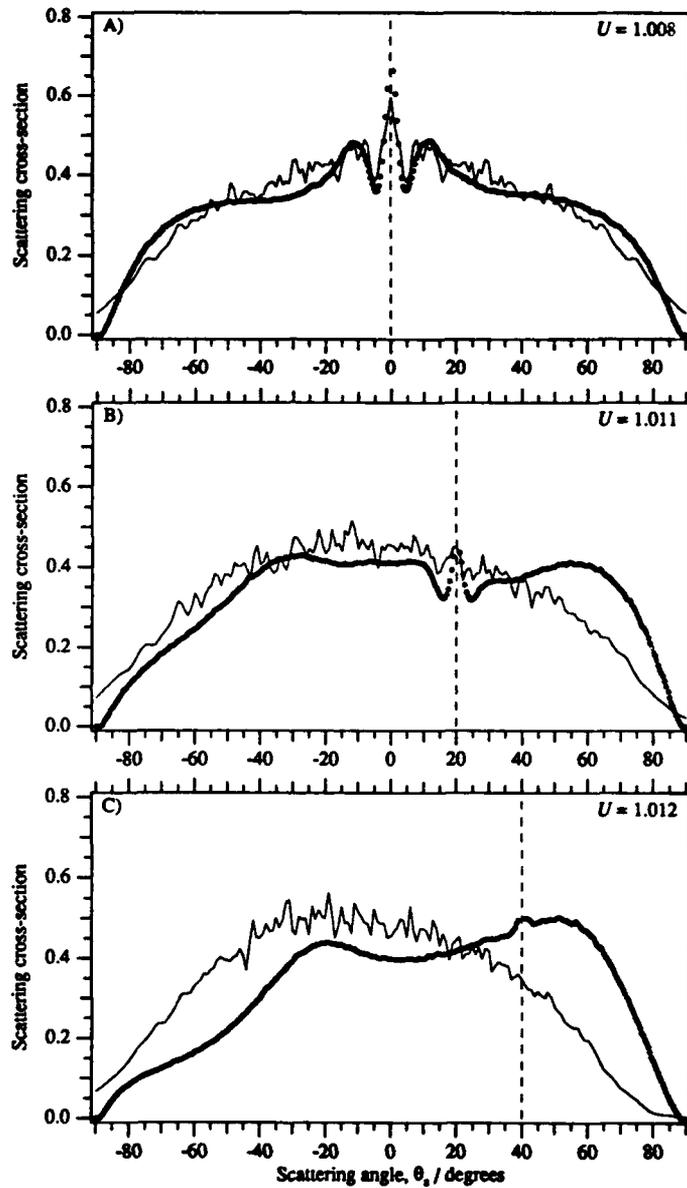
Figure 4.6: Comparisons between experimentally measured [o] and theoretically predicted [—] scattering cross-sections. Measurements: gold-coated diffuser #46; calculations: perfect conductor. $\tau/\lambda = 5.02$ and $\sigma_h/\lambda = 1.93$; $N = 2 \times 200$ realizations; surface length $L = 40\lambda$; sampling interval $\delta \approx \lambda/10$; wavelength $\lambda = 0.633 \ \mu m$. $\Xi_{ss}(\theta_i, \theta_s)$: A) $\theta_i = 0°$, B) $\theta_i = -20°$, C) $\theta_i = -40°$.

tend to be slightly broader than the corresponding *pp* measurements, although they do maintain basically the same features; the *pp* measurements tend to show slightly more backward scattering than the corresponding *ss* measurements. The differences between the experimentally determined cross-sections for the two polarizations is possibly due to the finite conductivity of the gold coating; each polarization being subject to different reflectivities and absorptions.

Wavelength $\lambda = 1.15 \ \mu m$

We next consider the case of light scattering from the same diffuser (#46) but this time for a *p* polarized incident beam whose wavelength $\lambda = 1.15 \ \mu m$. The statistical parameters are now scaled to the values $\tau/\lambda = 2.76$ and $\sigma_h/\lambda = 1.06$. A strong backscatter peak is observed experimentally at normal incidence; see Figure 4.7a. The minima and maxima on both sides of the peak are not as well defined as they are for the shorter wavelength $\lambda = 0.633 \ \mu m$ in Figure 4.5a. Comparing the peaks for the two wavelengths at normal incidence, the width taken between the minima appears to have doubled from $\lambda = 0.633 \ \mu m$ to $\lambda = 1.15 \ \mu m$. Generally, for the longer wavelength, more energy is backscattered forming broader, enhanced peaks particularly in the case of $-20°$ incidence but, conversely, more light is scattered beyond the backscatter direction for the shorter wavelength.

The fit between experiment and theory is good for normal incidence, particularly the width of the backscatter peak, although the subsidiary maxima are not well defined. At $-20°$ incidence the agreement of the overall incoherent distribution is reasonable, although the theory fails to predict a backscatter peak for the number of realizations considered, whereas strong backscatter enhancement is observed experimentally. The agreement for $-40°$ is not so good with too much light being forward-scattered in the simulation and, again, there is no backsatter peak.

The same comments can generally be made about the comparisons between experiment and theory for the scattering of an *s* polarized light beam; see Figure 4.8. The calculations do not predict such marked minima about the backscatter peak for normal incidence in Figure 4.8a, but otherwise the agreement is good. For $-20°$ incidence the curves generally agree quite well, but slightly more light is observed to be backward scattered than is predicted theoretically. Comparing the calculated results
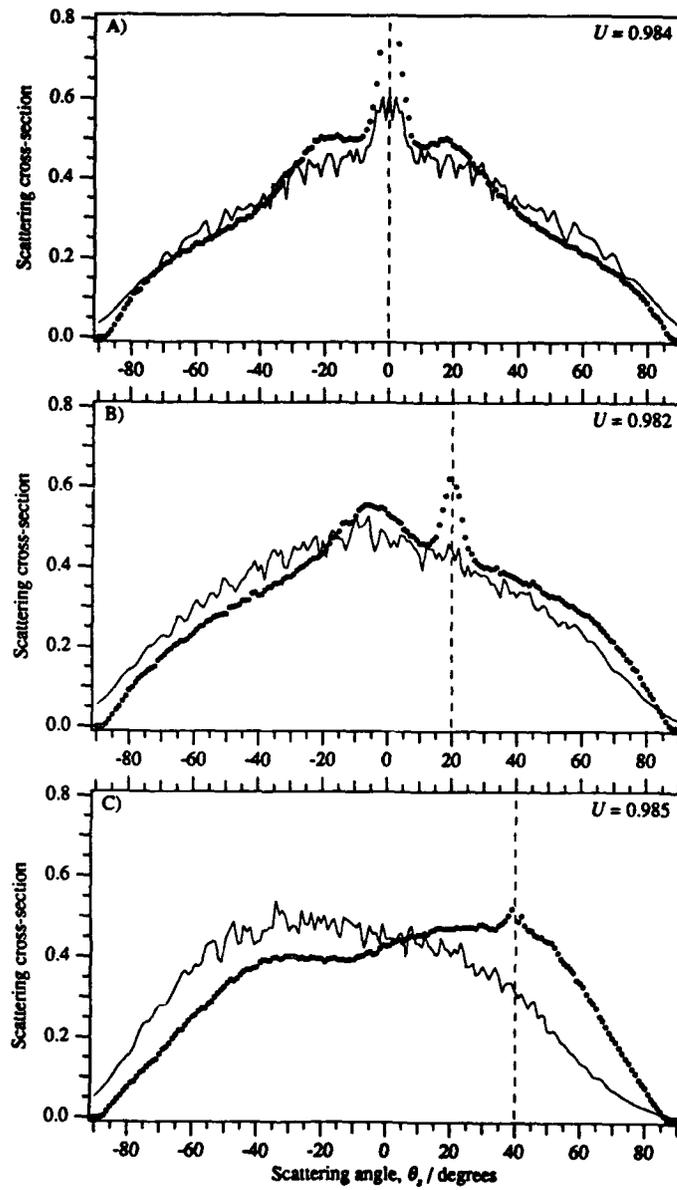
Figure 4.7: Comparisons between experimentally measured [o] and theoretically predicted [——] scattering cross-sections. Measurements: gold-coated diffuser #46; calculations: perfect conductor. $\tau/\lambda = 2.76$ and $\sigma_h/\lambda = 1.06$; $N = 2 \times 200$ realizations; surface length $L = 40\lambda$; sampling interval $\Delta \approx \lambda/10$; wavelength $\lambda = 1.15\ \mu m$. $\Xi_{pp}(\theta_i,\theta_s)$: A) $\theta_i = 0°$, B) $\theta_i = -20°$, C) $\theta_i = -40°$.
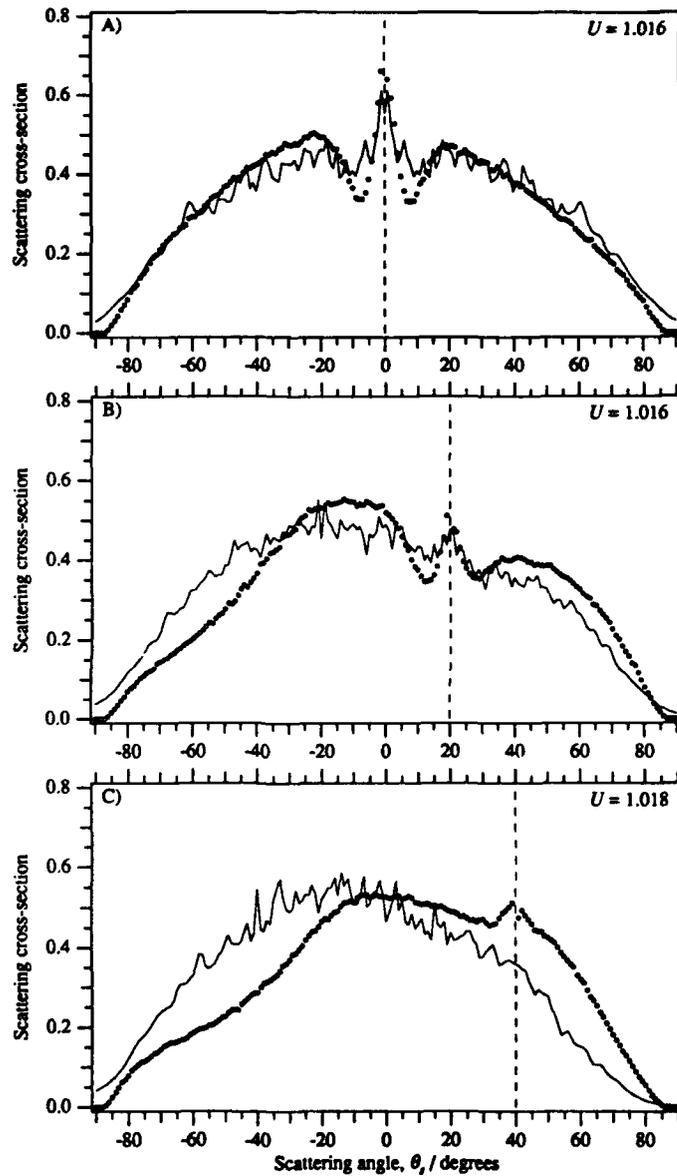
Figure 4.8: Comparisons between experimentally measured [o] and theoretically predicted [——] scattering cross-sections. Measurements: gold-coated diffuser #46; calculations: perfect conductor. $\tau/\lambda = 2.76$ and $\sigma_h/\lambda = 1.06$; $N = 2 \times 200$ realizations; surface length $L = 40\lambda$; sampling interval $\Delta \approx \lambda/10$; wavelength $\lambda = 1.15 \ \mu m$. $\Xi_{ss}(\theta_i, \theta_s)$: A) $\theta_i = 0°$, B) $\theta_i = -20°$, C) $\theta_i = -40°$.

in Figures 4.7b and 4.8b, there is more evidence of a backscatter peak being predicted for an s polarized incident beam, although neither compare to the experimental peaks. A similar comment can be made for $-40°$ incidence, in that the theory predicts more light to be scattered in the forward direction than is observed experimentally. It is interesting to note that whilst the experimental data show marked differences with the increase in wavelength, the simulations show virtually none.

Wavelength $\lambda = 3.39 \ \mu m$

The next case we consider is the scattering of a p polarized incident beam whose wavelength $\lambda = 3.39 \ \mu m$. The diffuser remains unchanged (gold-coated #46) and the same incidence angles are considered; see Figure 4.9. The roughness parameters are proportionately scaled to the values $\tau/\lambda = 0.937$ and $\sigma_h/\lambda = 0.361$. The most striking feature of the experimental measurement for normal incidence is the very broad enhanced backscatter peak and the pronounced minima and maxima adjacent to the peak. This is in contrast to the poorly defined structure observed for the same polarization at the wavelength $\lambda = 1.15 \ \mu m$ in Figure 4.7a. For $-20°$ incidence a strong backscatter peak is still present and, apart from a slight skewness, the structure observed for normal incidence merely appears to have followed the backscatter direction. At $-40°$ incidence the minima and maxima beyond backscattering ($\theta_s > 40°$) have blended into the diffusely scattered light, but the backscatter peak itself is still evident. However, for the shorter wavelengths ($\lambda = 0.633 \ \mu m$ and $1.15 \ \mu m$) the backscatter peak has all but vanished for $-40°$ incidence.

The numerically calculated cross-section for normal incidence agrees well with the measured cross-section in Figure 4.9a; the minima are not so well defined and the backscatter peak is not as strong, although its width compares very well. In Figure 4.9b the two curves are comparable from forward grazing $\theta_s = -90°$ up to backscatter, but the calculations then fall short of the measurements towards backward grazing $\theta_s = 90°$. There is no real backscatter peak predicted, although a strong peak is observed experimentally. For $-40°$ incidence there is too much emphasis on forward scattered light in the calculated cross-section, whereas the measured cross-section actually peaks at backscatter.

The comparisons between experiment and theory for the case of an s polarized
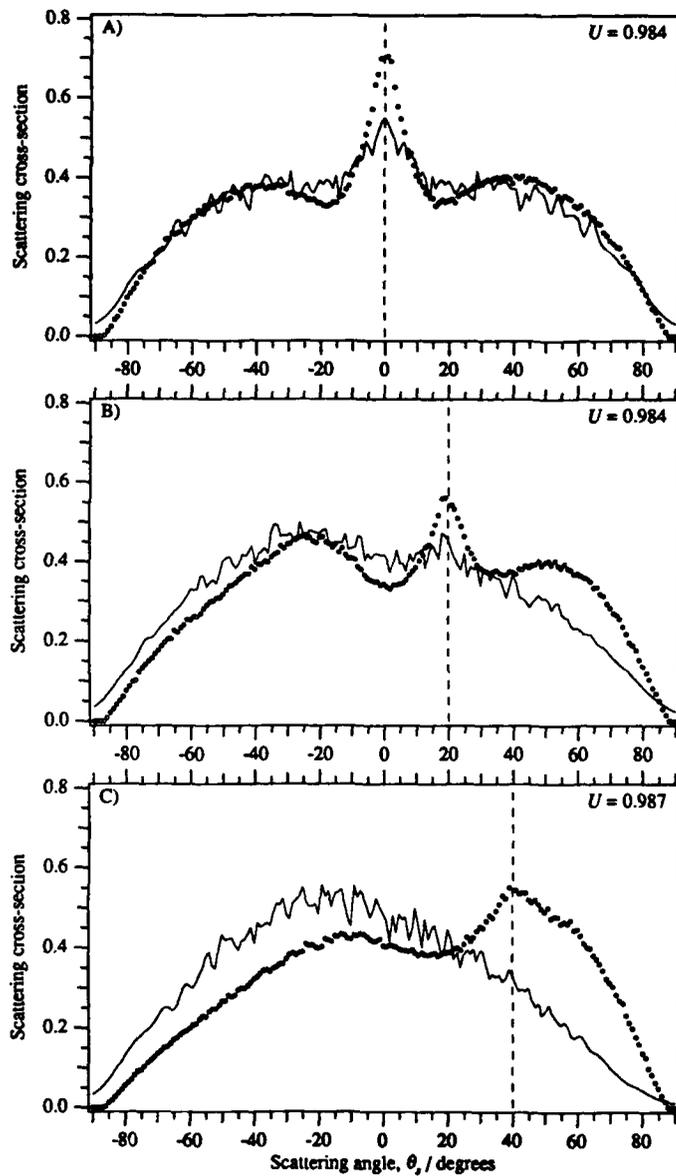
Figure 4.9: Comparisons between experimentally measured [o] and theoretically predicted [——] scattering cross-sections. Measurements: gold-coated diffuser #46; calculations: perfect conductor. $\tau/\lambda = 0.937$ and $\sigma_h/\lambda = 0.361$; $N = 2 \times 200$ realizations; surface length $L = 40\lambda$; sampling interval $\Delta \approx \lambda/10$; wavelength $\lambda = 3.39~\mu m$. $\Xi_{pp}(\theta_i, \theta_s)$: A) $\theta_i = 0°$, B) $\theta_i = -20°$, C) $\theta_i = -40°$.

incident beam are shown in Figure 4.10. For normal incidence the backscatter peak is strong and very wide with no particular subsidiary structure to it. This is in stark contrast to the corresponding measurement for the wavelength $\lambda = 1.15\ \mu m$ where the minima are particularly well defined. The backscatter peak remains the dominant feature of the scattered light up to $-40°$ incidence as it does for the p polarized case in Figure 4.9. The calculated cross-section for normal incidence is in general agreement with the measured cross-section, although the experimental backscatter peak has better definition. For higher angles of incidence the calculated results predict too much forward scattering and nothing like the degree of backscatter enhancement that the experiments show.

Wavelength $\lambda = 10.6\ \mu m$

The final case we consider for the gold-coated diffuser is the scattering of a far infrared wavelength $\lambda = 10.6\ \mu m$. At this long wavelength the surface parameters are scaled to the values $\tau/\lambda = 0.300$ and $\sigma_h/\lambda = 0.115$. The scattering cross-sections in Figures 4.11 and 4.12 are the incoherent components only; the coherent components, although of interest in long wavelength and perturbative studies, will be ignored here. For all of the incidence angles considered in Figure 4.11 it is interesting to note that, despite there being a very strong coherent reflection, the diffuse pp radiation is most strongly scattered in the backscatter direction although no peak is actually observed. The calculated cross-sections in Figure 4.11 agree well with the experimentally measured cross-sections.

Figure 4.12 shows the incoherent scattering cross-sections for an s polarized incident beam. For normal incidence the measured incoherent cross-section exhibits an almost Gaussian-like distribution, but again the dominant feature of the total cross-section is the coherent component. For $-20°$ incidence the diffusely scattered radiation becomes skewed towards forward scattering directions. Increasing the incidence angle to $-40°$ has little effect on the overall distribution, but does increase the energy in the coherent component. The calculated incoherent cross-sections in Figure 4.12 show favourable agreement with the experimental measurements for all of the incidence angles considered.

Apart from the case we have just considered, the best overall comparisons between
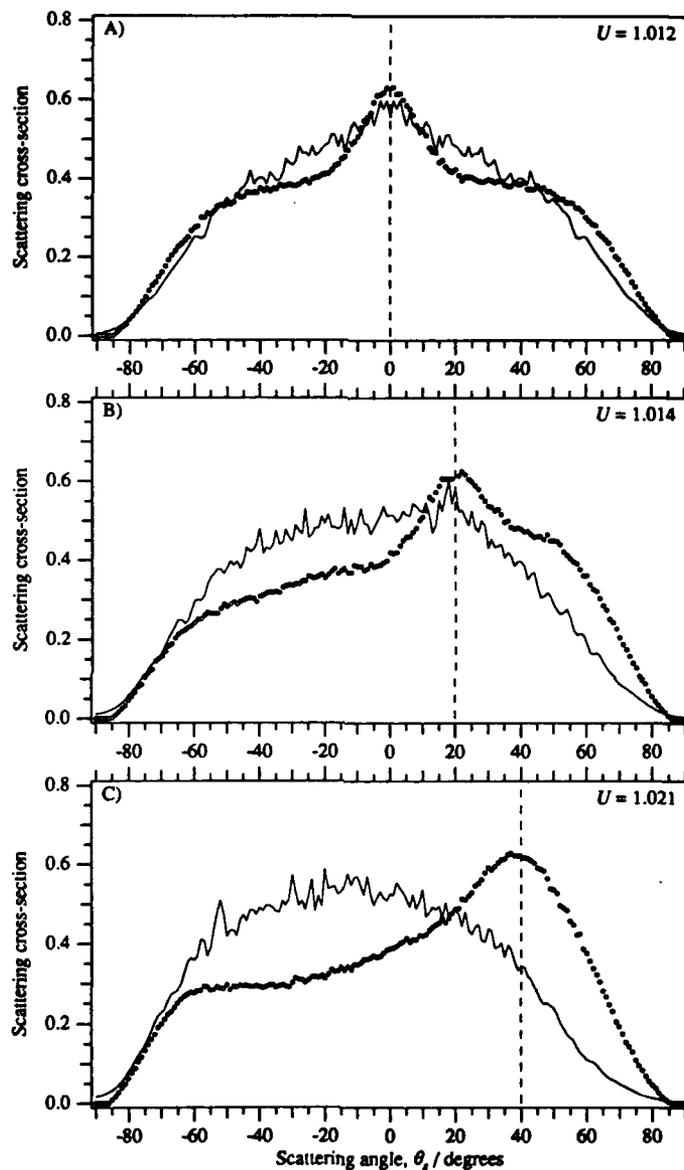
Figure 4.10: Comparisons between experimentally measured [o] and theoretically predicted [—] scattering cross-sections. Measurements: gold-coated diffuser #46; calculations: perfect conductor. $\tau/\lambda = 0.937$ and $\sigma_h/\lambda = 0.361$; $N = 2 \times 200$ realizations; surface length $L = 40\lambda$; sampling interval $\Delta \approx \lambda/10$; wavelength $\lambda = 3.39\ \mu m$. $\Xi_{ss}(\theta_i, \theta_s)$: A) $\theta_i = 0°$, B) $\theta_i = -20°$, C) $\theta_i = -40°$.
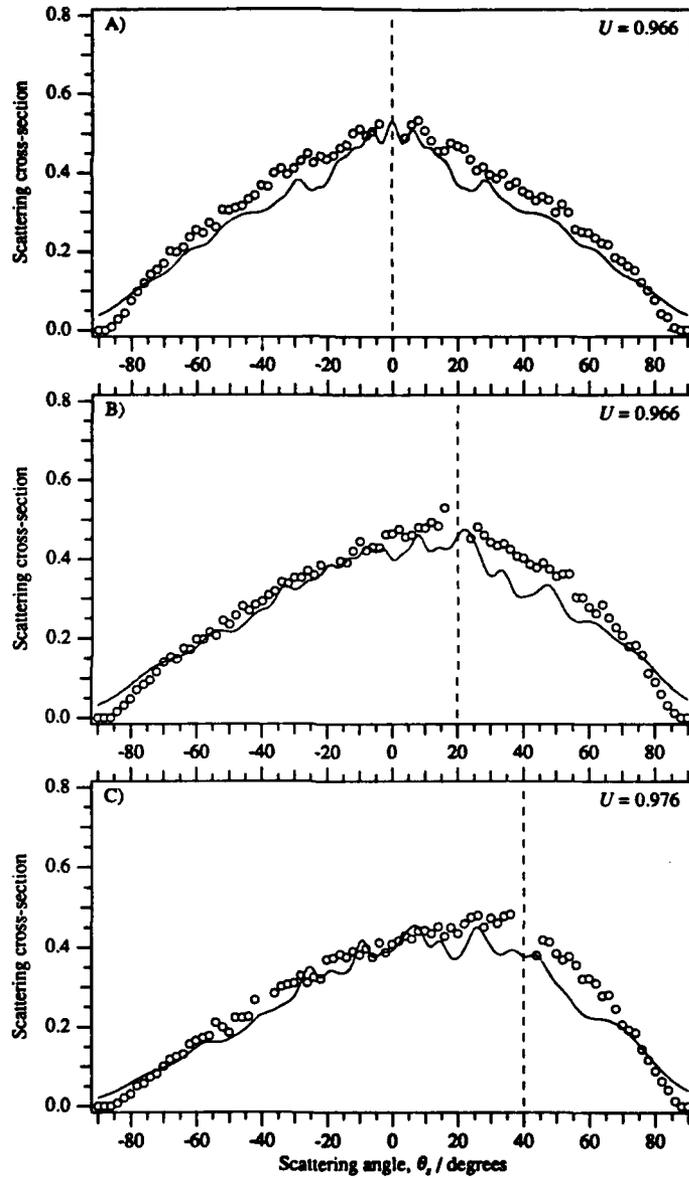
Figure 4.11: Comparisons between experimentally measured [o] and theoretically predicted [—] scattering cross-sections. Measurements: gold-coated diffuser #46; calculations: perfect conductor. $\tau/\lambda = 0.300$ and $\sigma_h/\lambda = 0.115$; $N = 2 \times 200$ realizations; surface length $L = 12\lambda$; sampling interval $\Delta \approx \lambda/20$; wavelength $\lambda = 10.6 \ \mu m$. $\Xi_{pp}(\theta_i, \theta_s)$: A) $\theta_i = 0°$, B) $\theta_i = -20°$, C) $\theta_i = -40°$.
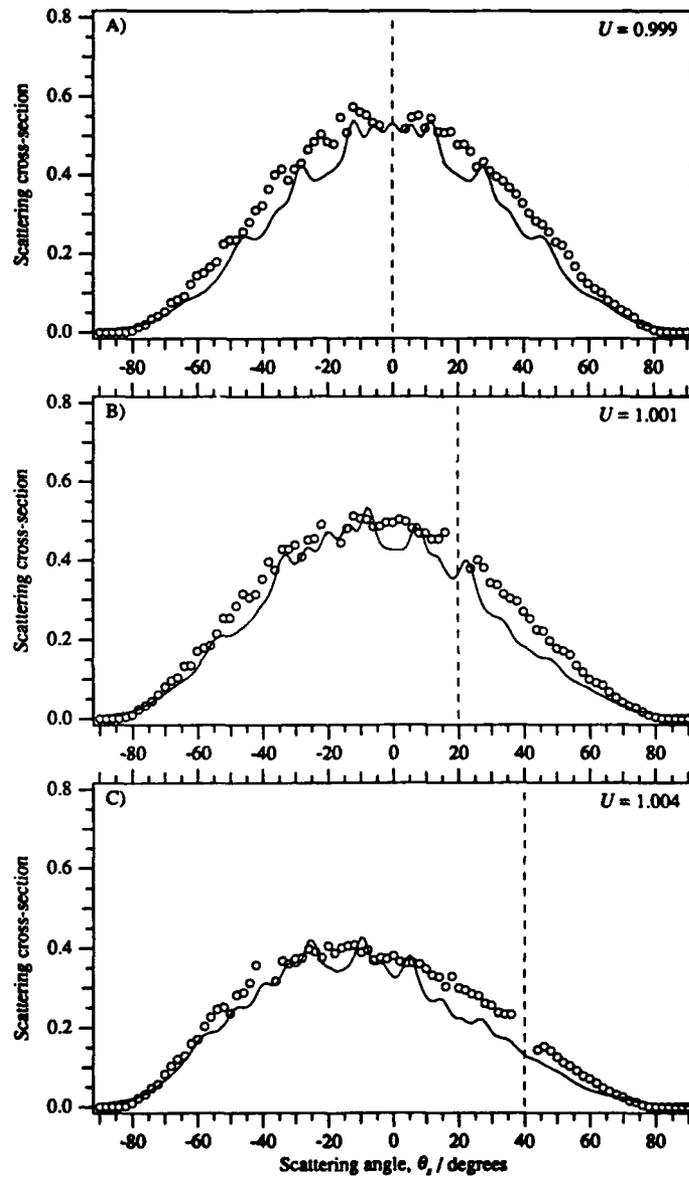
Figure 4.12: Comparisons between experimentally measured [o] and theoretically predicted [——] scattering cross-sections. Measurements: gold-coated diffuser #46; calculations: perfect conductor. $\tau/\lambda = 0.300$ and $\sigma_h/\lambda = 0.115$; $N = 2 \times 200$ realizations; surface length $L = 12\lambda$; sampling interval $\Delta \approx \lambda/20$; wavelength $\lambda = 10.6 \ \mu m$. $\Xi_{ss}(\theta_i, \theta_s)$: A) $\theta_i = 0°$, B) $\theta_i = -20°$, C) $\theta_i = -40°$.

experimental observation and theoretical prediction occur for the wavelength $\lambda =$ 1.15 μm, when the statistical roughness is characterized by the parameters $\tau/\lambda = 2.76$ and $\sigma_h/\lambda = 1.06$.

4.5.2 Discussion

At each illuminated point of a diffusing surface there will be a surface current induced by the incident field. Each element of the surface will act as a tiny source radiating fields towards other surface elements and also into the propagating reflection and transmission fields. In this model a surface element may preferentially radiate fields away from the surface, suggesting a 'single' event, but its surface current generating the fields may contain contributions from other elements — a 'multiple' event. The degree to which the surface elements mutually contribute to their currents will depend strongly on the local slopes and curvatures of the profile compared to the wavelength. Clearly large slopes and curvatures will support more 'multiple' interactions whereas low sloped, slowly ·   ·ting surfaces would tend to favour 'single' scattering. The meanings of single anu multiple scattering become somewhat ambiguous when the surface structures become smaller than a wavelength.

In analogy with the studies of light scattering from volume suspensions of microspheres [2, 43, 45, 80], one possible mechanism for backscatter enhancement from surfaces is the co-operative effect between forward and time-reversed light paths — a multiple scattering effect. Considering the fields radiated by each surface element to be decomposed into plane-wave components, we can concentrate on one such component from a particular element which strikes another element; that surface element may then, in turn, radiate a plane-wave component in the backscatter direction. Such a sequence may be described as being a two-fold event, but can generally consist of m individual interactions. In Figure 4.13 are shown two $m = 3$-fold events which involve the same scattering elements, but whose sequences are reversed with respect to each other. When $\theta = 0°$, the out-going wave vector is in opposition to the in-coming wave vector, and is by definition the backscatter direction. The two wave components will then have the same amplitude and phase, and interfere constructively to give an enhanced intensity. Away from backscatter there will be a non-zero phase difference introduced between the two waves and their phases will soon become uncorrelated re-
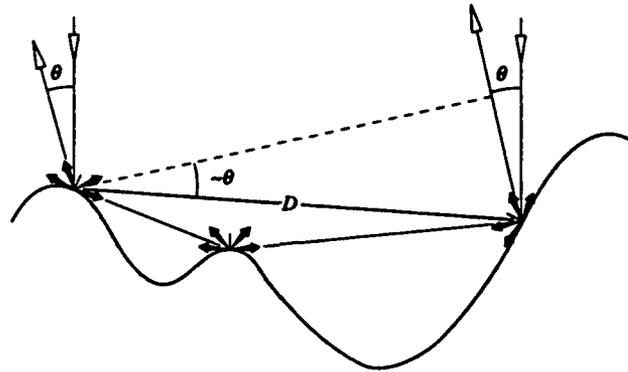
Figure 4.13: Introduction of a phase difference, away from backscatter, between forward and time-reversed light paths for an $m = 3$-fold scattering event.

sulting in the waves adding incoherently, i.e. no interference term. It is clear then that in the vicinity of the backscatter direction, the peak will be enhanced approximately by a factor of two over the incoherent intensity of $m \geq 2$-fold events.

Near normal incidence, the phase difference $\Delta\phi$ introduced between forward and time-reversed light paths, at an angle θ away from backscatter, can be obtained from Figure 4.13 and is proportional to

$$\Delta\phi \propto \frac{2\pi}{\lambda} D\theta$$

where D is the distance separating the first and last scattering elements. Taken over all possible scattering paths we obtain the averaged relation

$$\langle \Delta\phi \rangle \propto \frac{2\pi}{\lambda} \langle D \rangle \theta \tag{4.37}$$

for a particular angular deviation θ from backscatter. We would therefore expect maxima in the light field to occur when $\langle \Delta\phi \rangle = 2\pi n$, where $n = 0, \pm1, \pm2, \ldots$ and the corresponding minima to occur when $\langle \Delta\phi \rangle = 2\pi(n + 1/2)$. The visibility of these interference effects (fringes) will greatly depend on the standard deviation of the phase difference $\sigma_{\Delta\phi}$ which, in turn, will depend on the standard deviation of the distance parameter σ_D. From simple statistical arguments we can write

$$\sigma_{\Delta\phi} = \frac{\Delta\phi}{D} \sigma_D$$

$$\propto \frac{2\pi}{\lambda}\theta\sigma_D$$

From equation (4.37) the first subsidiary maximum ($n = 1$) occurs at an angle

$$\theta \propto \frac{\lambda}{\langle D \rangle}$$

away from backscatter and, hence, we can show that

$$\sigma_{\Delta\phi} \propto \frac{2\pi}{\langle D \rangle}\sigma_D \tag{4.38}$$

When scattering from a volume, the mean distance parameter $\langle D \rangle$ can potentially be quite large (tens of wavelengths), but presumably so can its standard deviation σ_D since no subsidiary maxima are observed in volume scattering experiments — $\sigma_{\Delta\phi}$ is then too large and the interference effects are washed out for $n \geq 1$. For light scattering from a random, metallic surface the longer distances D will generally be limited by the mean separation between major peaks across the surface profile. Hence σ_D will not be so large for scattering from a surface as it can be from a volume, and so $\sigma_{\Delta\phi}$ will also be smaller. This simple analysis may explain why, in some cases, subsidiary maxima can be observed in experimental light scattering from surfaces but not from volumes.

From equation (4.37) the first subsidiary minimum occurs when $n = 0$ and allows us to find a relation for the angular width of the backscatter peak between the minima:

$$\Delta\theta_{b_s} \propto \frac{\lambda}{\langle D \rangle} \tag{4.39}$$

Considering the experimental results presented in Figures 4.5 – 4.10 we are able to obtain the set of data in Table 4.2, relating to the backscatter peak widths for $0°$ and $-20°$ incidence. For an $m = 2$-fold event, the mean distance $\langle D \rangle$ represents the elastic mean-free-path of the light interaction at the surface. The mean distance between two consecutive peaks on a Gaussian surface is of the order of 2τ [56, Appendix A], and hence we can intuitively say that

$$\Delta\theta_{b_s} \propto \frac{\lambda}{\tau}$$

Figure 4.14 represents the *pp* data from Table 4.2 together with some extra data points measured from other diffusers available in our laboratory. The relationships

Pol^n	Wavelength	Backscatter peak width		
	λ / μm	$\theta_i = 0°$	$\theta_i = -20°$	
pp	0.633	10.0°	9.0°	±0.1°
or	1.15	21°	17°	±1.0°
TM	3.39	36°	35°	±2.0°
ss	0.633	9.4°	8.5°	±0.1°
or	1.15	16°	16°	±1.0°
TE	3.39	45°	35°	±2.0°

Table 4.2: Angular widths (in degrees) of the experimental enhanced backscatter peaks.
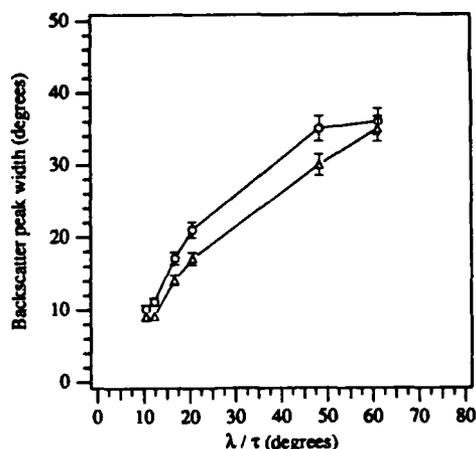
Figure 4.14: Variation of experimentally measured backscatter peak widths as a function of λ/τ. In each case a *p* polarized light beam is reflected from a gold-coated diffuser. Incidence angles $\theta_i = 0°$ [o] and $\theta_i = -20°$ [□].

between the backscatter peak widths and the ratio λ/τ are approximately linear in, what is termed, the 'geometric optics' limit as $\lambda \rightarrow 0$.

The peak widths are consistently smaller for $-20°$ incidence than for normal incidence. A case for why this is so may be based around the following arguments. Physically the only change that occurs as the direction of the incident beam is varied, is the degree of shadowing — shadows are cast across the surface by the incident beam, but there is also the shadowing of observation, i.e., an illuminated point may not be visible. This would suggest that if one half of a valley is in shadow, then any multiple interactions across the width of the valley will have to end up back on the illuminated half in order to be backscattered, requiring at least an $m = 3$-fold interaction. As the degree of shadowing is increased, the contributions from short-

range, low-order interactions will be reduced resulting in $\langle D \rangle$ increasing. Hence from equation (4.39) the width of the backscatter peak will decrease with increasing angle of incidence. The shadowing argument may also be used to explain the reduction in height of the backscatter peak as the incidence angle is increased; the effect of shadowing will generally reduce the possible number of light paths that will support retroreflection, and hence reduce the backscattered energy.

Another interesting observation from the experimental results is in the relative strengths of the subsidiary maxima about the backscatter peak, between the two polarizations *p* and *s*. For $\lambda = 0.633 \ \mu m$ the subsidiary structure appears slightly stronger for *s* incident polarization than it does for *p* polarization. Again for $\lambda = 1.15 \ \mu m$ the difference is more evident with the *pp* data exhibiting shallow structures as opposed to the very deep minima present for the *ss* data. However, the trend is reversed for $\lambda = 3.39 \ \mu m$ with the *pp* data exibiting well defined minima and maxima, whereas the *ss* measurement has no structures at all. The visibility of the interference effects believed to give rise to this structure is governed by $\sigma_{\Delta\phi}$ in equation (4.38), but an explanation of the factors determining which polarization structure dominates has yet to be found.

4.5.3 Dielectric scattering (reflection)

The diffuser used in this experimental investigation is a dielectric replica of diffuser #46 which was gold-coated for the previous study. The replication technique is described in § 3.5 and is shown to faithfully reproduce the surface profile. Analyzing transmission and reflection values of a flat, dielectric sample relative to a distilled water standard, the refractive and absorptive indices were obtained for the relevant wavelengths [21, Chapter 2].

Wavelength $\lambda = 0.633 \ \mu m$

The first case of light scattering from a dielectric diffuser that we consider is of a *p* polarized light beam whose wavelength $\lambda = 0.633 \ \mu m$. At this wavelength the surface roughness parameters have the values $\tau/\lambda = 5.02$ and $\sigma_h/\lambda = 1.93$, and the refractive index $n = 1.411$. Figure 4.15 shows the comparisons between experimental measurement and numerical simulation based on a perfect dielectric for the incidence

Wavelength λ / μm	Refractive index, n $\pm 0.1\%$	Absorptive index
0.63	1.411	$6.0 \pm 3.0 \times 10^{-8}$
1.15	1.399	$3.5 \pm 1.2 \times 10^{-6}$
3.40*	1.412	$4.0 \pm 2.2 \times 10^{-2}$
10.60*	1.510	$9.1 \pm 2.2 \times 10^{-2}$

*The absorptive indices for these wavelengths were calculated using Kramer's-Kronig analysis [31, appendix B].

Table 4.3: Refractive and absorptive indices of the dielectric medium at the investigation wavelengths.

angles $0°$, $-20°$, and $-40°$. The backscatter direction in each graph is denoted by a vertical dashed line and can also be recognized by the blind-spot in the experimental data. It should be mentioned that at the time of measurement the experimental data were not normalized in an absolute sense, although the beam power incident on the diffuser was unchanged for each measurement. For comparison purposes, the experimental data have been normalized such that the total reflected power for p and s polarizations at normal incidence is equal to that predicted by the theoretical results. Although the comparisons will be qualitative in nature, the calculations have been shown to agree reasonably well at normal incidence for metallic scattering, and there is no reason to believe that this should not also be the case for dielectric scattering.

The scattered-light distribution observed for normal incidence ($\theta_i = 0°$) has an almost Lambertian-like appearance [refer to § 2.6]. Comparing this measurement to the one for the gold-coated diffuser in Figure 4.5a, the distribution is qualitatively similar except for the total absence of any backscatter structure. As the incidence angle is increased, the dielectric measurements maintain a similar distribution being slightly skewed towards backscatter. The only feature which emerges is a null reflectance at $\theta_s \sim 65°$ for $-40°$ incidence, which is a consequence of the Brewster phenomenon for p polarized light. The fact that this effect is present at all suggests that the scattering mechanisms at the surface are predominantly *single* interactions.

Comparison with the numerical calculations for normal incidence shows favourable agreement, although the theory appears to predict some structure at backscatter. Reasonable agreement is found for $-20°$ incidence with slightly too much light around the backscatter direction. The comparison for $-40°$ incidence is very good with the only slight discrepancy occuring towards the forward grazing angle $\theta_s = -90°$ where
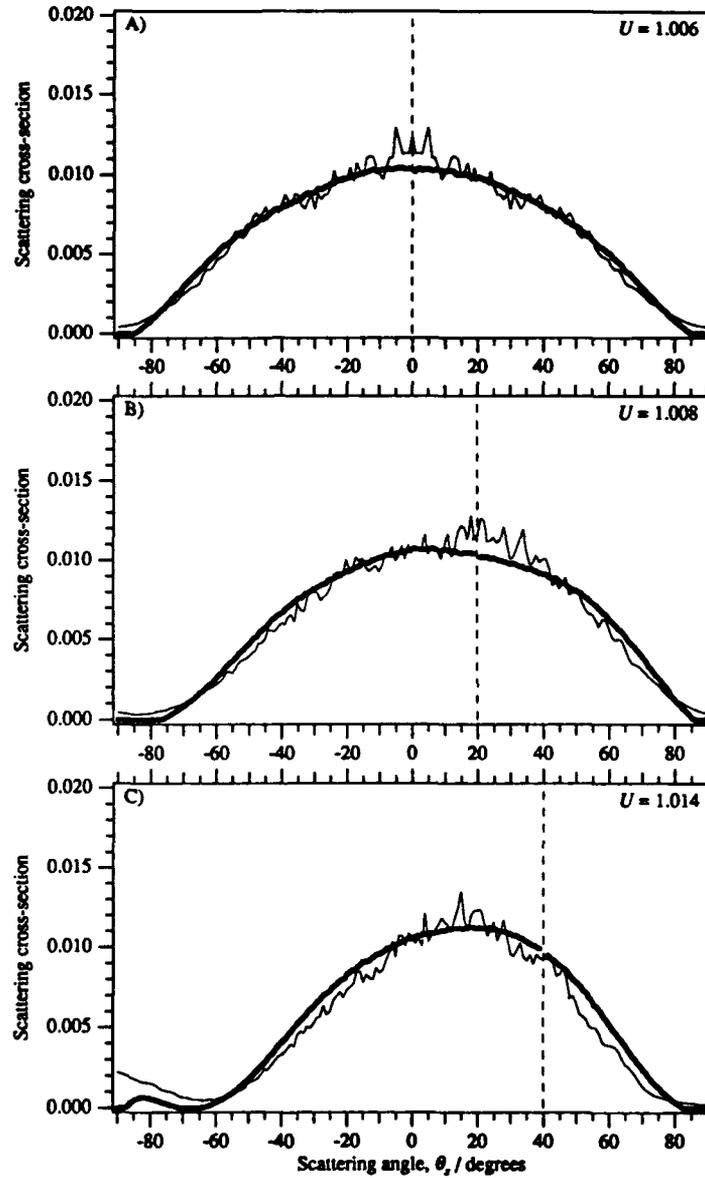
Figure 4.15: Comparisons between experimentally measured [o] and theoretically pre-
dicted [——] scattering cross-sections. Measurements: dielectric diffuser #46; calculations:
perfect dielectric. $\tau/\lambda = 5.02$ and $\sigma_h/\lambda = 1.93$; $N = 2 \times 200$ realizations; surface length
$L = 40\lambda$; sampling interval $\Delta \approx \lambda/10$; refractive index $n = 1.411$; wavelength $\lambda = 0.633~\mu m$.
$\Xi_{pp}^{rc}(\theta_i, \theta_s)$: A) $\theta_i = 0°$, B) $\theta_i = -20°$, C) $\theta_i = -40°$.

the calculation does not fall to zero. It is thought that this is an artifact of the simulation only accounting for a finite length of surface.

The corresponding measurements for an s polarized incident beam are shown in Figure 4.16. The measured cross-section for normal incidence exhibits considerably more structure than the pp measurement in Figure 4.15a. A greater amount of light is reflected at large scatter angles and there is the presence of a small backscatter peak. Both of these observed features may be explained by considering Fresnel's coefficients of light reflection from a flat, dielectric medium. Since the pp measurement for normal incidence does not exhibit the Brewster phenomenon, we may assume that we are on the portion of the Fresnel reflectivity curves between zero degrees and the Brewster angle. Along this portion, the reflectivity of a p polarized wave is falling to zero with increasing angle whereas that of an s polarized wave is increasing, and hence more s polarized light is scattered at larger angles. Since s polarized waves have higher reflectivities than p waves, we would expect any multiple scattering related phenomena to at least be present in the ss measurement. The presence of a small backscatter peak in Figure 4.16a and its absence from Figure 4.15a would therefore suggest a multiple scattering mechanism for this phenomenon.

The comparisons between experiment and theory are quite favourable for all of the incidence angles considered. The main differences occur at grazing scatter angles ($\theta_s = \pm 90°$) and the peak reflectance of the forward scattered light. An interesting point to note is that, in both experiment and theory, the two polarizations for each incidence angle have the same scattering cross-section at backscatter.

To investigate the effects of multiple scattering from a dielectric diffuser, it is a simple matter to increase the surface reflectivity in the numerical calculations through the refrative index n. Figure 4.17 shows some calculated scattering cross-sections in reflection for diffuser #46 at normal incidence. The lower pair of curves represent p and s scattering for $n = 1.411$, while the upper curves are the corresponding cross-sections for $n = \sqrt{10.0}$. The increase in reflectivity of the dielectric medium is apparent, and a sharp backscatter peak with subsidiary maxima is observed in the ss calculation. It would appear that there is still an insufficient multiple scattering contribution for backscatter enhancement of p polarized waves to occur. Calculations have shown that p polarized enhancement can be induced for nominal values of refractive index if the surface is strongly diffusing ($\tau/\lambda \simeq 3$ and $\sigma_h/\lambda \simeq 2$) [56, Chapter 6].
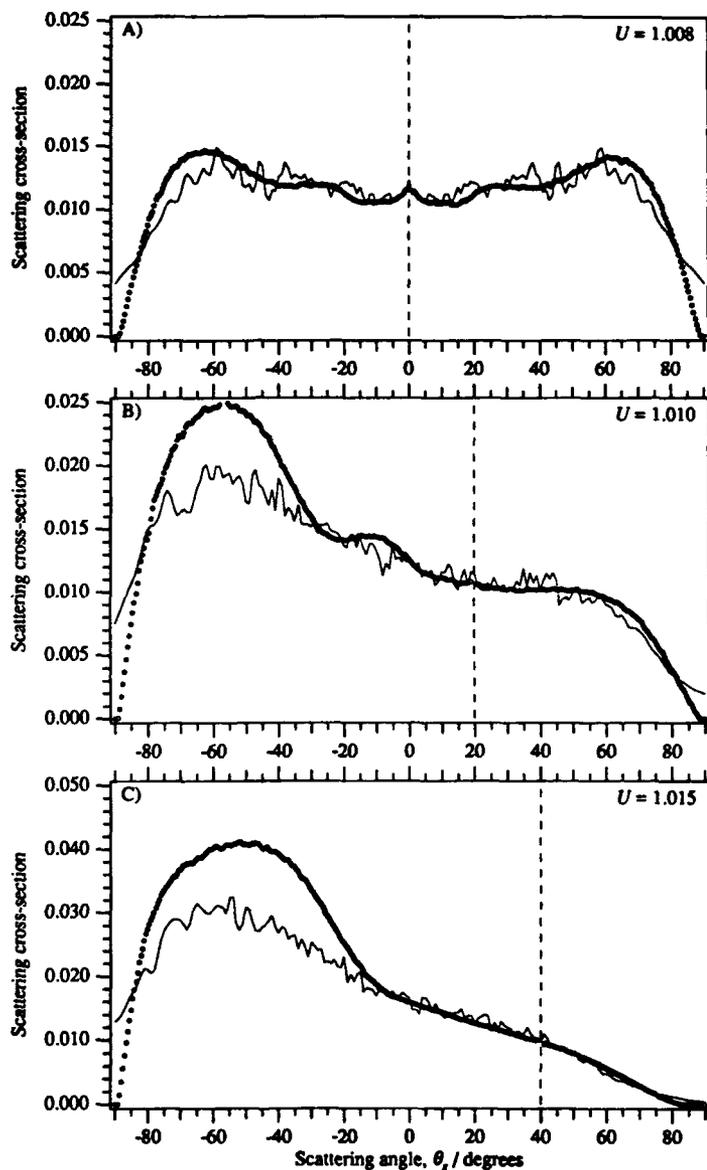
Figure 4.16: Comparisons between experimentally measured [o] and theoretically predicted [——] scattering cross-sections. Measurements: dielectric diffuser #46; calculations: perfect dielectric. $\tau/\lambda = 5.02$ and $\sigma_h/\lambda = 1.93$; $N = 2 \times 200$ realizations; surface length $L = 40\lambda$; sampling interval $\Delta \approx \lambda/10$; refractive index $n = 1.411$; wavelength $\lambda = 0.633\ \mu m$. $\Xi_{ss}^{re}(\theta_i, \theta_s)$: A) $\theta_i = 0°$, B) $\theta_i = -20°$, C) $\theta_i = -40°$.
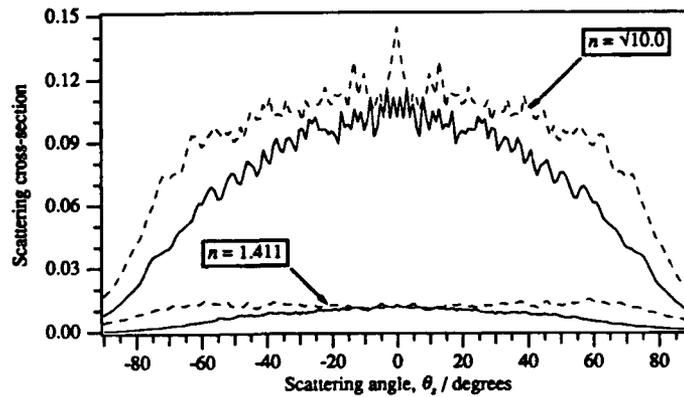
Figure 4.17: Numerically calculated scattering cross-sections for p [——] and s [- - -] incident polarizations in reflection. $\tau/\lambda = 5.02$ and $\sigma_h/\lambda = 1.93$; $N = 2 \times 200$ realizations; surface length $L = 40\lambda$; sampling interval $\Delta \approx \lambda/10$; the refractive index has been artificially increased from $n = 1.411$ to $n = \sqrt{10.0}$; wavelength $\lambda = 0.633$ μm. $\Xi^{rc}(0°, \theta_s)$.

Wavelength $\lambda = 1.15$ μm

The next case we consider is the scattering of a p polarized light beam of wavelength $\lambda = 1.15$ μm from a dielectric diffuser of refractive index $n = 1.399$. The surface roughness parameters are now scaled to the values $\tau/\lambda = 2.76$ and $\sigma_h/\lambda = 1.06$. The experimental data presented in Figures 4.18 and 4.19 have been normalized in the same way as for the wavelength $\lambda = 0.633$ μm to facilitate a comparison with the theoretical calculations. The measured pp scattering cross-sections in Figure 4.18 show broadly the same features as for the shorter wavelength in Figure 4.15. The main difference occurs for $-40°$ incidence where the cross-section peaks more sharply near the backscatter direction. The numerical calculations agree quite favourably with the experimental data except, again, around backscatter for $-40°$ incidence.

The experimental and theoretical scattering cross-sections for an s polarized incident beam are shown in Figure 4.19. The more smoothed appearance of the measurements compared to those in Figure 4.16 are as expected for an increase in the illuminating wavelength. Away from normal incidence, observations show that more light is scattered in the backscatter direction and towards grazing ($\theta_s = 90°$) with the increase in wavelength. For normal incidence the calculated cross-section is generally
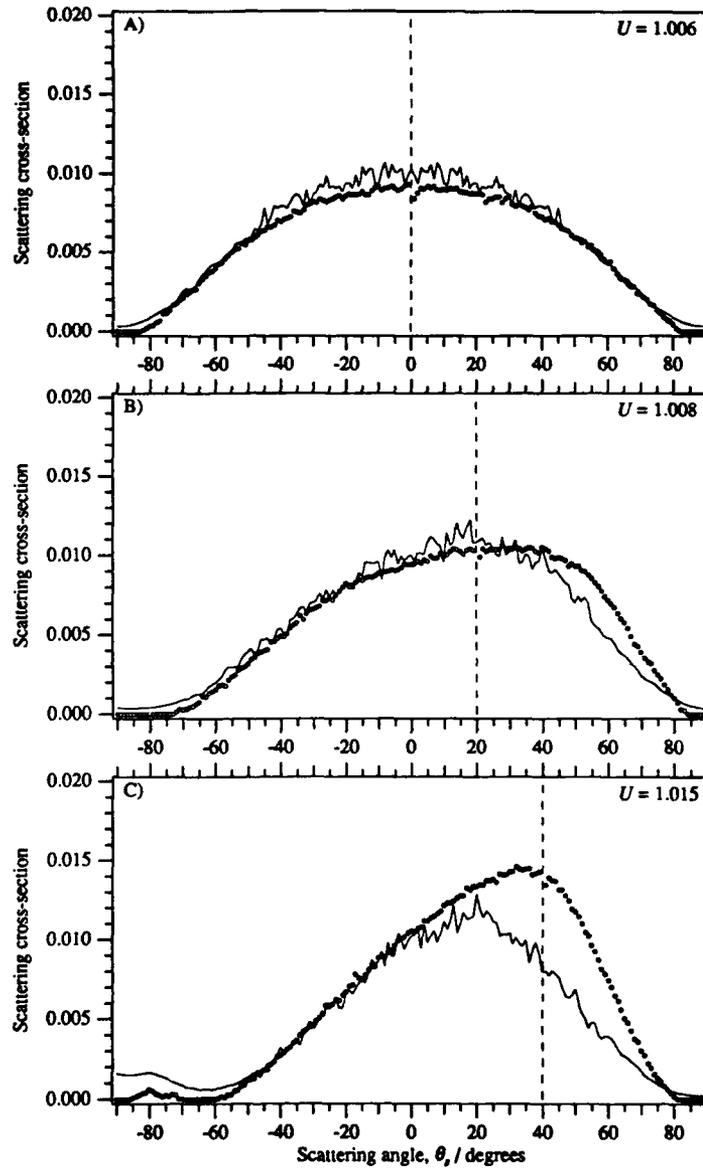
Figure 4.18: Comparisons between experimentally measured [o] and theoretically predicted [——] scattering cross-sections. Measurements: dielectric diffuser #46; calculations: perfect dielectric. $\tau/\lambda = 2.76$ and $\sigma_h/\lambda = 1.06$; $N = 2 \times 200$ realizations; surface length $L = 40\lambda$; sampling interval $\Delta \approx \lambda/10$; refractive index $n = 1.399$; wavelength $\lambda = 1.15 \ \mu m$. $\Xi_{pp}^{re}(\theta_i, \theta_s)$: A) $\theta_i = 0°$, B) $\theta_i = -20°$, C) $\theta_i = -40°$.
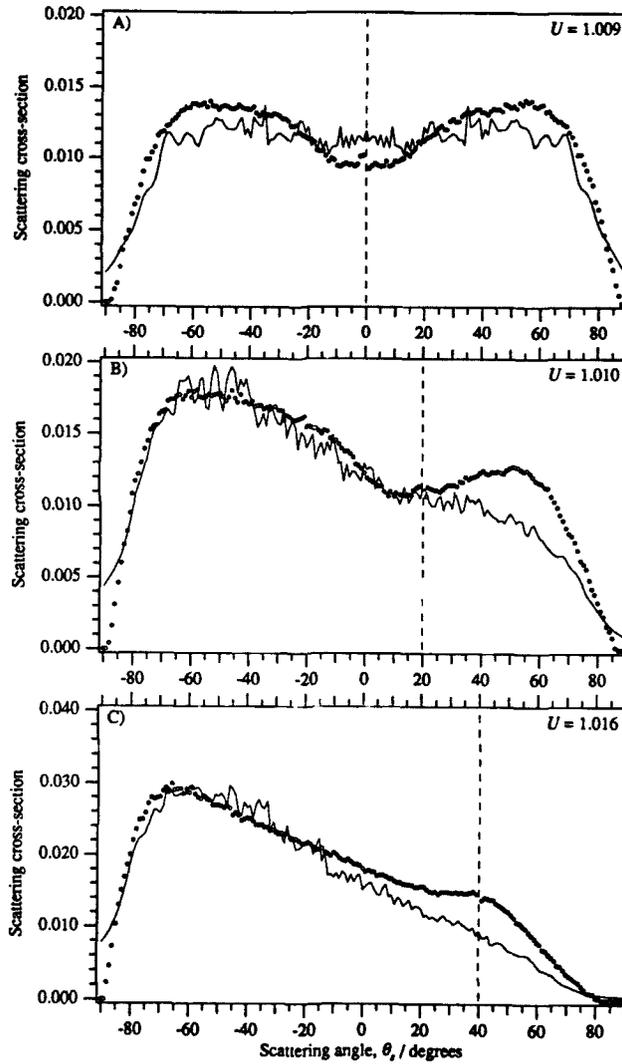
Figure 4.19: Comparisons between experimentally measured [o] and theoretically predicted [—] scattering cross-sections. Measurements: dielectric diffuser #46; calculations: perfect dielectric. $\tau/\lambda = 2.76$ and $\sigma_h/\lambda = 1.06$; $N = 2 \times 200$ realizations; surface length $L = 40\lambda$; sampling interval $\Delta \approx \lambda/10$; refractive index $n = 1.399$; wavelength $\lambda = 1.15\ \mu m$. $\Xi_{ss}^{rc}(\theta_i, \theta_s)$: A) $\theta_i = 0°$, B) $\theta_i = -20°$, C) $\theta_i = -40°$.

too flat and featureless compared to the experimenta! cross-section; for $-20°$ incidence their is good agreement up to backscatter, but does not predict the observed peak in the diffusely scattered light at $\theta_s \approx 60°$. The simulation for $-40°$ incidence shows broad agreement with the experimental result although, again, not enough light is backward scattered at larger angles.

Wavelength $\lambda = 3.39 \ \mu m$

Increasing the wavelength further to $\lambda = 3.39 \ \mu m$ the roughness parameters are then $\tau/\lambda = 0.937$ and $\sigma_h/\lambda = 0.361$. Comparing the cross-sections in Figures 4.20 and 4.21 to those for the shorter wavelengths, similar features can be seen. In comparing the cross-sections between experiment and theory at this wavelength, little more need be mentioned other than the agreements are very good across all of the incidence angles considered.

4.5.4 Comments on computational rigour

Although the calculated scattering cross-sections satisfy the energy conservation criterion to within 5% [see the unitaritity values U in each Figure], some general comments on computational rigour can be drawn from the comparisons with experimental metal and dielectric results. On the whole the computations agree well wi.h the experimental observations near normal incidence but agreement lessens for increasing incidence angle, particularly for the reflective metallic surface. One possible cause of this reduction may stem from describing the diffusing surface at uniform *horizontal* intervals rather than at uniform intervals *along* the profile itself. It is therefore the valley walls which are least defined in such a description, and it is these portions of the surface which become more strongly illuminated away from normal incidence. Inadequate description of the field amplitudes along these portions, from the incident field and multiple interactions, may lead to the observed emphasis of forward-scattered radiation for higher incidence angles, whereas the experiments show stronger backward scatter. It may also explain why the calculations sometimes fail to predict backscatter enhancement away from normal incidence; a particular case in point is for the wavelength $\lambda = 3.39 \ \mu m$ scattered from the metallic diffuser in Figures 4.9 and 4.10. One of the best qualitative agreements overall is found to occur for the dielectric diffuser
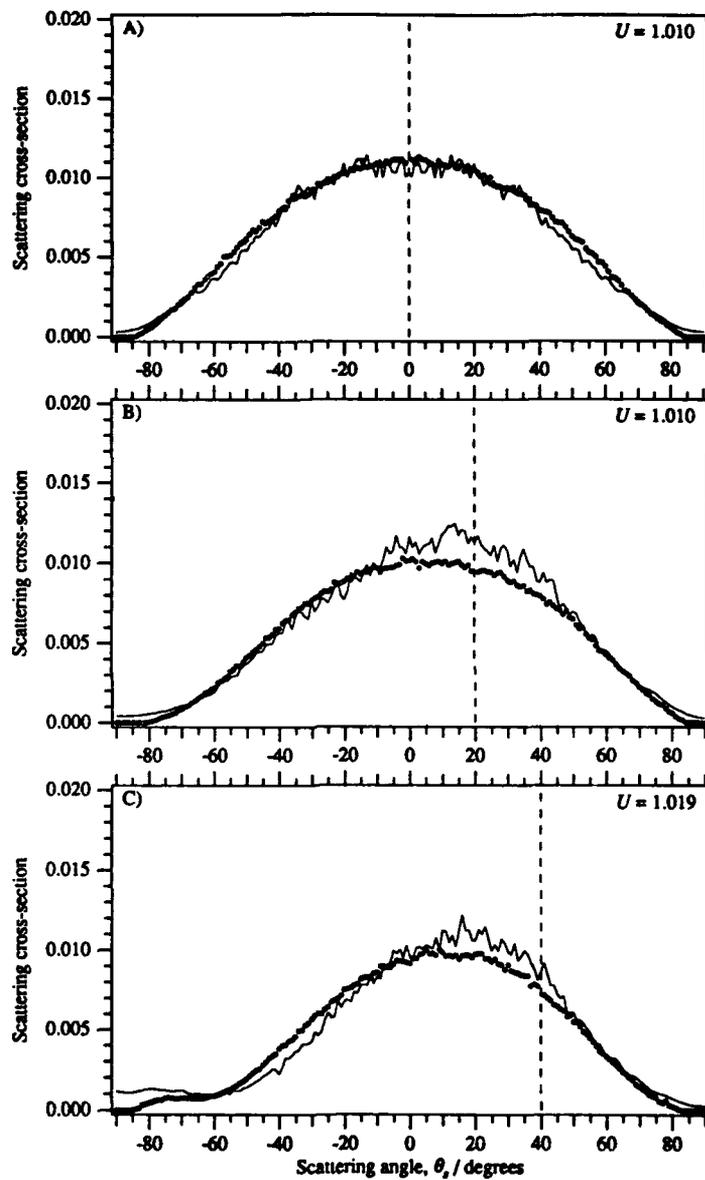
Figure 4.20: Comparisons between experimentally measured [o] and theoretically predicted [——] scattering cross-sections. Measurements: dielectric diffuser #46; calculations: perfect dielectric. $\tau/\lambda = 0.937$ and $\sigma_h/\lambda = 0.361$; $N = 2 \times 200$ realizations; surface length $L = 40\lambda$; sampling interval $\Delta \approx \lambda/10$; refractive index $n = 1.412$; wavelength $\lambda = 3.39 \ \mu m$. $\Xi_{pp}^{re}(\theta_i, \theta_s)$: A) $\theta_i = 0°$, B) $\theta_i = -20°$, C) $\theta_i = -40°$.
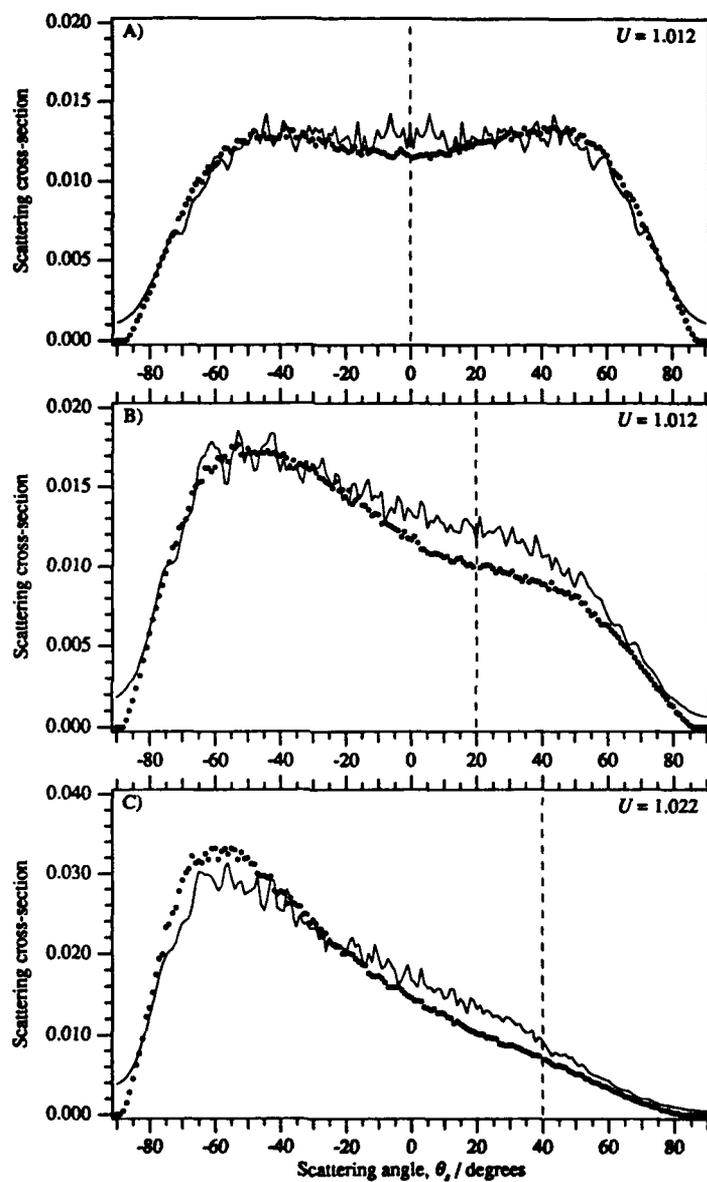
Figure 4.21: Comparisons between experimentally measured [o] and theoretically predicted [—] scattering cross-sections. Measurements: dielectric diffuser #46; calculations: perfect dielectric. $\tau/\lambda = 2.76$ and $\sigma_h/\lambda = 1.06$; $N = 2 \times 200$ realizations; surface length $L = 40\lambda$; sampling interval $\Delta \approx \lambda/10$; refractive index $n = 1.412$; wavelength $\lambda = 3.39~\mu m$. $\Xi_{ss}^{re}(\theta_i, \theta_s)$: A) $\theta_i = 0°$, B) $\theta_i = -20°$, C) $\theta_i = -40°$.

at the wavelength $\lambda = 3.39$ μm, i.e. single scattering of long wavelengths.

4.5.5   Dielectric scattering (transmission)

Leaving surface reflection at the wavelength $\lambda = 10.6$ μm to the experimental synopsis in § 4.6, we now consider the field transmitted below a dielectric, random surface when illuminated from free-space above. The diffuser used for this investigation is a dielectric replica of diffuser #39, but this time in the form of a parallel-sided slab [refer to § 3.5]. For the illuminating wavelength $\lambda = 0.633$ μm the surface roughness parameters are $\tau/\lambda = 4.69$ and $\sigma_h/\lambda = 1.86$, and the refractive index $n = 1.411$. For comparison purposes, the experimental data presented in Figures 4.22 and 4.23 have been normalized to provide the best fit with the numerical results for normal incidence. It should be pointed out that the data have been converted via Snell's refraction law, assuming refraction at a plane face, to represent transmission *within* the medium.

The scattering cross-sections of both p and s incident polarizations in Figures 4.22 and 4.23 are virtually identical. The vertical dashed line in each graph represents the direction of specular transmission in the absence of surface roughness, i.e., Snell's refraction angle at a plane dielectric interface. Introducing slight roughness to a flat dielectric surface, one would expect the transmitted light to be concentrated around the refraction angle. However, for the roughness parameters of diffuser #39 an interesting effect is observed [61]. The peak transmission actually occurs closer to the 'straight-through' direction than the refraction angle. The surface roughness has the effect of making the light ignore the change in refractive index as it enters the dielectric medium.

An explanation of this observed effect may be found from the following discussion. As the incidence angle is increased, the local angle of incidence at each point on the surface will either increase or decrease according to the direction of the local slope. For nearly transparent media, the scattering mechanisms are dominated by single interactions. As a consequence, the contributions to the transmitted light from slopes whose local incidence angle is increasing will be reduced, since they will be less strongly illuminated. The transmitted light will therefore consist mainly of singly scattered light paths with low local incidence angles. These paths will experience
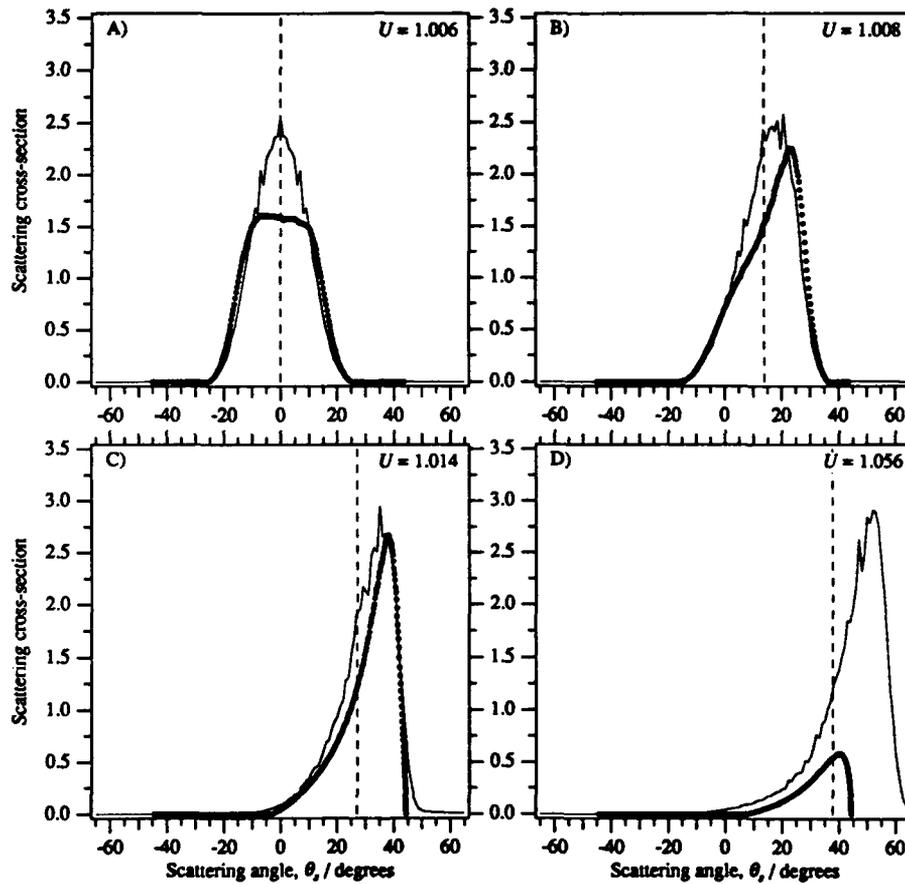
Figure 4.22: Comparisons between experimentally measured [o] and theoretically predicted [——] scattering cross-sections in transmission. Measurements: dielectric diffuser #39; calculations: perfect dielectric. $\tau/\lambda = 4.69$ and $\sigma_h/\lambda = 1.86$; $N = 2 \times 200$ realizations; surface length $L = 40\lambda$; sampling interval $\Delta \approx \lambda/10$; refractive index $n = 1.411$; wavelength $\lambda = 0.633 \ \mu m$. $\Xi_{pp}^{tr}(\theta_i, \theta_s)$: A) $\theta_i = 0°$, B) $\theta_i = -20°$, C) $\theta_i = -40°$, D) $\theta_i = -60°$.
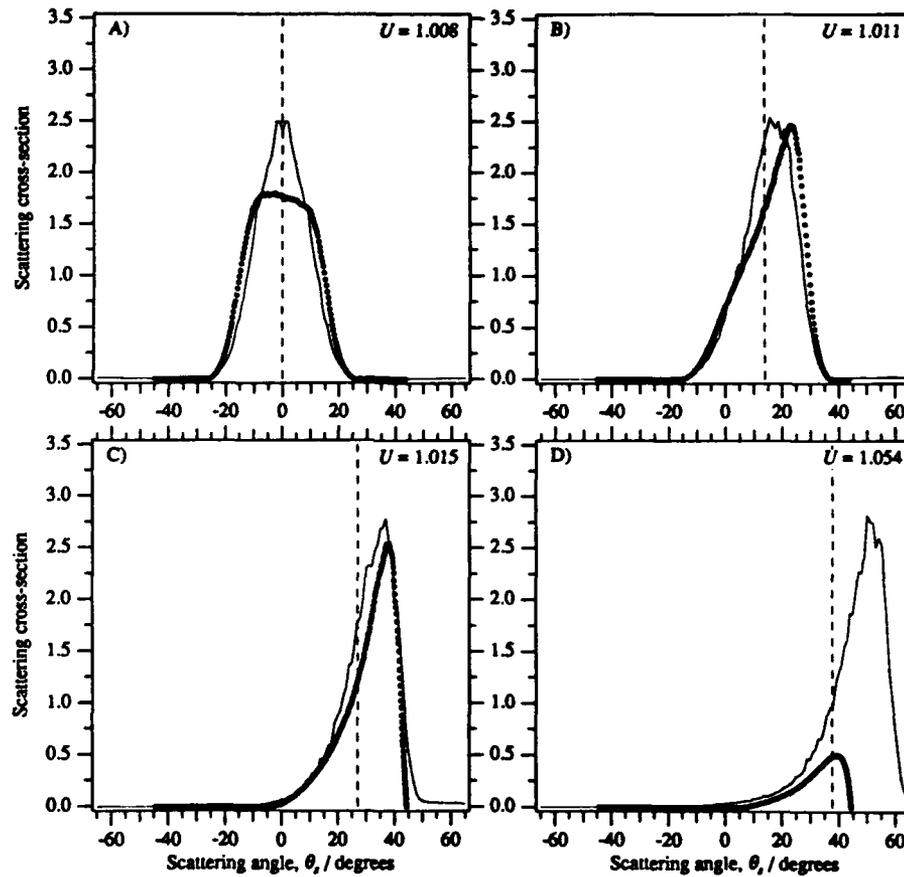
Figure 4.23: Comparisons between experimentally measured [o] and theoretically predicted [——] scattering cross-sections in transmission. Measurements: dielectric diffuser #39; calculations: perfect dielectric. $\tau/\lambda = 4.69$ and $\sigma_h/\lambda = 1.86$; $N = 2 \times 200$ realizations; surface length $L = 40\lambda$; sampling interval $\Delta \approx \lambda/10$; refractive index $n = 1.411$; wavelength $\lambda = 0.633 \ \mu m$. $\Xi_{ss}^{tr}(\theta_i,\theta_s)$: A) $\theta_i = 0°$, B) $\theta_i = -20°$, C) $\theta_i = -40°$, D) $\theta_i = -60°$.

little refraction away from the direction of the incident beam for a moderate index of refraction. If we increase the refractive index in the simulation, we would therefore expect the light to be more diffusely scattered in transmission because of stronger refraction. This is indeed the case as the results in Figure 4.24 show when the refractive index is increased to $n = \sqrt{10.0}$. The transmission scattering cross-section
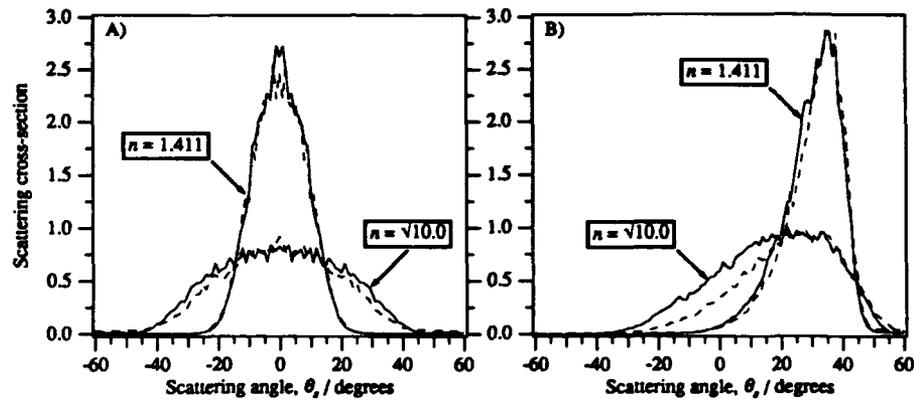
Figure 4.24: Numerically calculated scattering cross-sections for p [——] and s [- - -] incident polarizations in transmission. $\tau/\lambda = 5.02$ and $\sigma_h/\lambda = 1.93$; $N = 2 \times 200$ realizations; surface length $L = 40\lambda$; sampling interval $\Delta \approx \lambda/10$; the refractive index has been artificially increased from $n = 1.411$ to $n = \sqrt{10.0}$; wavelength $\lambda = 0.633 \ \mu m$. $\Xi^{tr}(\theta_i, \theta_s)$: A) $\theta_i = 0°$, B) $\theta_i = -40°$.

is no longer predominantly peaked in one direction. From the studies presented in § 6.2.2 it is shown that single scattering is still the dominant mechanism despite the increase in reflectivity.

The experimental measurements in Figures 4.22 and 4.23, although supporting the theoretical findings, do require a certain amount of comment. It was originally thought that the rather flat-topped appearance of the measurements for normal incidence were somehow due to misalignment of the diffuser and/or the illuminating beam [61, page 1262]. However, subsequent studies of simulated light scattering have suggested that these measurements are actually correct, but are obtained from a diffuser with different roughness parameters [refer to § 6.2.2].

Although the diffuser was very carefully prepared for these transmission experiments, its back face inevitably contained the small curvatures of the original meniscus,

but did appear flat to the eye. This would potentially affect the measured scattering cross-sections, although the comparisons are still quite good. The abrupt cut-off seen in Figures 4.22c and 4.23d at $\theta_t \approx 45°$ is due to total-internal-reflection at the diffuser's back face; the detectable light falls within a cone defined by the angle $|\theta| \leq \arcsin(1/1.411) \approx 45.1°$. Although the majority of the transmitted light for $-60°$ incidence is internally reflected, the overlapping measured and calculated values are reasonably comparable.

4.6   Experimental synopsis

The figures which follow form the main content of the experimentally determined scattering cross-sections presented in this dissertation. Figures 4.25 – 4.26 represent the scattering of light by a highly reflective diffuser (gold-coated diffuser #46) for incidence angles $\theta_i = 0° \rightarrow -60°$, over the wavelength range $\lambda = 0.633 - 10.6~\mu m$; both Ξ_{pp} and Ξ_{ss} cross-sections are presented. The data have been normalized assuming 100% reflectivity of the gold coating. Other than the comments on various effects observed in earlier sections, the presence of a specular component appearing in the $\Xi_{ss}(-60°, \theta_s)$ measurement for the wavelength $\lambda = 3.39~\mu m$ [Figure 4.26c] is brought to the reader's attention. At this wavelength the surface roughness parameters have the values $\tau/\lambda = 0.937$ and $\sigma_h/\lambda = 0.361$. The specular components in the measurements for the wavelength $\lambda = 10.6~\mu m$ have been omitted.

Figures 4.27 – 4.28 represent the scattering of light in reflection by an identical, transparent diffuser (dielectric diffuser #46) for incidence angles $\theta_i = 0° \rightarrow -60°$, over the wavelength range $\lambda = 0.633 - 10.6~\mu m$; both Ξ_{pp} and Ξ_{ss} cross-sections are presented. The data have not been normalized in an absolute sense, but the measurements for each individual wavelength are relatively comparable. Specular components are again present in the $\Xi(-60°, \theta_s)$ measurements for the wavelength $\lambda = 3.39~\mu m$ [Figure 4.28c], but this time for both incident polarizations. The specular components in the measurements for the wavelength $\lambda = 10.6~\mu m$ have been omitted.

$$\lambda = 0.633 \ \mu m \qquad\qquad \lambda = 1.15 \ \mu m$$
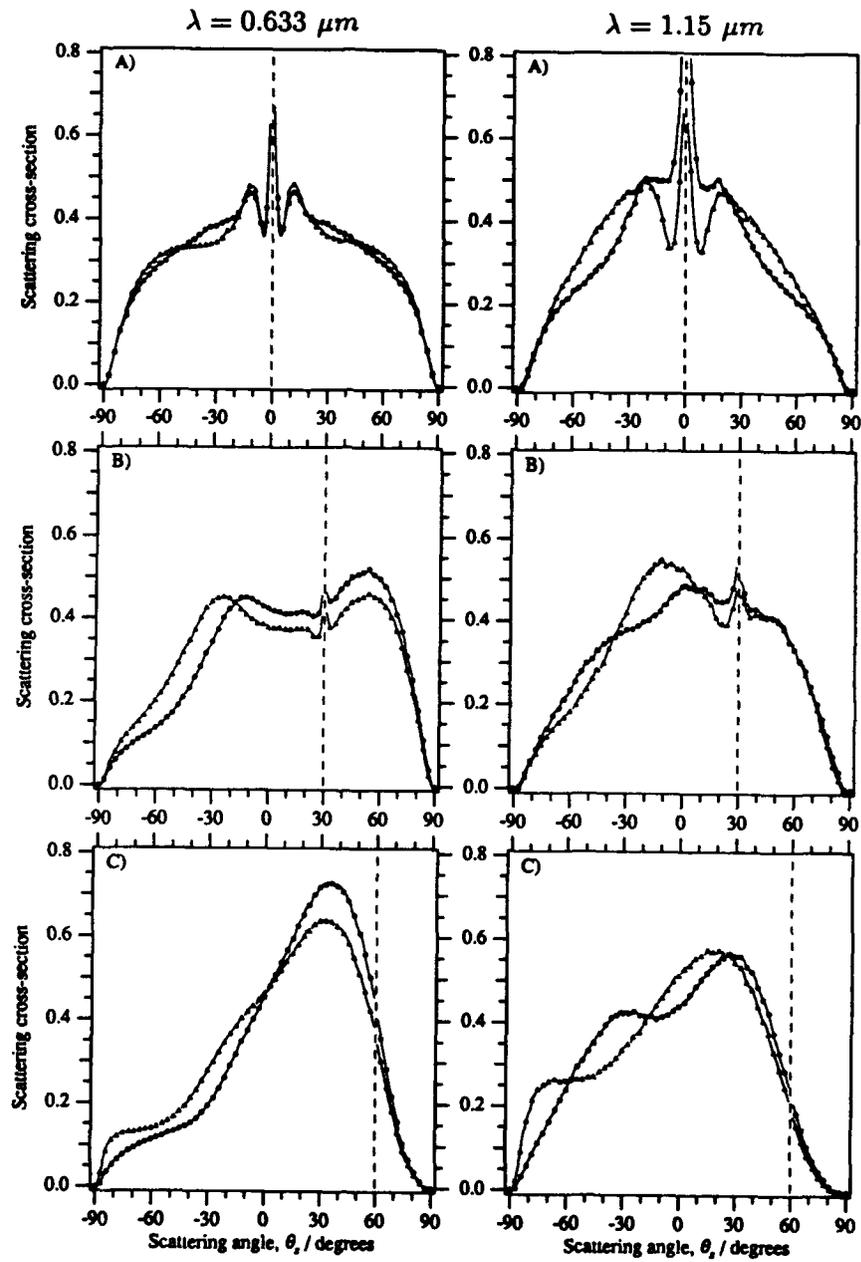
Figure 4.25: Experimental scattering cross-sections measured from gold-coated diffuser #46 for the indicated wavelengths. $\tau = 3.18 \ \mu m$ and $\sigma_h = 1.22 \ \mu m$. $\Xi_{pp}(\theta_i, \theta_s)$ [o]; $\Xi_{ss}(\theta_i, \theta_s)$ [$\triangle$]: A) $\theta_i = 0°$, B) $\theta_i = -30°$, C) $\theta_i = -60°$.

$$\lambda = 3.39 \ \mu m \qquad \qquad \lambda = 10.6 \ \mu m$$
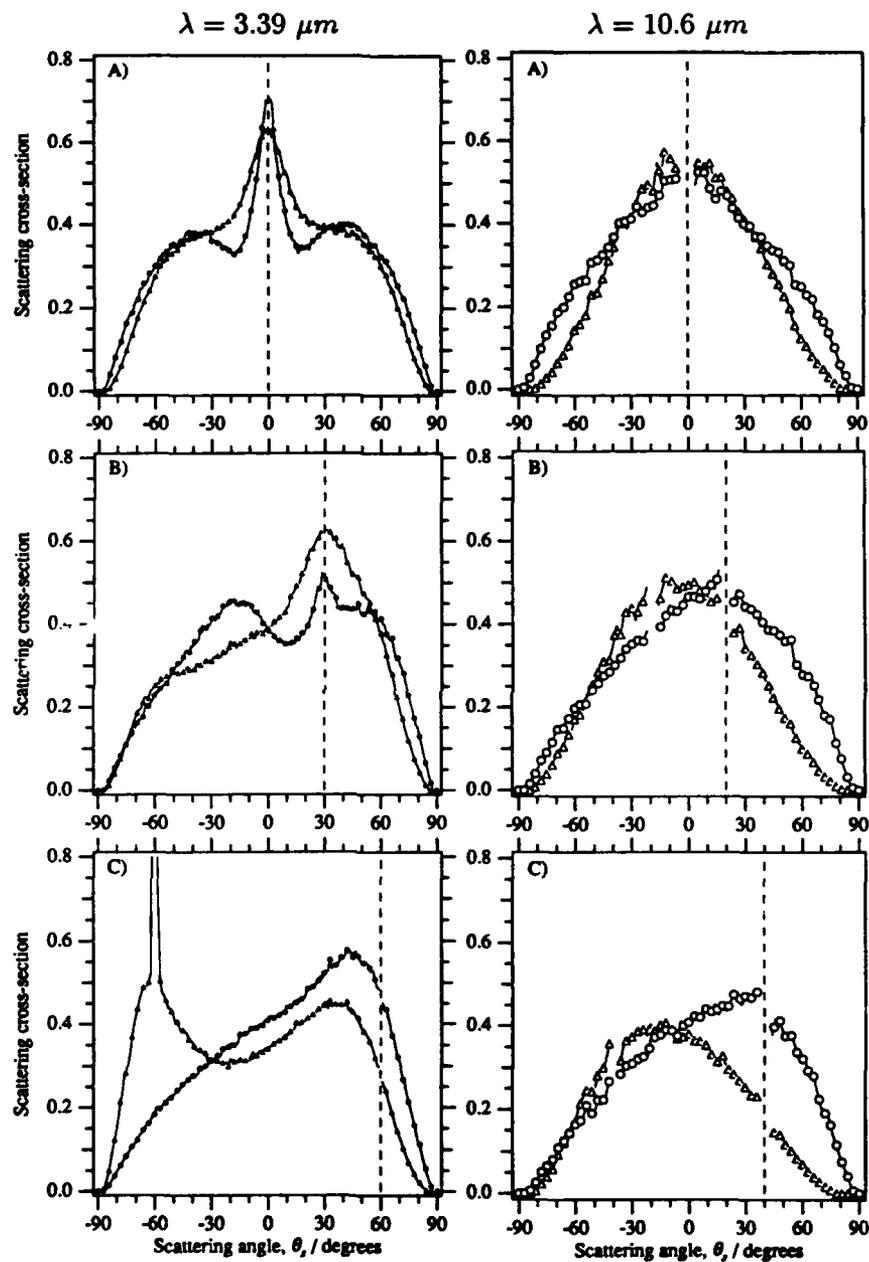
Figure 4.26: Experimental scattering cross-sections measured from gold-coated diffuser #46 for the indicated wavelengths. $\tau = 3.18 \ \mu m$ and $\sigma_h = 1.22 \ \mu m$. $\Xi_{pp}(\theta_i, \theta_s)$ [o]; $\Xi_{ss}(\theta_i, \theta_s)$ [▲]. Wavelength $\lambda = 3.39 \ \mu m$: A) $\theta_i = 0°$, B) $\theta_i = -30°$, C) $\theta_i = -60°$. Wavelength $\lambda = 10.6 \ \mu m$: A) $\theta_i = 0°$, B) $\theta_i = -20°$, C) $\theta_i = -40°$.

$$\lambda = 0.633 \ \mu m \qquad\qquad \lambda = 1.15 \ \mu m$$
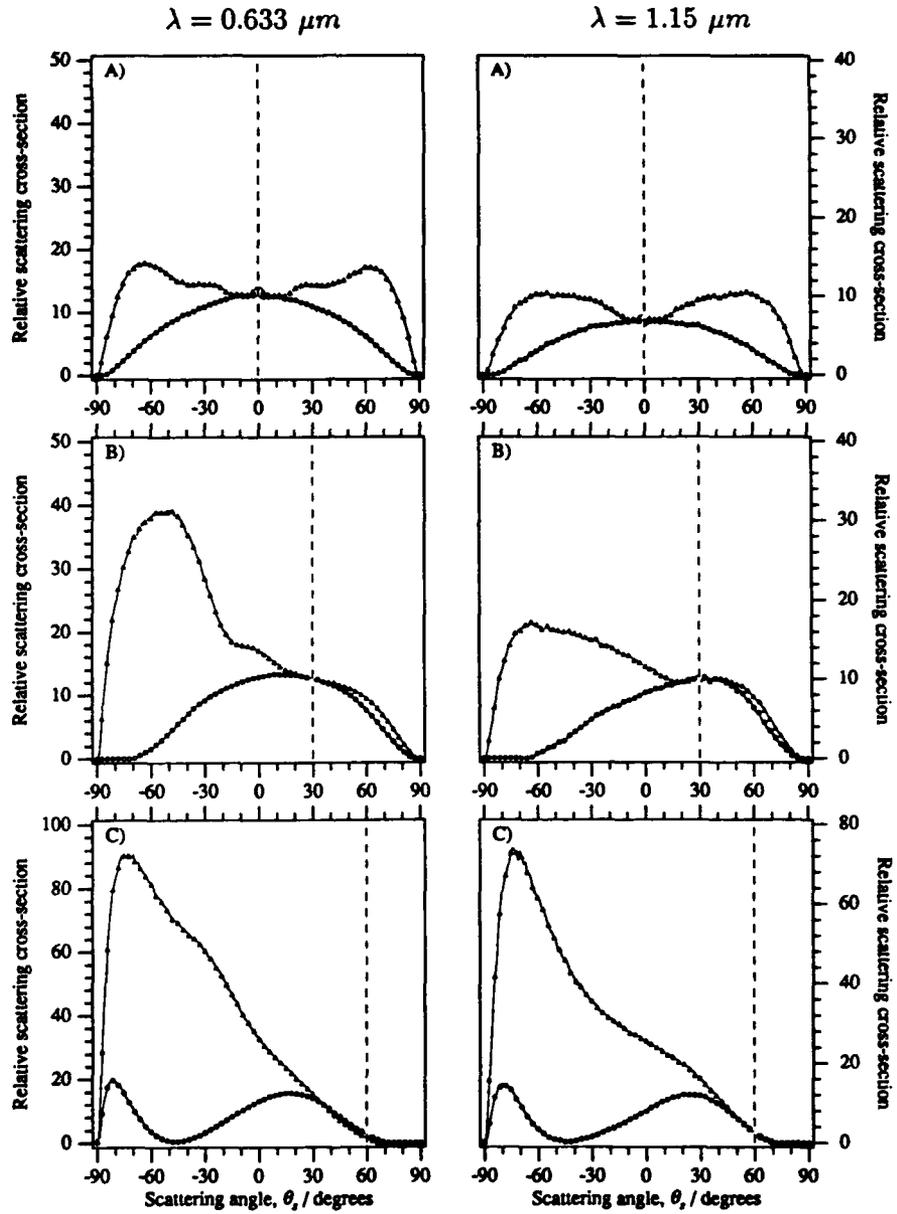
Figure 4.27: Experimental scattering cross-sections measured from dielectric diffuser #46 for the indicated wavelengths. $\tau = 3.18 \ \mu m$ and $\sigma_h = 1.22 \ \mu m$. $\Xi_{pp}^{re}(\theta_i, \theta_s)$ [o]; $\Xi_{ss}^{re}(\theta_i, \theta_s)$ [▲]: A) $\theta_i = 0°$, B) $\theta_i = -30°$, C) $\theta_i = -60°$.

$$\lambda = 3.39 \ \mu m \qquad \lambda = 10.6 \ \mu m$$
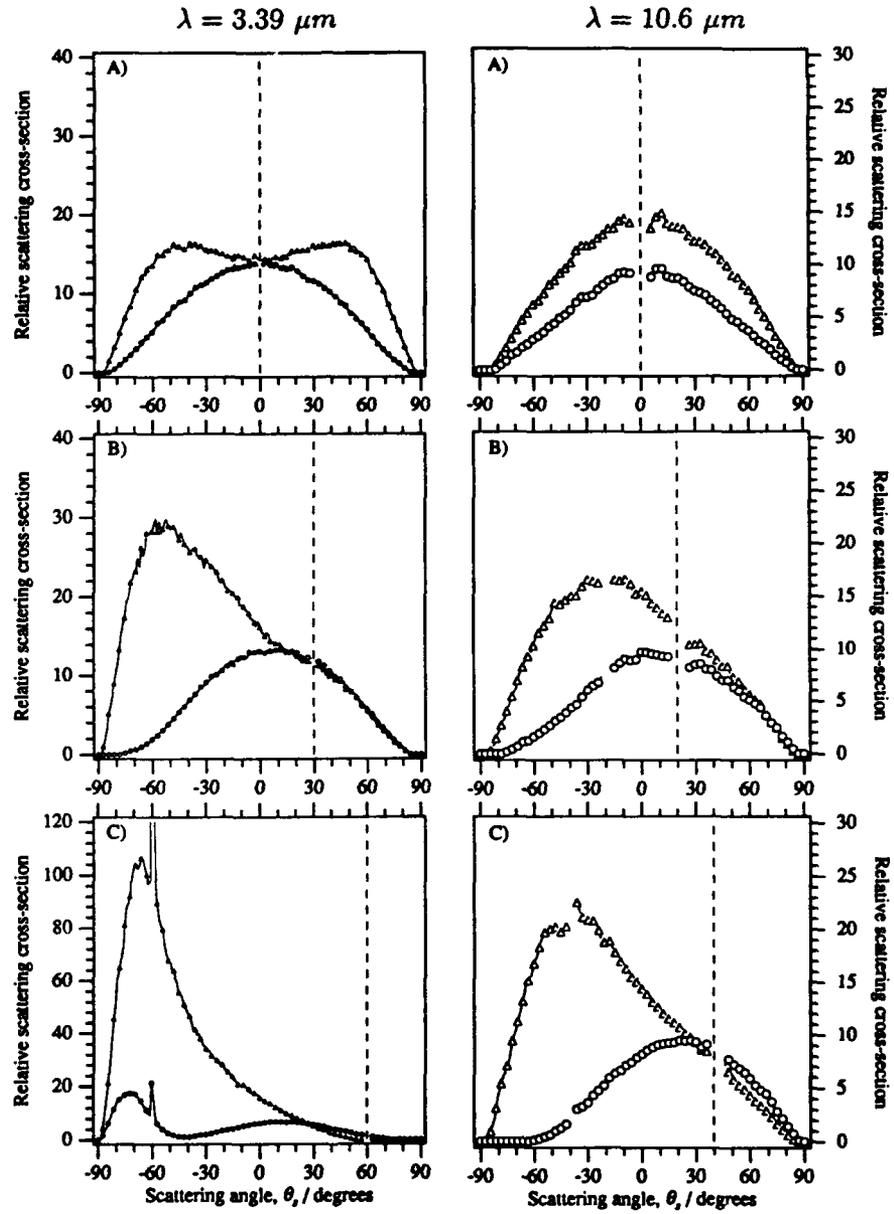
Figure 4.28: Experimental scattering cross-sections measured from dielectric diffuser #46 for the indicated wavelengths. $\tau = 3.18 \ \mu m$ and $\sigma_h = 1.22 \ \mu m$. $\Xi_{pp}^{rc}(\theta_i, \theta_s)$ [o]; $\Xi_{ss}^{rc}(\theta_i, \theta_s)$ [$\triangle$]. Wavelength $\lambda = 3.39 \ \mu m$: A) $\theta_i = 0°$, B) $\theta_i = -30°$, C) $\theta_i = -60°$. Wavelength $\lambda = 10.6 \ \mu m$: A) $\theta_i = 0°$, B) $\theta_i = -20°$, C) $\theta_i = -40°$.

Chapter 5

An Analytic Approach to Electromagnetic Scattering

5.1 Introduction

The discussion in Chapter 4 led to an exact solution for the far-zone light fields scattered from a known surface profile $h = h(x)$, expressed as an integral equation. Discretization of the profile allowed the integral to be approximated by a set of matrix equations summed over the points describing the profile. Due to its limited length, numerically calculated results for a particular profile are subject to a large degree of speckle-noise. The signal-to-noise ratio can be increased by running many calculations on independent, yet statistically identical, random profiles and taking their average. Such an approach is described as being a *Monte-Carlo* simulation, expressing the final solution as the mean of a large number of independent realizations.

The problem addressed in this chapter is that of finding an analytic solution for the far-zone light field scattered by a rough surface of known statistics. That is, the solution is analytic in so far as only the statistics of the surface profile are required, not the form of the profile itself. Numerical evaluation of the analytic solution therefore requires only one 'realization'.

One branch of electromagnetic theory which describes the interaction of electric and magnetic fields with media, in a well-formulated way, is that of *transmission line* propagation. The conversion of Maxwell's field equations with appropriate boundary conditions into so-called *Telegraphist's Equations* is discussed in detail by Schelkunoff [71] for a number of illustrative examples. This conversion makes it possible to apply the well-documented techniques of treating transmission lines [24] to aid

the solution of one-dimensional field problems with complicated boundary conditions. The transmission line approach to the problem of rough surface scattering has been addressed by R. E. Collin and is discussed in detail in this chapter.

5.2   Formulation of the problem

Consider two parallel, semi-infinite, dielectric slabs separated by a vacuum. The field in and between the slabs, generated by a suitable source, can be expressed in terms of transverse electric and magnetic modes which satisfy certain boundary conditions at the dielectric interfaces. If a pure TE or TM mode is launched along this leaky waveguide then the field at any point can be described in terms of this mode. Now, consider that a small but discont..uous change in the waveguide's cross-section is introduced at some point. The effect of this discontinuity on a wave in one mode is to generate waves in other modes propagating in opposite directions from the discontinuity. Describing a continuously varying cross-section as a set of short, constant cross-sections, a fluctuating boundary therefore represents the continuous coupling of modes along the waveguide. At the limit of one dielectric slab being moved to infinity, the problem becomes that of a source above a dielectric half-space; by describing the dielectric interface as a random function, the problem of light scattering from randomly rough surfaces can be formulated.

5.2.1   TM (p) polarization eigenfunction spectrum

Consider a magnetic line source $\mathbf{J}_m = J_m \hat{z}$ generating a magnetic field $\mathbf{H} = H\hat{z}$ above a flat, dielectric half-space as illustrated in Figure 5.1. From the discussion of TM waves in § 4.3.2, Maxwell's equations

$$\frac{1}{\varepsilon_r(y)}\nabla \times \mathbf{H} = -i\omega\varepsilon_0 \mathbf{E} \tag{5.1a}$$

$$\nabla \times \mathbf{E} = i\omega\mu_r\mu_0 \mathbf{H} - \mathbf{J}_m \tag{5.1b}$$

are subject to the boundary conditions

$$H^+ = H^- \tag{5.2a}$$

$$\frac{\partial H^+}{\partial y} = \frac{1}{\kappa}\frac{\partial H^-}{\partial y} \tag{5.2b}$$
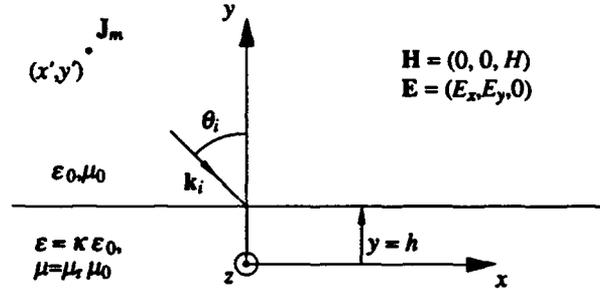
Figure 5.1: Magnetic line source above a flat, dielectric half-space. The parameters κ and μ_r are the relative permittivity and permeability of the medium, respectively.

at the interface $y = h$. The symbols + and − denote evaluation above and below the interface respectively. The magnetic line current $J_m = I_m \, \delta(x - x')\delta(y - y')$, where $\delta(u)$ is a Dirac delta function situated at $u = 0$. Eliminating the electric field from equations (5.1a) and (5.1b), using the identity $\nabla \times (\phi \mathbf{a}) = \phi \nabla \times \mathbf{a} + \nabla \phi \times \mathbf{a}$, we can show that

$$\frac{\partial^2 H}{\partial x^2} + \varepsilon_r(y)\frac{\partial}{\partial y}\left(\frac{1}{\varepsilon_r(y)}\frac{\partial H}{\partial y}\right) + \mu_r\varepsilon_r(y)k_0^2 H = -i\omega\varepsilon_r(y)\varepsilon_0 I_m \, \delta(x - x')\delta(y - y')$$

From the brief discussion in Appendix B (§ A.2.1), we can construct a Green's function $G = G(x, y)$ which satisfies the inhomogeneous equation

$$\frac{\partial^2 G}{\partial x^2} + \varepsilon_r(y)\frac{\partial}{\partial y}\left(\frac{1}{\varepsilon_r(y)}\frac{\partial G}{\partial y}\right) + \mu_r\varepsilon_r(y)k_0^2 G = -\varepsilon_r(y)\,\delta(x - x')\delta(y - y') \qquad (5.3)$$

where G satisfies the same continuity conditions (5.2a,b) as H.

It is possible to synthesize a two-dimensional Green's function from two associated one-dimensional Green's functions. Let us assume that we have two Green's functions $G_x(x)$ and $G_y(y)$ which satisfy the equations

$$\frac{\partial^2 G_x}{\partial x^2} + \lambda_x G_x = -\delta(x - x')$$

and

$$\varepsilon_r(y)\frac{\partial}{\partial y}\left(\frac{1}{\varepsilon_r(y)}\frac{\partial G_y}{\partial y}\right) + \left(\mu_r\varepsilon_r(y)k_0^2 + \lambda_y\right)G_y = -\varepsilon_r(y)\,\delta(y - y') \qquad (5.4)$$

where the separation parameters λ_x and λ_y are complex. We can combine $G_x(x)$ with $G_y(y)$ to give $G(x, y)$ by the relation

$$G(x, y) = \frac{1}{2\pi i}\oint_C G_x(x; \lambda_x = -\lambda_y)G_y(y; \lambda_y)\,d\lambda_y \qquad (5.5)$$

where C is a contour in the complex λ_y plane, enclosing all singularities of G_y and excluding those of G_x. Substituting for $G(x,y)$ in equation (5.3) we find the result that

$$\frac{1}{2\pi i} \oint_C G_y(y; \lambda_y) \, d\lambda_y = \epsilon_r(y) \, \delta(y - y') \tag{5.6}$$

which will form the basis of our eigenfunction expansion of the transverse Green's function $G_y(y)$.

Away from the source at $x = x'$, G_x satisfies the homogeneous equation

$$\frac{\partial^2 G_x}{\partial x^2} + \lambda_x G_x = 0$$

which has the general solution

$$G_x(x) = C \, e^{i\sqrt{\lambda_x}|x-x'|}$$

describing wave propagation parallel to the flat dielectric slab and outward from the source. In Appendix B, a brief discussion of the Stürm-Liouville equation leads to condition (A.16) which the Green's function must satisfy at the source. Applying this condition to G_x, the proportionality constant C is determined with the result that

$$G_x(x) = \frac{-1}{2i\sqrt{\lambda_x}} e^{i\sqrt{\lambda_x}|x-x'|}$$

which has a branch point at $\lambda_x = 0$. Assuming that the source is in the vacuum ($y' > h$), the transverse Green's function G_y above the interface [$y > h$, $\epsilon_r(y) = 1$, $\mu_r(y) = 1$] has the general solution

$$G_y(y) = C_1 \, e^{ik_{y0}|y-y'|} + C_2 \, e^{ik_{y0}(y-h)} \tag{5.7}$$

where C_1 and C_2 are constants and $k_{y0}^2 = k_0^2 + \lambda_y$. The first term in equation (5.7) represents the source contribution and the second term represents plane-wave reflection from the surface. Below the surface [$y < h$, $\epsilon_r(y) = \kappa$, $\mu_r(y) = \mu_r$] $G_y(y)$ can be shown to have the general solution

$$G_y(y) = C_3 \, e^{-ik_{y1}(y-h)}$$

where $k_{y1}^2 = \mu_r \kappa k_0^2 + \lambda_y$, and represents transmission into the dielectric slab. Applying the continuity conditions at the boundary and condition (A.16) at the source, the

transverse Green's function is found to be

$$G_y(y) = \begin{cases} -\dfrac{1}{2ik_{y0}}e^{ik_{y0}|y-y'|} - \dfrac{R}{2ik_{y0}}e^{-ik_{y0}2h}e^{ik_{y0}(y+y')} & y \geq h \\[4mm] -\dfrac{(1+R)}{2ik_{y0}}e^{ik_{y0}(y'-h)}e^{-ik_{y1}(y-h)} & y \leq h \end{cases} \quad (5.8)$$

where the reflection coefficient

$$R = \frac{\kappa k_{y0} - k_{y1}}{\kappa k_{y0} + k_{y1}}$$

In the complex λ_y plane, G_y has a simple pole from the reflection coefficient when $\kappa k_{y0} + k_{y1} = 0$ which corresponds to a surface-wave mode. G_y also has branch points at $\lambda_y = -k_0^2$ and $\lambda_y = -\mu_r\kappa k_0^2$, i.e. points in the complex plane which can not be enclosed by a contour if λ_y is to remain single-valued on that contour. Introducing branch cuts from these points which can not be crossed by a contour, λ_y is forced to be single-valued along any contour in the plane. Away from its singularities we require G_y to be analytic in the far-zone, i.e. as $|y| \to \infty$. Thus we choose the branch of our complex plane such that $\Im m[k_{y0}, k_{y1}] > 0$, i.e. $\exp(ik_{y0}[y + y']) \to 0$ as $y \to +\infty$ and $\exp(-ik_{y1}[y - h]) \to 0$ as $y \to -\infty$; introducing the branch cuts illustrated in Figure 5.2 ensures that this condition is satisfied. From the Cauchy integral formula
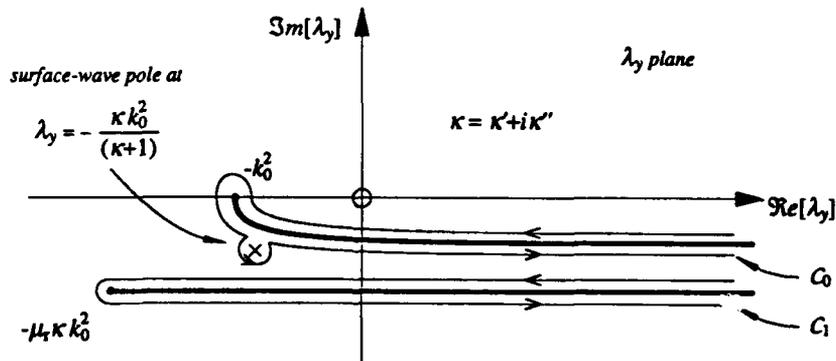
Figure 5.2: Eigenfunction expansion of the transverse Green's function G_y by contour integration. Allowing for small losses in the dielectric medium $\kappa = \kappa' + i\kappa''$. The contour C encloses all singularities of $G_y(y; \lambda_y)$ and is equivalent to $C_0 + C_1$ around each branch cut and the surface-wave pole.

the closed contour C in equation (5.6) is equivalent to the contour $C_0 + C_1$ around the

branch cuts in Figure 5.2. The phases φ of the complex values $k_{y0} = \sqrt{k_0^2 + \lambda_y}$ and $k_{y1} = \sqrt{\mu_r \kappa k_0^2 + \lambda_y}$ are limited to the range $0 \le \varphi \le \pi$ (the square-root halves the phase of the exponent's argument) along both contours, and so the imaginary term is always positive, i.e. $\sin(\varphi) \ge 0$.

Considering only the contribution from contour $\mathcal{C}_0$ (ignoring the surface-wave pole) we can show, by a change of variables, that

$$\frac{1}{2\pi i} \int_{\mathcal{C}_0} G_y \, d\lambda_y = \frac{1}{2\pi i} \int_{-\infty}^{\infty} G_y 2 k_{y0} \, dk_{y0} = \varepsilon_r(y) \, \delta(y - y')$$

Along the lower side of $\mathcal{C}_0$, k_{y0} becomes negative and so the integral can be transformed as follows:

$$
\begin{aligned}
\int_{-\infty}^{\infty} G_y(k_{y0}) k_{y0} dk_{y0} &= \int_0^{\infty} G_y(-k_{y0}') k_{y0}' dk_{y0}' + \int_0^{\infty} G_y(k_{y0}) k_{y0} dk_{y0} \\
&= \int_0^{\infty} [G_y(k_{y0}) - G_y(-k_{y0})] \, k_{y0} dk_{y0}
\end{aligned}
$$

and the magnitude sign in G_y can then be dropped. Substituting for G_y from equation (5.8), after a small amount of algebra we obtain the symmetrical expression for $y \ge h$

$$
\begin{aligned}
\frac{1}{2\pi} \int_0^{\infty} &\left[\frac{1}{\sqrt{R}} e^{-ik_{y0}(y-h)} + \sqrt{R} \, e^{ik_{y0}(y-h)} \right] \times \\
&\times \left[\frac{1}{\sqrt{R}} e^{-ik_{y0}(y'-h)} + \sqrt{R} \, e^{ik_{y0}(y'-h)} \right] dk_{y0} = \varepsilon_r(y) \, \delta(y - y')
\end{aligned}
$$

over the range $k_{y0} \ge 0$, and similarly

$$
\begin{aligned}
\frac{1}{2\pi} \int_0^{\infty} &\left[\frac{1}{\sqrt{R}} + \sqrt{R} \right] e^{-ik_{y1}(y-h)} \times \\
&\times \left[\frac{1}{\sqrt{R}} e^{-ik_{y0}(y'-h)} + \sqrt{R} \, e^{ik_{y0}(y'-h)} \right] dk_{y0} = \varepsilon_r(y) \, \delta(y - y')
\end{aligned}
$$

for $y \le h$. From these equations we can recognize the eigenfunction identity

$$\int_0^{\infty} \psi_0(k_{y0}, y) \psi_0(k_{y0}, y') \, dk_{y0} = \varepsilon_r(y) \, \delta(y - y')$$

The normalized eigenfunctions can be identified as being

$$\psi_0(k_{y0}, y) = \frac{1}{\sqrt{2\pi}} \begin{cases} \dfrac{1}{\sqrt{R}} e^{-ik_{y0}(y-h)} + \sqrt{R} \, e^{ik_{y0}(y-h)} & y \ge h \\[3mm] \left[\dfrac{1}{\sqrt{R}} + \sqrt{R} \right] e^{-ik_{y1}(y-h)} & y \le h \end{cases} \tag{5.9}$$

for $k_{y0} \geq 0$, and can also be shown to satisfy the orthogonality relationship

$$\int_{-\infty}^{\infty} \psi_0(k_{y0}, y)\psi_0(k'_{y0}, y)\frac{1}{\varepsilon_r(y)}\, dy = \delta(k_{y0} - k'_{y0}) \tag{5.10}$$

The eigenfunction set $\psi_0(k_{y0}, y > h)$ represents the *radiation-waves* which can propagate to the far-zone above the surface. Below the surface the eigenfunction $\psi_0(k_{y0}, y < h)$ can propagate to the transmission far-zone in a non-absorbing dielectric medium.

Considering the contribution from contour $\mathcal{C}_1$ we can show that

$$\frac{1}{2\pi i} \int_{\mathcal{C}_1} G_y\, d\lambda_y = \frac{1}{2\pi i} \int_{-\infty}^{\infty} G_y 2k_{y1}\, dk_{y1} = \varepsilon_r(y)\, \delta(y - y')$$

Along contour $\mathcal{C}_1$, k_{y0} does not change sign but k_{y1} becomes negative along the lower side; transforming the integral as before:

$$\int_{-\infty}^{\infty} G_y(k_{y1})k_{y1}\, dk_{y1} = \int_0^{\infty} [G_y(k_{y1}) - G_y(-k_{y1})]k_{y1}\, dk_{y1}$$

Rearranging the integrand to be symmetrical in y and y', and noting that $k_{y1}/k_{y0} = \kappa(1 - R)/(1 + R)$, we get

$$\frac{1}{2\pi} \int_0^{\infty} -\kappa\frac{(1 - R)^2}{R} e^{ik_{y0}(y-h)} e^{ik_{y0}(y'-h)}\, dk_{y1} = \varepsilon_r(y)\, \delta(y - y')$$

over the range $k_{y1} \geq 0$ for $y \geq h$, and

$$\frac{1}{2\pi} \int_0^{\infty} \kappa\frac{(1 - R)}{R} e^{ik_{y0}(y-h)} \left[R\, e^{-ik_{y1}(y-h)} - e^{ik_{y1}(y-h)} \right]\, dk_{y1} = \varepsilon_r(y)\, \delta(y - y')$$

for $y \leq h$. As before, we can see the eigenfunction identity

$$\int_0^{\infty} \psi_1(k_{y1}, y)\psi_1(k_{y1}, y')\, dk_{y1} = \varepsilon_r(y)\, \delta(y - y')$$

The normalized eigenfunctions can be identified as being

$$\psi_1(k_{y1}, y) = \frac{i\sqrt{\kappa}}{\sqrt{2\pi R}} \begin{cases} (1 - R)\, e^{ik_{y0}(y-h)} & y \geq h \\[2mm] \left[e^{ik_{y1}(y-h)} - R\, e^{-ik_{y1}(y-h)} \right] & y \leq h \end{cases} \tag{5.11}$$

for $k_{y1} \geq 0$, and can be shown to satisfy the orthogonality relationship

$$\int_{-\infty}^{\infty} \psi_1(k_{y1}, y)\psi_1(k'_{y1}, y)\frac{1}{\varepsilon_r(y)}\, dy = \delta(k_{y1} - k'_{y1}) \tag{5.12}$$

Over the contour $\mathcal{C}_1$ the phase of the complex parameter k_{y0} varies from $\pi/2$ to π as shown in Figure 5.3. Propagation above the surface $(y > h)$ only occurs for real
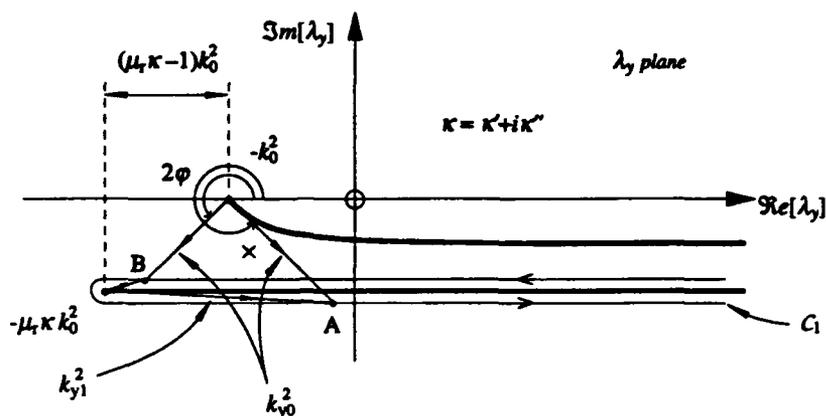
Figure 5.3: Phase φ of k_{y0} as λ_y moves along C_1: (A) $|k_{y1}| > \sqrt{\mu_r\kappa - 1}\,k_0$, $\varphi \to \pi$; (B) $|k_{y1}| < \sqrt{\mu_r\kappa - 1}\,k_0$, $\varphi \to \pi/2$.

k_{y0}, i.e. when

$$k_{y1} > \sqrt{\mu_r\kappa - 1}\,k_0$$

e.g. case (A) in Figure 5.3. However, the phase of k_{y0} leads to the exponential factor

$$e^{-i|k_{y0}|(y-h)}$$

which represents a propagating wave above but *towards* the surface, and so does not contribute to the scattered field in the far-zone above the surface. When

$$k_{y1} < \sqrt{\mu_r\kappa - 1}\,k_0$$

e.g. case (B) in Figure 5.3, the phase of k_{y0} leads to the exponential factor

$$e^{-|k_{y0}|(y-h)}$$

which represents a wave decaying with height above the surface. Below the surface, the eigenfunctions are of a similar form to the radiation-wave eigenfunctions $\psi_0(k_{y0}, y > h)$ and can propagate to the transmission far-zone if excited in a non-absorbing medium. The set of eigenfunctions ψ_1 are known as *lateral-waves* and it can be shown that they are orthogonal to the radiation-wave eigenfunctions ψ_0, i.e.

$$\int_{-\infty}^{\infty} \psi_0(k_{y0}, y)\psi_1(k_{y1}, y)\frac{1}{\varepsilon_r(y)}dy = 0 \tag{5.13}$$

The final contribution to the eigenvalue spectrum is the discrete term (residue) due to the surface-wave pole. Integration around the contour enclosing the pole at $\kappa k_{y0} + k_{y1} = 0$ leads to the expression

$$i\kappa\, e^{ik_{y0}(y-h)} e^{ik_{y0}(y'-h)} = \delta_{y,y'}$$

for $y \geq h$, and for $y \leq h$

$$i\kappa\, e^{-ik_{y1}(y-h)} e^{ik_{y0}(y'-h)} = \delta_{y,y'}$$

where $\delta_{y,y'}$ is the Kronecker delta function. We can therefore determine the eigenmodes describing the surface-wave to be

$$\psi_s(k_{y0} = -\tfrac{k_{y1}}{\kappa}, y) = \frac{(1+i)}{\sqrt{2}}\sqrt{\kappa}\begin{cases} e^{ik_{y0}(y-h)} & y \geq h \\ e^{-ik_{y1}(y-h)} & y \leq h \end{cases}$$

Assuming that $\mu_r \approx 1$, the condition $\kappa k_{y0} + k_{y1} = 0$ can be rearranged to give

$$\tan(\theta_i) = \sqrt{\kappa}$$

where θ_i is the angle of incidence. Hence it is clear that *excitation of the surface-wave occurs for a TM wave incident at the Brewster angle of incidence.*

Due to our choice of branch cuts, the condition that $\Im m[k_{y0}, k_{y1}] > 0$ is imposed over the entire complex plane. At the surface-wave pole, then, the imaginary parts of k_{y0} and k_{y1} are positive and non-zero. Hence the exponential terms in the eigenmodes ψ_s can be shown to decay with distance above *and* below the surface — the wave is truly confined to the surface of the dielectric slab and does not contribute to the far-zone fields.

5.2.2   TE (s) polarization eigenfunction spectrum

Consider an electric line source $\mathbf{J}_e = J_e\hat{z}$ generating an electric field $\mathbf{E} = E\hat{z}$ above a flat, dielectric half-space as illustrated in Figure 5.4. Following the discussion of TE waves in § 4.3.1, Maxwell's equations

$$\frac{1}{\mu_r(y)}\nabla \times \mathbf{E} = i\omega\mu_0\mathbf{H} \qquad (5.14a)$$

$$\nabla \times \mathbf{H} = -i\omega\epsilon_r(y)\epsilon_0\mathbf{E} + \mathbf{J}_e \qquad (5.14b)$$
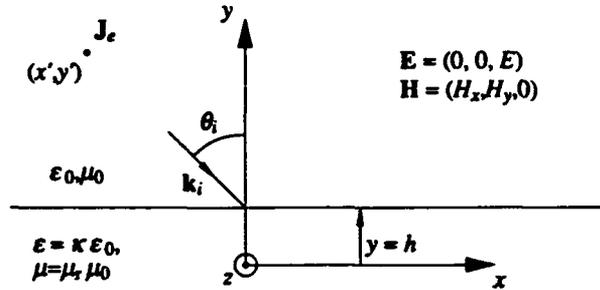
Figure 5.4: Electric line source above a flat, dielectric half-space. The parameters κ and $\mu_r(y)$ are the relative permitivitty and permeability of the medium, respectively.

are subject to the continuity conditions

$$E^+ = E^- \tag{5.15a}$$

$$\frac{\partial E^+}{\partial y} = \frac{1}{\mu_r}\frac{\partial E^-}{\partial y} \tag{5.15b}$$

at the dielectric boundary $y = h$. Eliminating the magnetic field between equations (5.14a) and (5.14b), by taking the curl of equation (5.14a), we can show that

$$\frac{\partial^2 E}{\partial x^2} + \mu_r(y)\frac{\partial}{\partial y}\left(\frac{1}{\mu_r(y)}\frac{\partial E}{\partial y}\right) + \mu_r(y)\varepsilon_r(y)k_0^2\, E = -i\omega\mu_r(y)\mu_0 I_e\, \delta(x - x')\delta(y - y')$$

where $J_e = I_e\, \delta(x - x')\delta(y - y')$. In order to find the TE eigenfunction spectrum we need to find the Green's function $G(x, y)$ which satisfies the equation

$$\frac{\partial^2 G}{\partial x^2} + \mu_r(y)\frac{\partial}{\partial y}\left(\frac{1}{\mu_r(y)}\frac{\partial G}{\partial y}\right) + \mu_r(y)\varepsilon_r(y)k_0^2\, G = -\mu_r(y)\, \delta(x - x')\delta(y - y')$$

where G satisfies the same conditions (5.15a,b) as E at the interface. Following a procedure similar to that discussed in § 5.2.1 for TM waves we can find two Green's functions $G_x(x)$ and $G_y(y)$ which satisfy equation (5.5). The transverse Green's function $G_y(y)$ can be written in terms of an eigenfunction expansion using contour integration in the complex plane. The integral along the contour enclosing the singularities of G_y is equivalent to two branch-cut integrals, yielding two sets of eigenfunctions ψ_0 and ψ_1. Essentially identical expressions for ψ_0 and ψ_1 are found for TE modes as were found for TM modes in § 5.2.1; the only exception being the expression for the

reflection coefficient

$$R_{TE} = \frac{\mu_r k_{y0} - k_{y1}}{\mu_r k_{y0} + k_{y1}} \qquad R_{TM} = \frac{\kappa k_{y0} - k_{y1}}{\kappa k_{y0} + k_{y1}}$$

For $\mu_r \approx 1$ there is no solution to $\mu_r k_{y0} + k_{y1} = 0$ and hence there is no singularity from the reflection coefficient in the complex plane. In contrast to TM incident radiation, there is therefore no equivalent Brewster angle for TE waves and no surface-wave modes are excited.

The TE eigenfunctions can be shown to satisfy the orthogonality relationships

$$\int_{-\infty}^{\infty} \psi_j(k_{yj}, y) \psi_j(k'_{yj}, y) \frac{1}{\mu_r(y)} dy = \delta(k_{yj} - k'_{yj}) \qquad j = 0, 1$$

and

$$\int_{-\infty}^{\infty} \psi_0(k_{y0}, y) \psi_1(k_{y1}, y) \frac{1}{\mu_r(y)} dy = 0$$

For brevity, the eigenfunctions derived for TM incident waves will be used, without loss of generality, for the proceeding analysis. Due to the symmetry that exists between the magnetic and electric fields in Maxwell's equations, general expressions for TM and TE waves are related via the transformations

$$I_e \rightarrow I_m \qquad I_m \rightarrow -I_e \qquad \varepsilon \leftrightarrow \mu \qquad \mathbf{E} \rightarrow \mathbf{H} \qquad \mathbf{H} \rightarrow -\mathbf{E} \qquad (5.16)$$

yielding expressions identical to those derived from first principles.

5.2.3 The primary field

When both the source and the observer are both above the interface, the primary field at the point of observation is the sum of the field due to the source itself and that of its image below the interface. From Figure 5.5 we can derive an expression for the primary field above and below a flat, dielectric interface. Assuming $r' = \sqrt{x'^2 + y'^2} \gg h$, we can employ simple geometry to show the relations

$$R_1 \approx r' + x \sin \theta_i - y \cos \theta_i$$
$$R_2 \approx r' + x \sin \theta_i + (y - 2h) \cos \theta_i$$

where θ_i is the angle of incidence. The field due to the line source and its image is given by

$$H_p(x, y) = -\frac{k_0 Y_0 I_m}{4} \left[H_0^2(k_0 R_1) + R(\theta_i) H_0^2(k_0 R_2) \right]$$
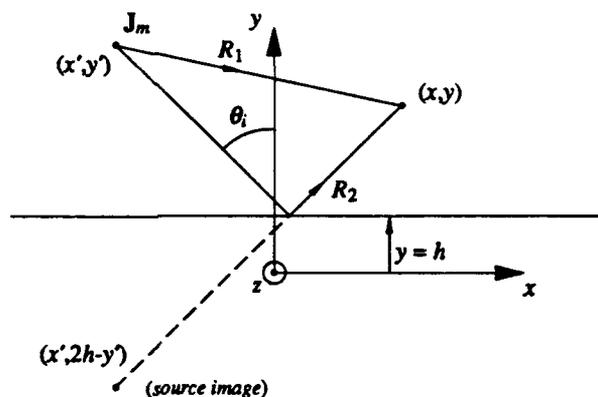
Figure 5.5: Calculation of the primary field above a flat, dielectric slab.

where $H_0^2(kr)$ is the zero-th order Hankel function of the second kind and $Y_0 = \sqrt{\varepsilon_0/\mu_0}$ is the wave admittance of free-space. In the far-zone the asymptotic value of the Hankel function is [1, eqn. 9.23]

$$\lim_{r \to \infty} H_0^2(kr) = \sqrt{\frac{2}{\pi kr}}\, e^{i(kr - \frac{\pi}{4})}$$

hence we can express the primary field above the surface $(y > h)$ as

$$H_p(x, y) = H_0 \sqrt{R(k_{y0}^i)}\, e^{i(k_x x - k_{y0} h)} \left[\sqrt{R(k_{y0}^i)}\, e^{ik_{y0}'(y-h)} + \frac{1}{\sqrt{R(k_{y0}^i)}} e^{-ik_{y0}'(y-h)} \right] \quad (5.17)$$

where $k_x = k_0 \sin \theta_i$, $k_{y0} = k_0 \cos \theta_i$ and the complex wave amplitude at the origin H_0 is

$$H_0 = -\frac{k_0 Y_0 I_m}{4} \sqrt{\frac{2}{\pi k_0 r'}} e^{i(k_0 r' - \frac{\pi}{4})} \quad (5.18)$$

By comparing equation (5.17) with equation (5.9) we can express the primary field in terms of the continuous eigenfunction spectrum $\psi_0(k_{y0}, y > h)$:

$$\lim_{r' \to \infty} H_p(x, y) = H_0 \sqrt{2\pi R(k_{y0}^i)}\, e^{i(k_x x - k_{y0} h)} \psi_0(k_{y0}^i, y) \quad (5.19)$$

This expression can also be shown to hold for an observer below the surface $(y < h)$, where the eigenfunction is then described by $\psi_0(k_{y0}, y < h)$. In this case the transverse wave-vector is $k_{y1} = \sqrt{\mu_r \kappa}\, k_0 \cos \theta_{1i}$ where the transmission angle satisfies Snell's law of refraction $\sin^2 \theta_i = \kappa \sin^2 \theta_{1i}$.

5.3   Scattering from a small step height

For a remote line source above a flat, dielectric half-space the primary field can be expressed in terms of the radiation-wave eigenfunction $\psi_0(k_{y0}^i, y)$ alone on both sides of the interface. The radiation-wave and lateral-wave eigenfunctions are orthogonal and so, in the absence of any variation of the surface profile, no lateral-waves are excited. Consequently all fields can be expressed as an expansion of the radiation-wave eigenfunctions only

$$H(x,y) = \int_0^\infty \left[a(k_{y0})e^{ik_x x} + b(k_{y0})e^{-ik_x x} \right] \psi_0(k_{y0}, y)\, dk_{y0}$$

where $a(k_{y0})$ and $b(k_{y0})$ are the forward and backward propagating amplitudes respectively.

If we introduce a small but discontinuous step of height δh at a point along the dielectric surface, the eigenfunctions ψ_0 and the amplitudes a and b will be perturbed by a small amount after the step. The perturbation may itself lead to excitation of other modes, e.g. lateral-waves. Since only radiation-waves and lateral-waves can propagate to the far-zone, we need only consider field expansions about the step in terms of these modes; see Figure 5.6. The field after the step $(x > x_s)$ may be
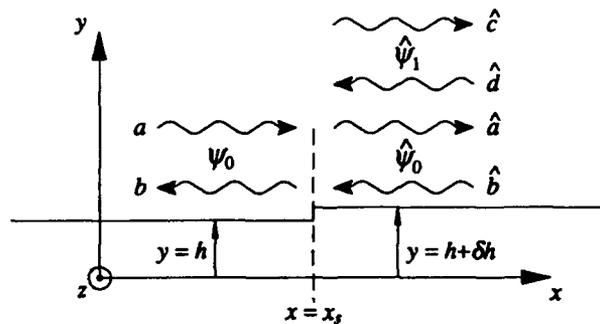
Figure 5.6: Introduction of a small step height δh to the flat, dielectric half-space.

expanded as

$$\begin{aligned} H(x,y) &= \int_0^\infty \left[\hat{a}(k_{y0})e^{ik_x x} + \hat{b}(k_{y0})e^{-ik_x x} \right] \hat{\psi}_0(k_{y0}, y)\, dk_{y0} + \\ &\quad + \int_0^\infty \left[\hat{c}(k_{y1})e^{ik_x x} + \hat{d}(k_{y1})e^{-ik_x x} \right] \hat{\psi}_1(k_{y1}, y)\, dk_{y1} \end{aligned}$$

where the perturbed parameters

$$\hat{a} = a + \delta a \qquad \hat{b} = b + \delta b \qquad \hat{c} = \delta c \qquad \hat{d} = \delta d$$

and the eigenfunctions

$$\hat{\psi}_0 = \psi_0(k_{y0}, y; h + \delta h) = \psi_0 + \delta\psi_0$$
$$\hat{\psi}_1 = \psi_1(k_{y1}, y; h + \delta h) = \psi_1 + \delta\psi_1$$

assuming a small step height $\delta h \ll h$.

The magnetic field is subject to boundary conditions (5.2a,b) at the step. Continuity of the field H (5.2a) at $x = x_s$ to first order gives us

$$\int_0^\infty \left[\delta a\, e^{ik_x x_s} + \delta b\, e^{-ik_x x_s}\right] \psi_0\, dk_{y0} = -\int_0^\infty \left[a\, e^{ik_x x_s} + b\, e^{-ik_x x_s}\right] \delta\psi_0\, dk_{y0} -$$
$$- \int_0^\infty \left[\delta c\, e^{ik_x x_s} + \delta d\, e^{-ik_x x_s}\right] \psi_1\, dk_{y1} \qquad (5.20)$$

Requiring continuity of the quantity $\varepsilon_r^{-1}(y)\partial H/\partial x$ (5.2b) at $x = x_s$, we can similarly show that

$$\int_0^\infty \left[a\, e^{ik_x x_s} - b\, e^{-ik_x x_s}\right] k_x \frac{\psi_0}{\varepsilon_r(y)}\, dk_{y0} = \int_0^\infty \left[\hat{a}\, e^{ik_x x_s} - \hat{b}\, e^{-ik_x x_s}\right] k_x \frac{\hat{\psi}_0}{\hat{\varepsilon}_r(y)}\, dk_{y0} +$$
$$+ \int_0^\infty \left[\delta c\, e^{ik_x x_s} - \delta d\, e^{-ik_x x_s}\right] k_x \frac{\psi_1}{\hat{\varepsilon}_r(y)}\, dk_{y1} \qquad (5.21)$$

Ultimately we need to obtain expressions for the perturbation amplitudes $\delta a, \delta b, \delta c$, and δd of the fields produced by the step in addition to the primary field. These extra fields will be shown to consist of two terms: one being the total scattered field due to the step, while the other exactly cancels the source-image term of the primary field.

5.3.1 The reflected field

Multiplying equation (5.20) by $\psi_0(k'_{y0}, y)/\varepsilon_r(y)$ and integrating over all y, we can invoke the orthogonality relations (5.10) and (5.13) to obtain

$$\delta a(k'_{y0})e^{ik'_x x_s} + \delta b(k'_{y0})e^{-ik'_x x_s} = -\int_0^\infty dk_{y0} \left[a\, e^{ik_x x_s} + b\, e^{-ik_x x_s}\right] \int_{-\infty}^\infty dy \frac{\delta\psi_0 \psi'_0}{\varepsilon_r(y)} \qquad (5.22)$$

where $\psi'_0 = \psi_0(k'_{y0}, y)$. Similarly from equation (5.21) we can show that

$$a(k'_{y0})e^{ik'_x x_s} - b(k'_{y0})e^{-ik'_x x_s} = \int_0^\infty dk_{y0} \frac{k_x}{k'_x} \left[\hat{a}\, e^{ik_x x_s} - \hat{b}\, e^{-ik_x x_s}\right] \int_{-\infty}^\infty dy \frac{\hat{\psi}_0 \psi'_0}{\hat{\varepsilon}_r(y)} \qquad (5.23)$$
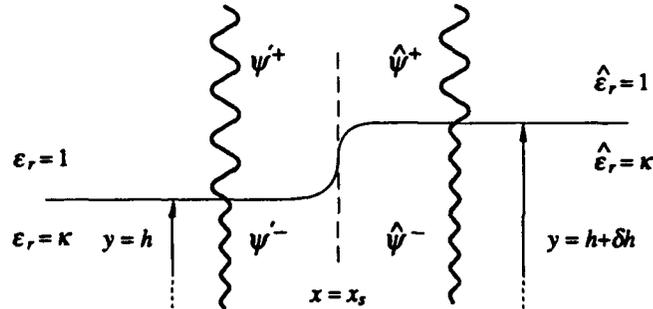
Figure 5.7: Transition of transverse eigenfunctions across a small step height.

where $\hat{\varepsilon}_r(y \leq h + \delta h) = \kappa$. With reference to Figure 5.7 the integral over y can be evaluated as follows:

$$\int_{-\infty}^{\infty} dy \frac{\hat{\psi}_0 \psi_0'}{\hat{\varepsilon}_r(y)} = \int_{-\infty}^{h} dy \frac{\hat{\psi}_0^- \psi_0'^-}{\varepsilon_r(y)} + \int_{h}^{h+\delta h} dy \frac{\hat{\psi}_0^- \psi_0'^+}{\varepsilon_r(y)} + \int_{h}^{\infty} dy \frac{\hat{\psi}_0^+ \psi_0'^+}{\varepsilon_r(y)} - \int_{h}^{h+\delta h} dy \frac{\hat{\psi}_0^+ \psi_0'^+}{\varepsilon_r(y)}$$

$$= \int_{-\infty}^{\infty} dy \frac{\hat{\psi}_0 \psi_0'}{\varepsilon_r(y)} + \int_{h}^{h+\delta h} dy \left[\frac{\hat{\psi}_0^-}{\kappa} - \hat{\psi}_0^+ \right] \psi_0'$$

To first order in δh, the last term may be approximated by

$$\int_{h}^{h+\delta h} dy[\cdots] \approx \left(\frac{1-\kappa}{\kappa} \right) \psi_i|_{y=h} \, \psi_j'|_{y=h} \, \delta h$$

where we have assumed that $\hat{\psi}_0^-\big|_h = \hat{\psi}_0^+\big|_h \approx \psi_0^-\big|_h$. Substituting for the perturbed parameters $\hat{a}$, $\hat{b}$, and $\hat{\psi}_0$ we can readily show to first order that equation (5.23) reduces to

$$\delta a(k_{y0}')e^{ik_x'x_s} - \delta b(k_{y0}')e^{-ik_x'x_s} \approx \int_0^\infty dk_{y0} \frac{k_x}{k_x'} \left[a\, e^{ik_x x_s} - b\, e^{-ik_x x_s} \right] \times$$

$$\times \left\{ \left(\frac{\kappa-1}{\kappa} \right) \psi_0|_{y=h} \, \psi_0'|_{y=h} \, \delta h - \int_{-\infty}^{\infty} dy \frac{\delta\psi_0\psi_0'}{\varepsilon_r(y)} \right\} \qquad (5.24)$$

Considering only the forward propagating waves (x increasing) we can ignore the backward amplitude b without loss of generality, and by eliminating $\delta b'$ between equations (5.22) and (5.24) we can find the perturbation amplitude $\delta\, a'$

$$2\,\delta a(k_{y0}')e^{ik_x'x_s} = \left(\frac{\kappa-1}{\kappa} \right) \int_0^\infty dk_{y0} \frac{k_x}{k_x'} a\, e^{ik_x x_s} \, \psi_0|_{y=h} \, \psi_0'|_{y=h} \, \delta h -$$

$$- \int_0^\infty dk_{y0} \left(1 + \frac{k_x}{k_x'} \right) a\, e^{ik_x x_s} C_0(k_{y0}, k_{y0}') \qquad (5.25)$$

The coupling integral C_0 is given by

$$C_0(k_{y0}, k'_{y0}) = \lim_{M \to \infty} \int_{-M}^{M} \delta\psi_0(k_{y0}, y)\psi_0(k'_{y0}, y) \frac{1}{\varepsilon_r(y)} dy \qquad (5.26)$$

where the perturbation eigenfunction

$$\delta\psi_0 = \psi_0(k_{y0}, y; h + \delta h) - \psi_0(k_{y0}, y; h)$$

and can be shown to be of the form

$$\delta\psi_0 = \frac{1}{\sqrt{2\pi}} \begin{cases} -ik_{y0}\delta h \left[\sqrt{R}\, e^{ik_{y0}(y-h)} - \frac{1}{\sqrt{R}} e^{-ik_{y0}(y-h)} \right] & y \geq h \\[2mm] ik_{y1}\delta h \left[\frac{1}{\sqrt{R}} + \sqrt{R} \right] e^{-ik_{y1}(y-h)} & y \leq h \end{cases} \qquad (5.27)$$

for a small step height $\delta h \ll h$. Substituting $\delta\psi_0$ into equation (5.26) and replacing $(y - h)$ by the new variable y, the terms evaluated at the limits $y = \pm M$ tend to zero as $M \to \infty$ if small losses are assumed. The surviving terms at the boundary $y = 0$ lead to the expression

$$C_0(k_{y0}, k'_{y0}) = \frac{\delta h}{2\pi\kappa\sqrt{RR'}} \left[\left(\frac{1 + RR'}{k_{y0} + k'_{y0}} + \frac{R + R'}{k_{y0} - k'_{y0}} \right) \kappa k_{y0} - \frac{(1 + R)(1 + R')}{k_{y1} + k'_{y1}} k_{y1} \right]$$

Using the relations

$$k_{y0}^2 + k_x^2 = k_0^2 \qquad k_{y1}^2 + k_x^2 = \mu_r\kappa k_0^2 \qquad k_{y0}^2 - k'_{y0}{}^2 = k_{y1}^2 - k'_{y1}{}^2$$

we can show, after a certain amount of algebra, that the coupling integral can be expressed by

$$\left(1 + \frac{k_x}{k'_x} \right) C_0 = \frac{2\delta h}{\pi k'_x \sqrt{RR'}} \frac{k_{y0}k'_{y0}}{(k'_x - k_x)} \frac{\left[(k_{y1}k'_{y1} - \kappa k_x^2)(\kappa - 1) - \kappa^2 k_0^2(\mu_r - 1) \right]}{(\kappa k_{y0} + k_{y1})(\kappa k'_{y0} + k'_{y1})}$$

Hence, substituting for C_0 and the eigenfunctions $\psi_0|_h$ and $\psi'_0|_h$, equation (5.25) can be rewritten as

$$\delta a(k'_{y0})e^{ik'_x x_s} = \int_0^\infty dk_{y0} a(k_{y0})e^{ik_x x_s} \frac{\delta h}{\pi k'_x \sqrt{RR'}} \frac{k_{y0}k'_{y0}}{(k'_x - k_x)} \times$$
$$\times \frac{\left[(\kappa k_x k'_x - k_{y1}k'_{y1})(\kappa - 1) + \kappa^2 k_0^2(\mu_r - 1) \right]}{(\kappa k_{y0} + k_{y1})(\kappa k'_{y0} + k'_{y1})} \qquad (5.28)$$

Expressing the primary field in equation (5.19) as an eigenfunction expansion in ψ'_0

$$H_p(x, y) = \int_0^\infty a(k'_{y0})e^{ik'_x x_s}\psi_0(k'_{y0}, y)dk'_{y0}$$

we can multiply throughout by $\psi_0(k_{y0}, y)/\varepsilon_r(y)$ and invoke the orthogonality relationship (5.10) to yield the forward propagating amplitude

$$a(k_{y0})e^{ik_x x} = H_0\sqrt{2\pi R(k_{y0}^i)}\, e^{i(k_x^i x - k_{y0}^i h)}\delta(k_{y0} - k_{y0}^i)$$

From equation (5.28) we can then show that the perturbation amplitude is given by

$$\delta a(k_{y0}')e^{ik_x' x_s} = \frac{\delta h}{\pi k_x'\sqrt{R'}}\frac{k_{y0}^i k_{y0}'}{(k_x^i - k_x')}\mathcal{K}_r\sqrt{2\pi}\,H_0 e^{i(k_x^i x_s - k_{y0}^i h)}$$

where

$$\mathcal{K}_r = \frac{\left[(k_{y1}^i k_{y1}' - \kappa k_x^i k_x')(\kappa - 1) - \kappa^2 k_0^2(\mu_r - 1)\right]}{(\kappa k_{y0}^i + k_{y1}^i)(\kappa k_{y0}' + k_{y1}')}$$

The first order, forward-propagating, radiation field scattered by the step above the surface is given by

$$H_s^r(x, y) = \int_0^\infty \delta a(k_{y0}')e^{ik_x' x}\psi_0(k_{y0}', y)\, dk_{y0}' \qquad x > x_s$$

and is in *addition* to the specular component of the primary field; there is no contribution from lateral waves above the surface. If we make the assumption that our randomly rough, dielectric surface is *gently varying* with *small slopes*, we can describe the surface as a series of small step heights such as the one we have just considered. A perturbed wave amplitude δa will be generated at each step and is assumed to propagate along x *without* further scattering. For a surface which extends from $-L$ to L, the total scattered field accumulated over all of the steps along the surface is then given by

$$\begin{aligned}H_s^r(x, y) &= \int_{-L}^L dx_s\frac{dh}{dx_s}\int_0^\infty dk_{y0}'\frac{k_{y0}^i k_{y0}'}{\pi k_x' R'}\frac{\mathcal{K}_r}{(k_x^i - k_x')}H_0 e^{i(k_x^i - k_x')x_s}e^{ik_x' x}e^{-ik_{y0}^i h} \times \\ &\quad \times \left[R'\,e^{ik_{y0}'(y-h)} + e^{-ik_{y0}'(y-h)}\right]\end{aligned}$$

where we have assumed that

$$\delta h \approx \frac{dh}{dx_s}dx_s$$

Considering only the waves propagating upwards from the surface, i.e. the term $\exp(ik_{y0}'[y - h])$, the accumulated scattered field can then be written as

$$H_s^r(x, y) = \int_{-L}^L dx_s\frac{dh}{dx_s}\int_0^\infty dk_{y0}'\frac{k_{y0}^i k_{y0}'}{\pi k_x'}\frac{\mathcal{K}_r}{(k_x^i - k_x')}H_0 e^{i(k_x^i - k_x')x_s}e^{-i(k_{y0}' + k_{y0}^i)h}e^{ik_x' x}e^{ik_{y0}' y}$$

Integrating the surface integral by parts we obtain

$$H_s^r(x,y) = \int_{-L}^{L} dx_s \int_0^\infty dk'_{y0} \frac{k_{y0}^i k'_{y0}}{\pi k'_x} \frac{\mathcal{K}_r}{(k_{y0}^i + k'_{y0})} H_0 e^{i(k_x^i - k'_x)x_s} e^{-i(k'_{y0}+k'_{y0})h} e^{ik'_x x} e^{ik'_{y0} y} -$$

$$- \int_0^\infty dk'_{y0} \frac{k_{y0}^i k'_{y0}}{\pi k'_x} \frac{\mathcal{K}_r}{(k_{y0}^i + k'_{y0})} H_0 e^{-i(k'_{y0}+k'_{y0})h_0} e^{ik'_x x} e^{ik'_{y0} y} 2 \frac{\sin([k_x^i - k'_x]L)}{(k_x^i - k'_x)} \qquad (5.29)$$

where the surface height smoothly tends to a constant value $h = h_0$ for $|x_s| \geq L$.

The last integral in equation (5.29) can be shown to have a special property for a surface of infinite extent. For large L

$$\lim_{L \to \infty} \frac{\sin([k_x^i - k'_x]L)}{(k_x^i - k'_x)} = \pi \delta(k_x^i - k'_x) \qquad (5.30)$$

and changing the integration variable using the transformation

$$dk'_{y0} = -\frac{k'_x}{k'_{y0}} dk'_x$$

the integral reduces to

$$\Rightarrow -H_0 \frac{\left[(k_{y1}^i{}^2 - \kappa k_x^i{}^2)(\kappa - 1) - \kappa^2 k_0^2(\mu_r - 1) \right]}{(\kappa k_{y0}^i + k_{y1}^i)^2} e^{ik'_{y0}(y - 2h_0)} e^{ik_x^i x}$$

Using the relation

$$k_{y1}^2 = k_{y0}^2 + (\mu_r \kappa - 1)k_0^2$$

we can show that the integral can be further reduced to give

$$\Rightarrow -\frac{(\kappa k_{y0}^i - k_{y:}^i)}{(\kappa k_{y0}^i + k_{y1}^i)} H_0 e^{ik'_{y0}(y-2h_0)} e^{ik_x^i x} \Rightarrow -R(\theta_i) H_0 e^{ik'_{y0}(y-2h_0)} e^{ik_x^i x}$$

which exactly cancels the *specularly* reflected component of the primary field [equation (5.19)]. The remaining integral in equation (5.29) therefore represents the total scattered field above the surface, given by

$$H_s^r(x,y) = \int_{-L}^{L} dx_s \int_0^\infty dk'_{y0} \frac{k_{y0}^i k'_{y0}}{\pi k'_x} \frac{\mathcal{K}_r}{(k_{y0}^i + k'_{y0})} H_0 e^{i(k_x^i - k'_x)x_s} e^{-i(k'_{y0}+k'_{y0})h} e^{ik'_x x} e^{ik'_{y0} y} \qquad (5.31)$$

If the surface is flat ($h = h_0$) and of infinite extent, the surface integral gives

$$\lim_{L \to \infty} \int_{-L}^{L} dx_s \, e^{i(k_x^i - k'_x)x_s} = 2\pi \delta(k_x^i - k'_x) \qquad (5.32)$$

which demonstrates that the specular component is recovered for a flat surface.

We wish to evaluate the scattered field H_s^r in the far-zone, i.e. for large arguments x, y. Integration over k_{y0}' in equation (5.31) can therefore be achieved by the method of steepest descents (stationary phase) which is discussed briefly in Appendix C in relation to this equation. From equation (A.18) the resulting expression for the far-zone scattered field in reflection can be shown to equal

$$H_s^r(x,y) = \int_{-L}^{L} dx_s \frac{ik_0 Y_0 I_m}{2\pi} \frac{C_i C_s \left[(C_{1i} C_{1s} \mu_r - S_i S_s)(1 - \frac{1}{\kappa}) + 1 - \mu_r \right]}{(C_i + C_s)(C_i + \sqrt{\frac{\mu_r}{\kappa}} C_{1i})(C_s + \sqrt{\frac{\mu_r}{\kappa}} C_{1s})} \times$$
$$\times \frac{e^{ik_0(r+r')}}{\sqrt{rr'}} e^{ik_0(S_i - S_s)x_s} e^{-ik_0(C_i + C_s)h(x_s)}$$

where we have substituted for H_0 from equation (5.18) and the symbols have the following identities:

$$\begin{aligned}
C_i &= \cos \theta_i & S_i &= \sin \theta_i \\
C_s &= \cos \theta_s & S_s &= \sin \theta_s \\
C_{1i} &= \cos \theta_{1i} & C_{1s} &= \cos \theta_{1s}
\end{aligned}$$

The angular directions in vacuum and dielectric are related by Snell's law of refraction

$$\sin \theta_i = \sqrt{\mu_r \kappa} \sin \theta_{1i} \qquad \sin \theta_s = \sqrt{\mu_r \kappa} \sin \theta_{1s}$$

Employing the duality relations (5.16) the far-zone TE field in reflection can be shown to equal

$$E_s^r(x,y) = \int_{-L}^{L} dx_s \frac{ik_0 I_m}{2\pi Y_0} \frac{C_i C_s \left[(C_{1i} C_{1s} \kappa - S_i S_s)(1 - \frac{1}{\mu_r}) + 1 - \kappa \right]}{(C_i + C_s)(C_i + \sqrt{\frac{\kappa}{\mu_r}} C_{1i})(C_s + \sqrt{\frac{\kappa}{\mu_r}} C_{1s})} \times$$
$$\times \frac{e^{ik_0(r+r')}}{\sqrt{rr'}} e^{ik_0(S_i - S_s)x_s} e^{-ik_0(C_i + C_s)h(x_s)}$$

5.3.2 The transmitted field

Multiplying equation (5.20) by $\psi_1(k_{y1}', y)/\varepsilon_r(y)$ and integrating over all y, we can invoke the orthogonality relations (5.12) and (5.13) to obtain

$$\delta c(k_{y1}')e^{ik_x'x_s} + \delta d(k_{y1}')e^{-ik_x'x_s} = -\int_0^{\infty} dk_{y0} \left[ae^{ik_x x_s} + be^{-ik_x x_s} \right] \int_{-\infty}^{\infty} dy \frac{\delta \psi_0 \psi_1'}{\varepsilon_r(y)} \quad (5.33)$$

where $\psi_1' = \psi_1(k_{y1}', y)$. We can similarly show from equation (5.21) that

$$\delta c(k_{y1}')e^{ik_x'x_s} - \delta d(k_{y1}')e^{-ik_x'x_s} = -\int_0^{\infty} dk_{y1} \frac{k_x}{k_x'} \left[\hat{a}e^{ik_x x_s} - \hat{b}e^{-ik_x x_s} \right] \times$$

$$\times \left\{ \left(\frac{\kappa - 1}{\kappa} \right) \psi_0|_{y=h} \; \psi_1'|_{y=h} \; \delta h - \int_{-\infty}^{\infty} dy \frac{\delta \psi_0 \psi_1'}{\hat{\epsilon}_r(y)} \right\} \tag{5.34}$$

Again considering only forward propagating waves, the amplitude $\delta d'$ can be eliminated between equations (5.33) and (5.34) to give

$$2 \, \delta c(k_{y1}') e^{ik_x' x_s} = \left(\frac{\kappa - 1}{\kappa} \right) \int_0^{\infty} dk_{y0} \frac{k_x}{k_x'} a e^{ik_x x_s} \; \psi_0|_h \; \psi_1'|_h \; \delta h -$$

$$- \int_0^{\infty} dk_{y0} \left(1 + \frac{k_x}{k_x'} \right) a e^{ik_x x_s} C_1(k_{y1}, k_{y1}') \tag{5.35}$$

The coupling integral C_1 is given by

$$C_1 = \lim_{L \to \infty} \int_{-L}^{L} \delta \psi_0(k_{y0}, y) \psi_1(k_{y1}', y) \frac{1}{\epsilon_r(y)} dy$$

Substituting for the eigenfunction perturbation $\delta \psi_0$ [equation (5.27)] and the lateral-wave eigenfunctions ψ_1 [equation (5.11)], the coupling integral can be shown to satisfy the equation

$$\left(1 + \frac{k_x}{k_x'} \right) C_1(k_{y0}, k_{y0}') = -\frac{\delta h 4 \sqrt{\kappa} k_{y0} k_{y1}' \left[(1 - \kappa)(k_{y0}' k_{y1} - k_{y0}^2) - (\mu_r \kappa - 1) k_0^2 \right]}{2 \pi i k_x' \sqrt{RR'}(k_x' - k_x)(\kappa k_{y0} + k_{y1})(\kappa k_{y0}' + k_{y1}')}$$

Hence, substituting for C_1, the eigenfunctions $\psi_0|_h$, $\psi_1'|_h$, and the primary field amplitude $a(k_{y0})$ equation (5.35) can be expressed as

$$\delta c(k_{y1}') e^{ik_x' x_s} = \frac{\delta h \sqrt{\kappa}}{i \pi k_x' \sqrt{R'}} \frac{k_{y0}^i k_{y1}'}{(k_x' - k_x^i)} \mathcal{K}_t \sqrt{2\pi} H_0 e^{i(k_x' x_s - k_{y0}^i h)}$$

where

$$\mathcal{K}_t = \frac{(1 - \kappa)(k_{y0}' k_{y1}^i + k_x^i k_x') + \kappa k_0^2 (1 - \mu_r)}{(\kappa k_{y0}^i + k_{y1}^i)(\kappa k_{y0}' + k_{y1}')}$$

The first-order, forward-propagating field scattered by the step below the surface is given by

$$H_s^t(x, y) = \int_0^{\infty} \left[\delta a(k_{y1}') \psi_0(k_{y1}', y) + \delta c(k_{y1}') \psi_1(k_{y1}', y) \right] e^{ik_x' x} dk_{y1}' \qquad x > x_s$$

and is in *addition* to the primary field. There are therefore contributions from both the radiation *and* lateral wave eigenfunctions in transmission.

Further analytical treatment of the transmission problem is complicated by the number of contributions to the far-field and is beyond the scope of the present work. However, if we were to ignore the radiation wave term involving ψ_0 and apply the

same analysis as was used for the reflection case, we arrive at the following expression for the transmitted far-zone field

$$H_s^t(x,y) = \int_{-L}^{L} dx_s \frac{ik_1 Y_0 I_m}{2\pi} \frac{C_i C_{1s} \left[1 - \mu_r - (C_{1i}C_s\sqrt{\mu_r\kappa} + S_i S_s)(1 - \frac{1}{\kappa})\right]}{(C_i - \sqrt{\mu_r\kappa}C_{1s})(C_i + \sqrt{\frac{\mu_r}{\kappa}}C_{1i})(C_s + \sqrt{\frac{\mu_r}{\kappa}}C_{1s})} \times$$
$$\times \frac{e^{i(k_1 r + k_0 r')}}{\sqrt{rr'}} e^{ik_0(S_i - S_s)x_s} e^{-ik_0(C_i - \sqrt{\mu_r\kappa}C_s)h(x_s)}$$

where $k_1 = \sqrt{\mu_r\kappa}\, k_0$. This expression is identical to that presented by Bahar applying "full-wave" analysis to the transmission problem [11, equation (2.24)] and does *not* include all possible wave contributions. Further study of this expression reveals some anomolous asymptotes whch are introduced as a result of the stationary phase evaluation. Quite clearly this expression is not an adequate solution of the transmission problem.

5.3.3 Comparison with "full-wave" theory

The expressions derived in sections 5.3.1 and 5.3.2 for the fields scattered by a randomly rough surface are identical to those presented by Bahar employing "full-wave" theory [6, equations (3.2a),(3.7a)]. Bahar's formulation ir tially involves a complete wave expansion (radiation, lateral, and surface-waves) of the transverse fields in terms of local basis functions for a flat surface. Using the orthogonal properties of these functions, Maxwell's equations are converted into a set of coupled, first-order, differential equations. These *telegraphist's equations* relate the longitudinal, propagation amplitudes via mode-coupling and source terms. The equations for the amplitudes are solved using an iterative approach. Ignoring mode-coupling, the initial solutions correspond to the primary fields; then, ignoring further source contributions, the amplitudes obtained represent first-order coupling between modes excited by the primary fields [5, page 1514]. An explicit dependence on the surface slope in the field expansion is removed using an integration by parts. The integrated term is then disregarded as being an edge-effect [4, page 366], but is actually the exact negative of the surface component from the primary field which is not considered. The misinterpretation of this term is corrected in more recent applications of the full-wave theory [11, page 1876].

Bahar has applied the basic formulation of the full-wave theory to many situations, including the two-dimensional scattering problem [7] even though use of the tele-

graphist's equations is limited to one-dimensional problems only. The transmission line approach to rough surface scattering gives a clearer, physical model of the approximations made in the content of full-wave theory, as applied to the one-dimensional scattering problem. The expressions derived for the scattered fields are physically justifiable within the confines of the assumptions made; primarily the theory is only valid for low-sloped surfaces although there is no limitation on the surface height.

In this theory, the primary field above a flat, dielectric surface is described by an incident plane wave and its specular reflection from the surface. Similarly, below the surface the primary field is described by the specularly transmitted wave. This approximation is valid while the surface profile is slowly varying; the scattered fields are then due to the scattering of these primary fields by small step heights in the surface profile.

The scattering theory so far described considers the total scattered field to be the sum of the contributions from each horizontal, surface element dx' as in Figure 5.8, i.e.

$$H_s^r = \int dH_s^r \qquad\qquad H_s^t = \int dH_s^t$$

where

$$dH_s^r = C^r S^r(\theta_i, \theta_s)\frac{e^{ik_0 r}}{\sqrt{r}}e^{ik_0(S_i - S_s)x_s}e^{-ik_0(C_i + C_s)h(x_s)}dx_s \qquad (5.36a)$$

$$dH_s^t = C^t S^t(\theta_i, \theta_{1s})\frac{e^{ik_1 r}}{\sqrt{r}}e^{ik_0(S_i - S_s)x_s}e^{-i(k_0 C_i - k_1 C_{1s})h(x_s)}dx_s \qquad (5.36b)$$

The parameters C^r and C^t are suitable constants, while S^r and S^t are the scattering coefficients. Bahar's prescription for removing the restriction of small slopes is to consider the fields in equations (5.36a,b) to be valid for surface elements at an arbitrary angle γ, whereupon the angles are measured with respect to the local surface normal; see Figure 5.9. Thus equations (5.36a & b) from the regular full-wave theory become

$$dH_s^r = C^r S^r(\theta_i - \gamma, \theta_s + \gamma)\frac{e^{ik_0 r}}{\sqrt{r}}e^{ik_0(S_i - S_s)x_s}e^{-ik_0(C_i + C_s)h(x_s)}\frac{dx_s}{\cos(\gamma(x_s))}$$

$$dH_s^t = C^t S^t(\theta_i - \gamma, \theta_{1s} - \gamma)\frac{e^{ik_1 r}}{\sqrt{r}}e^{ik_0(S_i - S_s)x_s}e^{-i(k_0 C_i - k_1 C_{1s})h(x_s)}\frac{dx_s}{\cos(\gamma(x_s))}$$

in the extended full-wave theory. The directions of the stationary-phase points in the
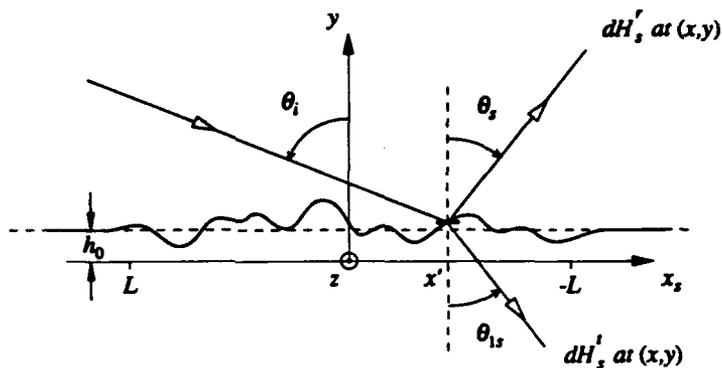
Figure 5.8: Differential fields scattered by an elemental, horizontal strip dx'_s.
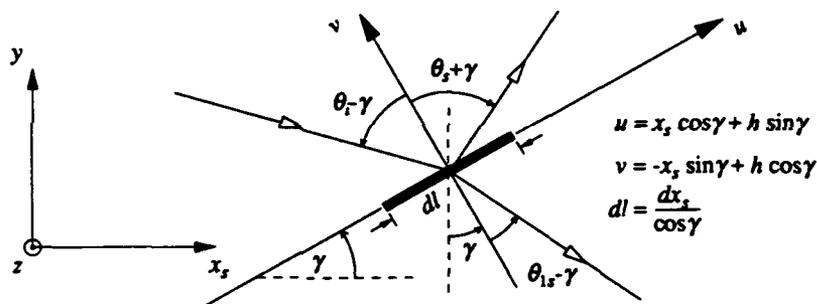
Figure 5.9: Coordinate transformation of an angled elemental strip in the extended full-wave theory.

scattered fields have been transformed to

$$
\begin{array}{lll}
\theta_s & \longrightarrow & \theta_s + \gamma \qquad \text{(reflected field)} \\
\theta_{1s} & \longrightarrow & \theta_{1s} - \gamma \qquad \text{(transmitted field)}
\end{array}
$$

and their corresponding angles in the opposing half-space are calculated from Snell's law:

$$
\begin{array}{lll}
\sin \theta_{1s}^{\gamma} & = & \sin(\theta_s + \gamma)/\sqrt{\kappa} \qquad \text{(reflected field)} \\
\sin \theta_s^{\gamma} & = & \sqrt{\kappa}\sin(\theta_{1s} - \gamma) \qquad \text{(transmitted field)}
\end{array}
$$

It is interesting to note that the arguments of the exponents in equations (5.36a,b) are invariant to coordinate transformation. The differential scattered radiation fields are made to vanish when the incident or scatter angles are grazing with respect to

the local tangent plane [6, page 18], i.e.

$$\theta_i - \gamma \to \pm\frac{\pi}{2} \qquad \theta_s + \gamma \to \pm\frac{\pi}{2} \qquad \theta_{1s} - \gamma \to \pm\frac{\pi}{2} \tag{5.37}$$

and so incorporates a primitive shadowing function [8, page 334].

5.4 The mean scattered power

For a far-zone, scattered field of the form

$$\lim_{r \to \infty} H_s(\mathbf{r}) = \mathcal{H}_s(\theta_i, \theta_s; h, \gamma)\frac{e^{ikr}}{\sqrt{r}}$$

the mean, differential, scattering cross-section (DSCS) [equation (4.30)] is given by

$$\Xi_{pp}(\hat{\mathbf{r}}) = \frac{\left\langle |\mathcal{H}_s(\theta_i, \theta_s; h, \gamma)|^2 \right\rangle}{|H_0|^2 \, 2L \cos\theta_i} \tag{5.38}$$

where $\langle \cdots \rangle$ indicates a statistical average over the heights and slopes of the surface.

The scattered field at any point can be described as a sum of the coherent and incoherent fields at that point. The coherent, or *mean* field, $\mathcal{H}_C$ is given by

$$\mathcal{H}_C = \langle \mathcal{H}_s \rangle$$

The incoherent field $\mathcal{H}_I$ is therefore

$$\begin{aligned} \mathcal{H}_I &= \mathcal{H}_s - \mathcal{H}_C \\ &= \mathcal{H}_s - \langle \mathcal{H}_s \rangle \end{aligned}$$

The mean, scattered power P_s in the direction θ_s is given by

$$\begin{aligned} P_s &\sim \left\langle |\mathcal{H}_s|^2 \right\rangle \\ &= \langle (\mathcal{H}_I + \mathcal{H}_C)(\mathcal{H}_I^* + \mathcal{H}_C^*) \rangle \\ &= \left\langle |\mathcal{H}_I|^2 \right\rangle + |\mathcal{H}_C|^2 \end{aligned}$$

since $\mathcal{H}_C \langle \mathcal{H}_I^* \rangle = \mathcal{H}_C^* \langle \mathcal{H}_I \rangle = 0$. The coherent power $P_C = |\mathcal{H}_C|^2$ is generally localized to the specular direction, whereas the incoherent power $P_I = \left\langle |\mathcal{H}_I|^2 \right\rangle$ may be finite in any direction. The coherent component dominates the total scattered power when the surface is flat. Introducing surface roughness, the incoherent power increases at

the expense of the coherent power until, for sufficiently large roughness, the radiation is almost entirely incoherently scattered.

Since both the height h and the slope $s = \tan \gamma$ are random variables, calculation of the coherently scattered power requires the joint probability density function $p(h(x_s), s(x_s))$. Bahar assumes that the heights and slopes are independent for Gaussian surfaces [9, page 5217], thus

$$p(h, s) = p_h(h) p_s(s)$$

Assuming zero-mean, Gaussian densities we can write

$$
\begin{aligned}
p_h(h) &= \frac{1}{\sqrt{2\pi}\,\sigma_h} \exp\left(-\frac{h^2}{2\sigma_h^2}\right) \\
p_s(s) &= \frac{1}{\sqrt{2\pi}\,\sigma_s} \exp\left(-\frac{s^2}{2\sigma_s^2}\right)
\end{aligned}
$$

where σ_h is the rms height and σ_s is the rms slope. Since $s = \tan \gamma$ we can construct $p_\gamma(\gamma)$ from the relation

$$p_\gamma(\gamma) = p_s(s)\frac{ds}{d\gamma} = \frac{1}{\sqrt{2\pi}\,\sigma_s \cos^2 \gamma} \exp\left(-\frac{\tan^2 \gamma}{2\sigma_s^2}\right)$$

The mean field for a particular pair of incident and scatter angles is then found by evaluating the integral

$$\mathcal{H}_C = \langle \mathcal{H}_s \rangle = \int_{-\frac{\pi}{2}}^{\frac{\pi}{2}} d\gamma \int_{-\infty}^{\infty} dh\, \mathcal{H}_s(h, \gamma) p_h(h) p_\gamma(\gamma)$$

Averaging over the surface height involves the integral

$$\int_{-\infty}^{\infty} \exp\left(-ivh - \frac{h^2}{2\sigma_h^2}\right) \frac{dh}{\sqrt{2\pi}\,\sigma_h} = \exp\left(-\frac{v^2 \sigma_h^2}{2}\right)$$

where

$$
v = \begin{cases} k_0 \cos \theta_i + k_0 \cos \theta_s, & \text{(reflected field)} \\ k_0 \cos \theta_i - k_1 \cos \theta_{1s}, & \text{(transmitted field)} \end{cases}
$$

In reflection, $X(v) = \exp(-v^2 \sigma_h^2/2)$ is the one-dimensional characteristic function for the surface height. The remaining integral over γ can be evaluated numerically for each pair of angles θ_i, θ_s in reflection and θ_i, θ_{1s} in transmission, setting the integrand to zero whenever the slope is such that the local incident or scatter angles exceed grazing, i.e. conditions (5.37).

Calculation of the incoherently scattered power P_I, or the *variance*, involves evaluation of the integral

$$\left\langle |\mathcal{H}_s|^2 \right\rangle = \left\langle \int_{-L}^{L}\int_{-L}^{L}\mathcal{H}_s(h,\gamma)\mathcal{H}_s^*(h',\gamma')\,dx_s dx_s' \right\rangle$$

requiring the joint probability function $p(h(x_s),\gamma(x_s);h(x_s'),\gamma(x_s'))$. Assuming uncorrelated heights and slopes, averaging over the surface height involves the integral

$$\int_{-\infty}^{\infty}\int_{-\infty}^{\infty}\exp\left(-iv[h-h']\right)p_h(h;h')\,dh\,dh'$$

where, for joint Gaussian statistics [equation (3.5)],

$$p_h(h;h') = \frac{1}{2\pi\sigma_h^2\sqrt{1-\varrho^2}}\exp\left(-\frac{h^2-2\varrho hh'+h'^2}{2\sigma_h^2(1-\varrho^2)}\right)$$

The correlation coefficient for a Gaussian surface is given by equation(3.7)

$$\varrho = \exp\left(-\frac{(x_s-x_s')^2}{\tau^2}\right)$$

where τ is the $1/e$ correlation length. Integration over the heights yields the function

$$\chi_2(v,-v) = \exp\left(-v^2\sigma_h^2(1-\varrho)\right)$$

which is the joint characteristic function for the case of reflection.

Bahar assumes that the slope density is of the form

$$p_s(s,s') = p(s)\,\delta(s-s') = \frac{1}{\sqrt{2\pi}\,\sigma_h}\exp\left(-\frac{s^2}{2\sigma_s^2}\right)\delta(s-s')$$

indicating that the slopes are more strongly correlated than the heights. Making this approximation we can numerically evaluate the resulting slope integral

$$\int_{-\frac{\pi}{2}}^{\frac{\pi}{2}}\mathcal{H}_s(h,\gamma)\mathcal{H}_s^*(h',\gamma)p_\gamma(\gamma)\,d\gamma$$

The slope dependence $\gamma(x_s)$ is then removed from the remaining surface integral which involves

$$\int_{-L}^{L}\int_{-L}^{L}e^{-v^2\sigma_h^2(1-\varrho)}e^{-ik_0(\sin\theta_s-\sin\theta_i)(x_s-x_s')}dx_s\,dx_s'$$

Making the substitutions $l = x_s - x_s'$ and $w = x_s + x_s'$ the integral can be numerically evaluated from the equivalent expression

$$\frac{1}{2}\int_{-2L}^{2L}e^{-v^2\sigma_h^2[1-\varrho(l)]}e^{-iwl}\left(4L-2\,|l|\right)\,dl$$

where $u = k_0 \sin \theta_s - k_0 \sin \theta_i$. Hence, considering the reflected radiation field to be of the form

$$\mathcal{H}_s = \int_{-L}^{L} \mathcal{C}\, S(\gamma) e^{i(ux_s - vh)} \frac{dx_s}{\cos \gamma}$$

for a particular pair of incident and scatter angles, θ_i and θ_s, the total mean scattered power can be numerically calculated from the expression

$$P_s \sim \left\langle |\mathcal{H}_s|^2 \right\rangle = \frac{|\mathcal{C}|^2}{\sqrt{2\pi}\,\sigma_s} \int_{-\frac{\pi}{2}}^{\frac{\pi}{2}} \left[\frac{S(\gamma)}{\cos^2 \gamma} \right]^2 e^{-\frac{\tan^2 \gamma}{2\sigma_s^2}} d\gamma \int_{-2L}^{2L} e^{-v^2 \sigma_h^2 [1 - \rho(l)]} \cos(ul)\,(2L - |l|)\, dl$$

We can then evaluate the mean, differential scattering cross-section from the expression given in equation (5.38).

5.5   Numerical results

The results presented in this section concentrate on the largely single-scattering, dielectric diffuser #46 for the wavelengths $\lambda = 0.633\ \mu m$ and $10.6\ \mu m$. The *regular* theory describes the analysis developed in this chapter and the *extended* theory includes the modifications proposed by Bahar [6] to remove the limitations of low slopes.

The results from the regular theory in Figure 5.10 ($\lambda = 0.633\ \mu m$) show quantitative agreement with the rigorous calculations in Figures 4.15 and 4.16. Away from normal incidence the Ξ_{pp} cross-sections are larger than expected in the backscatter direction but show good qualitative agreement with the experimental results in Figure 4.27. The limitations of the regular theory are actually exaggerated in the extended theory calculations and the magnitudes of the cross-sections are generally much higher than many rigorous calculations suggest for diffuser #46 [52, 70]. The extended calculations show poor qualitative agreement with the experimental measurements in Figure 4.27.

Similar comments apply to the results in Figure 5.11 for the wavelength $\lambda = 10.6\ \mu m$. The regular calculations show reasonable qualitative agreement with the experimental results in Figure 4.28 and quantitative agreement with rigorous calculations, although Ξ_{pp} is slightly higher than expected for normal incidence. The extended theory calculations in Figure 5.11 again do not compare as favourably as the regular calculations.

Metallic scattering results for both regular and extended theories do not compare well with experimental measurements. This is primarily due to the lack of multiple
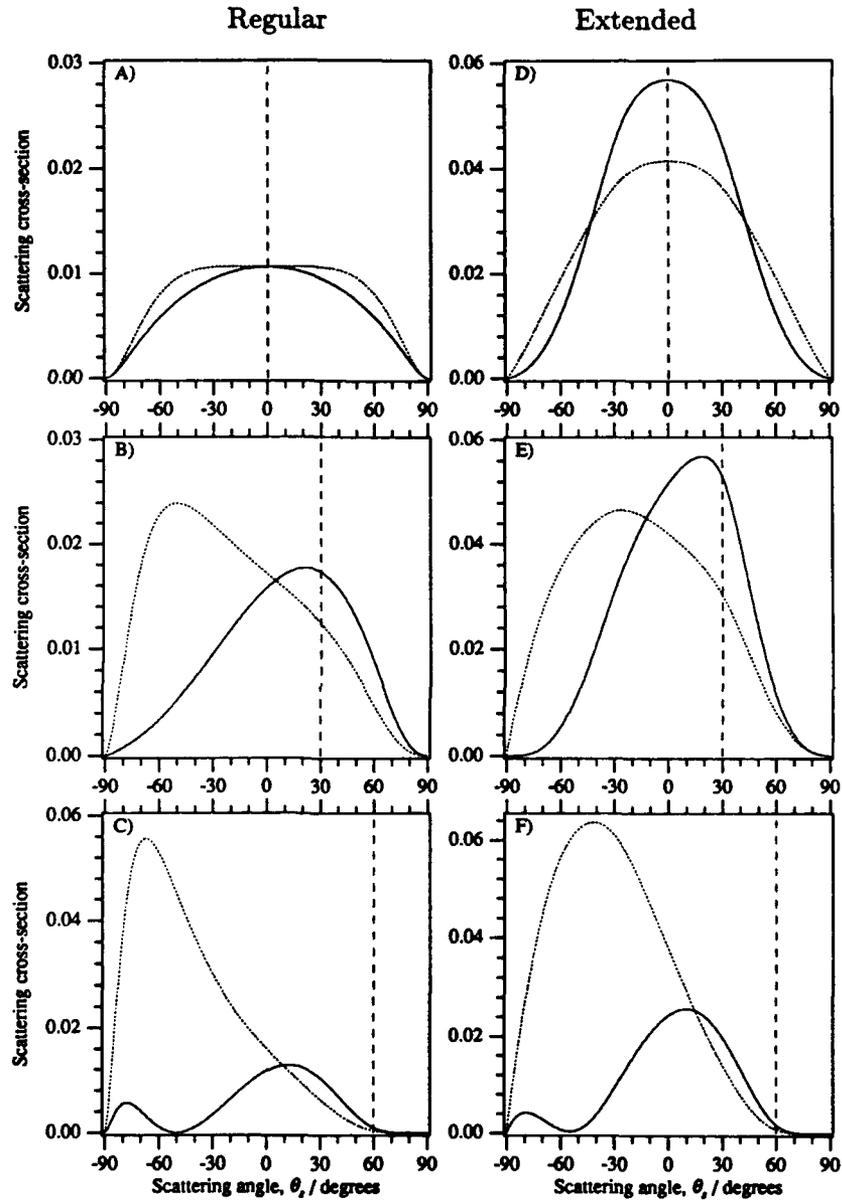
Regular   Extended

Figure 5.10: Regular and extended full-wave calculations for dielectric diffuser #46. $\tau/\lambda = 5.02$ and $\sigma_h/\lambda = 1.93$; surface length $L = 40\lambda$; refractive index $n = 1.411$; wavelength $\lambda = 0.633 \ \mu m$. $\Xi_{pp}^{re}(\theta_i, \theta_s)$ [——]; $\Xi_{ss}^{re}(\theta_i, \theta_s)$ [· · ·]: A) $\theta_i = 0°$, B) $\theta_i = -30°$, C) $\theta_i = -60°$.
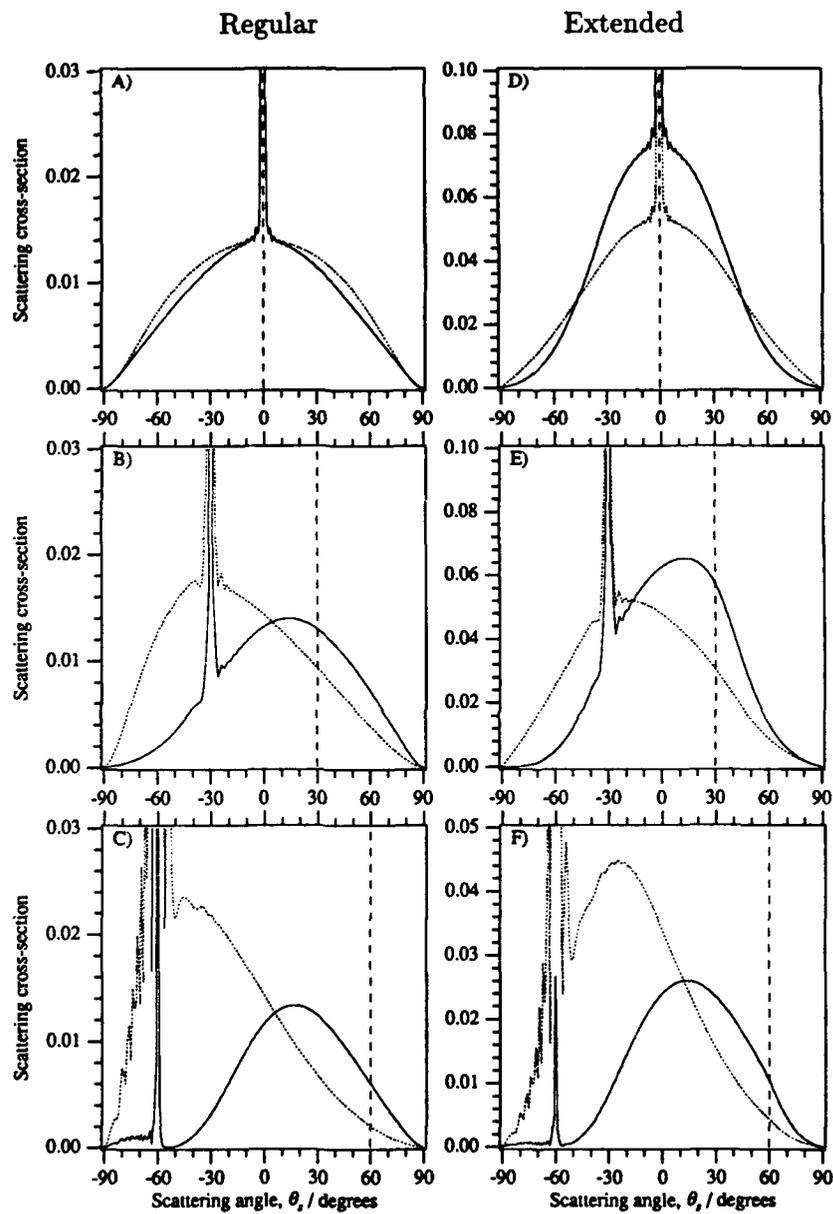
Regular   Extended

Figure 5.11: Regular and extended full-wave calculations for dielectric diffuser #46. $\tau/\lambda =$ 0.30 and $\sigma_h/\lambda = 0.12$; surface length $L = 40\lambda$; refractive index $n = 1.51$; wavelength $\lambda = 10.6~\mu m$. $\Xi_{pp}^{re}(\theta_i,\theta_s)$ [——]; $\Xi_{ss}^{re}(\theta_i,\theta_s)$ [- - -]: A) $\theta_i = 0°$, B) $\theta_i = -30°$, C) $\theta_i = -60°$. Coherent components not removed.

scattering in the formulations. Calculations from both theories suggest no evidence of a backscatter peak being predicted. For metallic diffuser #46 the extended scattering theory exhibits a peak *close* to backscatter for incidence angles $|\theta_i| \gtrsim 20°$; however, this peak is not present near normal incidence, contrary to all experimental observations of backscatter enhancement. There are a number of features introduced by Bahar's modifications which, had they been introduced *a priori*, would have invalidated the original formulation. These features are discussed in more detail by Collin [25]. The "backscatter" peaks predicted by the extended theory are thought to be artifacts of the modifications to the regular theory.

Chapter 6

Graphic Results and Observations

6.1 Introduction

In previous chapters, the main content of the work has concentrated on investigating the planar scattering of transversley polarized light, TE (s) and TM (p), by a one-dimensional, randomly rough diffuser through numerical simulation and experimental demonstration. This work has provided a reliable database of experimentally determined scattering cross-sections for identical, gold-coated and dielectric diffusers ($\tau \approx 3\ \mu m$, $\sigma_h \approx 1\ \mu m$) over the wavelength range 0.63—10.6 μm. Aside from variations of the modal TE and TM cross-sections, there are interesting investigations that can be carried out which reveal more of the scattering mechanisms' nature. This chapter contains some of the more unusual aspects of light scattering from one-dimensional diffusers encountered during this research.

6.2 Geometric ray-tracing

Although the notion of treating propagating electromagnetic waves as a bundle of non-diffracting rays seems a little diverse, geometric ray-tracing has enjoyed successful application in the field of Applied Optics for many years. The physics of the interaction between a light-ray and a flat, dielectric medium is described by Snell's invariant $n \sin\theta$, which can be used to determine the propagation directions of both reflected and refracted light-rays. For the case of a flat, metallic medium only the reflected rays need to be considered. Modulation of the energy 'carried' by each ray is determined by Fresnel's reflection and transmission coefficients. Geometric ray-tracing assumes that the 'wavelength' of a ray is too small to experience any

161

diffractive effects by edges or apertures; i.e. $\lambda \rightarrow 0$, sometimes referred to as the 'geometric optics limit'. Tracing rays from a randomly rough surface, we can therefore assume a local tangent plane approximation to apply Snell's law and Fresnel's equations at each interaction. The far-field distribution of the scattered light is, in part, determined by the ray number density; the number of rays in a certain direction collected over a finite angular interval, e.g. every half a degree.

Using the method described in § 4.4.1, random surface profiles of the required Gaussian statistics can be numerically generated for a Monte Carlo simulation. The length of each surface is somewhat arbitrary, since doubling the length has the same averaging effect as tracing from two independent surfaces. Since the rays do not diffract there are no 'edge-effects' due to the finite surface length, although anomolous scattering near grazing angles can occur if the incident ray bundle fills the entire surface. The ray-tracing algorithm used to produce the following calculations generates a random profile described by 4096 points. Although only the central 2000 points (equivalent to 80 μm) are illuminated, the entire profile length is taken into account before a ray can propagate to the far-field. This algorithm minimizes anomolous scattering near grazing angles.

One of the main advantages of adopting a ray-tracing approach to light scattering is the ease with which the single and multiple scattering contributions can be separated from each other. The shadowing effects of illumination and observation are also inherent to the ray-tracing mechanism. Thus the main ingredients of rigorous scattering theories are included in this simple treatment of the problem.

6.2.1 Metallic, coherent ray-tracing

To simulate illumination of the rough surface by a coherent light beam, such as that from a laser, the path length of each ray can be taken into account before the scattered light intensity is calculated. This 'coherent' ray-trace will go some way towards revealing any interference mechanisms that affect the distribution of the scattered light. For a particular surface realization, the light amplitude in a given direction will have a number of phase contributions from different points on the surface. Each realization produces something looking like a speckle pattern, and the final scattering cross-section is expressed as the mean of an ensemble of surface realizations. For

these coherent calculations, 10000 rays were traced per surface and the cross-sections were averaged over 1000 realizations.

Figure 6.1 shows the results of a coherent ray-trace from an impenetrable surface with the statistical parameters of diffuser #46 ($\tau = 3.18\ \mu m$, $\sigma_h = 1.22\ \mu m$) for the 'wavelength' $\lambda = 0.633\ \mu m$. The incidence angle is $\theta_0 = -10°$ and the backscat-
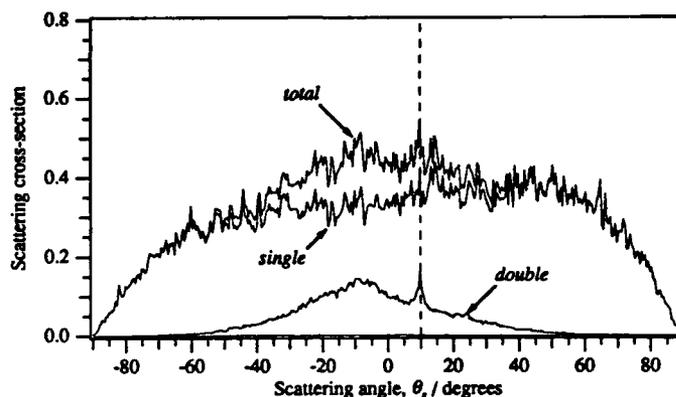
Figure 6.1: Coherent ray-trace calculations for an impenetrable diffuser. $\tau = 3.18\ \mu m$, $\sigma_h = 1.22\ \mu m$. $\Xi(-10°, \theta_s)$.

ter direction is denoted by the vertical dashed line. The surface is assumed to have 100% reflectivity, independent of polarization, so only one cross-section is generated. The *total* curve is the coherent sum of the *single*, *double*, and *triple*-scatter contributions. The single-scatter curve exhibits a slight bias towards backward scattering angles ($\theta_s > 0°$), whereas the double-scatter rays favour the forward scattering angles ($\theta_s < 0°$) producing an enhanced peak in the backscatter direction. It is interesting *to note that the peak is approximately twice the height of the diffusely scattered* light in neighbouring angles of the double-scatter curve. This peak is solely due to the constructive interference between forward and time-reversed light paths along the surface, which can only occur in the backscatter direction. The triple-scatter contribution at this incidence angle is negligable.

In analogy to the comparisons between rigorous theory and experimental measurements in Figure 4.6, Figure 6.2 compares the ray-trace cross-sections with the same *s* polarized, experimental data (gold-coated diffuser #46, wavelength $\lambda = 0.633\ \mu m$).

For normal incidence an enhanced backscatter peak is observed in the double-scatter contribution of Figure 6.2a. The total scattering cross-section agrees very well with experimental measurement for the scattering angles $|\theta_s| \gtrsim 12°$. Although the double-scatter contribution does contain a backscatter peak, it does not exhibit the subsidiary structure that accompanies the peak in the experimental measurement. For $\theta_0 = -20°$ incidence, Figure 6.2b, the total-scatter contribution is in good agreement with the experimental data except near backscatter. The double-scatter term is skewed towards forward scattering angles and has a very small backscatter peak but, again, there is no subsidiary structure. The comparison between the cross-sections for $\theta_0 = -40°$, Figure 6.2c, is still favourable with the emphasis on backward scattered light. The double-scatter term does not exhibit a backscatter peak, but the experimental peak is not very large anyway. With the increase in incidence angle the triple-scatter term is just visible.

Of the comparisons between rigorous theory versus experiment and ray-tracing versus experiment, the simplistic ray-tracing model seems to more correctly predict the distribution of the diffusely scattered light. Although the rigorous theory does not agree very well with the experimental cross-sections for large incidence angles, similar theoretical studies do tend to support these calculated results. One criticism that has been levelled at the experimental measurements, in defence of the theories, is that the true surface parameters τ and σ_h may be different from the measured values, or that the diffuser contains extra scattering structures. However, the ray-tracing calculations demonstrate that it is possible for a surface with the quoted parameters for diffuser #46 to scatter light as strongly as the experiments suggest.

Increased surface roughness

A surface with steeper slopes and deeper features will scatter light more strongly through an increase in multiple scattering. An incoherent ray-trace was used to calculate the possible effects on the individual scattering components for the surface parameters $\tau = 2.0\ \mu m$ and $\sigma_h = 2.0\ \mu m$. The cross-sections in Figure 6.3 represent the ray number density only, no coherent interference effects are included. The single-scatter cross-section has a broad distribution, but is dominated by the multiple scattering components. The largest proportion of the rays have been double-scattered,
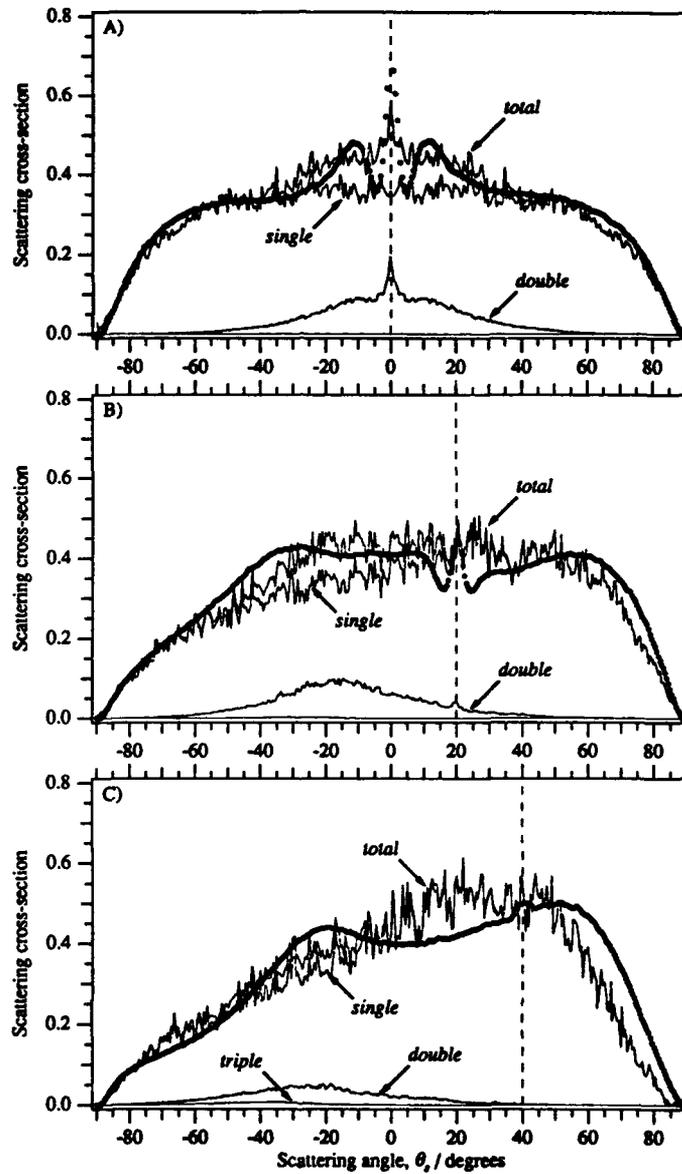
Figure 6.2: Comparisons between coherent ray-trace calculations for an impenetrable diffuser and experimental *ss* cross-sections for diffuser #46. $\tau = 3.18\ \mu m$, $\sigma_h = 1.22\ \mu m$. $\Xi(\theta_0, \theta_s)$: A) $\theta_0 = 0°$, B) $\theta_0 = -20°$, C) $\theta_0 = -40°$.
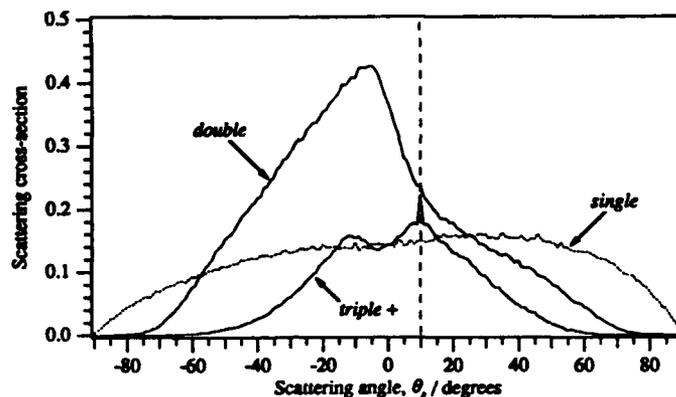
Figure 6.3: Incoherent ray-trace calculations for an impenetrable diffuser. $\tau = 2.0 \ \mu m$, $\sigma_h = 2.0 \ \mu m$; incidence angle $\theta_0 = -10°$.

but a considerable number have also undergone three or more scattering events and the triple-scatter cross-section displays a peak in the backscatter direction. Although the double-scatter cross-section would contribute a coherent peak, higher orders of multiple scattering send a ray preferentially in the backscatter direction.

6.2.2 Dielectric, incoherent ray-tracing

Where the ray-trace for the metallic diffuser was *coherent*, by an *incoherent* ray-trace we mean that the ray's path length is of no consequence, and the light intensity is calculated purely on the basis of ray density in a given direction. The dielectric ray-tracing algorithm is otherwise the same as that used for the metallic ray-trace, except for the provision of a transmitted field. Each incident ray is allowed to generate a total of 14 rays which account for three scattering events in reflection and transmission. The ray-trace also allows for the possibility of 'tunneling' through the surface valley walls. For these incoherent calculations, 2000 rays were traced per surface and the cross-sections were averaged over 600 surface realizations.

Reflected field

Figure 6.4 shows the ray-trace scattering cross-sections calculated in reflection for dielectric diffuser #46 with a refractive index of $n = 1.411$. Individual contribu-
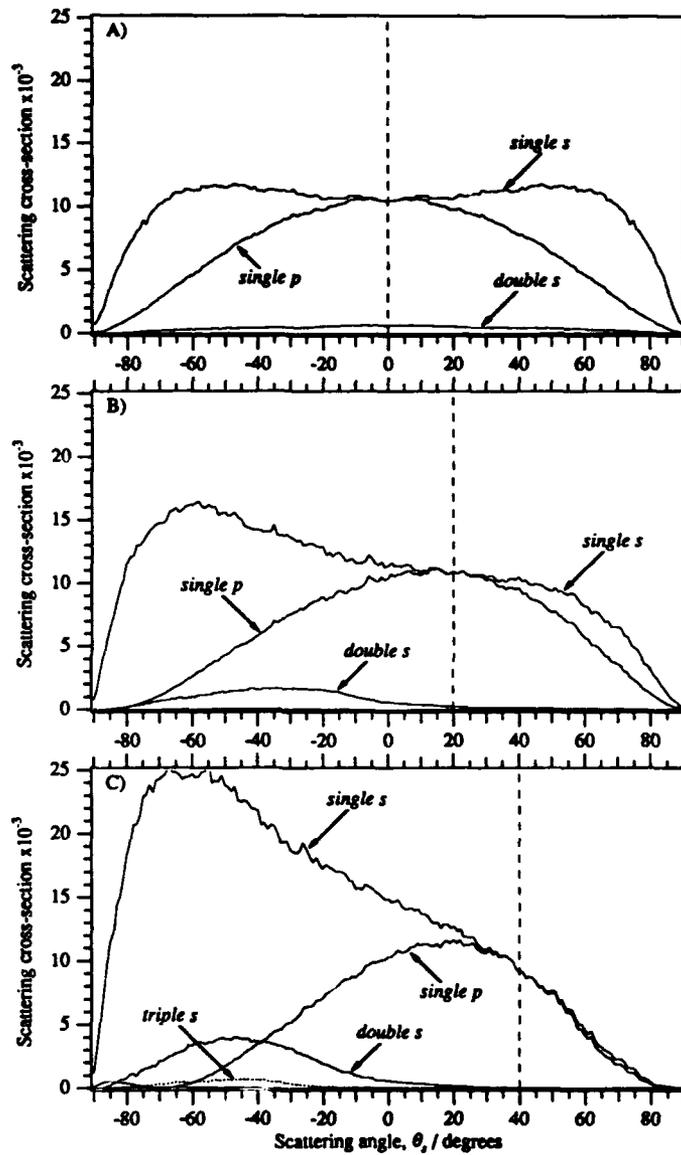
Figure 6.4: Incoherent ray-trace cross-sections in reflection for a dielectric diffuser. $\tau = 3.18\ \mu m$, $\sigma_h = 1.22\ \mu m$; refractive index $n = 1.411$. $\Xi_{pp}^{re}(\theta_0, \theta_s)$; $\Xi_{ss}^{re}(\theta_0, \theta_s)$: A) $\theta_0 = 0°$, B) $\theta_0 = -20°$, C) $\theta_0 = -40°$.

tions from the single and double-scatter rays have been separated for the incident polarizations p and s. The contribution from triple-scatter rays is negligable.

For normal incidence, Figure 6.4a, single-scattering is the dominant reflection mechanism for both polarizations. The double-scatter s cross-section has a low but broad distribution, whereas that for p is virtually zero. At backscatter the single-scatter cross-sections are equal, indicating that the backscattered light is due to near-normal reflection from horizontal portions of the surface. This is to be expected for reflection dominated by single-scattering. Increasing the incidence angle to $\theta_0 = -20°$, Figure 6.4b, the distributions have become skewed and the single-scatter cross-sections still meet at backscatter, again indicating near-normal reflection but this time from tilted surface elements. The double-scatter s cross-section has increased in forward scattering angles ($\theta_s < 0°$) but has diminished in backward angles ($\theta_s > 0°$). For $\theta_0 = -40°$, Figure 6.4c, the increase in Fresnel reflectance with incidence angle has meant an increase in multiple scattering for s polarized rays, but the reflection of p polarized rays is almost entirely single scattering. The single-scatter cross-sections still meet at backscatter and the p cross-section has a null reflectance at $\theta_s \approx -70°$ due to the Brewster effect.

The graphs shown in Figure 6.5 compare the *total* ray-trace cross-sections to the rigorous calculations and experimental data of § 4.5.3. The comparisons between ray-trace and experiment are surprisingly good, particularly for the p polarized cross-sections. What is even more surprising is that the ray-trace cross-sections are virtually identical to those of the rigorous calculations. It would therefore appear that light scattering from a dielectric surface, even one as rough as diffuser #46, can be explained simply from geometrical arguments.

Transmitted field

Continuing our study of ray-tracing from a dielectric diffuser, we now consider the scattering cross-sections in transmission. On the strength of the comparisons between experiment and rigorous theory in § 4.5.3, the ray-trace cross-sections in Figure 6.6 are compared with rigorous calculations for dielectric diffuser #46. As was found for the case of reflection, the ray-trace cross-sections are almost indistinguishable from those of the rigorous calculations. The transmission effects demonstrated in § 4.5.3
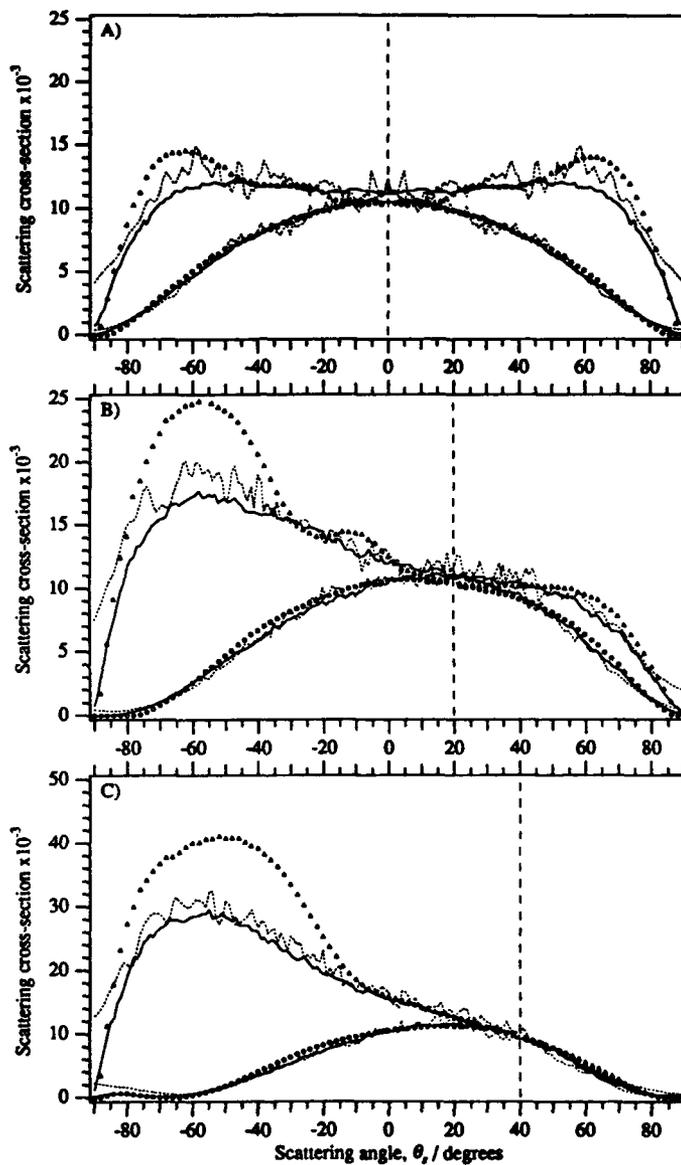
Figure 6.5: Comparisons between ray-trace [——], rigorous theory [- - -], and experimental scattering cross-sections in reflection for a dielectric diffuser. $\tau/\lambda = 5.02\ \mu m$, $\sigma_h/\lambda = 1.93\ \mu m$; refractive index $n = 1.411$. $\Xi^{re}_{pp}(\theta_0, \theta_s)$ [o]; $\Xi^{re}_{ss}(\theta_0, \theta_s)$ [△]: A) $\theta_0 = 0°$, B) $\theta_0 = -20°$, C) $\theta_0 = -40°$.
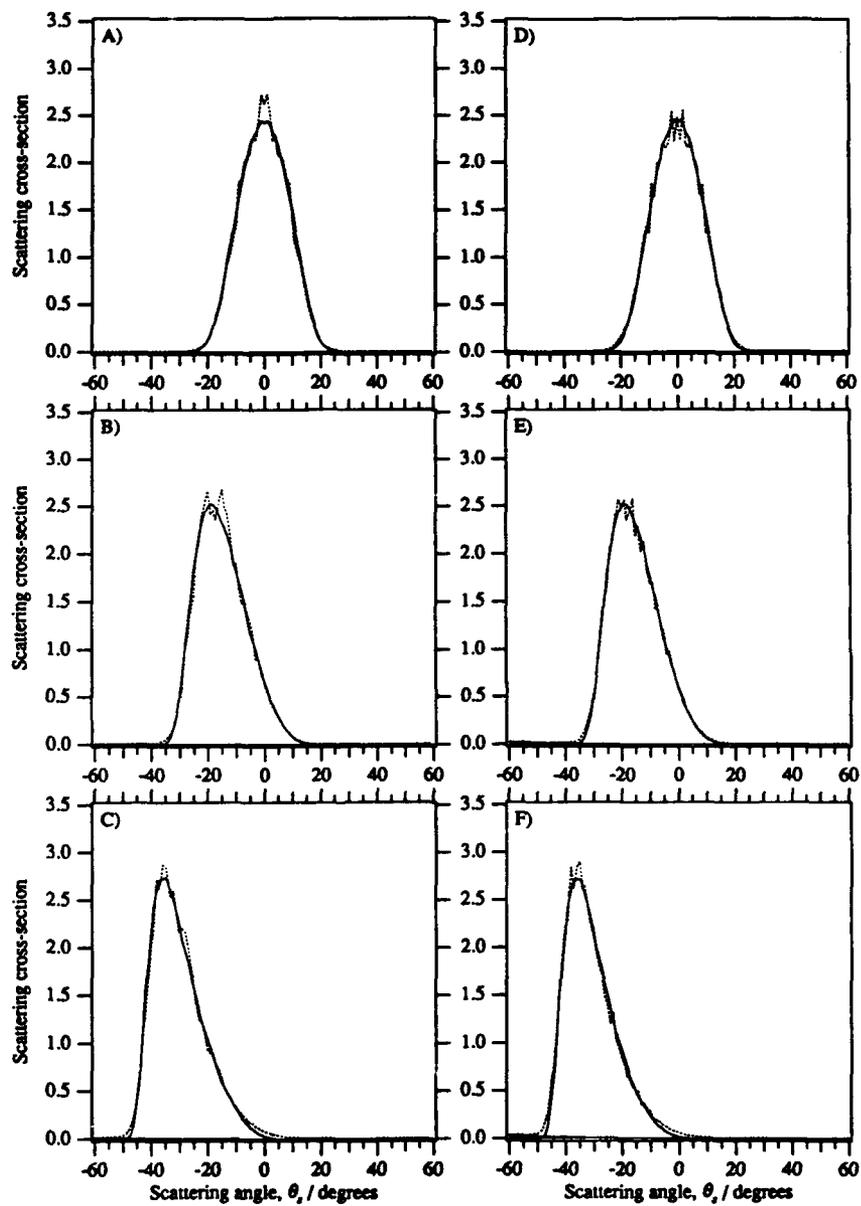
Figure 6.6: Comparisons between transmission cross-sections from ray-trace [——] and rigorous [- - -] calculations for a dielectric diffuser. $r/\lambda = 5.02\ \mu m$, $\sigma_h/\lambda = 1.93\ \mu m$; refractive index $n = 1.411$. $\Xi^{tr}_{pp}(\theta_0,\theta_s)$: A) $\theta_0 = 0°$, B) $\theta_0 = -20°$, C) $\theta_0 = -40°$; $\Xi^{tr}_{ss}(\theta_0,\theta_s)$: D) $\theta_0 = 0°$, E) $\theta_0 = -20°$, F) $\theta_0 = -40°$.

and reference [61] can therefore be explained in terms of simple refraction at local tangent planes.

Unlike the reflected cross-sections, the multiple-scattering contributions in transmission are virtually nil even for high incidence angles. It is not until we expand the vertical axes that we can see where the multiply scattered rays are directed; see Figure 6.7. For normal incidence, Figures 6.7a and 6.7d, the double scattered rays are confined to widely separated lobe structures which peak at $|\theta_s| \approx 70°$ and are completely excluded from the single-scatter cross-section. The triple-scattered rays have a broad distribution over all scattering angles and peak at $\theta_s = 0°$. Multiple scattering for s polarization appears stronger than for p. Increasing the incidence angle, the backward scattered lobe of the double-scatter cross-section rapidly diminishes and the single and double cross-sections overlap each another.

The comparisons between the scattering cross-sections in Figure 6.7 elegantly illustrate the strength of the ray-tracing model. The rigorous calculations quite evidently include the effects of multiple scattering but, by itself, the theory is unable to separate them out from the single scattering contribution. In combination with the ray-trace calculations, all of the components in the rigorous, transmission scattering cross-sections have been identified. An unusual fringing effect, which is not reproduced by the ray-trace, occurs at the overlap between the single and double-scatter cross-sections. The effect is most evident for normal incidence and is not thought to be an artifact of the finite surface length in the calculations. An explanation of this apparent interference effect has yet to be found.

Increased reflectivity

The effects of increasing the refractive index, and hence the reflectivity, of the dielectric medium was examined in § 4.5.3. Using the analytical power of the ray-tracing model we can investigate what effects this has on individual components of the scattered light. Comparisons between the ray-trace and rigorous calculations in reflection are shown in Figure 6.8 for dielectric diffuser #46 with a refractive index of $n = \sqrt{10.0}$. The increase in surface reflectivity can be seen from the magnitudes of the cross-sections compared to those of Figure 6.4a. Despite the high reflectivity, the p polarized, double-scatter cross-section in Figure 6.8a is still small. This effect
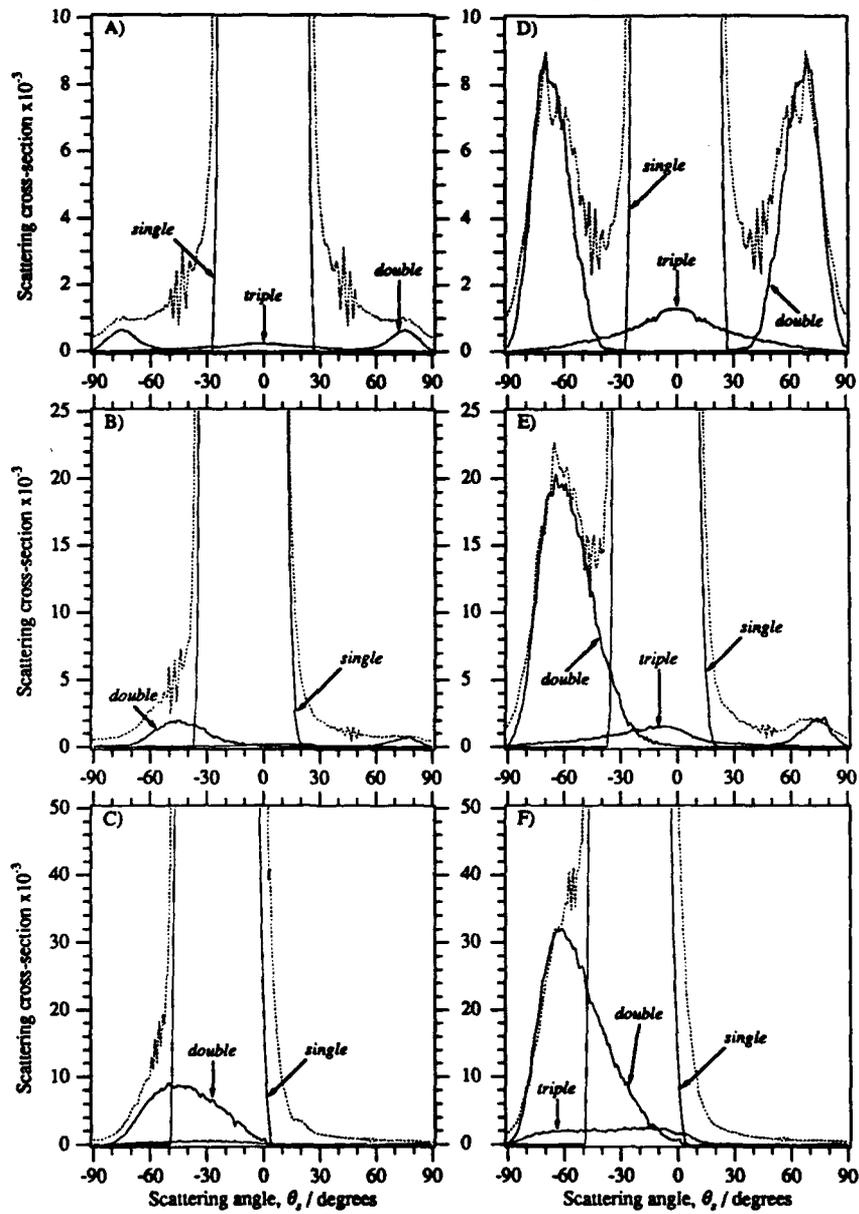
Figure 6.7: Expanded views of the transmission scattering cross-sections from the ray-trace [——] and rigorous [- - -] calculations. $\Xi_{pp}^{tr}(\theta_0, \theta_s)$: A) $\theta_0 = 0°$, B) $\theta_0 = -20°$, C) $\theta_0 = -40°$; $\Xi_{ss}^{tr}(\theta_0, \theta_s)$: D) $\theta_0 = 0°$, E) $\theta_0 = -20°$, F) $\theta_0 = -40°$.
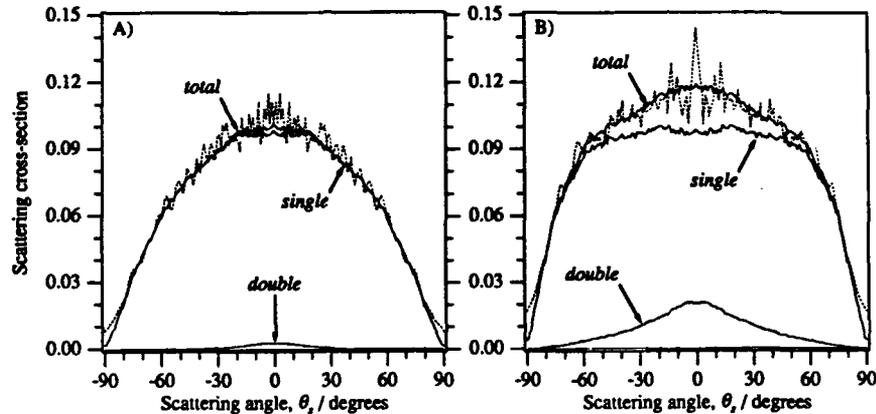
Figure 6.8: Comparisons between the reflection cross-sections from ray-trace [——] and rigorous [- - -] calculations for a dielectric diffuser. $\tau/\lambda = 5.02$, $\sigma_h/\lambda = 1.93$; refractive index $n = \sqrt{10.0}$. A) $\Xi^{re}_{pp}(0°, \theta_s)$; B) $\Xi^{re}_{ss}(0°, \theta_s)$.

explains the observation of Michel [56, chapter 6] when inducing backscatter enhancement in the multiple scattering contribution from highly reflecting dielectric surfaces; to increase this component appreciably requires a strongly diffusing surface. The s polarized, double-scatter cross-section in Figure 6.8b actually exceeds the single-scatter cross-section of Figure 6.4a and, had the ray-trace been coherent, would have produced an enhanced backscatter peak.

In transmission, the scattered light was previously found to have a lower and broader distribution inside a dielectric medium with a high reflectivity; see Figure 4.24. From Figures 6.9b and 6.9d we can see that the increased width of the transmitted peak is a single scattering effect, produced by the increase in the medium's refractive power. Comparing Figures 6.9b and 6.9d to Figures 6.7a and 6.7d, we can see that the double-scatter cross-sections have increased, particularly for p polarization. Surprisingly, however, there is no appreciable contribution from the triple-scatter component for both polarizations.

Increased surface roughness

Studying the transmitted field scattered by a dielectric diffuser (§ 4.5.5), it was noted that the experimental data had a flat-topped appearence for normal incidence. With
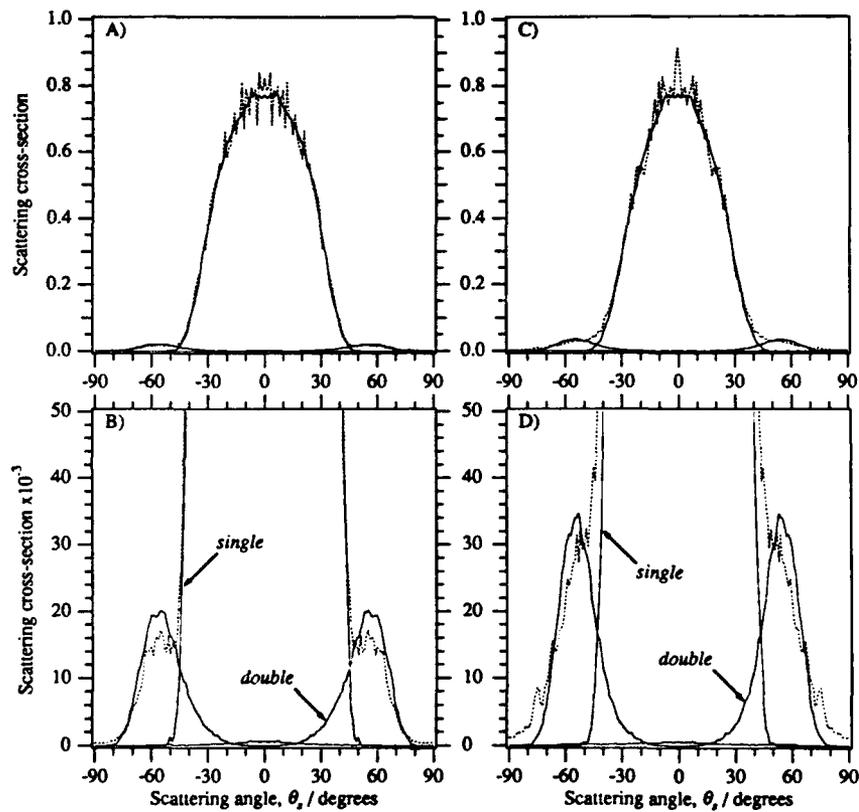
Figure 6.9: Comparisons between the transmission cross-sections from ray-trace [——] and rigorous [- - -] calculations for a dielectric diffuser. $\tau/\lambda = 5.02$, $\sigma_h/\lambda = 1.93$; refractive index $n = \sqrt{10.0}$. A) $\Xi^{tr}_{pp}(0°, \theta_s)$, C) $\Xi^{tr}_{ss}(0°, \theta_s)$. B and D are expanded views of A and C, respectively.

the aid of the ray-tracing model, calculations have shown that similar transmission cross-sections are obtained for Gaussian surfaces with slightly larger σ_h values, i.e. for deeper surfaces. Figure 6.10 compares the ray-trace cross-sections calculated for the parameters $\tau = 3.18 \ \mu m$ and $\sigma_h = 1.75 \ \mu m$ to those from rigorous calculations for dielectric diffuser #46 ($\tau = 3.18 \ \mu m$, $\sigma_h = 1.22 \ \mu m$). The dominance of single scattering in transmission makes the cross-sections quite sensitive to changes in the surface roughness parameters. Increasing σ_h further produces more flat-topped cross-sections similar to the experimental results in Figures 4.22A and 4.23A, but also widens their distributions.
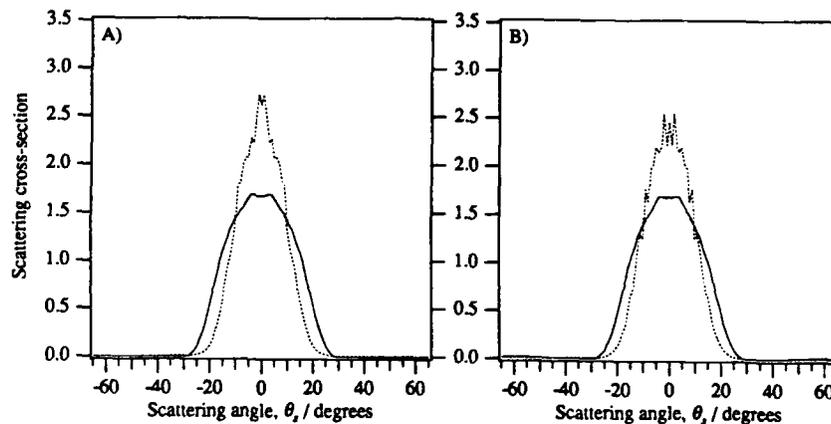
Figure 6.10: Calculated scattering cross-sections in transmission for normal incidence. $\tau = 3.18 \ \mu m$, refractive index $n = 1.411$, wavelength $\lambda = 0.633 \ \mu m$; ray-trace [——] $\sigma_h = 1.75 \ \mu m$, rigorous theory [- - -] $\sigma_h = 1.22 \ \mu m$. A) $\Xi^{tr}_{pp}(0°,\theta_s)$, B) $\Xi^{tr}_{ss}(0°,\theta_s)$.

Visible light scattering from an air/dielectric interface as rough as diffuser #46 is dominated by single-scattering mechanisms. This suggests that the range of validity for single-scattering theories, such as the Kirchhoff Approximation, is greater for dielectric scattering problems compared to their limited application in metallic problems. The surface roughness limits at which the ray-trace cross-sections deviate from the corresponding rigorous calculations has not been investigated.

In the next section we experimentally investigate Stokes' polarization parameters of light scattered in reflection by identical metallic and dielectric diffusers. Despite straightforward calculation of the parameters from the expressions in § 2.5.1, few

numerical studies have been reported of the parameters for light scattered from randomly rough surfaces [20].

6.3 Measurement of Stokes' parameters

The four Stokes parameters completely describe the polarization state of a light field. Expressing the parameters as a column vector, the scattering properties of an illuminated body can be described by a 4×4 Mueller matrix relating the scattered and incident Stokes vectors. Experimental measurement of all 16 matrix elements *for a general scattering object can be a lengthy process. The measurements involve* combinations of incident and detected polarizations and require stable experimental conditions (e.g. illuminating beam power) [13]. However, for an object such as a one-dimensional diffuser, symmetry reduces the number to just four non-vanishing, independent elements [81] and the task is greatly simplified [refer to § 2.5.1].

In accord with previously presented measurements, we shall adopt the Stokes vector

$$\mathcal{S} = (I_p, I_s, U, V)$$

I_p and I_s are the, by now, familiar p and s scattering cross-sections, while U and V are the differences between $+45°/ - 45°$ linear polarizations ($U = I_+ - I_-$) and right/left circular polarizations ($V = I_R - I_L$), respectively. The scattering properties of a one-dimensional diffuser are then described by the Mueller matrix $\tilde{M}$, such that

$$\mathcal{S} = \begin{bmatrix} m_{11} & 0 & 0 & 0 \\ 0 & m_{22} & 0 & 0 \\ 0 & 0 & m_{33} & m_{34} \\ 0 & 0 & -m_{34} & m_{33} \end{bmatrix} \mathcal{S}_0$$

relating the scattered Stokes vector $\mathcal{S}$ to the incident vector $\mathcal{S}_0$. From the discussion in § 2.5.1 it is possible to selectively measure each of the elements m_{11}, m_{22}, m_{33}, and m_{34} by suitable combinations of incident and detected polarization states. The elements m_{11} and m_{22} were directly measured for the incident Stokes vectors $\mathcal{S}_0 = \mathcal{S}_p = (1,0,0,0)$ and $\mathcal{S}_0 = \mathcal{S}_s = (0,1,0,0)$, respectively. Measurement of elements m_{33} and m_{34} was achieved for the incident vector $\mathcal{S}_0 = \mathcal{S}_+ = \frac{1}{2}(1,1,2,0)$, detecting the $\pm 45°$ linear and circularly polarized scattered light, respectively.

6.3.1   Metallic scattering

To begin our discussion of Stokes' parameters, Figure 6.11 shows the scattering cross-sections measured from gold-coated diffuser #46 at the wavelength $\lambda = 0.633$ μm for normal incidence. It is difficult to make an absolute measurement of the total power scattered by the diffuser; surface waves induced by the random roughness carry energy away from both p and s polarized light fields on real metals. Although the p polarized fields couple more strongly with surface waves, the absorption losses ($\sim$ 5% for p) have been neglected and both p and s cross-sections have been normalized to unity. Likewise, the small losses ($\sim 3\%$) have been ignored in the $\pm45°$ linear and circularly polarized cross-sections, the sums of the respective measurements having been normalized to unity. The resulting analysis of these measurements will therefore differ from the true results by a normalization factor of order unity.

Figure 6.11a shows the familiar p and s scattering cross-sections for normal incidence with strong backscatter structures. The cross-sections in Figure 6.11b represent the scattered light linearly polarized at the angles $\pm45°$ to the plane of incidence [refer to Figure 2.4]; the incident beam is linearly polarized at $+45°$, $S_0 = S_+$. The I_- cross-section shows a small backscatter peak, whereas the peak for I_+ is quite pronounced with strong subsidiary structures. For larger scattering angles I_+ gradually reduces to a low, constant value before vanishing at the grazing scattering angles. I_-, on the other hand, slowly increases until $|\theta_s| \approx 50°$ and then drops to zero in a similar fashion to I_p and I_s. The comparison between the I_R and I_L cross-sections in Figure 6.11c shows that there is a remarkable difference in their backscattered structures. The backscatter peak for I_L is barely visible, whereas that for I_R is almost as strong as the enhancement for both I_p and I_s in Figure 6.11a. I_R is the dominant cross-section for $|\theta_s| \lesssim 50°$ but then falls below I_L towards the grazing angles.

The measurements of the I_p and I_s cross-sections demonstrate the phenomenon of backscatter enhancement when a diffuser is illuminated by the fundamental modes TM and TE. However, the $I_\pm$ and I_R cross-sections graphically reveal information about the scattering mechanisms at the diffuser's surface. Considering a planar scattering model, an explanation for some of the observed effects may be found in the following discussion.
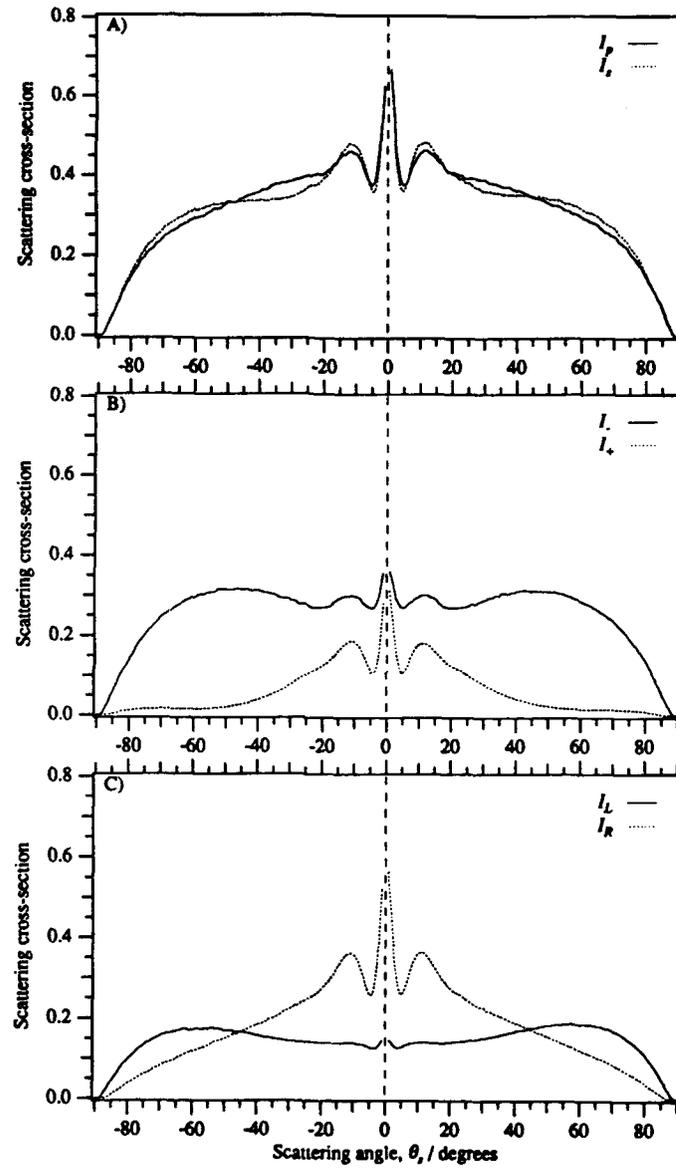
Figure 6.11: Stokes' parameters of the light scattered from gold-coated diffuser #46. $\tau = 3.18 \ \mu m$, $\sigma_h = 1.22 \ \mu m$; wavelength $\lambda = 0.633 \ \mu m$; incidence angle $\theta_0 = 0°$.

Discussion

The incident beam in Figures 6.11b and 6.11c is linearly polarized at an angle of $+45°$ to the plane of incidence. We shall assume that a local tangent plane model can be applied to the interaction of a plane wave component of the incident beam with the diffusing surface. The transmitted field inside a good conducting metal is heavily attenuated and decays rapidly with depth. The complex refractive index of the metal and continuity of the tangential electric fields at the surface introduce phase shifts between the p and s electric fields. These phase shifts are described by the complex Fresnel reflection coefficients $\tilde{r}_p = |r_p|e^{i\phi_p}$ and $\tilde{r}_s = |r_s|e^{i\phi_s}$. Examining the real and imaginary components of $\tilde{r}_p$ and $\tilde{r}_s$ we can write

$$\tilde{r}_p = |r_p|e^{i(\delta+\epsilon)} \qquad\qquad \tilde{r}_s = -|r_s|e^{i\delta}$$

where δ and ϵ are positive, real phases, dependent on the metal's complex refractive index $n = n_R + in_I$ and the local incidence angle. Considering a plane wave component of the reflected field, the difference between the two reflectivities produces a left-handed, elliptically polarized state after the first reflection, as illustrated in Figure 6.12. The reflected light from such single interactions will be predominantly orientated at an angle of $-45°$ to the plane of incidence and left-hand polarized. This would explain the broad distributions of the I_- and I_L cross-sections in Figures 6.11b and 6.11c. If the reflected field interacts with the surface a second time, it will become more elliptically polarized, its handedness will be reversed, and it will be orientated at $+45°$ to the plane of incidence. We would therefore expect the I_+ and I_R cross-sections to represent light which has been scattered twice from the surface, i.e. *double* scattering. The presence of large backscatter peaks for I_+ and I_R, and their absence from I_- and I_L, strongly supports the argument that backscatter enhancement is a *multiple* scattering phenomenon [63]. The small backscatter structure for I_- in Figure 6.11b is almost certainly due to a small $-45°$ linear component of the elliptically polarized, double-scattered fields. Measurements of the corresponding polarization cross-sections for $\theta_0 = -20°$ and $\theta_0 = -40°$, Figures 6.13 and 6.14, show basically the same features as for normal incidence, but skewed with the increase in incidence angle. The backscatter peak remains a feature of the I_+ and I_R cross-sections.

Constructing Stokes' parameters from the measured scattering cross-sections, we present the four Mueller matrix elements in Figure 6.15 for each incidence angle,
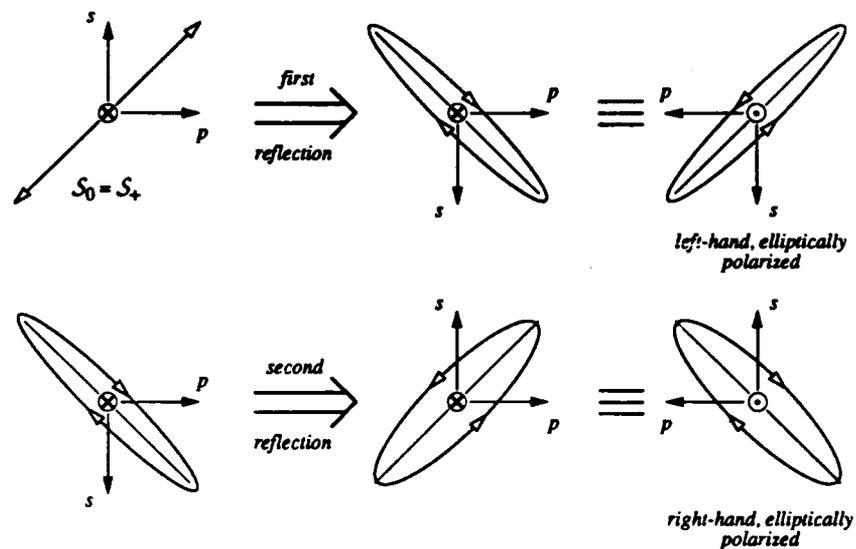
Figure 6.12: Effects of single and double scattering from a flat, gold surface on +45° linearly polarized light.

describing the scattering properties of the gold-coated diffuser #46 for the wavelength $\lambda = 0.633\ \mu m$. Although the above discussion suggests qualitative reasons for some of the observed features, quantitative explanation of the individual matrix elements calls for a fundamental understanding of Stokes' parameters and light interaction with real media. The true scattering mechanisms will be complicated by sub-wavelength surface structures and rotation of the polarization ellipse through differential reflection of the p and s electric fields. The dependence of Fresnel's coefficients on the metal's refractive index indicates that the matrix elements m_{33} and m_{34} are likely to be more strongly dependent on the material properties of the diffuser than m_{11} and m_{22}.

6.3.2   Dielectric scattering

To conclude our discussion of Stokes' parameters, we now consider the complete description of a one-dimensional, dielectric diffuser's scattering properties. To maintain the general theme throughout this dissertation of comparisons between identical
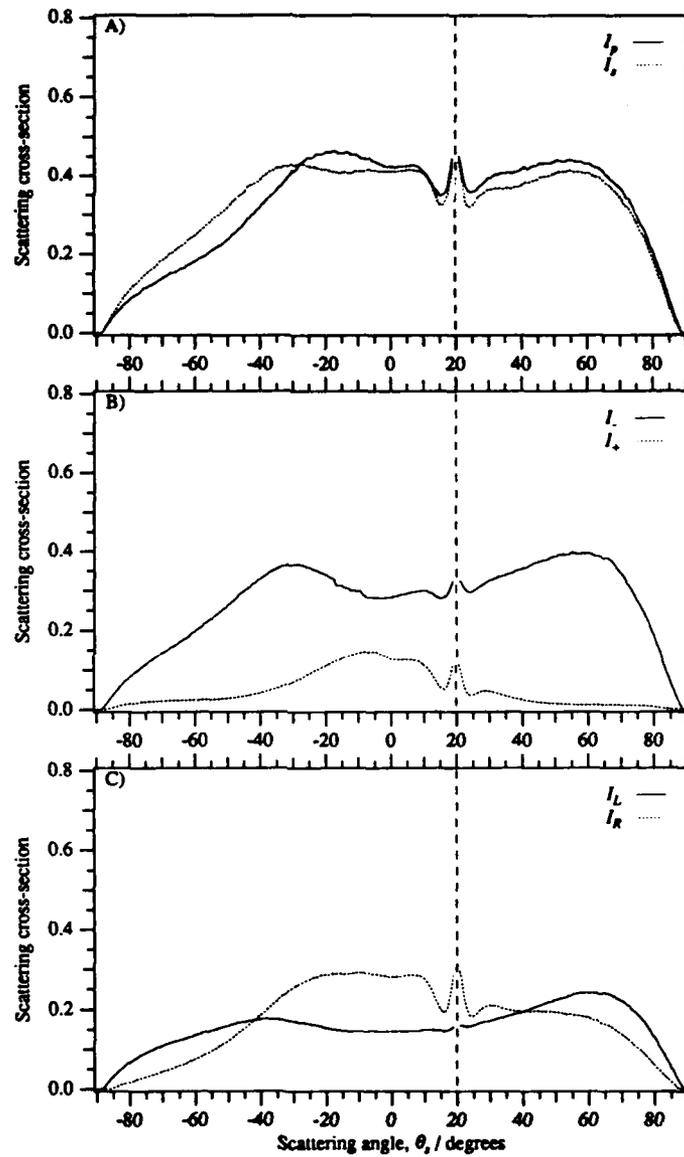
Figure 6.13: Stokes' parameters of the light scattered from gold-coated diffuser #46. $\tau = 3.18\ \mu m$, $\sigma_h = 1.22\ \mu m$; wavelength $\lambda = 0.633\ \mu m$; incidence angle $\theta_0 = -20°$.
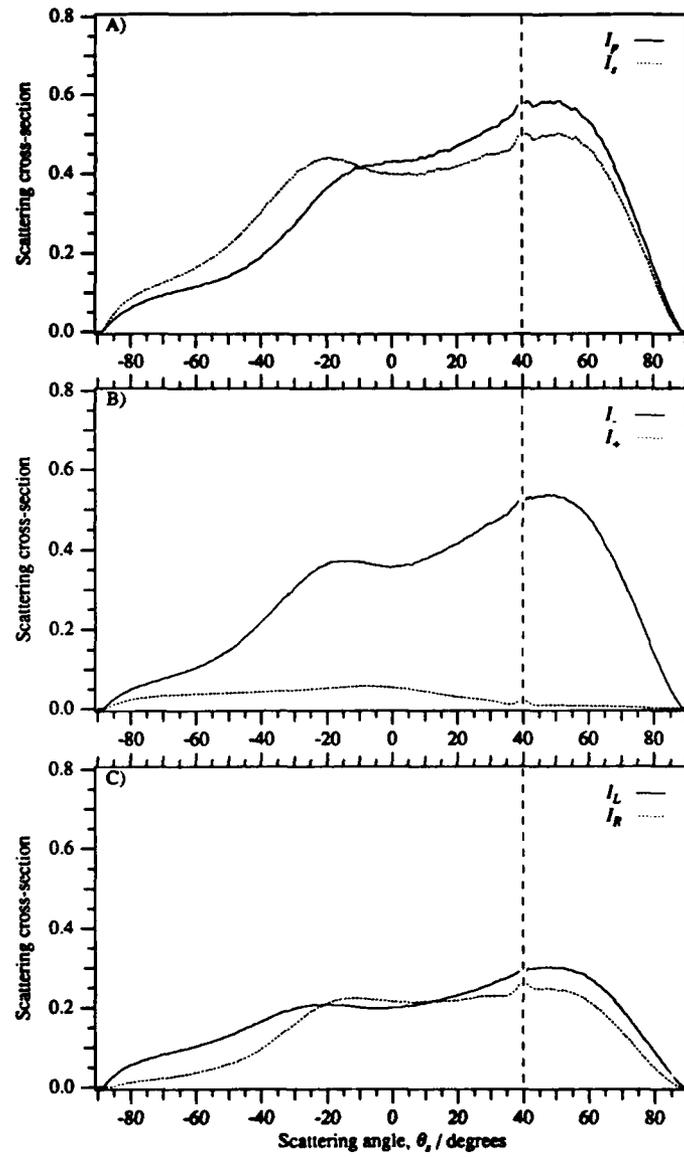
Figure 6.14: Stokes' parameters of the light scattered from gold-coated diffuser #46. $\tau = 3.18\ \mu m$, $\sigma_h = 1.22\ \mu m$; wavelength $\lambda = 0.633\ \mu m$; incidence angle $\theta_0 = -40°$.
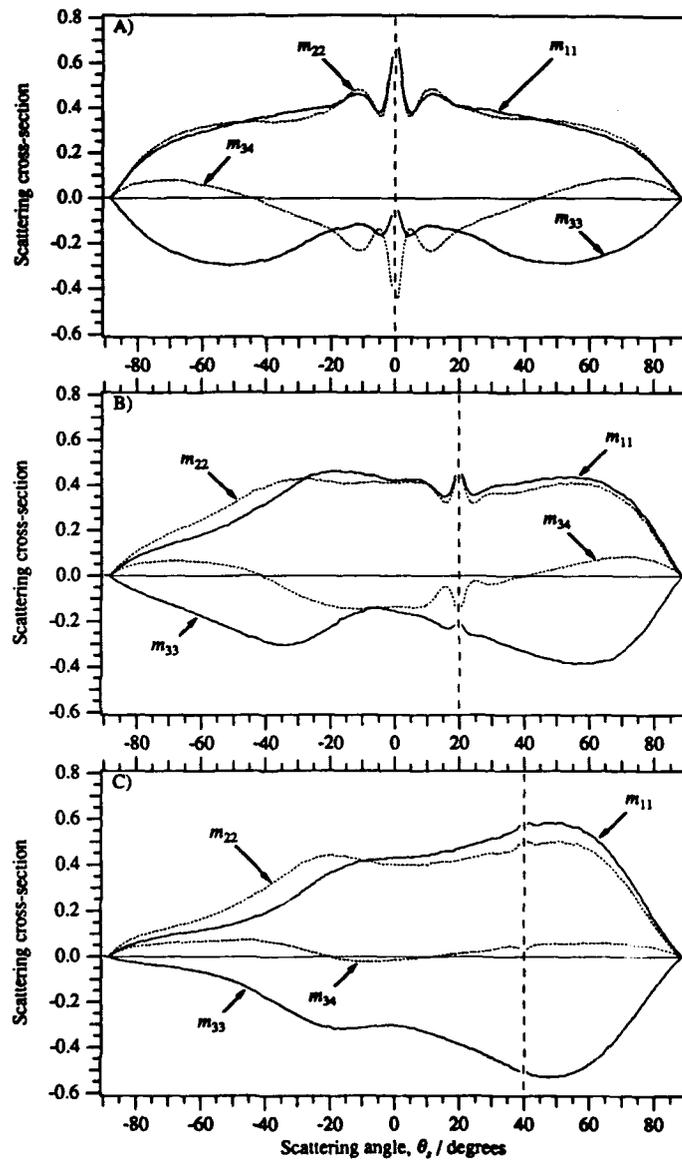
Figure 6.15: The Mueller matrix elements which describe the scattering properties of the gold-coated diffuser #46; wavelength $\lambda = 0.633\ \mu m$. A) $\theta_0 = 0°$, B) $\theta_0 = -20°$, C) $\theta_0 = -40°$.

metallic and dielectric diffusers, Stokes' parameters of the light scattered by dielectric diffuser #46 have been measured for the wavelength $\lambda = 0.633\ \mu m$. The refractive index of the dielectric medium at this wavelength is $n = 1.411$ and has a negligable imaginary component ($\Im m[n] < 10^{-7}$). The cross-sections presented for the dielectric diffuser have not been normalized in an absolute manner, although they are relatively comparable.

The cross-sections I_p and I_s in Figure 6.16A are the same as were previously reported in § 4.5.3 for the incident polarizations TM and TE, respectively. The measurements in Figure 6.16b represent the cross-sections I_+ and I_- for an incident beam, linearly polarized at an angle of $+45°$ to the plane of incidence, i.e. $S_0 = S_+$. I_- has an almost featureless distribution for $|\theta_s| \lesssim 50°$ and appears to be the average of I_p and I_s. Plotting I_+ against the expanded, right-hand axis has revealed a clearly defined enhanced backscatter peak with subsidiary maxima. An explanation of this remarkable result can be found in the following discussion.

Discussion

It has already been established in § 4.5.3 that light reflection from this transparent diffuser is dominated by single scattering mechanisms. Since the refractive index has virtually no imaginary component, Fresnel's reflection coefficients are real and have the forms illustrated in Figure 6.17. The I_p cross-section in Figure 6.16a does not exhibit a null reflectance other than at the grazing angles. From Figure 6.17 we may therefore assume that the local incidence angle for the first reflection is less than the Brewster angle $|\theta_i| < \theta_B$, in which case the reflection coefficients may be written as $r_p = |r_p|$ and $r_s = -|r_s|$. Applying the same arguments as in the discussion for metallic scattering, we can show that the I_- cross-section is dominated by single interactions, whereas I_+ will be sensitive to any double scattering events. We can clearly see that the I_+ cross-section in Figure 6.16b exhibits enhanced backscatter including subsidiary maxima, an effect not observed before from a dielectric diffuser in such detail.

Towards grazing scattering angles, p reflectance will be suppressed as the local incidence angle approaches the Brewster angle $|\theta_i| \to \theta_B$ and the reflected light will tend to be s polarized. This explains the lobe structure observed for I_+ at scattering
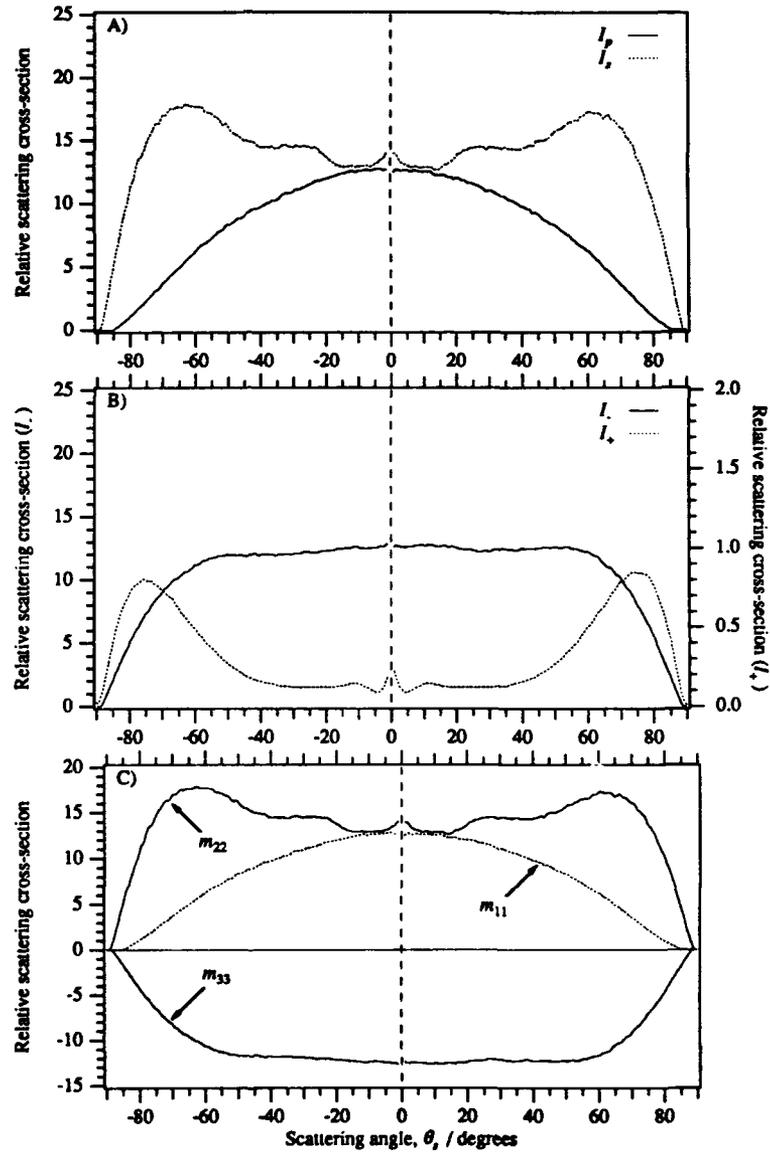
Figure 6.16: A) and B) Stokes' parameters of linearly polarized light scattered from dielectric diffuser #46. $\tau = 3.18\ \mu m$, $\sigma_h = 1.22\ \mu m$; refractive index $n = 1.411$; wavelength $\lambda = 0.633\ \mu m$; incidence angle $\theta_0 = 0°$. C) Characteristic Mueller matrix elements of dielectric diffuser #46 for $\theta_0 = 0°$.
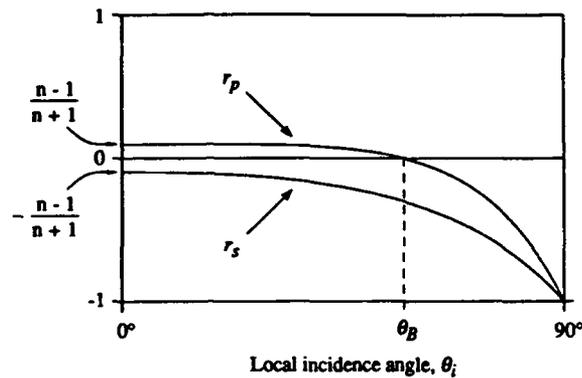
Figure 6.17: Fresnel's amplitude reflection coefficients for p and s polarized light. Reflection from a flat, dielectric medium of real refractive index n.

angles $|\theta_s| \gtrsim 50°$. Since the reflection coefficients are real, the scattered light will remain linearly polarized, only its amplitude and orientation will be altered. For normal incidence, the I_+ cross-section is much smaller than I_-, hence measuring I_- is similar to measuring I_p and I_s simultaneously. Although the right and left circular cross-sections are not presented, measurements have shown that they are negligably different from each other. This indicates that the reflection coefficients are indeed real, since the scattered light has no preferred handedness. Combining the measured scattering cross-sections we can construct the Mueller matrix elements from Stokes' parameters; see Figure 6.16c. The fourth element m_{34} vanishes for light which is linearly polarized, leaving only three, non-zero matrix elements for a non-absorbing, dielectric medium.

Similar measurements have been taken from the same diffuser for the incidence angle $\theta_0 = -20°$; see Figure 6.18. A small backscatter peak is still visible for $\theta_0 = -20°$ in the expanded I_+ cross-section of Figure 6.18b. The lobe structure of I_+ has become exaggerated towards foward grazing angles as the light becomes more s polarized (note the null reflectance in the I_p cross-section of Figure 6.18a while that of I_s is still appreciable). Increasing the incidence angle to $\theta_0 = -40°$, Figure 6.19b, I_+ and I_- become more skewed but no backscatter peak is displayed for I_+. Experimentally, a peak was still observed in the backscatter direction at this incidence angle when the detector was switched to a higher sensitivity.
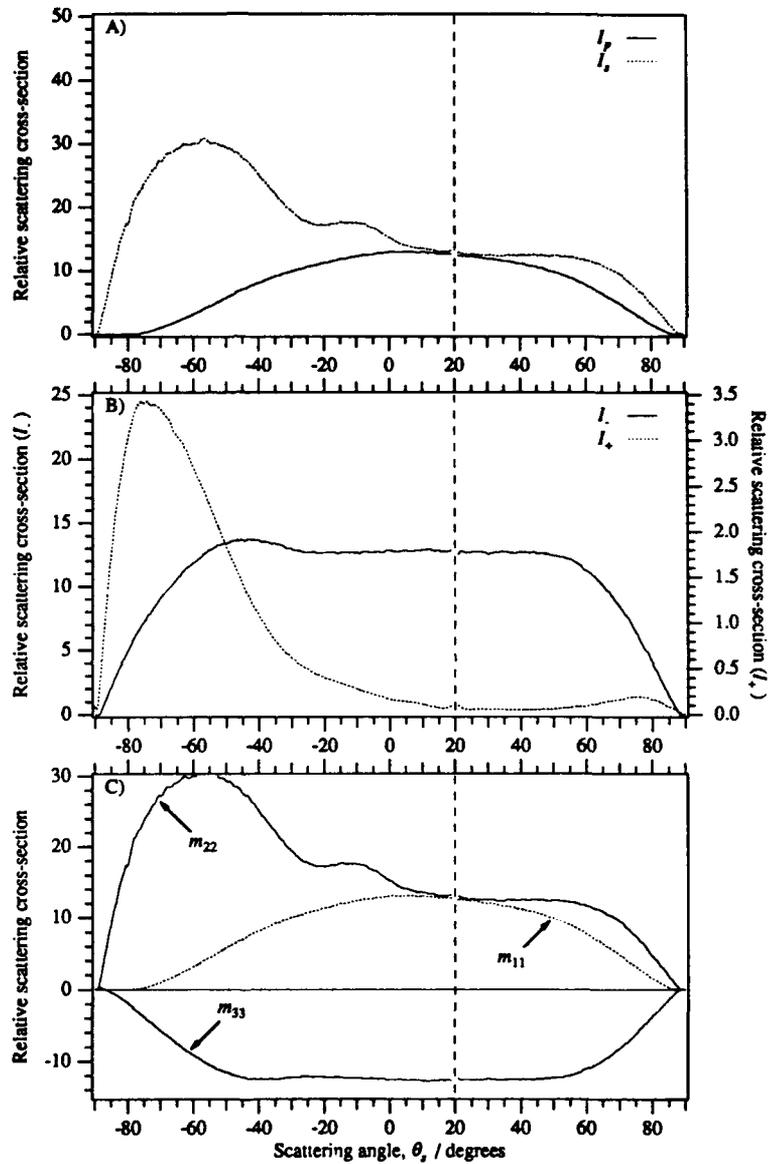
Figure 6.18: A) and B) Stokes' parameters of linearly polarized light scattered from dielectric diffuser #46. $\tau = 3.18\ \mu m$, $\sigma_h = 1.22\ \mu m$; refractive index $n = 1.411$; wavelength $\lambda = 0.633\ \mu m$; incidence angle $\theta_0 = -20°$. C) Characteristic Mueller matrix elements of dielectric diffuser #46 for $\theta_0 = -20°$.
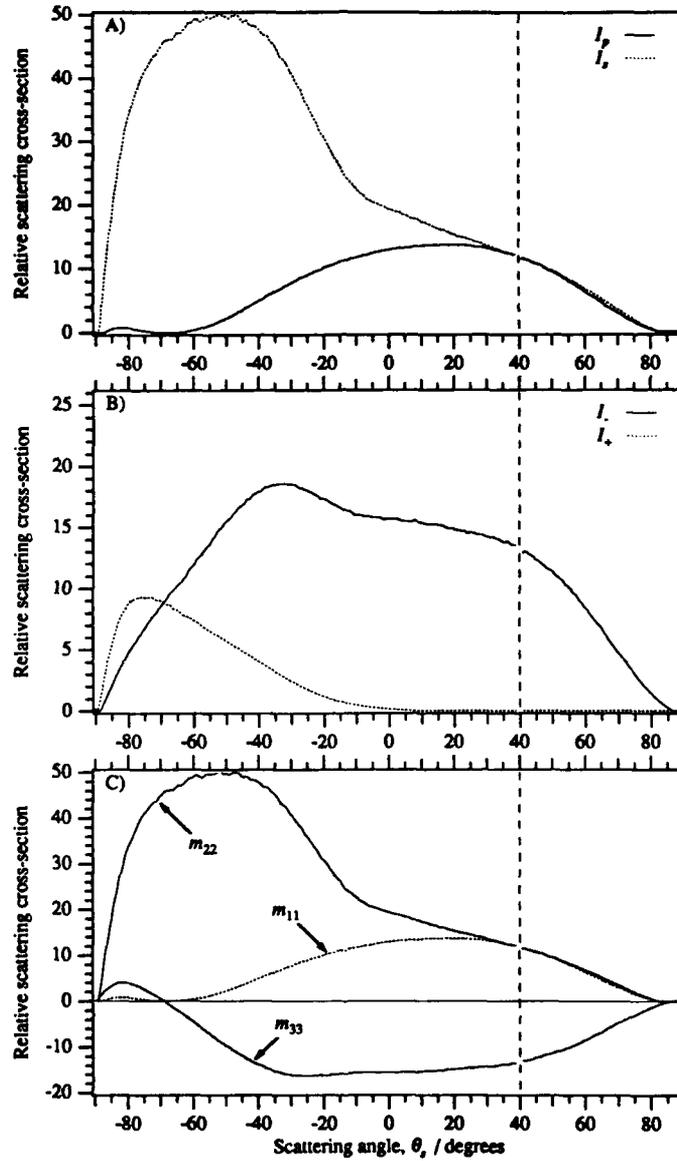
Figure 6.19: A) and B) Stokes' parameters of linearly polarized light scattered from dielectric diffuser #46. $\tau = 3.18\ \mu m$, $\sigma_h = 1.22\ \mu m$; refractive index $n = 1.411$; wavelength $\lambda = 0.633\ \mu m$; incidence angle $\theta_0 = -40°$. C) Characteristic Mueller matrix elements of dielectric diffuser #46 for $\theta_0 = -40°$.

Comparing the Mueller matrix elements for the dielectric diffuser in Figures 6.16c, 6.18c, and 6.19c to those for the metallic diffuser in Figure 6.15, apart from the different scattering distributions of m_{11} and m_{22}, it is clear that elements m_{33} and m_{34} are strongly dependent on the diffuser's material properties.

6.4   Thin-film, dielectric diffusers

In sections 4.5.3 and 6.2.2 we have shown how enhanced backscattering can be induced in the light scattering properties of dielectric diffusers, which do not otherwise show the effect. Although the angular dependence of the scattering cross-sections in Figure 6.8 was not particularly sensitive to an increase in the refractive index, the degree of multiple scattering was greatly affected leading to backscatter enhancement of s polarized light. Replacing the semi-infinite dielectric medium by a thin-film, dielectric diffuser on a reflecting substrate, the p and s scattering cross-sections are completely changed and exhibit strongly enhanced backscatter.

6.4.1   Diffuser fabrication

Employing the methods described in § 3.3.3, a randomly rough diffuser can be etched into the surface of a photoresist-coated substrate. The method of transferring the rough surface into a thin dielectric film is unfortunately a destructive one, and so the photoresist profile must be characterized at this stage.

Preparing a sample of the silicone elastomer used to form the dielectric replicas in § 3.5, a few drops are applied to the centre of the photoresist diffuser. By spinning the substrate on a turntable, the elastomer spreads to form an approximately uniform film over the rough surface. The thickness of the film can be controlled to a certain extent by the spin-speed and the quantity of elastomer; ~ 10 drops of silicone spun at ~ 2000 r.p.m. can produce a film thickness of ~ 10 μm. After curing (see § 3.5), the dielectric film is removed by immersing the substrate in acetone. The photoresist dissolves away and, with a little encouragement, the thin film floats to the surface. If the film has some directionality (e.g. a one-dimensional diffuser) it should be identified in some way *before* immersion, e.g. removal of a corner. The best method of removing the film from the surface, without touching it, is to scoop it out onto an aluminium slide mount *diffusing-side-down*. For a one-dimensional diffuser this is not

a trivial problem since the surface corrugations have to be aligned. The elastomer is a fairly robust material, even as a thin film, and will not degrade if it takes some time to remove from the acetone bath! With a certain amount of dexterity and luck, the mounted diffuser will look something like the illustration in Figure 6.20. The final
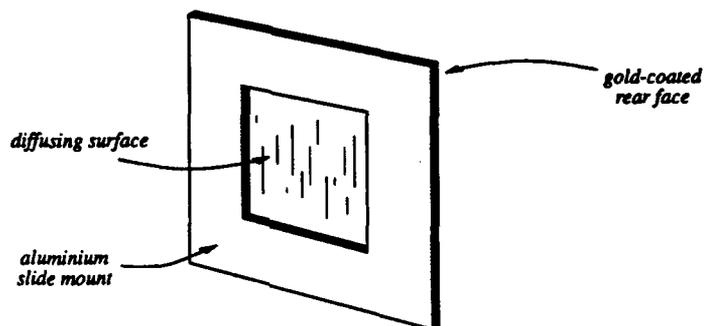
Figure 6.20: Mounting of a one-dimensional, thin-film, dielectric diffuser allowing access to front and back faces.

stage is the application of a gold-coating to the plane, back face using standard evaporation techniques. The coating process itself should be fairly quick since prolonged exposure to high temperatures can cause the elastomer to distort.

6.4.2   Experimental measurements

The motivation for investigating this type of scattering system came from the work of Jakeman and Tapster [41, 42, 75] studying the light scattering properties of a deep, random phase screen placed in front of a mirror. This particular system displays a strongly enhanced intensity in the backscatter direction.

The scattering cross-sections presented in Figure 6.21 were measured from dielectric diffuser #50, with approximately 9 μm separating the diffusing surface from its gold-coated substrate. The original photoresist surface of diffuser #50 was characterized as having the statistical parameters $\tau = 3.06 \pm 0.05$ μm and $\sigma_h = 1.15 \pm 0.02$ μm, using the methods described in § 3.4. The cross-sections for normal incidence, Figures 6.21a and 6.21d, have a normal-like distribution about a strong peak in the backscatter direction. Subsidiary peaks are observed for the shorter wavelength,
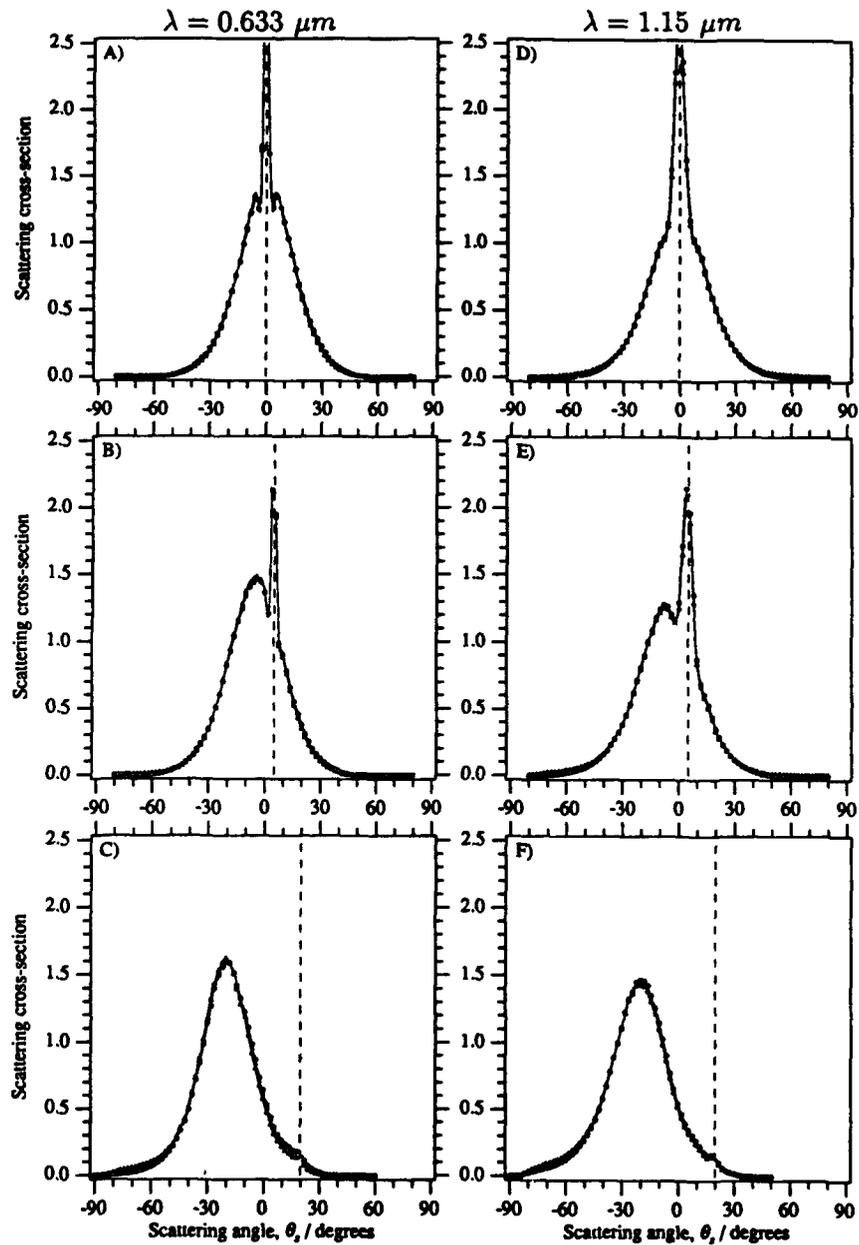
Figure 6.21: Experimental scattering cross-sections measured from thin-film, dielectric diffuser #50 on a gold-coated substrate. $\tau = 3.06\ \mu m$, $\sigma_h = 1.15\ \mu m$; mean thickness $\approx$ 9 μm. $\Xi_{pp}(\theta_0,\theta_s)$ [o]; $\Xi_{ss}(\theta_0,\theta_s)$ [Δ]: A) and D) $\theta_0 = 0°$, B) and E) $\theta_0 = -5°$, C) and F) $\theta_0 = -20°$. Refractive index $n(\lambda = 0.633\ \mu m) = 1.411$; $n(\lambda = 1.15\ \mu m) = 1.399$.

whereas the longer wavelength only exhibits a wider backscatter peak. Increasing the incidence angle, the normal distribution remains centered about the specular direction $\theta_s = \theta_0$ and the backscatter peak gradually reduces in size. For $\theta_0 = -20°$ incidence, Figures 6.21c and 6.21f, the width of the incoherently scattered distribution is just wide enough for a small backscatter peak to be observed. Rigorous calculations of light scattering from thin-film diffusers have shown close quantitative agreement with the experimental results in Figure 6.21b [47].

The scattering cross-sections presented in Figure 6.22 were measured from diffuser #50, but this time for the longer wavelength $\lambda = 3.39\ \mu m$. The dominant feature in all of these cross-sections is the coherent reflection in the specular direction. Although no peak is observed, the cross-sections do show a slight bias in the backscatter direction. Interesting fringe structure accompanies the coherent reflection and is quite vivid for $\theta_0 = -20°$, Figure 6.22d. This structure is thought to be caused by the interference between plane wave components reflected from the diffusing surface and the flat substrate, in a manner similar to that from a Fabry-Perot interferometer.

Using a physical optics approach, Jakeman identifies two possible mechanisms leading to backscatter enhancement [42]. The first is the constructive interference between time-reversed light paths, as previously encountered in § 4.5.2, except the reflecting substrate allows passage through *different* surface inhomogeneities. The second mechanism relies on the reflecting substrate lying in the focusing region of the diffusing surface. Each lens-like asperity will form a focus at some point below the surface, in much the same way as the patterns are formed on the floor of a shallow pool of disturbed water. If the focus occurs on the substrate, the reflected light will pass back through the same lens-like asperity producing a random 'corner-cube' effect and geometrical backscatter enhancement.

The focusing region occurs approximately at a depth δ given by

$$\delta \approx \frac{1}{2\sqrt{3}} \frac{\tau^2}{\sigma_h} \frac{n}{(n-1)}$$

The mean thickness of diffuser #50 is $d \approx 9\ \mu m$ compared with a focusing depth of $\delta \approx 8.2\ \mu m$, which would explain the strong enhancement observed in Figure 6.21. Moving the reflecting substrate away from the focusing region, the corner-cube mechanism would not be supported and the interference backscattering mechanism would
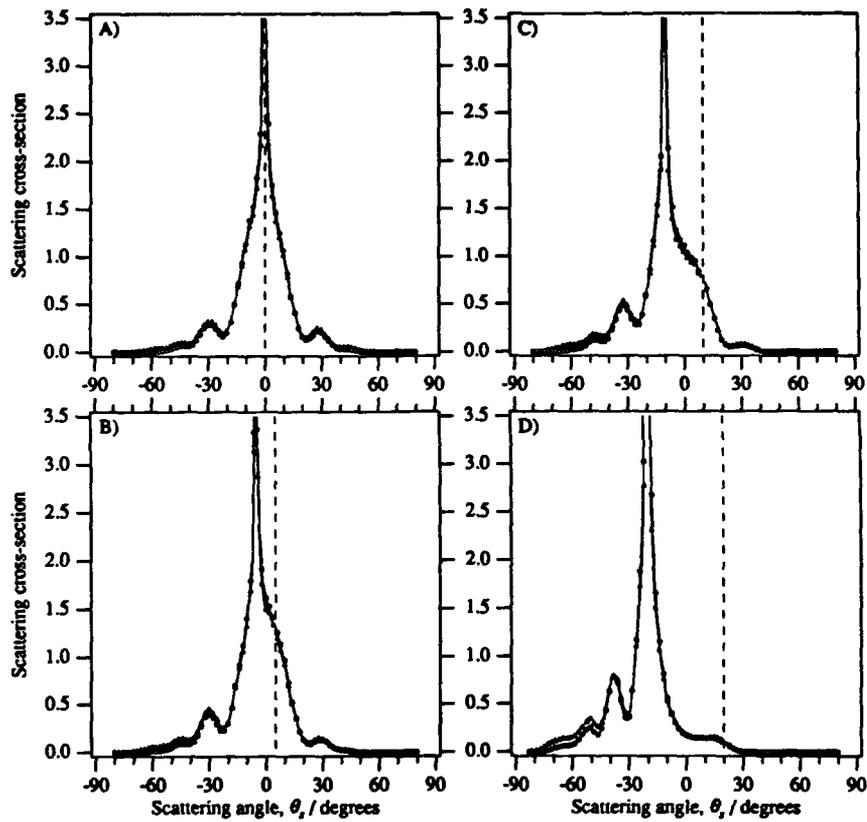
Figure 6.22: Scattering cross-sections measured from thin-film, dielectric diffuser #50 on a gold-coated substrate. $\tau = 3.06$ μm, $\sigma_h = 1.15$ μm; mean thickness $d \approx 9$ μm; wavelength $\lambda = 3.39$ μm; refractive index $n = 1.412$. $\Xi_{pp}(\theta_0, \theta_s)$ [o]; $\Xi_{ss}(\theta_0, \theta_s)$ [△]: A) $\theta_0 = 0°$, B) $\theta_0 = -5°$, C) $\theta_0 = -10°$, D) $\theta_0 = -20°$.

dominate. The reflecting substrate allows for the first and last scattering events along a light path to be widely separated. From the discussion in § 4.5.2 we would therefore expect the backscatter peak to be reduced in size and considerably narrower for a thick film, dielectric diffuser. The scattering cross-sections in Figure 6.23 were measured from diffuser #52 which has the parameters $\tau = 3.70 \pm 0.08$ μm and $\sigma_h = 1.30 \pm 0.02$ μm, and a mean thickness of $d \approx 50$ μm. The incoherent distri-
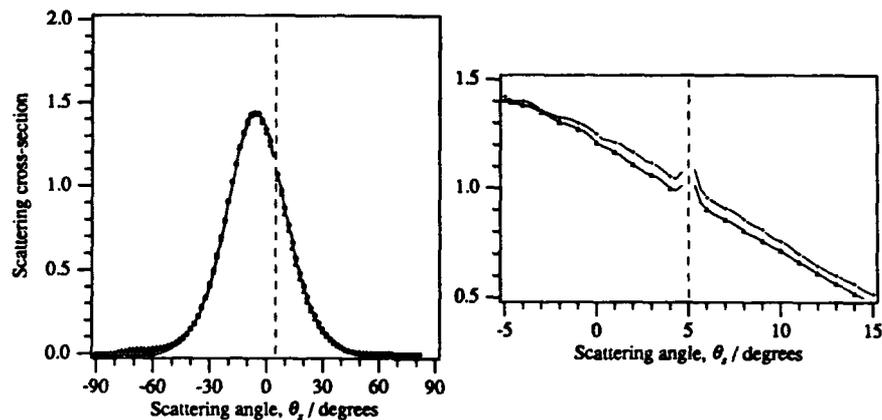
Figure 6.23: Scattering cross-sections measured from thin-film, dielectric diffuser #52 on a gold-coated substrate. $\tau = 3.70$ μm, $\sigma_h = 1.30$ μm; mean thickness $d \approx 50$ μm. $\Xi_{pp}(\theta_0, \theta_s)$ [o]; $\Xi_{ss}(\theta_0, \theta_s)$ [▵]: $\theta_0 = -5°$. Wavelength $\lambda = 0.633$ μm; refractive index $n = 1.411$.

butions are very similar to those of diffuser #50 except for the apparent absence of a backscatter peak. In fact the peak is so narrow that it is below the resolution of the measuring equipment. The inset graph was measured over a very short range of angles around backscatter and displays a small, narrow peak in each cross-section.

The photograph in Figure 6.24a emphasizes how narrow the backscatter peak is. Diffuser #52 is inside the spherical screen and is illuminated by a diverging, *s* polarized laser beam ($\lambda = 0.633$ μm) which enters through the small hole. The black lines represent the horizontal and vertical directions; the surface corrugations are parallel to the vertical direction. As can be seen from the photograph, the one-dimensional nature of the diffuser confines the scattered light to a narrow distribution about the horizontal plane. A bright vertical line can be seen across the entrance hole and this is the enhanced backscatter peak; its position does not change as the diffuser
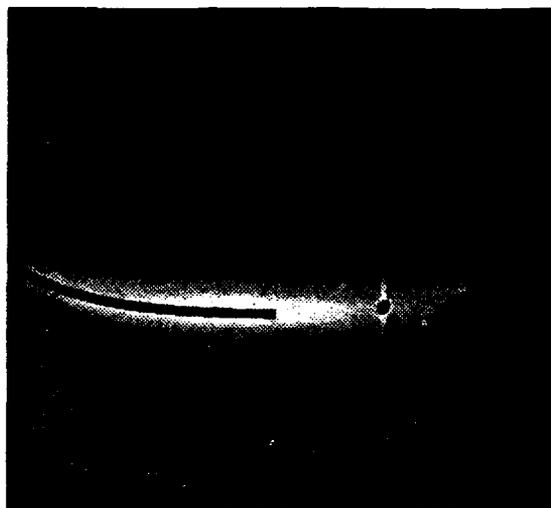
Figure 6.24: Demonstrations of the light scattering properties of thin-film, dielectric diffuser #52; $\tau = 3.7\ \mu m$, $\sigma_h = 1.3\ \mu m$, $\lambda = 0.633\ \mu m$. Upper photograph: planar light scattering; a narrow backscatter peak can be seen across the entrance hole. Lower photograph: oblique incidence; the scattered light describes a conic surface but displays no enhancement.

is rotated about its vertical axis.

An interesting effect occurs if the diffuser is tilted about its horizontal axis instead of its vertical axis. In Figure 6.24b the diffuser has been rotated through 45° about its mean surface normal and then tilted backwards slightly. The incident linear polarization has also been rotated through 45°. The scattered light is no longer confined to a plane but, instead, describes the surface of a cone. As can be seen from the photograph there is no enhanced backscatter; the incoherently scattered light is smoothly distributed over the conic surface. The term *backscatter* is used rather loosely here because, strictly speaking, there is no backscattered light. If the mechanisms producing the backscatter peak were still supported the peak would appear between the horizontal and vertical markers on the screen.

What has happened here is that the time-reversal symmetry between scattering events has been broken. Because the dielectric medium is transparent and many wavelengths thick, there is likely to be only one light path connecting any two scattering centres; light incident on the second scattering centre will be transmitted and reflected to a third scattering centre, not the first. Hence there are no interference effects in the incoherently scattered light.

If we now examine diffuser #50 under the same experimental conditions as for diffuser #52 an unusual effect is revealed. Diffuser #50 has a much thinner dielectric film than diffuser #52 and we have already seen how its enhanced backscatter peak is much wider. This is demonstrated in the planar scattering geometry of Figure 6.25a compared to that of Figure 6.24a. If the diffuser is now rotated and tilted as before, we can see from the photograph in Figure 6.25b that the peak and minima associated with backscatter remain features of the scattered light. Although time-reversal symmetry was broken for diffuser #52, diffuser #50 apparently still supports some form of time-reversible scattering mechanism. Arguments for a possible mechanism may be found in the following discussion.

Discussion

Dielectric slabs on conducting planes can support TEM surface waves [24, page 485]. These surface waves propagate in a zig-zag fashion within the slab in much the same way as an optical fibre guides a light field. The incident and scattered radiation
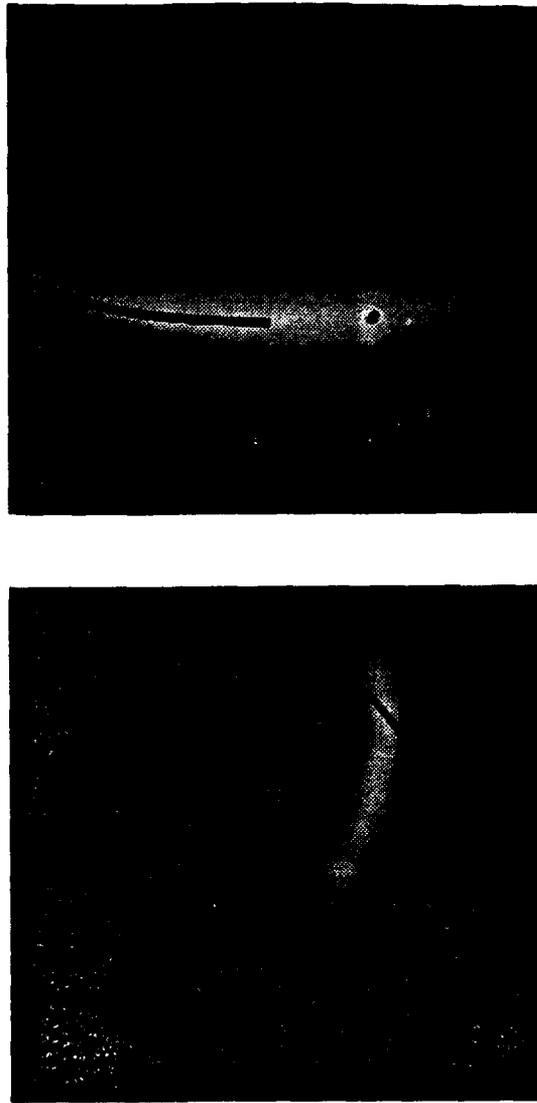
Figure 6.25: Demonstrations of the light scattering properties of thin-film, dielectric diffuser #50; $\tau = 3.1\ \mu m$, $\sigma_h = 1.1\ \mu m$, $\lambda = 0.633\ \mu m$. Upper photograph: planar light scattering; a wide backscatter peak can be seen across the entrance hole. Lower photograph: oblique incidence; the scattered light describes a conic surface and also displays enhanced structure.

fields can couple with surface waves via the surface roughness of the air/dielectric interface. In this way surface waves can form the intermediate, time-reversible step between two scattering events, leading to interference effects in the scattered light fields. The reason why diffuser #52 does not support a time-reversible mechanism, as Figure 6.24b suggests, is presumably because the surface waves are too strongly damped in the thicker dielectric film, but this has yet to be confirmed.

6.5   Antibackscatter enhancement

6.5.1   Experimental observation

The investigations of oblique scattering from thin-film, dielectric diffusers leads us to the final scattering system which will be considered in this chapter. We return to the case of scattering from a one-dimensional, metallic difuser, but this time for obliquely incident light, i.e. the incidence plane is not perpendicular to the surface grooves.

For this experiment we have used an aluminium-coated diffuser (#5) with the roughness parameters $\tau \sim 3\ \mu m$ and $\sigma_h \sim 2\ \mu m$. During fabrication this diffuser was over-developed to expose parts of the substrate; whilst being very rough the diffuser also produces a coherent reflection, enabling the specular direction to be determined. The photograph in Figure 6.26a shows the usual case where the incident and scattered light fields are co-planar. Strong backscatter enhancement is observed across the entrance hole and, although the photograph is not clear, up to second order minima were seen. The specular reflection actually coincides with the first order maximum to the right of the backscatter peak.

Rotating the diffuser through 45° and tilting it backwards slightly, the incidence plane is no longer perpendicular to the grooves and the scattered light describes a conic surface. As can be seen from the in Figure 6.26b, the scattering mechanisms responsible for the enhanced backscatter in Figure 6.26a produce the same structures in the *antibackscatter* direction (the mirror image of the backscatter direction, the mirror being parallel to the mean surface normal and perpendicular to the grooves). The specularly reflected light is actually at the intersection of the scattered light and the upper vertical marker. Rotating the linear polarization of the incident beam had no effect on the antibackscatter structure. Figure 6.27 illustrates the scattering geometry for this case.
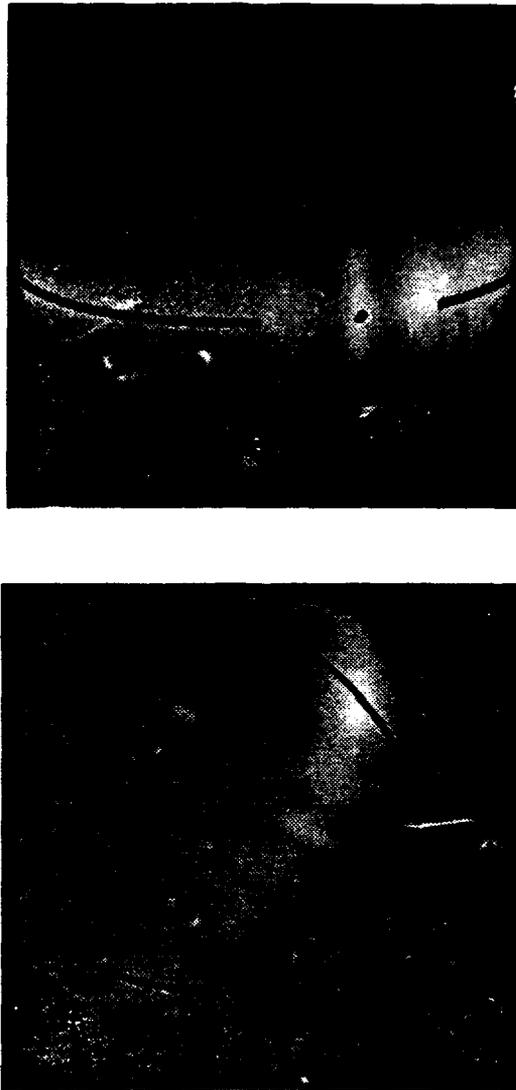
Figure 6.26: Demonstrations of the light scattering properties of aluminium-coated diffuser #5; $\tau \sim 3\ \mu m$, $\sigma_h \sim 2\ \mu m$, $\lambda = 0.633\ \mu m$. Upper photograph: planar light scattering; strong backscatter structure can be seen around the entrance hole. Lower photograph: oblique incidence; the scattered light describes a conic surface and also displays enhanced structure.
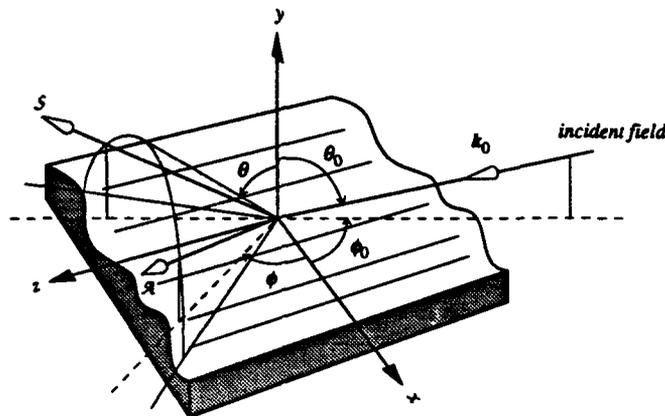
Figure 6.27: The scattering geometry for oblique incidence. The scattered light describes a conical surface orientated parallel to the surface grooves, determined by the dispersion relation $k_0^2 = k_x^2 + k_y^2 + k_z^2$. $\mathcal{A}$: antibackscatter direction, $\theta = \theta_0$, $\phi = \phi_0$; $\mathcal{S}$: specular direction, $\theta = \theta_0$, $\phi = \pi - \phi_0$.

This observation of antibackscatter enhancement supports theoretical studies carried out by Depine of oblique incidence scattering from randomly rough surfaces and random impedance planes [28, 27]. The work of Depine suggests that the enhancement in the conical scattering case (antibackscatter) is closely related to the surface wave phenomena associated with backscatter enhancement in planar scattering problems; a result which was suggested in the discussion at the end of § 6.4.2 as an explanation of the antibackscatter enhancement observed from thin-film, dielectric diffuser #50 in Figure 6.25b. It would appear then that the phenomenon of enhanced backscattering from one-dimensional diffusers is a special case of the more general oblique incidence problem; the enhanced features in the obliquely scattered light are present for all of the diffusers except the thick-film, dielectric diffuser #52 in Figure 6.24.

The broad, enhanced structure of the scattered light is present for oblique illumination of diffusers #5 and #50. In comparison the much narrower structure displayed by diffuser #52 is only present for the true case of light scattered back towards the source. The difference between the angular widths of the enhanced structures is indicative of the scales over which the scattering mechanisms occur; wide structures suggest that the light is scattered within a small region, whereas the narrow structures

indicate long range scattering mechanisms.

Chapter 7

Concluding Remarks

The scattering of light from one-dimensional, randomly rough diffusers has been investigated through controlled optical experiments and comparisons with light scattering simulations from a number of theoretical studies. The experiments were carried out using characterized Gaussian diffusers having statistical roughness parameters of the same order as the illuminating wavelength τ, $\sigma_h \sim \lambda$, where τ is the $1/e$ correlation length, σ_h is the r.m.s. height, and λ is the radiation wavelength. This degree of roughness is sometimes referred to as the *resonance regime* of scattering, falling between the perturbation (small scale) and physical optics/Kirchhoff (large scale) regimes. The mathematical models which were considered include the numerical solution of a rigorous integral equation; an analytical transmission-line approach equivalent to Bahar's "full wave" scattering theory; and geometrical ray-tracing.

In chapter two, results are presented of the scattering cross-sections for a flat surface of compacted $BaSO_4$ powder. Apart from the Lambertian-like distribution expected from this reflection standard, a sharply defined backscatter peak was observed in the incoherently scattered light. The reflected light was strongly depolarized from the incident linear TM and TE polarizations due to multiple scattering within the $BaSO_4$ medium. In accord with multiple scattering theories, a possible mechanism for the enhanced backscatter peak is the constructive interference between forward and time-reversed light paths which occurs in the backscatter direction [2]. From the discussion in § 4.5.2, higher order interference effects are washed out by multiple scattering which explains why no subsidiary structures were observed. The differences in backscatter enhancement between co and cross-polarized measurements are compatible with volume scattering phenomena [2, 67]. In particular the cross-

polarized light paths are only partially coherent in the backscatter direction and do not give as strong an enhancement as the co-polarized paths.

Fabrication and characterization of randomly rough diffusers is discussed in chapter three. A method is described of replicating the diffusing profile into a transparent, dielectric medium enabling the scattering properties of a metallic diffuser to be compared to those of its dielectric replica. The diffusers considered throughout this dissertation have been rough in only one dimension, i.e. they are random gratings. The reason for this is to accomodate presently developed rigorous models which are limited to scattering in one dimension only; the production of one-dimensional, characterized diffusers is therefore of great importance in these early stages of development.

In chapter four, rigorous integral equations are presented for the far-field TM and TE scattering cross-sections from a derivation based on the Helmholtz-Kirchhoff integral equation. Theoretical calculations for one-dimensional, perfectly conducting and non-absorbing dielectric diffusers are critically compared with experimental measurements from characterized diffusers. Over the visible and near infra-red wavelengths considered, the measurements from a gold-coated diffuser (a good conductor) exhibit strong backscatter enhancement, whereas those from an identical dielectric diffuser show no enhancement at all. Theoretical studies in chapter six demonstrate that one difference between metallic and dielectric scattering is the degree to which multiple-scattering mechanisms contribute to the light field in relation to those of single-scattering. The interaction mechanisms for dielectric diffusers of the type investigated are almost entirely single-scattering because the medium is highly transparent. At each localized interaction most of the incident light is transmitted and only a small amount is reflected from the surface. These arguments and the observed differences between the metallic and dielectric scattering cross-sections tend to indicate that backscatter enhancement is a multiple scattering phenomenon. A simple geometrical argument, based on a multiple scattering mechanism, suggests the linear relationship

$$\Delta\theta \propto \frac{\lambda}{\tau}$$

where $\Delta\theta$ is the backscatter peak width. Analysis of the experimental cross-sections from metallic diffusers for the shorter wavelengths appears to support this relation, particularly towards the geometrical optics limit ($\lambda \rightarrow 0$).

Agreement between rigorous theory and experimental measurements is quite reasonable near normal incidence, but generally deteriorates for larger incidence angles; the metallic experimental results for all but the longest wavelength considered exhibit enhanced backscatter peaks up to 40° incidence, unlike the calculations. The theory, however, does reproduce all of the general features observed in the experiments on metallic and dielectric diffusers. The best agreement between theory and experiment, including large incidence angles, was found to be when the surface parameters were smaller than the illuminating wavelength $\tau, \sigma_h \lesssim \lambda/3$. For this scale of surface roughness a coherent, or specular, component is present and increases in strength as the surface appears shallower to the incident wavelength. No backscatter enhancement was observed for the longest wavelength considered ($\lambda = 10.6 \ \mu m$), although the incoherently scattered TM radiation did exhibit a maximum in the backscatter direction.

The analysis discussed in chapter five uses a transmission line approach to solve the one-dimensional scattering problem and leads to an analytical solution. This solution differs from the integral equation method described in chapter four in that it only requires the statistical parameters of the surface profile to calculate the scattering cross-sections, not an ensemble of random profiles. The final expressions for the scattered fields only require numerical evaluation for each pair of incidence and scatter angles, which is far less computationally intensive than the Monte-Carlo method. The formulation of an analytic solution poses a more complicated problem to solve than does the problem of scattering from a deterministic profile. The electromagnetic fields above and below a flat, semi-infinite, vacuum/dielectric interface illuminated by a plane wave are shown to be composed of two continuous eigenmode expansions (radiation and lateral waves) and a discrete expansion (surface waves). The first stage in the transmission line approach is to introduce a small step height into the flat dielectric surface. The height discontinuity introduces a small perturbation to the eigenmode expansions which, to first order, is the field scattered by the step. Treating a rough surface as a sequence of discontinuous steps, the total single-scattered field can be described as the continuous integral along the surface of all such locally perturbed fields. Modelling a surface profile in this way has no limitation on the surface height which can be represented, but will only be valid for surfaces with low slopes and large curvatures. This analysis leads to a set of field equations for a one-

dimensional, randomly rough diffuser which are identical to those presented by Bahar employing "full-wave" theory [6]. Despite implied accuracy by Bahar the calculations in chapter five indicate that, for surface structures in the resonance regime, there are large discrepancies between the experimental measurements and "full-wave" theory. The best agreement is found to occur for scattering from a dielectric diffuser when considering the so-called "iterative" solution outlined above. Light scattering from a dielectric surface is dominated by single-scatter interactions, yet Bahars "extended" full-wave theory does not reproduce the qualitative features observed in the experimental scattering cross-sections. The validity of the steps transforming the iterative solutions into the extended full-wave solutions must therefore be in question.

The third model which was used to investigate how light is scattered by rough surfaces is that of geometrical ray-tracing and is considered in chapter six. Conceptually the principles behind light rays and their interaction with media are simplistic but, having said that, the calculated cross-sections are remarkably similar to the experimental measurements. Taking the phase of each ray into account and treating a metallic diffuser as an impenetrable surface, it is demonstrated how a backscatter peak is present only in the double-scatter (multiple scattering) term. Light scattered from an identical dielectric diffuser is dominated by single-scatter interactions and so multiple-scatter mechanisms are very much suppressed. The absence of a backscatter peak in this calculation demonstrates how backscatter enhancement is associated with multiple scattering mechanisms. What the geometrical model loses in mathematical rigour it gains in analytical power. This is particularly well demonstrated in the calculations of the field transmitted by a dielectric diffuser. It is shown how small but distinct terms in the scattering cross-sections can be attributed solely to multiple scattering contributions.

A complete description of the polarization state of a light field can be achieved by measuring its Stokes parameters. The scattering properties of a diffuser can then be described in terms of a Mueller matrix relating the parameters of the scattered field to those of the incident field. Symmetry can usually be invoked to reduce the number of elements needed for a complete description of the matrix. For a one-dimensional diffuser there are only four independent matrix elements. The elements for identical metallic and dielectric diffusers are presented in chapter six over a range of incidence angles for one wavelength. The measurements yield results which are con-

sistent with identifiable scattering events at the surface; i.e. the contributions from single and double-scattering events are separated. There is strong experimental evidence to support the argument that backscatter enhancement is a multiple-scattering phenomenon. A particular case is where a dielectric scattering cross-section exhibits a very small, but clearly defined, backscatter peak with subsidiary structures which can not be explained by single-scattering arguments.

An alternative form of scattering system is investigated in chapter six, that of a thin-film, dielectric diffuser mounted on a reflecting substrate. The light reflected from such a system is almost entirely multiply scattered since the dielectric medium is highly transparent. The diffusers are analogous to the combination of a random phase screen placed in front of a plane mirror. Experimental and theoretical studies of phase screens with mirrors suggest that they can support a number of multiply scattered, backscatter mechanisms [41]. The experimental cross-sections from the thin-film diffusers certainly exhibit very strong backscatter peaks. It is demonstrated how the width of the peak diminishes as the reflecting substrate is moved away from the diffusing surface. In keeping with diffraction theory, narrower features in the scatter pattern tend to indicate scattering interactions over larger portions of the surface. One would therefore expect that long range mechanisms are dominant for thicker film diffusers.

The final scattering case considered is that of light obliquely incident onto metallic and thin-film, dielectric diffusers. In this case the incident wavevector has a component parallel to the corrugations of the one-dimensional diffuser and the scattered light describes a conic surface. From the photographs presented in chapter six it is clear that the backscatter enhancement so far investigated is a special case of the oblique incidence problem. The structures associated with enhanced backscatter actually appear in the so-called antibackscatter direction (the image of the backscatter direction in a mirror which is parallel to the mean surface normal and perpendicular to the surface grooves). Surface waves excited by the incident radiation could form the intermediate, time-reversible step between the incoming and outgoing waves. Interference effects will then still be present in oblique incidence scattering provided that the forward and reverse surface waves are coherent with one another. The thicker of the two thin-film diffusers only exhibits enhanced scattering close to the true backscatter direction and therefore appears to introduce partial coherence between the interfer-

ing light paths. Precisely which mechanisms lead to antibackscatter enhancement is not intuitively obvious but clearly they are at the root of the enhanced backscatter phenomenon.

Future work

The present studies of rough surface light scattering are leading to a better understanding of how electromagnetic radiation interacts with real materials. Increasingly powerful analytical tools are being developed to curb the limitations of current theoretical models. In particular, advances have been made in theoretical treatments of the two-dimensional scattering problem. There are, however, aspects of light scattering unique to the one-dimensional problem which need to be more fully understood. What Stokes' parameters actually reveal about the scattering mechanisms is not well known, but the simple measurements and calculations for one-dimensional systems may yield valuable information applicable to more complicated systems. Of immediate relevance to enhanced backscattering mechanisms are studies of the oblique incidence problem and the conditions under which antibackscatter enhancement occurs. There is no equivalent problem for scattering from a two-dimensional surface.

Appendix A

Mathematical Appendix

A.1   The Helmholtz-Kirchhoff Integral Equation

If a volume $\mathcal{V}$ is bounded by a surface S, then for two scalar functions φ and ψ which are finite, continuous, and can be differentiated twice in the region $\mathcal{V}$,

$$\int_{\mathcal{V}} \left(\varphi \nabla^2 \psi - \psi \nabla^2 \varphi \right) dV = \oint_S (\varphi \nabla \psi - \psi \nabla \varphi) \cdot d\mathbf{S} \tag{A.1}$$

which is known as *Green's second theorem*. The proof of this theorem stems from Gauss' Law (or the divergence theorem) which relates the net outflow of a scalar field from the volume $\mathcal{V}$ (likening the field to a fluid) to its flux through the enclosing surface S. The surface element $d\mathbf{S} = \mathbf{n}dS$, where $\mathbf{n}$ is the unit normal and is positive when pointing outwards from the enclosed volume. The enclosing surface may consist of a number of separate surfaces, such as those shown in Figure A.1. In this case the
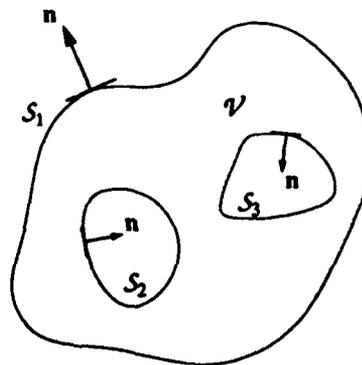
Figure A.1: Volume $\mathcal{V}$ bounded by three surfaces: S_1, S_2, and S_3.

surface integral in equation (A.1) becomes

$$\oint_S (\cdots) \cdot d\mathbf{S} = \oint_{S_1} (\cdots) \cdot d\mathbf{S} + \oint_{S_2} (\cdots) \cdot d\mathbf{S} + \oint_{S_3} (\cdots) \cdot d\mathbf{S}$$

Green's theorem is a very important relationship for solving boundary-value problems in electromagnetic theory.

Many problems in electromagnetic theory can be reduced from the vectorial, transverse-wave descriptions of Maxwell's equations to source-free, scalar-wave equations of the form

$$\nabla^2 \phi(\mathbf{r}) + k^2 \phi(\mathbf{r}) = 0$$

which is known as the *scalar Helmholtz equation*. The field $\phi(\mathbf{r})$ describes some scalar component of, e.g., the electric field, either E_x, E_y, or E_z, and the constant $k = 2\pi/\lambda$ is the wavenumber. In the presence of sources $j(\mathbf{r})$ (i.e. contained in the volume of interest) the field $\phi(\mathbf{r})$ is a solution of the inhomogeneous Helmholtz equation

$$\nabla^2 \phi(\mathbf{r}) + k^2 \phi(\mathbf{r}) = -j(\mathbf{r}) \tag{A.2}$$

Green's second theorem can be used to obtain a solution to equation (A.2) within a volume $\mathcal{V}$, subject to certain boundary conditions at the enclosing surface $\mathcal{S}$.

In order to implement equation (A.1) a second, arbitrary, well-behaved scalar field must be found. The field $G(\mathbf{R}) = (1/4\pi R)\, e^{ikR}$ can be shown to satisfy the Helmholtz equation

$$\nabla^2 G(\mathbf{R}) + k^2 G(\mathbf{R}) = 0$$

in a region away from the origin (i.e. $R \neq 0$). In a small, spherical volume $\Delta \mathcal{V}$ of diminishing radius R' about the origin, $G(\mathbf{R})$ can also be shown to satisfy the integral equation

$$\lim_{R' \to 0} \int_{\Delta \mathcal{V}} \left(\nabla^2 G + k^2 G \right) dV = -1$$

In other words, $G(\mathbf{R})$ is a solution of the equation

$$\nabla^2 G(\mathbf{r}, \mathbf{r}') + k^2 G(\mathbf{r}, \mathbf{r}') = -\delta(\mathbf{r} - \mathbf{r}') \tag{A.3}$$

where $\mathbf{R} = \mathbf{r} - \mathbf{r}'$, and $\mathbf{r}'$ is the location of a unit (delta) source. The function $G(\mathbf{r}, \mathbf{r}') = (1/4\pi |\mathbf{r} - \mathbf{r}'|)\, e^{ik|\mathbf{r} - \mathbf{r}'|}$ is commonly referred to as the *spherical Green's function* or *propagation function*. The form of the Green's function depends on the equation which governs the system; it describes the response of a particular system to a unit

(delta) impulse, as may be seen by comparing equation (A.3) with equation (A.2). The delta function $\delta(\mathbf{r})$ has the property that

$$\int_\mathcal{V} \psi(\mathbf{r})\delta(\mathbf{r} - \mathbf{r}')\,dV = \begin{cases} \psi(\mathbf{r}') & \text{if } \mathbf{r}' \text{ is contained in } \mathcal{V} \\ 0 & \text{if } \mathbf{r}' \text{ is outside } \mathcal{V} \end{cases} \tag{A.4}$$

Consider the situation illustrated in Figure A.2. A volume $\mathcal{V}$ is enclosed by a
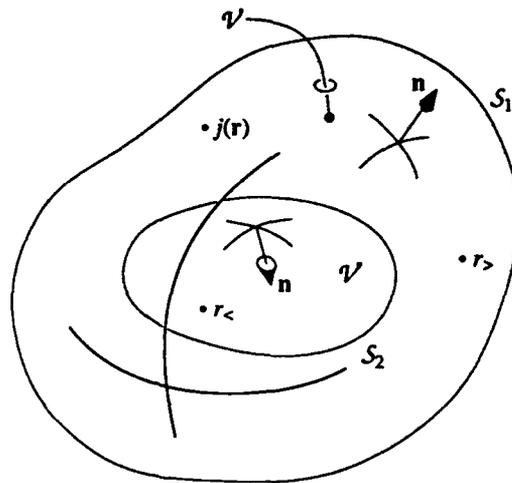
Figure A.2: Volume $\mathcal{V}$ contains a source $j(\mathbf{r})$ and is bounded by surfaces S_1 and S_2. The surface normals n are positive, pointing outwards from $\mathcal{V}$.

surface $S = S_1 + S_2$, with appropriately directed surface normals n. The region *outside* S_1 will be ignored, but the region *outside* S_2 is identified as the volume $\mathcal{V}'$. The volume $\mathcal{V}$ contains source(s) $j(\mathbf{r})$ and volume $\mathcal{V}'$ is a homogeneous, source-free, scattering medium. The labels $r_>$ and $r_<$ denote any points inside the regions $\mathcal{V}$ and $\mathcal{V}'$ respectively.

A.1.1 External field solutions

For an observer in region $\mathcal{V}$, the scalar fields ϕ and G satisfy the inhomogeneous Helmholtz equations

$$\nabla^2\phi(\mathbf{r}) + k^2\phi(\mathbf{r}) = -j(\mathbf{r}) \tag{A.5}$$

$$\nabla^2 G(\mathbf{r},\mathbf{r}_>) + k^2 G(\mathbf{r},\mathbf{r}_>) = -\delta(\mathbf{r} - \mathbf{r}_>) \tag{A.6}$$

Substituting $\nabla^2\phi$ and $\nabla^2 G$ into equation (A.1) and using equation (A.4), we obtain the relation

$$\phi(\mathbf{r}_>) = \int_V j(\mathbf{r})G(\mathbf{r},\mathbf{r}_>)\,dV + \oint_{S_1+S_2}[G(\mathbf{r}_s,\mathbf{r}_>)\nabla\phi(\mathbf{r}_s) - \phi(\mathbf{r}_s)\nabla G(\mathbf{r}_s,\mathbf{r}_>)]\cdot d\mathbf{S} \quad \text{(A.7)}$$

where $\mathbf{r}_s$ denotes a point on the bounding surface S. The volume integral in equation (A.7) is clearly the incident field

$$\int_V j(\mathbf{r})G(\mathbf{r},\mathbf{r}_>)\,dV = \phi_{in}(\mathbf{r}_>)$$

The surface integral in equation (A.7) takes into account the presence of any sources outside the bounding surface S. If the surface S_1 is extended outwards to enclose an infinite region, i.e. $V \to \infty$, then it will contain *all* sources (V' is source-free) and as such the surface integral contribution from S_1 can be shown to vanish. Equation (A.7) can then be written as

$$\phi(\mathbf{r}_>) = \phi_{in}(\mathbf{r}_>) + \Sigma^+(\mathbf{r}_>) \quad \text{(A.8)}$$

where

$$\Sigma^+(\mathbf{r}) = \oint_{S_2^+}[\phi(\mathbf{r}_s)\nabla G(\mathbf{r}_s,\mathbf{r}) - G(\mathbf{r}_s,\mathbf{r})\nabla\phi(\mathbf{r}_s)]\cdot d\mathbf{S} \quad \text{(A.9)}$$

The surface element $\mathbf{n}dS$ has been replaced by $-\mathbf{n}dS$ (i.e. the normal points outwards from region V') and S_2^+ is a bounding surface which is infinitesimally close to the true surface S_2 when approached from region V. At the limit $S_2^+ \to S_2$, equation (A.9) represents the external field contribution from the surface of the scattering region V', i.e. it is the surface-scattered or reflected field. Equation (A.8) is known as the *Helmholtz-Kirchhoff integral equation*, describing the total field outside the scattering medium.

For an observer in region V', $\mathbf{r}_>$ is replaced by $\mathbf{r}_<$ in equation (A.6) and, substituting $\nabla^2\phi$ and $\nabla^2 G$ into equation (A.1), we find, with the help of equation (A.4),

$$0 = \phi_{in}(\mathbf{r}_<) + \Sigma^+(\mathbf{r}_<) \quad \text{(A.10)}$$

Equation (A.10) states that the incident field in volume V' due to the sources in volume V is exactly cancelled by the field induced on the surface S_2^+ (which effectively encloses region V'). This is, in essence, the fundamental principal behind the *Ewald-Oseen extinction theorem* [65].

A.1.2 Internal field solutions

In order to obtain an expression for the field inside volume $\mathcal{V}'$ we must solve the following Helmholtz equations for the source-free region

$$\nabla^2 \phi(\mathbf{r}) + k'^2 \phi(\mathbf{r}) = 0$$
$$\nabla^2 G(\mathbf{r},\mathbf{r}_<) + k'^2 G(\mathbf{r},\mathbf{r}_<) = -\delta(\mathbf{r}-\mathbf{r}_<)$$

Again using equations (A.1) and (A.4), we find for an observer in $\mathcal{V}'$

$$\phi(\mathbf{r}_<) = -\Sigma^-(\mathbf{r}_<) \tag{A.11}$$

where

$$\Sigma^-(\mathbf{r}) = \oint_{S_2^-} [\phi(\mathbf{r}_s)\nabla G(\mathbf{r}_s,\mathbf{r}) - G(\mathbf{r}_s,\mathbf{r})\nabla\phi(\mathbf{r}_s)] \cdot d\mathbf{S}$$

The surface integral $\Sigma^-(\mathbf{r})$ is similar to $\Sigma^+(\mathbf{r})$ except that the limiting case as $S_2^- \to S_2$ is taken approaching S_2 from *inside* the region $\mathcal{V}'$. Equation (A.11) represents the *transmitted* field in a source-free medium, the surface integral $\Sigma^-(\mathbf{r}_<)$ taking account of sources outside S_2^-.

The final solution to be found, for the effects of the internal field as observed from the external region $\mathcal{V}$, is obtained following similar arguments as for the previous cases and is

$$0 = \Sigma^-(\mathbf{r}_>) \tag{A.12}$$

i.e., there is no external field contribution from the integral over the surface just inside S_2. This is somewhat expected since region $\mathcal{V}'$ is source-free.

A.2 The Stürm-Liouville Equation

Many of the guided-wave problems in electromagnetic theory reduce to the solution of a differential equation which has the general form

$$\frac{d}{dx}\left[p(x)\frac{d\phi(x)}{dx}\right] + [q(x) + \lambda\sigma(x)]\,\phi(x) = 0 \tag{A.13}$$

and is known as the *Stürm-Liouville* equation. The functions $p(x)$, $q(x)$, and $\sigma(x)$ are generally continuous over the range of the problem $a \le x \le b$, and λ is a separation constant.

The solutions to equation (A.13) are found by applying certain boundary values at $x = a, b$. These *boundary conditions* may be of the form

$$\phi = 0 \qquad\qquad \frac{d\phi}{dx} = 0$$

or a linear combination of them both. For a given set of boundary conditions there exists an infinite number of possible solutions, or *eigenfunctions*, ϕ_n each with an associated constant, or *eigenvalue*, λ_n. It is a straightforward exercise to show that the orthogonality relationship that exists between two normalized eigenfunctions is

$$\int_a^b \phi_n(x)\phi_m(x)\sigma(x)\, dx = \left\{ \begin{array}{ll} 0 & n \neq m \\ 1 & n = m \end{array} \right.$$

where $\sigma(x)$ takes the form of a weighting function.

A.2.1 Green's function

A very important tool in the solution of boundary-value problems is the *Green's function*. Consider the inhomogeneous Stürm-Liouville equation

$$\frac{d}{dx'}\left[p(x')\frac{d\phi(x')}{dx'} \right] + [q(x') + \lambda\sigma(x')]\,\phi(x') = -f(x') \tag{A.14}$$

where $f(x')$ is an extended source or forcing function driving the system. The Green's function $G(x, x')$ is defined as being the solution of the equation when the driving force is a point source of unit strength, i.e.

$$\frac{d}{dx}\left[p(x)\frac{dG}{dx} \right] + [q(x) + \lambda\sigma(x)]\,G = -\delta(x - x') \tag{A.15}$$

where the Dirac delta function $\delta(u)$ represents a unit source situated at $u = 0$. The solutions to equation (A.14) over the range $a \leq x \leq b$ are subject to the boundary values specifying either ϕ, $d\phi/dx$, or their linear combination at $x = a, b$. If we multiply equation (A.14) by $G(x, x')$ and subtract the result from equation (A.15) multiplied by $\varphi(x)$, after an integration by parts, we obtain

$$\phi(x) = \int_a^b G(x, x')f(x')\, dx' + \left[G(x, x')p(x')\frac{d\phi(x')}{dx'} - \phi(x')p(x')\frac{dG(x, x')}{dx'} \right]\Big|_a^b$$

If the boundary values in the original problem are specified as being equal to zero, then we choose $G(x, x')$ to satisfy the same conditions whereupon the boundary terms vanish. The solution can then be expressed as

$$\phi(x) = \int_a^b G(x, x')f(x')\, dx'$$

which describes the solution as the superposition of point sources having the amplitudes $f(x') \, dx'$. For non-zero boundary values, e.g. $d\phi/dx = c$, choosing the corresponding Green's function condition to be zero, e.g. $dG/dx = 0$, enables the boundary term to be evaluated from known quantities.

From equation (A.15) a further condition on the Green's function can be found to hold at the source $x = x'$

$$\lim_{\delta \to 0} \left[\int_{x'-\delta}^{x'+\delta} dx \, \frac{d}{dx} \left[p(x) \frac{dG}{dx} \right] + \int_{x'-\delta}^{x'+\delta} dx \, [q(x) + \lambda \sigma(x)] \, G \right] = \lim_{\delta \to 0} \int_{x'-\delta}^{x'+\delta} -\delta(x - x') \, dx$$

Since the functions q, σ, and G are continuous at the source, the integral involving the term $q + \lambda \sigma$ vanishes, leaving the result that

$$p(x') \frac{dG}{dx} \bigg|_{x'-}^{x'+} = -1 \qquad (A.16)$$

at the source.

Expressing the Green's function as an expansion of the complete set of eigenfunctions, we can show that

$$G(x, x') = -\sum_{n=1}^{\infty} \frac{\phi_n(x) \phi_n(x')}{\lambda - \lambda_n}$$

which has poles at $\lambda = \lambda_n$. These poles are known as the *spectrum* of the Green's function. For finite range problems the spectrum is discrete. However, as the range *is increased the poles converge until, for an infinite range, the spectrum becomes* continuous and the Green's function has branch-point singularities instead of poles. This technique of expressing the Green's function as an expansion of the eigenfunction set is used in chapter 5 to find the transverse eigenfunctions for a line source above a flat, dielectric slab.

A.3 Asymptotic evaluation of the radiation field: Rayleigh's method of stationary phase

Far-zone reflection

The integral to be evaluated for large values of r is

$$I = \int_0^{\infty} dk'_{y0} \, f(k'_{y0}) e^{i \mathbf{k}'_0 \cdot \mathbf{r}} \qquad (A.17)$$

where

$$\mathbf{k}'_0 = k'_x \hat{i} + k'_{y0} \hat{j}$$

$$\mathbf{r} = x \hat{i} + y \hat{j}$$

For small changes in k'_{y0} the function $f(k'_{y0})$ is slowly varying. However, since r is very large, the function $\exp(i\mathbf{k}'_0 \cdot \mathbf{r})$ oscillates rapidly for similar changes in k'_{y0}. Therefore the contributions from various points along the range $0 \leq k'_{y0} \leq \infty$ will tend to cancel. The only contributions will come from points where, to first order, $\mathbf{k}'_0 \cdot \mathbf{r}$ does not vary with small changes in k'_{y0}. Such points are known as *stationary phase points* and occur where

$$\frac{d(\mathbf{k}'_0 \cdot \mathbf{r})}{dk'_{y0}} = 0$$

The function $f(k'_{y0})$ need only be evaluated at the stationary phase points, leaving the integral evaluation of $\exp(i\mathbf{k}'_0 \cdot \mathbf{r})$ only.

Making the substitutions $x = r \sin \theta_s$ and $y = r \cos \theta_s$, the stationary phase points can be shown to occur when

$$\frac{d(\mathbf{k}'_0 \cdot \mathbf{r})}{dk'_{y0}} = r \left[\cos \theta_s - \frac{k'_{y0}}{k'_x} \sin \theta_s \right] = 0$$

i.e.

$$k'_x = k_0 \sin \theta_s \qquad\qquad k'_{y0} = k_0 \cos \theta_s$$

Expanding $\mathbf{k}'_0 \cdot \mathbf{r}$ in a Taylor series about the stationary phase points

$$\mathbf{k}'_0 \cdot \mathbf{r} = k_0 r + \frac{1}{2} \frac{d^2(\mathbf{k}' \cdot \mathbf{r})}{dk'^2_{y0}} \left(k'_{y0} - k_0 \cos \theta_s \right)^2 + \cdots$$

since the first derivative is zero. The second derivative is given by

$$\frac{d^2(\mathbf{k}' \cdot \mathbf{r})}{dk'^2_{y0}} = -\frac{r}{k_0 \sin^2 \theta_s}$$

Making the substitution

$$\alpha = \sqrt{\frac{r}{2k_0 \sin^2 \theta_s}} \left(k'_{y0} - k_0 \cos \theta_s \right)$$

the integral can be written as

$$I = f(k'_{y0} = k_0 \cos \theta_s) e^{ik_0 r} \sqrt{\frac{2k_0}{r}} \sin \theta_s \int_{-\beta}^{\infty} d\alpha \, e^{-i\alpha^2}$$

where $\beta = k_0 \cot \theta_s \sqrt{r/2k_0}$. Away from grazing angles $(\theta_s \neq \pm \frac{\pi}{2})$

$$\int_{-\beta}^{\infty} d\alpha \, e^{-i\alpha^2} \sim \int_{-\infty}^{\infty} d\alpha \, e^{-i\alpha^2} = \sqrt{\pi} e^{-i\frac{\pi}{4}}$$

and the asymptotic integral (A.17) can therefore be evaluated from the expression

$$I = f(k'_{y0} = k_0 \cos \theta_s) e^{i(k_0 r - \frac{\pi}{4})} \sqrt{\frac{2\pi k_0}{r}} \sin \theta_s \qquad (A.18)$$

Bibliography

[1] Abramowitz, M. and Stegun, I. A. (editors), *Handbook of Mathematical Functions* (National Bureau of Standards, Washington, D.C., 1964).

[2] Akkermans, E., Wolf, P. E., and Maynard, R., "Coherent backscattering of light by disordered media: Analysis of the peak line shape", Physical Review Let. **56** (14), pp. 1471–1474 (1986).

[3] Andreasen, M. G., "Scattering from parallel metallic cylinders with arbitrary cross-sections", I. E. E. E. Trans. Ant. Propag. **AP-12**, pp. 746–754 (1964).

[4] Bahar, E., "Radio wave propagation over a rough variable impedance boundary: Part II — application of full-wave analysis", I. E. E. E. Trans. Ant. Propag. **AP-20** (3), pp. 362–368 (1972).

[5] Bahar, E., "Depolarization of electromagnetic waves excited by distributions of electric and magnetic sources in inhomogeneous multilayered structures of arbitrarily varying thickness. full wave solutions", J. Math. Phys. **14** (11), pp. 1510–1515 (1973).

[6] Bahar, E., "Full wave solutions for the scattered radiation fields from rough surfaces with arbitrary slope and frequency", I. E. E. E. Trans. Ant. Propag. **AP-28** (1), pp. 11–21 (1980).

[7] Bahar, E., "Full wave solutions for the depolarization of the scattered radiation fields by rough surfaces of arbitrary slope", I. E. E. E. Trans. Ant. Propag. **AP-29** (3), pp. 443–454 (1981).

[8] Bahar, E., "Scattering cross-sections for random rough surfaces: Full wave analysis", Radio Science **16** (3), pp. 331–341 (1981).

[9] Bahar, E., "Review of the full wave solutions for rough surface scattering and depolarization: Comparisons with geometric and physical optics, perturbation, and two-scale hybrid solutions", J. Geophys. Res. **92** (C5), pp. 5209–5224 (1987).

[10] Bahar, E. and Fitzwater, M. A., "Full wave theory and controlled optical experiments for enhanced scattering and depolarization by random rough surfaces", Optics Communications **63** (6), pp. 355–360 (1987).

[11] Bahar, E. and Fitzwater, M. A., "Full-wave copolarized nonspecular transmission and reflection scattering matrix elements for rough surfaces", J. Opt. Soc. Am. A **5** (11), pp. 1873–1882 (1988).

[12] Bennett, H. E., "Specular reflectance of aluminized ground glass and the height distribution of surface irregularities", J. Opt. Soc. Am. A **53** (12), pp. 1389–1394 (1963).

[13] Bickel, W. S. and Bailey, W. M., "Stokes vectors, mueller matrices, and polarized scattered light", Am. J. Physics **53** (5), pp. 468–478 (1985).

[14] Bohren, C. F. and Huffman, D. R., *Absorption and Scattering of Light by Small Particles* (Wiley, New York, 1983).

[15] Brown, G. S., "A comparison of approximate theories for scattering from rough surfaces", Wave Motion **7**, pp. 195–205 (1985).

[16] Brown, G. S., "A scattering result for rough surfaces having small height but arbtrary slope", Wave Motion **12**, pp. 475–483 (1990).

[17] Brown, G. S., "A new approach to the analysis of rough surface scattering", (in press) (1991).

[18] Bruce, N. C. and Dainty, J. C., "Multiple scattering from random rough surfaces using the kirchhoff approximation", J. Mod. Optics **38** (3), pp. 579–590 (1991).

[19] Bruce, N. C. and Dainty, J. C., "Multiple scattering from rough dielectric and metal surfaces using the kirchhoff approximation", J. Mod. Optics **38** (8), pp. 1471–1481 (1991).

[20] Bruce, N. C., Sant, A. J., and Dainty, J. C., "Mueller matrix for rough surface scattering using the kirchhoff approximation", submitted to Optics Communications (1991).

[21] Cacoullis, S., *Infrared Optical Constants of Volatile Liquids*, PhD thesis, Imperial College, University of London (1988).

[22] Celli, V., Maradudin, A. A., Marvin, A. M., and McGurn, A. R., "Some aspects of light scattering from a randomly rough metal surface", J. Opt. Soc. Am. A **2** (12), pp. 2225–2239 (1985).

[23] Church, E. L. and Takacs, P. Z., "Effects of the non-vanishing tip size in mechanical profile measurements", submitted to Surface Topography (1991).

[24] Collin, R. E., *Field Theory of Guided Waves* (McGraw-Hill, New York, 1960).

[25] Collin, R. E., "Electromagnetic scattering from perfectly conducting rough surfaces", Presented at the URSI meeting on Electromagentic Scattering, Boston Univ. (1991).

[26] Dainty, J. C. (editor), *Laser Speckle and Related Phenomena* volume 9 of *Topics in Applied Physics* (Springer-Verlag, Berlin, 1975).

[27] Depine, R. A., "Rigorous formulation of scattering at a randomly varying impedance plane: General case of oblique incidence", submitted to I. E. E. E. Trans. Ant. Propag. (1991).

[28] Depine, R. A., "Scattering of light from one-dimensional random rough surfaces: A new antispecular effect in oblique incidences", submitted to J. Opt. Soc. Am. A (1991).

[29] DeSanto, J. A. and Brown, G. S., "Analytical techniques for multiple scattering from rough surfaces", In Wolf, E. (editor), *Progress in Optics XXIII* pp. 1–62, Elsevier (1986).

[30] deWolf, D. A., "Backscatter enhancement: Random continuum and particles", J. Opt. Soc. Am. A **8** (3), pp. 465–471 (1991).

[31] Dolan, M. B., *The Infrared Optical Constants of Powders and Liquids*, PhD thesis, Imperial College, University of London (1987).

[32] Egan, W. G. and Hilgeman, T., "Retroreflectance measurements of photometric standards and coatings.", Applied Optics **15** (7), pp. 1845–1849 (1976).

[33] Egan, W. G. and Hilgeman, T., "Retroreflectance measurements of photometric standards and coatings. part 2", Applied Optics **16** (11), pp. 2861–2864 (1977).

[34] Fung, A. K. and Chen, M. F., "Numerical simulation of scattering from simple and composite random surfaces", J. Opt. Soc. Am. A **2**, pp. 2274–2284 (1985).

[35] Goodman, J. W., *Statistical Optics* (Wiley, New York, 1985).

[36] Gough, P. T. and Boerner, W.-M., "Depolarization of specular scatter as an aid to discriminating between a rough dielectric surface and an 'identical' rough metallic surface", J. Opt. Soc. Am. **69**, pp. 1212–1217 (1979).

[37] Gray, P. F., "A method of forming optical diffusers of simple, known statistical properties", Optica Acta **25** (8), pp. 765–775 (1978).

[38] Grum, F. and Luckey, G. W., "Optical sphere paint and a working standard of reflectance", Applied Optics **4** (11), pp. 2289–2294 (1965).

[39] Hapke, B. W., "A theoretical photometric function for the lunar surface", J. Geophys. Res. **68** (15), pp. 4571–4586 (1963).

[40] Hapke, B. W. and van Horn, H., "Photometric studies of complex surfaces, with applications to the moon", J. Geophys. Res. **68** (15), pp. 4545–4570 (1963).

[41] Jakeman, E., "Enhanced backscattering through a deep random phase screen", J. Opt. Soc. Am. A **5** (10), pp. 1638–1648 (1988).

[42] Jakeman, E., "The physical optics of enhanced backscattering", In Nieto-Vesperinas, M. and Dainty, J. C. (editors), *Scattering in Volumes and Surfaces* pp. 111–123, North-Holland (1990).

[43] Kaveh, M., Rosenbluh, M., Edrei, I., and Freund, I., "Weak localization and light scattering from disordered solids", Physical Review Let. **57** (16), pp. 2049–2052 (1986).

[44] Kim, M.-J., Dainty, J. C., Friberg, A. T., and Sant, A. J., "Experimental study of enhanced backscattering from one- and two-dimensional random rough surfaces", J. Opt. Soc. Am. A **7** (4), pp. 569–577 (1990).

[45] Kuga, Y. and Ishimaru, A., "Retroreflectance from a dense distribution of spherical particles", J. Opt. Soc. Am. A **1** (8), pp. 831–835 (1984).

[46] Lagendijk, A., van Albada, M. P., and van der Mark, M B., "Localization of light: The quest for the white hole", Physica **140A**, pp. 183–190 (1986).

[47] Maradudin, A. A., Lu, J. Q., Michel, T., Gu, Z.-H., Dainty, J. C., Sant, A. J., Méndez, E. R., and Nieto-Vesperinas, M., "Enhanced backscattering and transmission of light from random surfaces on semi-infinite substrates and thin films", Waves in Random Media **1** (3), pp. S129–S141 (1991).

[48] Maradudin, A. A., Méndez, E. R., and Michel, T., "Backscattering effects in the elastic scattering of *p*-polarized light from a large amplitude random metallic grating", Optics Letters **14** (3), pp. 151–153 (1989).

[49] Maradudin, A. A., Michel, T., McGurn, A. R., and Méndez, E. R., "Enhanced backscattering of light from a random grating", In *Annals of Physics* **203** pp. 255–307, Academic Press (1990).

[50] Maystre, D. and Dainty, J. C. (editors), *Modern Analysis of Scattering Phenomena* (I. O. P., 1991), special issue of Waves in Random Media **1** (3), 1991.

[51] Maystre, D. and Rossi, J. P., "Implementation of a rigorous vector theory of speckle for two-dimensional microrough surfaces", J. Opt. Soc. Am. A **3**, pp. 1276–1282 (1986).

[52] Maystre, D., Saillard, M., and Ingers, J., "Scattering by one- and two-dimensional randomly random surfaces", Waves in Random Media **1** (3), pp. S143–S155 (1991).

[53] McGurn, A. R. and Maradudin, A. A., "Localization effects in the elastic scattering of light from a randomly rough surface", J. Opt. Soc. Am. B **4** (6), pp. 910–926 (1987).

[54] McGurn, A. R., Maradudin, A. A., and Celli, V., "Localization effects in the scattering of light from a randomly rough grating", Physical Review B **31**, pp. 4866–4871 (1985).

[55] Méndez, E. R. and O'Donnell, K. A., "Observation of depolarization and backscattering enhancement in light scattering from gaussian random surfaces", Optics Communications **61** (2), pp. 91–95 (1987).

[56] Michel, T. R., *Enhanced Backscattering of Light from a Randomly Rough Grating*, PhD thesis, University of California (1990).

[57] Nicodemus, F. E., "Directional reflectance and emissivity of an opaque surface", Applied Optics **4** (7), pp. 767–773 (1965).

[58] Nicodemus, F. E., "Reflectance nomenclature and directional reflectance and emissivity", Applied Optics **9** (6), pp. 1474–1475 (1970).

[59] Nieto-Vesperinas, M., "Depolarization of electromagnetic waves scattered from slightly rough random surfaces: A study by means of the extinction theorem", J. Opt. Soc. Am. **72** (5), pp. 539–547 (1982).

[60] Nieto-Vesperinas, M. and Dainty, J. C. (editors), *Scattering in Volumes and Surfaces* (North-Holland, 1991).

[61] Nieto-Vesperinas, M., Sánchez-Gil, J. A., Sant, A. J., and Dainty, J. C., "Light transmission from a randomly rough dielectric diffuser: Theoretical and experimental results", Optics Letters **15** (22), pp. 1261–1263 (1990).

[62] Nieto-Vesperinas, M. and Soto-Crespo, J. M., "Monte-carlo simulations for scattering of electromagnetic waves from perfectly conductive random rough surfaces", Optics Letters **12** (12), pp. 979–981 (1987).

[63] O'Donnell, K. A. and Méndez, E. R., "Experimental study of scattering from characterized random surfaces", J. Opt. Soc. Am. A **4** (7), pp. 1194–1205 (1987).

[64] Oetking, P., "Photometric studies of diffusely reflecting surfaces with applications to the brightness of the moon", J. Geophys. Res. **71** (10), pp. 2505–2513 (1966).

[65] Pattanayak, D. N. and Wolf, E., "General form and a new interpretation of the Ewald-Oseen extinction theorem", Optics Communications **6** (3), pp. 217–220 (1972).

[66] Plonsey, R. and Collin, R. E., *Principles and Applications of Electromagnetic Fields* (McGraw-Hill, New York, 1961).

[67] Qu, D. N. and Dainty, J. C., "Polarization dependence of dynamic light scattering by dense disordered media", Optics Letters **13** (12), pp. 1066–1068 (1988).

[68] Saillard, M. and Maystre, D., "Scattering from metallic and dielectric rough surfaces", J. Opt. Soc. Am. A **7** (6), pp. 982–990 (1990).

[69] Sant, A. J., "Variation with wavelength of light scattered from identical, randomly rough metal and dielectric diffusers", In *ICO-15 (Conference Summaries)* (1990), paper 2B3.4.

[70] Sant, A. J., Dainty, J. C., and Kim, M.-J., "Comparison of surface scattering between identical, randomly rough metal and dieletric diffusers", Optics Letters **14** (21), pp. 1183–1185 (1989).

[71] Schelkunoff, S.A., "Conversion of Maxwell's equations into generalized telegraphist's equations", Bell Syst. Tech. J. **34**, pp. 995–1043 (1955).

[72] Shen, J. and Maradudin, A. A., "Multiple scattering of waves from random rough surfaces", Physical Review B **22**, pp. 4234–4240 (1980).

[73] Soto-Crespo, J.-M. and Nieto-Vesperinas, M., "Electromagnetic scattering from very rough random surfaces and deep reflection gratings", J. Opt. Soc. Am. A **6** (3), pp. 367–384 (1989).

[74] Soto-Crespo, J.-M., Nieto-Vesperinas, M., and Friberg, A. T., "Scattering from slightly rough random surfaces: A detailed study on the validity of the small perturbation method", J. Opt. Soc. Am. A **7** (7), pp. 1185–1201 (1990).

[75] Tapster, P. R., Weeks, A. R., and Jakeman, E., "Observation of backscattering enhancement through atmospheric phase screens", J. Opt. Soc. Am. A **6** (4), pp. 517–522 (1990).

[76] Thomas, T. R. (editor), *Rough Surfaces* (Longman, New York, 1982).

[77] Thorsos, E. I. and Jackson, D. R., "Backscattering enhancement with the dirichlet boundary condition", Presented at the Workshop on Enhanced Backscatter, Boston Univ. July 1989.

[78] Tsang, L. and Ishimaru, A., "Backscattering enhancement of random discrete scatterers", J. Opt. Soc. Am. A **1** (8), pp. 836-839 (1984).

[79] van Albada, M. P. and Lagendijk, A., "Observation of weak localization of light in a random medium", Physical Review Let. **55**, pp. 2692-2695 (1985).

[80] van Albada, M. P., van der Mark, M. B., and Lagendijk, A., "Observation of weak localization of light in a finite slab: Anisotropy effects and light-path classification", Physical Review Let. **58** (4), pp. 361-364 (1987).

[81] van de Hulst, H. C., *Light Scattering by Small Particles* (Dover, New York, 1981).

[82] Welford, W. T., "Optical estimation of statistics of surface roughness from light scattering measurements", Optics Quant. Elec. **9**, pp. 269-287 (1977).

[83] Wolf, P. E., Maret, G., Akkermans, E., and Maynard, R., "Optical coherent backscattering by random media: An experimental study", J. Phys. (France) **49**, pp. 63-75 (1988).

[84] Wright, W. D., *The Measurement of Colour* (Hilger and Watts, London, 1958).